CRANFIELD UNIVERSITY

DAWID BOSAK

NEW TECHNIQUES FOR THE ANALYSIS OF FLEXIBLE
OPERATION OF GAS TURBINE BASED SYSTEMS

SCHOOL OF AEROSPACE, TRANSPORT AND
MANUFACTURING
Gas Turbine Technology

Doctor of Philosophy
Academic Year: 2013–2017

Supervisor: Professor Pericles Pilidis
April 2017

CRANFIELD UNIVERSITY

SCHOOL OF AEROSPACE, TRANSPORT AND
MANUFACTURING
Gas Turbine Technology

Doctor of Philosophy

Academic Year: 2013–2017

DAWID BOSAK

New Techniques for the Analysis of Flexible Operation of
Gas Turbine Based Systems

Supervisor: Professor Pericles Pilidis
April 2017

I would like to dedicate this thesis to my loving family

vi

Declaration

I hereby declare that except where specific reference is made to the work of others, the contents of this dissertation are original and have not been submitted in whole or in part for consideration for any other degree or qualification in this, or any other university. This dissertation is my own work and contains nothing which is the outcome of work done in collaboration with others, except as specified in the text and Acknowledgements. This dissertation contains fewer than 45,000 words including appendices, bibliography, footnotes, tables and equations and has fewer than 100 figures.

Dawid Bosak
April 2017

Acknowledgements

First and most foremost I wish to thank my academic supervisor and mentor Professor Pericles Pilidis, the Head of Propulsion Engineering Centre at Cranfield University. His kindness, guidance and support has deeply influenced not only my PhD research, but also my personal development. It was the trust and freedom to explore that Professor Pilidis has given me, and over the years I experimented with many ideas in search to find a way in which I could make a positive impact on our society. Having a mentor who encouraged me, pushed me to further explore my abilities, and to whom I can always reach out for constructive advise is the most valuable and effective way to grow personally and professionally. And therefore, I feel very lucky and honoured to have experienced it.

I would like to express my deep gratitude to Christer Bjorkqvist, the Managing Director of the European Turbine Network (ETN) organisation in Belgium, who provided me with the wonderful opportunity to voluntarily join his team in September 2015, and get involved in various ETN activities across Europe. Christer has been a great mentor to me for all these years, who has majorly contributed to my understanding of the European power generation market. Thanks to many of our interesting discussions and brainstorming sessions, I gained appreciation of the current state-of-art and future prospects of European power generation, which helped me to focus on high impact issues during the years of my PhD research.

I gratefully acknowledge the Flex-E plant industrial consortium for funding my PhD, and providing me with all the help that I needed to complete my work. I would like to thank my industrial mentors Stuart Simpson, the Technical Head of Boiler Engineering, and Martin Faulkner, the Technical Head of Plant Modelling, at Uniper Technologies in the UK, who have guided me through the technical aspects of my PhD work. Their valuable support and commitment to my research has helped me in focusing on important and relevant technical matters.

I am especially grateful to Professor Theodosios Alexander, Dr Amin Rezaienia and Dr Gordon Paul from Queen Mary University of London for their support and invaluable feedback throughout my research. My deep appreciation also goes to Dr Bjorn Cleton from Cranfield University who helped and supported me in numerous ways during various stages of my PhD. A special thank you to Gréta Doláková for always being so supportive

Abstract

In the current European energy market, gas power plants are required to operate in cyclical modes to fill the gaps in renewable energy supply. Renewable sources have dispatch priority due to their relatively low variable operational costs. However, because of their high unpredictability, conventional power plants such as Combined Cycle Power Plants (CCPP) now operate with frequent load changes to fill the gaps in supply by participating in the balancing market. Substantial efforts to develop innovative solutions to the new challenges are invested by the commercial and research community, where investigation into improving understanding of complex part-load operation is of utmost techno-economical importance.

To date, main techniques used to simulate part-load operation of CCPPs were developed in the late twentieth century and are based on cumbersome and iterative methods requiring initial approximation of variables. In the wake of recent large scale renewable power installations, these techniques are not effective enough to carry complex optimisation studies to adopt CCPPs to quickly evolving market conditions. A number of improvements have been proposed; however, these modified methods are not able to cope with the required complexity and flexibility of studying various component layout optimisations and their impact on techno-economic performance.

The current work pursues a novel method for part-load performance estimation of CCPPs, which is less complex, more effective, and can be seamlessly applied to any further optimisation studies. Initially the technique has been developed based on binary-coded genetic algorithm. The method enables simulation of part-load performance without the need for making initial guess of variables, thus simplifying the procedure. The method has been validated against commercial software showing good agreement in the results. However, it has been concluded that the method does not provide a long term benefit to the research community because it is fundamentally based on search space iterations with unavoidable residual (error) in the solution, and requiring significant computational time. The complex optimisation studies conducted by other authors require a much simpler and flexible method. This led to the development of a novel Direct Solution Method (DSM), which provides a simple solution with zero residual without need for cumbersome iterations. The DSM has been validated against commercial software showing good agreement; thus proving to be a promising alternative to the existing techniques.

xi

To improve understanding of part-load gas turbine operation, a set of comprehensive maps have been developed. A Gas Turbine Operational Map allows study and visualisation of complex trade-offs arising from gas turbine load reduction strategies. The load change strategy will determine the life consumption of critical gas turbine components, which led to the development of a Life Consumption Map which takes into account low cycle fatigue and creep mechanisms.

Keywords

Contents

List of Figures

List of Tables

Nomenclature

Roman Symbols

A	surface area
Cp	constant specific heats
E	Young's modulus of elasticity
h	enthalpy
K	cyclic strength coefficient
l	length
$\dot{m}$	mass flow rate
m	mass
N	number of cycles
n	cyclic strain hardening exponent
P	pressure
$\dot{Q}$	heat rate
R	gas constant
r	blade radius
S	entropy
T	temperature
t	time
U	overall heat transfer coefficient
V	velocity

Greek Symbols

β DSM degradation factor

Δ change in the value of a variable

ε strain

η thermal efficiency

ρ density

σ stress

ω rotational speed

Superscripts

D   design-point condition

OD   off-design condition

Subscripts

amb   ambient conditions

ap   approach point

blade   conditions at blade surface

cooling   conditions of cooling gas

exhaust   gas turbine exhaust conditions

f   conditions at a point of failure

g   gas

in   inlet

isen   isentropic

lm   log mean

out   outlet

pp   pinch point

root   blade root

s steam

stack   heat recovery steam generator stack

tip   blade tip

Acronyms / Abbreviations

CCPP   combined cycle power plant

CE   cooling effectiveness

DSM   direct solution method

FV   fitness value

GA   genetic algorithm

HRSG   heat recovery steam generator

ISA   international standard atmosphere

LMP   Larson-Miller parameter

NTU   number of transfer units

PO   power output

SN   station number

TET   turbine entry temperature

TSO   transmission system operator

VIGV   variable inlet guide vane

Chapter 1

Motivation and introduction

The fundamental reason for this PhD is rooted in the specific needs created by changing worldwide energy market conditions. In recent years people are acknowledging the fear of climate change, as the result of which the world is currently undergoing major transformations, called by many the post-industrial revolution. To understand how the world has arrived at the current state of panic, and what drives the current struggles and uncertainties in the power generation market, it is necessary to study the chain of past events to gain a big picture view on the current issues and make informed decisions on what potential areas of novelty in research could be exploited. Winston Churchill once said "The farther backward you can look the farther forward you are likely to see". Keeping this in mind, a thorough overview of how the Earths climate has changed in the past and what drives the fear during current times is presented in this chapter. Then potential areas of novelty are recognised and identified, and the manner in which this PhD thesis contributes to knowledge with respect to current problems is presented in chapter 2.

Dr. Bethan Davies, a Glaciologist and lecturer at University of London said "In order to understand our climate, it is very important to look at the long-term view". Therefore, as many have acknowledged the importance of studying the past, in the following introductory chapter the 800,000 years of the past climate change is discussed with a focus on the current times and why today climate is an alarming issue.

1.1   The climate is changing

In paleoclimatology, it is an important work of climate scientists to reconstruct past climate conditions and establish patterns in climate data using proxies such as ice cores, microfossils in marine sediment cores, or annual growth rings in trees. The ice cores are cylinders of ice drilled notably in Greenland and Antarctica, where the snow accumulates in an ordered fashion while preserving stratigraphic layers. Scientists then extract samples of air bubbles from the ice cores to study worlds ancient atmosphere. This method provides records about air chemistry e.g. greenhouse gasses, going back over 650,000

1

years [1] (or 800,000 years [2]). The detailed records of temperature change are obtained by measuring changing concentrations of stable isotopes of oxygen or hydrogen (deuterium) across the length of the ice core.

Scientists began to drill ice cores the late 1960s, and the oldest records extends to 130,000 years in Greenland and 800,000 years in Antarctica. Figure 1.1 shows a continuous composite record of carbon dioxide measurements taken from two locations on the Antarctic plateau near Dome C where a drilled depth of 3,270 meters was reached by the European Project for Ice Coring in Antarctica (EPICA) providing records from 1950 and going back 800,000 years [3]. The second location is near Law Dome providing records from 2004 and going back 2,000 years [4]. To illustrate the most recent CO_2 growth, I have further supplemented the data with the longest direct measurements of carbon dioxide concentration in the Earths atmosphere recorded at Mauna Loa Observatory in Hawaii from 1958 to April 2016 [5].

The measurements of carbon dioxide and estimated temperature anomalies in figure 1.1 noticeably reveal eight long cold glacial states when we had ice ages with periodicity of around 100,000 years. Warmer climate periods between glacial are called interglacial, and we are currently in the Holocene epoch that begun at the end of the last ice age approximately 11,500 years ago during which the ice sheet reached as far as northern Germany. The CO_2 is a heat trapping gas acting as a thermostat regulating earth's atmospheric temperature. Thus, increase in concentration stimulates water vapour returns to the atmosphere, which has helped to melt the glaciers in each glacial cycles. Comparing to other greenhouse gases such as CH_4 or N_2O, the CO_2 remains in the atmosphere the longest. Therefore, It is notably evident and alarming that recent CO_2 concentration in the atmosphere significantly changed the path of a glacial cycle.

There are three independent international centres that calculate and provide global, northern and southern hemisphere average temperatures: Climatic Research Unit (CRU) at University of East Anglia in collaboration with the Hadley Centre at UK Met Office (HadCRUT) in the UK, NASA Goddard Institute for Space Studies (GISS) in the USA, and National Climatic Data Center (NCDC), as part of National Oceanic and Atmospheric Administration (NOAA) in the USA. Despite the fact that these centers use different methods to collect records and calculate global average temperature, the data shows a common agreement that the world is warming at warring rate since 1970. The top of figure 1.2 illustrates the famous hockey stick, which clearly indicates that the rate of change in carbon dioxide composition is dramatically increasing since the pre-industrial times when the industrial revolution begun in 1750 and fossil fuels become widely used. The bottom of figure 1.2 shows a 12 month moving average of global average temperature anomaly from NASA GISS center from 1980 to April 2016, supplemented with a reconstruction of Northern Hemisphere temperature anomalies provided by Moberg et al. for a period from year 1 to 1979 [7]. For completeness I have further supplemented a 50 years moving aver-
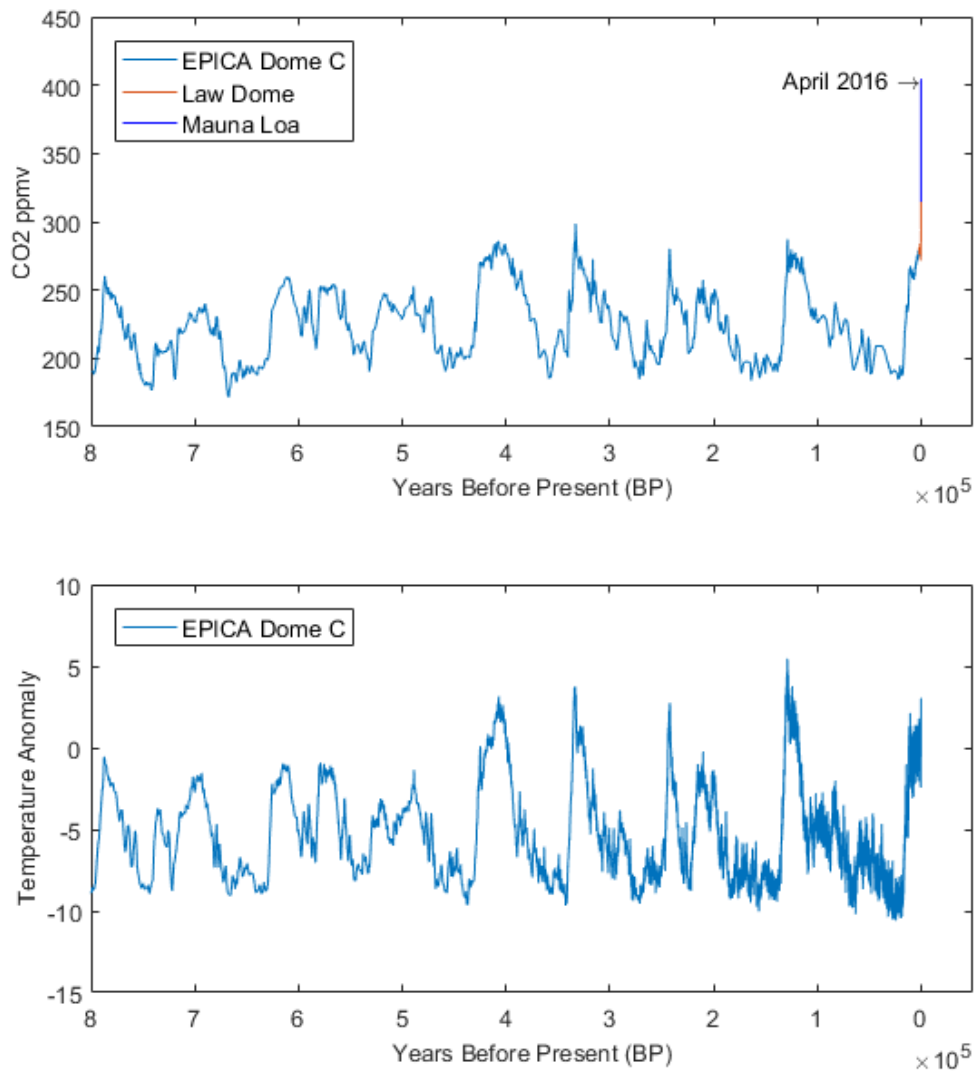
Fig. 1.1 (Top) Composite measurements of CO2 from the EPICA Dome C Ice Core [3], Law Dome Ice Core [4], and Mauna Loa Observatory in Hawaii [5]. (Bottom) Temperature anomalies estimated from deuterium measurements from the EPICA Dome C Ice Core [6] relative to the last 1,000 years average

age of estimated temperature from EPICA Dome C ice core providing records up to 1912.

There are two distinct periods in the bottom of figure 1.2: the Medieval Warm Period between approximately 950 to 1250 during the European Middle Ages, and the Little Ice Age conventionally defined as a period from 1300 to 1850. During the environmentally stimulated Little Ice Age the climate deteriorated substantially when the coldest period from 1645 and 1715 had a drop in average winter temperatures in the northern hemisphere as much as 1^oC below 1961 to 1990 level. Mann suggested that there is evidence that 17th century was the coldest century in Europe; however, it does not appear to have been unusually cold in other parts of the world [8]. The effect of the cooling has been dramatic and widely spread across Europe. Colder conditions influenced crop failures in the northern areas of Europe and increased disease and child mortality during that period. In France, a number of farms and villages were lost due to advancing front of the Mont Blanc glacier. In the UK, due to the environmental conditions and slow flowing it was not uncommon for River Thames to freeze up to two months at time giving birth to the Thames Frost Fairs in 1607, which was a spectacle full of shops, pubs, ice skating rinks, football pitches, bowling matches, shoemakers, barbers, and every possible form of entertainment including a parading elephant, all set up on the thick frozen river. During winter of 1814, Londoners awoke to find that temperatures fell to -13^oC bringing chaos on the roads and this year was also said to be the last ever to hold the Thames Frost Fairs. Thereafter, the climate had started to warm to the current state which makes freezing of River Thames very difficult to imagine. Geoffrey Parker, a Professor of history, suggested that there are lessons that we can learn from the Little Ice Age and apply them to tackle current global warming crisis [9]. Perhaps unlike our ancestors who faced the opposite climate changes to what we experience today, we have the resources and the technology to address it and embrace it.

It is widely acknowledged that the current debate on the climate change was ignited by Dr. James E. Hansen, director of NASAs Goddard Institute for Space Studies. On 23 June, 1988, he and other scientists testified before the U.S. Senate Energy and Natural Resources Committee that results from the climate study suggest with 99% confidence that the trend in global warming did not follow natural variations but it was caused by a human intervention [10]. It was the first time when a lead-scientist made a link between climate warming and human activities. He showed that if the trace gas emissions continue to grow at rates typical in the 1968 to 1988 period, the Earth will experience 1.5^oC increase (1951-1980 base period) in annual mean global surface air temperature by 2019.

Thereafter, for nearly 28 years the world is trying to cope with the increasing rate of global warming with most recent efforts and actions accelerated by the fact that increasing number of people are acknowledging the fear of changing climate. However, most recently it becomes apparent that Earths response to the changing conditions could be irreversible. Ceballos et al. concluded that exceptionally rapid loss of biodiversity over
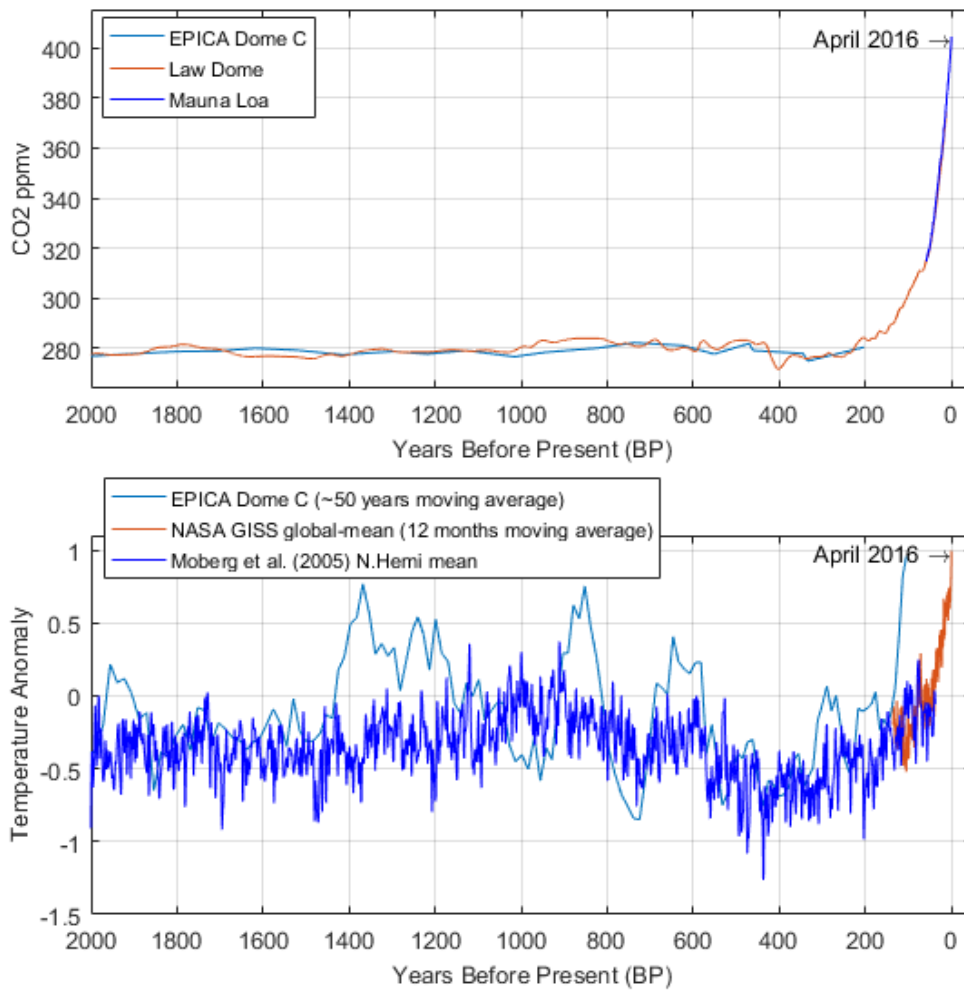
Fig. 1.2 2000 years of CO2 and temperature variations

Fig. 1.3 'A Frost Fair on the Thames at Temple Stairs', 1684

the last few centuries with rates increasing significantly from the XIX century indicates that Earth has entered a new extinction phase caused by climate change and deforestation which are mainly influenced by human activities [11]. It is thought provoking and quite alarming that in April 2016 global average temperature reported by three independent centers (discussed in the previous paragraphs) was in the range of $1.063^oC - 1.111^oC$. This indicates that the world has not done enough yet to diverge from the scenario originally proposed by Dr. Hansen in 1988. And as pointed out by many, the consequences of failing to limit global temperature raise would be disastrous.

On 22 April 2016, the date also designated as International Mother Earth Day, a historic Paris Agreement was signed by 171 countries in New York, USA, which is currently a record number for a new international treaty [12]. The treaty is regarded as highly significant and important for the development of international climate change law. Ban Ki-moon, UN Secretary General, said: "Paris will shape the lives of all future generations in a profound way - it is their future that is at stake". One of the main objectives of the agreement is according to Article 2, paragraph 1, and Article 4, paragraph 1, respectively:

> "Holding the increase in the global average temperature to well below 2^oC above pre-industrial levels and to pursue efforts to limit the temperature increase to 1.5^oC above pre-industrial levels, recognizing that this would significantly reduce the risks and impacts of climate change"

> "In order to achieve the long-term temperature goal set out in Article 2, Parties aim to reach global peaking of greenhouse gas emissions as soon as possible, recognizing that peaking will take longer for developing country Parties,

and to undertake rapid reductions thereafter in accordance with best available science, so as to achieve a balance between anthropogenic emissions by sources and removals by sinks of greenhouse gases in the second half of this century, on the basis of equity, and in the context of sustainable development and efforts to eradicate poverty."

This is a very ambitious global aim, which if achieved will completely transform our energy industry into sustainable, flexible, and environmentally friendly power generation solutions with net-zero emissions. Some have coined a term post-industrial revolution to reflect massive changes and uncertainty that many are now facing. However, the views on the success of the Paris Agreement are divided. Researchers from the Climate Action Tracker (CAT) released analyses which show that not enough progress has been done to date making the goal to hold global warming below 2^oC infeasible and 1.5^oC out of reach [13]. Christiana Figueres, executive secretary of the UN Framework Convention on Climate change, said the Paris Agreement is 10 years too late, and it has really put an incredible amount of pressure onto innovation, onto energy evolution. In contrary, Sir Richard Branson positively commented that committing to long-term net zero emissions goals will unleash new innovations, mobilise large-scale investment, and re-shape consumer behaviour, all of which will create new jobs and economic growth [14]. Bill Gates said that "energy miracle" is coming and it will change the world.

1.2   Identifying the overall direction of research

In the conclusion of the previous section, the renewable/clean power generation capacity is increasing in the global attempt to de-carbonise power generation market. However, the irregular nature of renewable sources e.g. wind and solar, presents a great challenge to balance when these sources are not available and the demand for electricity needs to be satisfied. The extent to which renewable sources are variable was experienced by Spain, where on the 17 September 2012 wind covered 1% of the instantaneous demand and one week later the production increased to 64% of the instantaneous demand [15]. The variable nature of renewables is expensive to balance; e.g. UK's Transmission System Operator, National Grid, reported total cost of balancing increased from £642M (2005-06) to £1.08B (2015-16), with projections further to reach £2B by 2020 [16]. These projections demonstrate that flexible operation of conventional fossil power stations is expected to continue playing a key role in the power generation market. The Combined Cycle Power Plants (CCPP) technology provides a promising solution and is expected to continue growing as a flexible balancing technology to the renewable capacity.

Combined Cycle Power Plants represent a 20% share of the total European power generation capacity, as reported by the Centralised Issuing Office (CIO). They contain gas turbine engines running on natural gas, which provide a promising low emissions solution

to balance unpredictable renewable power due to their superior load response characteristics compared to other conventional power plants such as coal or nuclear. Most of the current CCPPs were built decades ago and were not designed to operate in cyclic modes, which are now suffering frequent load changes to balance the grid. Consequently, these recent changes in market conditions lead to major cost-curring modes implemented by power plant owners, where even the most efficient power stations are being mothballed. This results in high consumer electricity prices; the UK Government reported a nearly 65% increase in average annual domestic electricity bills in the last 10 years. Therefore, more action is needed to stabilise the European energy market.

When the power plant is operated at load level other than what it was designed for, it is said to operate at *part-load* or at *off-design*. The need for research in performance analysis and optimisation of part-load operation of gas turbines and CCPPs has been identified by a number of authors. In 2009, Variny et al. argued that much more attention in published literature is paid to the analysis and optimisation of CCPP at full-load operation than to the part-load operation [17]. More recently in 2011, Rovira et al. stressed that most of the CCPP thermoeconomic published research focuses on the analyses, optimisation or design of CCPP at a design-point [18]. However, due to recent changes in the power generation market conditions and relatively fast response characteristics to load changes of CCPP, there is a need for more research in the thermoeconomic optimisation of CCPP at part-load operation. He also pointed out that the current economic models do not consider the decrease in CCPP thermal efficiency caused by part-load operation, and further research is needed to account for this change at off-design conditions. In 2012, Zachary conduced a study on the manner in which a CCPP is impacted by current power generation market conditions [19]. He states that due to continued growth in the renewable power generation portfolio, the gas turbine industry role will also grow to compensate for the irregular nature of renewable sources. Therefore, the cycling operation will play an important role in the future CCPP operation, and more research is needed to understand part-load performance. Most recently in 2013, Ol'khovskii published a comprehensive review of modern gas turbine and CCPP technology, and the progress achieved in this field by major Original Equipment Manufacturers (OEMs) such as Siemens, Mitsubishi, GE, and Alstom [20]. He analysed the objectives that these companies set for themselves for the near and more distant future, and concluded that prospective gas turbines and CCPPs are being developed for use in the variable part of load schedule with frequent and fast start-ups. This demonstrates that the industry is keen on improving CCPP operational flexibility, as it is a promising technology to pair with renewable energy sources.

It is, therefore, an objective of this thesis to investigate and innovate towards improving our current understanding of flexible CCPP operation. Two research questions have been formed to guide and structure the decisions and choices made throughout the duration of the PhD research.

Research question 1: how can we improve current techniques used to design and analyse complex performance trade-offs in gas turbine flexible operation?

Research question 2: are existing modelling techniques for CCPP off-design performance sufficient given current demands for flexible operation?

1.3   Novelty of this thesis

In addressing these research questions, the following novel contributions have been made:

- Development of a gas turbine Operational Flexibility Map (chapter 3). The technique allows for quick assessment of complex performance trade-offs in part load operation.

- Development of a gas turbine Life Consumption Map (chapter 3). The technique allows for quick assessment of life consumption of critical gas turbine components due to low cycle fatigue and creep mechanisms.

- New application of Genetic Algorithm as an alternative to traditional Newton-Raphson method with objective to solve a system of non-linear equations for off-design CCPP performance (chapter 5). This method allows for estimation of off-design performance without a need for making initial guess of selected variables.

- Development of a novel Direct Solution Method (DSM) for design and off-design performance modelling of bottoming water/steam cycle (chapters 4 and 6). The method provides less complex, and more accurate with zero residual (error) solution as compared to existing techniques.

1.4   A guide through the thesis

Chapter 1. A big picture view is presented on the topic of climate change. The motivation for this thesis is discussed and a gap in knowledge identified. The chapter concludes with a statement of novelty.

Chapter 2. An exhaustive description of the field is presented. The discussion begins with overview of existing techniques used for modelling CCPPs in off-design condition, with a focus on their advantages and disadvantages. Opinions and feedback from authors in published literature are accounted for, which guides development of potential solutions to improve existing techniques.

Chapter 3. Gas turbine load reduction strategies are investigated, and a novel method is presented. The Operational Flexibility Map allows for easier and more comprehensive

analysis of off-design operation of gas turbine systems. In the second half of the chapter Life Consumption Maps are developed to help plant operators estimate damage of critical gas turbine components due to low cycle fatigue and creep.

Chapter 4. Water/steam bottoming cycle is analysed in design-point operation. A flexible and robust algorithm is developed, which allows for modular modelling of various steam cycle layouts. In the second part of the chapter a novel Direct Solution Method for design point operation is developed and discussed.

Chapter 5. A new application is developed and discussed which applies Genetic Algorithm methodology to solve for off-design performance parameters of Combined Cycle Power Plants. Although the method demonstrates good agreement against validation trials, it is concluded that the method does not provide a long term benefit to part-load performance modelling of CCPP systems. As a result a new method is developed and discussed in chapter 6.

Chapter 6. Capabilities of the novel Direct Solution Method discussed in chapter 4 for design-point modelling are here expanded into the off-design regime. Model equations are derived from fundamental heat transfer and energy balance formulations. The results are validated against commercial PROATES and Ebsilon software showing good agreement.

Chapter 7. Conclusions and discussions about the novel results of this thesis, and how they link to the motivation discussed in chapter 1.

Chapter 2

Literature review

The objective of this chapter is to establish a theoretical framework of the subject area. The existing relevant techniques are critically reviewed and academic arguments of other authors are taken into account. The subject area is presented first in broad terms, with subsequent detailed discussions in the problem area. The chapter concludes with a summary of the current state of the research and clear demonstration of the gap in knowledge.

2.1 Gas turbines

2.1.1 Theory of operation

Most of the published part-load performance work studies the effect of two engine configurations, single-shaft and two-shaft, due to their different performance characteristics and common use in the power generation industry. Generally gas turbines used in CCPP have a single-shaft configuration. In this configuration a turbine drives both the compressor and the output load, and the shaft must rotate at synchronous speed irrespective of power level. Another configuration used in CCPP is aero-derivative multi-shaft gas generator and free power turbine. In this configuration, inside the gas generator, a turbine drives the compressor and a free power turbine on a separate shaft drives the output load. Unlike in the single-shaft configuration, the gas generator speed reduces with reduction in load. Detailed description of part-load performance parameters for single-shaft, and two-shaft gas turbine engines can be found in [21], [22], and [23]. The gas turbine control system controls the turbine entry temperature (TET) and the angle of the variable inlet guide vanes (VIGVs) to vary the power at part-load operation. Since TET is very difficult to measure directly, it is controlled by an algorithm that relates it to exhaust temperature, engine pressure ratio, air mass flow rate, and compressor exit temperature. Currently, there are two commonly used load-control strategies: a fuel-flow control and variable inlet guide vanes control. The latter can be further classified into control strategies which keep either exhaust temperature or turbine entry temperature constant. It is important to mention that the single and two-shaft engines react differently to the same load control strategies. In-

depth information on these load-control strategies can be found in [24], [25], and general principles of gas turbine control systems can be found in [21].

Kim at al. published a comparative analysis of part-load performance for single-shaft and two-shaft gas turbine engines [26]. He investigated engine part-load performance, recording TET, turbine exhaust temperature, engine pressure ratio, fuel flow rate, and exhaust gas mass flow rate. Two control strategies for changing load settings were used: fuel-flow control and VIGV control. The VIGVs are variable geometry stator blades fitted at the first few stages of a low pressure compressor. By closing VIGVs, the engine swallowing capacity is effectively reduced, which by definition reduces the amount of power output. Most of the large industrial gas turbine engines have 1-4 rows of VIGVs, which allow for up to 30% airflow reduction and corresponding 50% power reduction. Haglind studied the effect of part-load control strategy on a gas turbine performance for single and two-shaft configurations for a marine engine application [27]. The aim was to maintain gas turbine exhaust temperature to the extent possible in part-load by using a variable load area control strategy. In this approach the heat recovery capability in the heat recovery steam generator (HRSG) is maintained, while minimising decrease in gas turbine thermal efficiency. There exists a trade-off between optimum gas turbine load control strategy and performance of the bottoming steam cycle. Therefore, Kim studied the effect of control strategy on the part-load performance of CCPP [28]. He investigated effects of gas turbine engine performance and three load control strategies on CCPP operation: 1) fuel-flow control, 2) VIGV control up to 30% air flow reduction at constant TET and 3) VIGV control up to 15% air flow reduction at constant exhaust temperature. Kim concluded that the type of control strategy and range of VIGV control greatly affects the average combined cycle performance, and it suggested that care should be taken to adopt a control strategy appropriate for the load characteristics of the power plant. Similar findings have also been published by Haglind for marine applications [29].

During the operational life of a CCPP, the overall performance deteriorates. The reduction in maximum available power, increase in specific fuel consumption, and increase in turbine operating temperature with a consequent reduction in hot section component life will occur over time as the components of the CCPP degrade. Detailed background information on performance deterioration can be found in [21, p.516]. Westcott et al. gave a comprehensive overview of degradation mechanisms, sources and monitoring techniques for gas turbine, steam turbine engines, and CCPP [30]. The sources of degradation include: 1) build-up of deposits on both rotating and stationary blades causing fouling, 2) ingestion of hard particles causes erosion, 3) operation in salt water atmospheres causes corrosion, 4) increased seal clearances causing higher leakage flow, 5) external component failure such as clogging inlet filters, fouling condensers, or increased pressure drop in heat exchangers, and 6) physical damage such as foreign object damage. The rate at which the CCPP degrades depends on atmospheric conditions and the manner in which the plant is operated, and its effects cannot be neglected in valid performance analysis.

Therefore, it is important to develop current work allowing for seamless expansion of capability to study degradation effects. The effect of the various degradation mechanisms on the performance of gas turbine engines and CCPPs have been studied and published by many authors. Generally, in the performance simulation study either inlet air mass flow, flow enthalpy, or component efficiencies are varied to account for different degradation mechanisms. Zwebek et al. published results of degraded design-point performance for a single-shaft gas turbine engine configuration and CCPP [31], while the comparison for single-shaft and two-shaft engine configuration has been studied by Kurz et al. [32]. The results suggest that, for design-point analysis, 5% combined compressor and turbine deterioration due to fouling results in 8.3% CCPP power reduction, 2% CCPP thermal efficiency reduction. Whereas 5% combined compressor and turbine deterioration due to erosion results in 6.8% CCPP power reduction and 2.5% CCPP thermal efficiency reduction. This implies a rather significant effect of degradation on the design-point performance parameters. Despite its importance, there is however a lack of published study to accounts for effects of degradation on part-load operation of CCPP.

2.2 Combined Cycle Power Plants and power generation

Transmission System Operators (TSOs), as defined by the European Commission (EC), are entities whose sole responsibility is to transport energy using infrastructure on national and regional level. Under EC regulations, (CE) No. 714/2009 and (CE) No. 543/2013, the TSOs in Europe are required to publish data on the availability of networks, capacities, load and network outages. Example of such data is shown in figure 2.1 for Enfield CCPP station in north London area on the 17 February 2016. The solid line represents the Final Physical Notification (FPN), and the dotted line represents the Bid-Offer Acceptance Level (BOAL) in the balancing market. The FPN shows the best estimate of the level of generation that a unit delivered and it must be submitted to the TSO by specified deadline. The BOAL shows start, end, and load level of each Acceptance period used for short-term grid balancing. The balancing system is used by the System Operator to balance the supply in real-time, ensuring that it meets the demand at all the times. If there is a sudden drop in supply, e.g. due to change in renewable energy supply, the TSO will directly contact the registered Balancing Mechanism (BM) unit generator that can meet the load requirements in the most timely and economic way. An offer price is then placed by the TSO with a request to deviate from the original contracted FPN output. This offer must be higher than what the unit is paid for FPN, as it must compensate for increase in fuel consumption, and any other equipment deterioration due to plant cyclic operation. Therefore, due to variable nature of renewable energy sources the conventional power plants suffer from frequent load changes, and consequently higher variable operational costs.
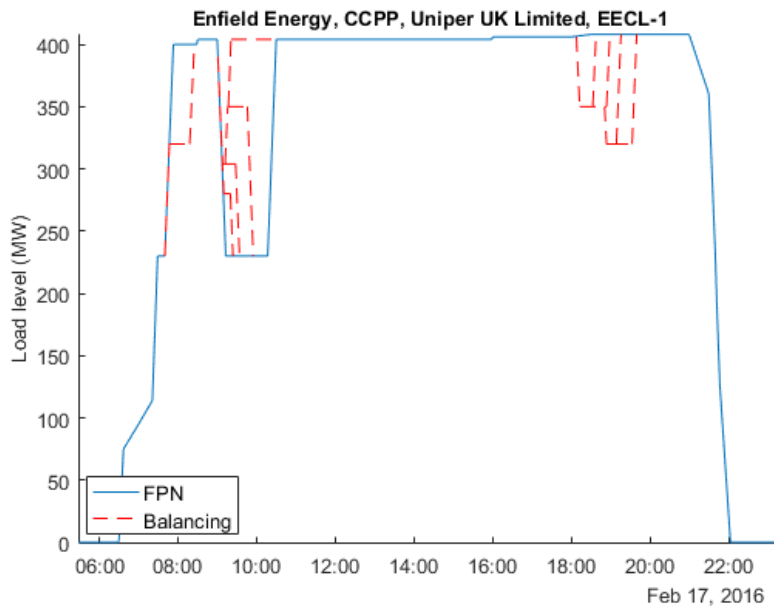
Fig. 2.1 Combined Cycle Power Plant (CCPP) load level profile on 17 February 2016. Dotted line shows load change in the balancing market (Balancing Mechanism Reporting System (BMRS))

With focus on flexibility, the TSO makes decisions on which BM unit should be dispatched to balance the grid where the following questions must be considered:

1. The cost of calling upon the balancing service

2. The system's technical difficulties and limitations (e.g. can the generation be dispatched from the location of demand?) and

3. Is the power plant able to ramp up quickly enough to meet the requirement?

Figure 2.2 shows an example of a typical electricity dispatch curve prepared by Timera Energy for 2013-14 period. The TSO dispatches power plants with priority to those who have lowest variable operation costs according to point 1 above. Therefore, renewable, nuclear and hydro (not shown) generation have priority, followed by coal, CCPP, and petroleum. The coal, CCPP, and petroleum power stations can vary their load relatively flexibly to match the demand. However, coal power stations are highly pollutant and petroleum have high operational costs, making the CCPP the most sustainable solution to balance the grid.

Currently the energy market in Europe is experiencing a major shift in the dispatch curve due to increasing amount of renewable power installations, and consequent changes in the operating regimes of conventional stations. The dispatch curve shifts to the right,
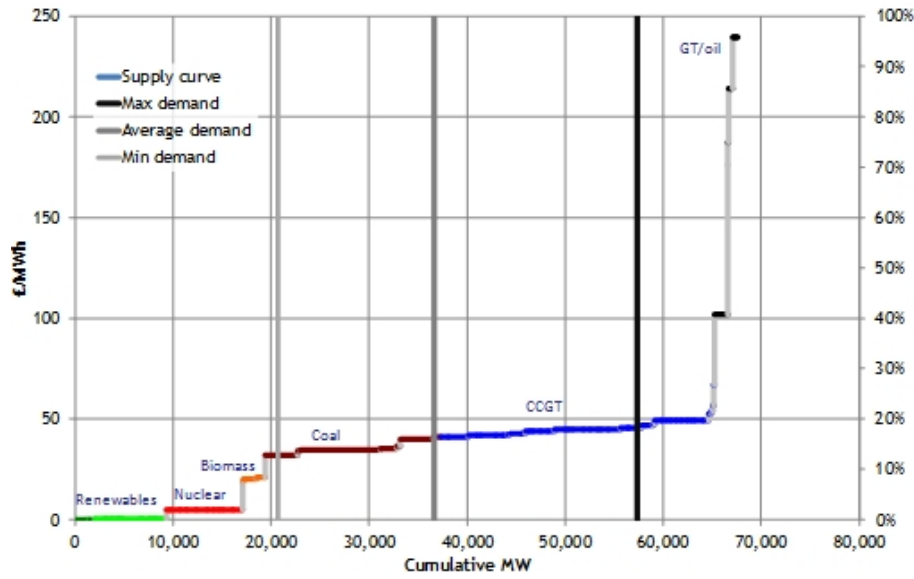
Fig. 2.2 Typical electricity dispatch curve

making some of the existing units with higher variable operational costs no longer profitable. These could be older power plants with poor overall performance, but also new highly efficient power plants with poor part-load performance. For example in March 2013, SSE announced it was closing its 734 MW Keadby CCPP due to adverse market conditions; it then re-opened in November 2015 after major improvements. Also on 30 March 2015, E.ON announced shutting down the Irsching 4 and 5 CCPP in Germany, with capacities 550 MW and 846 MW, respectively, ranking among the most efficient power plants in the world. It is evident that due to an increase in subsidised renewables, these units could no longer supply power profitably. Being able to provide much faster load response service at lower variable operational cost provides competitive advantage for conventional power plant operators. Therefore, the conventional power plants need to be more flexible at off-design operation.

The y-axis in figure 2.2 represents the cost each unit is charging for generating electricity. For a unit to generate profit, this cost needs to be higher than its variable cost of generating electricity. The unit cost of generating electricity, commonly abbreviated as COE, is typically represented in terms of $\frac{£}{MWh}$ and calculated with equation 2.1 [33].

$$COE = \frac{\beta C_{capital}}{LH} + \frac{C_{fuel}}{\eta} + \frac{C_{O\&M,fixed}}{LH} + \frac{C_{O\&M,variable}}{LH} \qquad (2.1)$$

Where a capital charge factor, β, multiplied by capital cost $C_{capital}$, gives the cost of servicing the capital required. H is plant utilisation in hours without considering the time spent during load change, and L is the plant output in kW. Thus the equation may be re-arranged into fixed and variable terms

$$COE = \underbrace{\frac{\beta C_{capital} + C_{O\&M,fixed}}{LH}}_{\text{fixed costs}} + \underbrace{\frac{C_{fuel}}{\eta} + \frac{C_{O\&M,variable}}{LH}}_{\text{variable costs}} \quad\quad (2.2)$$

Fixed costs are those that do not generally vary with plant electricity generation. The capital costs account for owner costs such as development, preliminary feasibility and engineering studies, environmental searches and relevant legal fees, also insurance costs and any taxes. The operations and maintenance ($O\&M$) costs that do not vary significantly with plant operation are considered fixed, whereas those directly incurred to generate electricity as considered variable.

According to Gulen et al. [34], the traditional COE equation is adequate for preliminary study and comparison between similar alternative projects rather than detailed and accurate assessment of the real generating costs. He proposed a modified formulation to account for load ramp periods, as shown in equation 2.3

$$COE = \underbrace{\frac{\beta C_{capital} + C_{O\&M,fixed}}{\overline{L}H\prime}}_{\text{fixed costs}} + \underbrace{\frac{C_{fuel}}{\overline{\eta}} + \frac{C_{O\&M,variable}}{\overline{L}H\prime}}_{\text{variable costs}} \quad\quad (2.3)$$

where $H\prime$ is the total effective operating hours, $\overline{L}$ is the mean effective plant output, and $\overline{\eta}$ is the mean effective plant thermal efficiency; and all variables are accounting for load change periods.

Gulen concluded that if flexible operation of CCPPs continues to dominate, the COE calculations must factor in the duration of load changes. Further, not taking into account related flexible operation, non-recoverable degradation, maintenance costs etc, can produce misleading results. It is, therefore, important in the current work to address the two research questions (section 1.2) with emphasis on improving capabilities for off-design performance modelling of CCPPs to enable more accurate evaluations of COE with equation 2.3. Furthermore, having more accurate estimates of COE will enable plant operators to more accurately evaluate profit margins and aid decisions regarding whether the plant should participate in the balancing market.

2.2.1   Theory of operation

A comprehensive overview of Combined Power Plants from the thermodynamic perspective is provided by Horlock [33]. Of interest in the current work is the most well-developed and commonly used in the industry - an Open Circuit/Closed Cycle Plant configuration which is commonly known as a Combined Cycle Power Plant (CCPP). In this configuration a steam turbine Rankine cycle is added to a gas turbine Joule cycle. Heat recovered from an open circuit gas turbine exhaust is used in a closed Rankine cycle to

raise steam, and as the result of combining these two cycles an improved power output and thermal efficiency is achieved. There exist a number of modifications that are commonly applied to gas turbines to either improve power output and/or fuel consumption. Further detailed information on recuperation, intercooling and reheat modifications have been described by Boyce [25].

- A recuperator is added to transfer heat from GT exhaust to the air at the compressor outlet; as a result, increased compressor exit temperature mean less fuel required to raise the temperature within the combustor to the desired value, thus improving thermal efficiency. For high pressure ratio engines, however, the compressor exit temperature may exceed exhaust temperature making use of recuperation process valueless.

- An intercooler is added to reduce temperature between the compressor sections. This is done to reduce the compressor power consumption and therefore increase the engine power output. However, this is done at the expense of reduced combustor inlet temperature which results in a reduction in thermal efficiency. The thermal efficiency can be restored for intercooled engines by a use of recuporator, or increased engine pressure ratio; however, this increases costs and complexity.

- A reheat is added to increase the engine power output by introducing additional fuel between stages of a turbine expansion. However, this is done at an expense of increased fuel consumption.

2.2.2   Case study

Figure 2.3 shows pictures of two existing Combined Cycle Power Plants. The two pictures from the left are the Heat Recover Steam Generators (HRSG). On the right side, from the top are shown: exhaust form the gas turbine engine, the finned superheater tube banks, and the steam turbine. The first thing to notice is the large size of the heat recovery steam generators which allow for efficient heat transfer from the gas turbine exhaust to the water/steam cycle. The exhaust duct from the gas turbine engine contains supplementary heating fuel manifolds. The exhaust gas then flows through the tube banks, which contain fins to maximise the heat transfer. The side-view of a three pressure HRSG cross-section is shown in figure 2.4, whereas top view cross-section is shown in figure 2.5.

Due to changing market conditions, these power plants are now required to operate in a flexible manner with frequent load changes. The plant performance modelling team simulates off-design conditions using either in-house (e.g. PROATES used by Uniper), or commercially available software (e.g. Ebsilon). These simulation tools are broadly based on existing iterative procedures which are discussed in detail in the following sections.

Fig. 2.3 On the left seen two Heat Recovery Steam Generators from two distinct CCPPs. On the right from the top: gas turbine exhaust, superheater tube banks, steam turbine (author's collection)
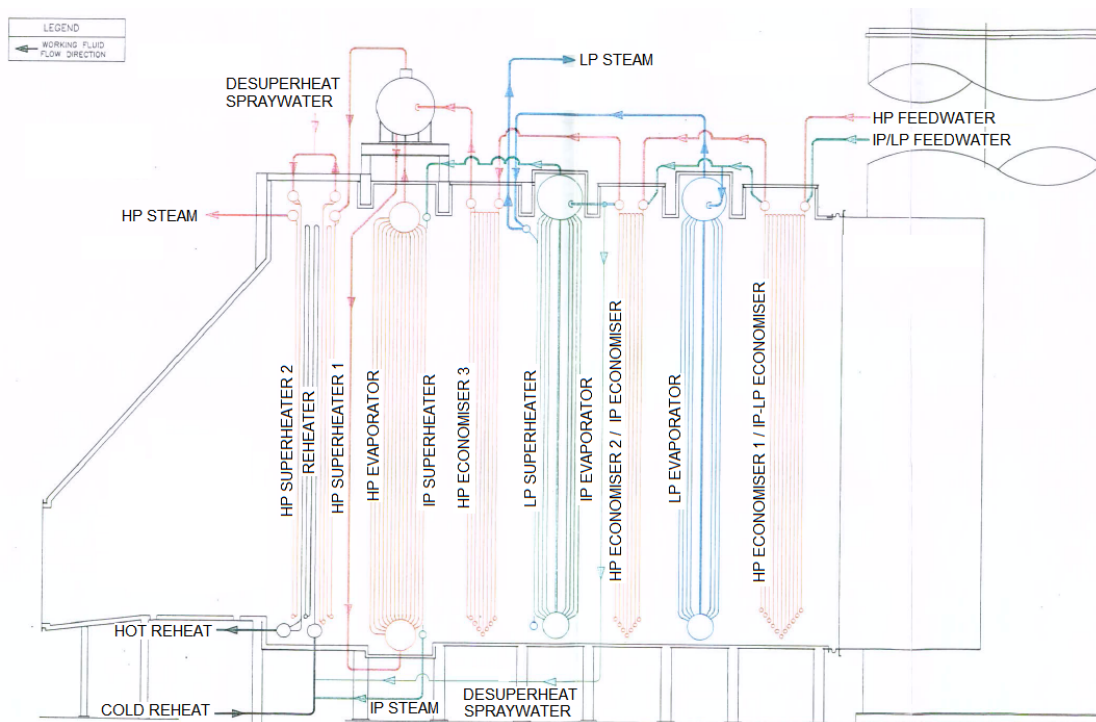

Fig. 2.4 Schematic of a three pressure Heat Recovery Steam Generator (private communications)
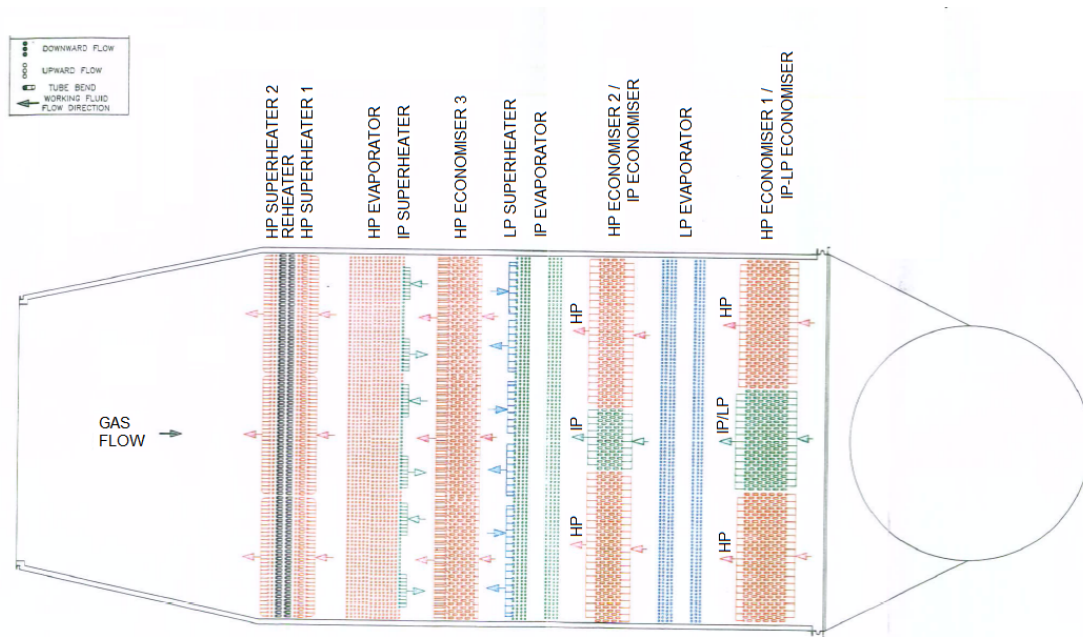
Fig. 2.5 Schematic of a three pressure Heat Recovery Steam Generator (private communications)

2.3 Existing techniques for modelling Combined Cycle Power Plants in off-design condition

Detailed discussion is presented on key methods currently used by the research and commercial community to evaluate off-design performance of a water/steam cycle. The analytical methods are based on the formulation of a set of non-linear equations that describe the off-design performance parameters. These equations are solved either using a sequential procedures or numerical methods, e.g., Newton-Raphson. In the following sections, sequential procedures developed decades ago and still in use today are discussed. The complete procedure for applying Newton-Raphson method to solving a system of non-linear equations is presented in the appendix section A.3.

2.3.1 R. Kehlhofer approach

In 1978, Kehlohofer published a methodology for calculating off-design operation of combined cycle power plants [35]. He suggested that the number of equations describing all components of the water/steam cycle have to be as small as possible. The derived system of equations, therefore comprised of energy and heat transfer equations for the heat exchangers, and steam cone equation for the steam turbine. The heat transfer equations are based on the Log Mean Temperature Difference (LMTD) method. Kehlhofer derived

energy and heat transfer equations to completely define the heat exchanger. The system of equations for one heat exchanger is shown in equations 2.4a and 2.4b. The size of this set of equations will depend on the number of heat exchangers in the system. Therefore, for a single pressure system with economiser, evaporator, superheater and condenser, the set will contain 8 equations. These equations are supplemented with a steam cone rule of the steam turbine, equation 2.5, increasing the total number of equations to 9.

Instead of solving the system of non-linear equations by means of generally valid numerical procedures, Hehlhofer proposed a procedure for obtaining a solution shown in figure 2.6. The procedure is highly guided by the initial approximation of live steam pressure, P_{FD}, and temperature, t_{FD}. Iterations are then performed to satisfy energy, heat transfer, and steam cone equations in the superheater which result in new set of t_{FD} and steam mass flow, $\dot{m}_{FD}$. The procedure then iterates to satisfy energy and heat transfer equations in the economiser and evaporator until it converges with a find value of P_{FD}. These steps are repeated until all equations for steam turbine, superheater, evaporator, and economiser are satisfied. Then preheating of feedwater is calculated. Lastly, condenser pressure and flow of bled steam are determined in a further iteration. Once all equations are satisfied, the off-design performance of the water/steam cycle is calculated. Kehlhofer applied his methodology to study combined cycle design and off-design performance, which he published in his book later in 1991 [23].

$$
\begin{cases}
\dot{Q}^{OD} = \dot{m}_s^{OD} \Delta h_s^{OD} = \dot{m}_g^{OD} \Delta h_g^{OD} & (2.4a) \\[2ex]
\dfrac{\Delta T_{lm}^{OD}}{\Delta T_{lm}^{D}} = \dfrac{U^D \dot{m}_g^{OD} \Delta h_g^{OD}}{U^{OD} \dot{m}_g^{D} \Delta h_g^{D}} & (2.4b)
\end{cases}
$$

$$
\frac{\dot{m}_s^{OD}}{\dot{m}_s^{D}} = \sqrt{\frac{p_a^{OD} v_a^{D}}{p_a^{D} v_a^{OD}}}
\tag{2.5}
$$

2.3.2   G. Gyarmathy approach

In 1989, Gyarmathy followed the methodology developed by Kehlhofer, and proposed a similar procedure for calculating off-design performance of a single pressure combined cycle power plant [36]. He developed a set of 17 equations comprising of energy balance, and heat transfer based on NTU method, with 17 unknowns. The set of equations comprises vaporization temperature, latent heat and Stodola choking relation shown in equation 2.6. The heat transfer and heat balance equations for economiser, evaporator and superheater are shown in equations 2.7 and 2.8, respectively, where *St* is a Stanton number. The set of equations is further supplemented with steam turbine relations in equation 2.9.
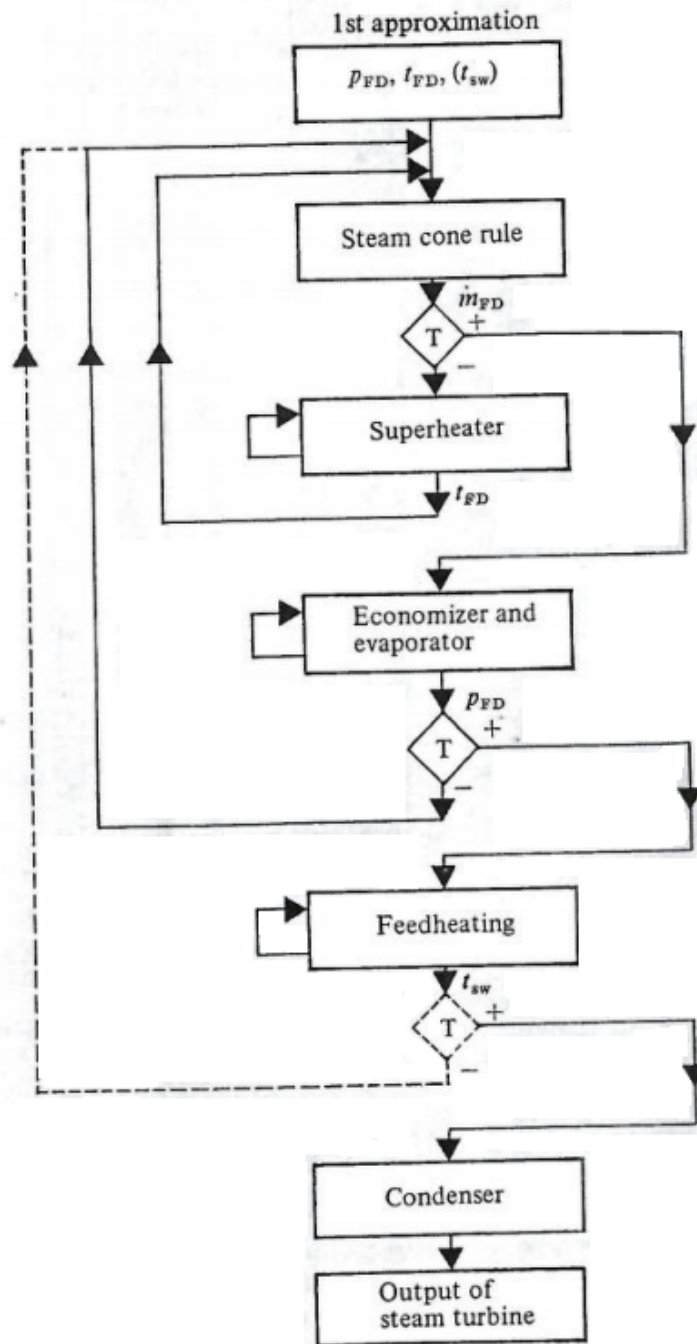
Fig. 2.6 Kehlhofer approach: off-design calculations procedure for predicting CCPP performance parameters [35]

The initial approximated guess must be made assuming values of live steam pressure, P_{ST}, and pinch point temperature differences for evaporator and superheater, ΔT_{vap} and ΔT_{SH}, respectively. The predictor-corrector loops then iterate as shown in figure 2.7. Upon convergence the off-design performance parameters are obtained.

$$
\begin{cases}
T_{vap} = f(P_{st}), & \text{vaporization temperature} \\
L = f(P_{st}), & \text{latent heat} \\
\dot{m} = \dot{m}_o(\frac{P_{st}}{P_{sto}})\sqrt{\frac{T_{sto}}{T_{st}}}, & \text{Stodola choking relation}
\end{cases}
\tag{2.6}
$$

$$
\begin{cases}
\dot{m}_g Cp_g(T_{g,4} - T_{g,5'}) = \dot{m}_s(L + Cp_s(T_{st} - T_{vap})), & \text{heat balance for superheater} \\
\dot{m}_g Cp_g(T_{g,5'} - T_{g,5''}) = \dot{m}_s Cp_w(T_{vap} - T_{sw})), & \text{heat balance for preheater} \\
\dot{m}_g Cp_g(T_{g,5''} - T_{g,5}) = \dot{m}_s Cp_w(T_{sw} - T_k)), & \text{heat balance for economiser} \\
\dot{m}_g Cp_g(T_{g,4} - T_{g,5''}) = \dot{m}_s(L + Cp_s(T_{st} - T_{vap})), & \text{heat balance for evaporator and superheater}
\end{cases}
\tag{2.7}
$$

$$
\begin{cases}
\dot{m}_w = \frac{\dot{m}_s Cp_s}{\dot{m}_g Cp_g}, & \text{heat transfer for superheater} \\
St = St_o \frac{\dot{m}_g}{\dot{m}_{go}}, & \text{heat transfer for superheater} \\
NTU_{sh} = NTU_{sho}\frac{St}{St_o}, & \text{heat transfer for superheater} \\
\frac{\dot{m}_s}{1-\dot{m}_s}ln\frac{T_{g,5'} - T_{vap}}{T_{g,4} - T_{st}} = \psi_{sh}, & \text{heat transfer for superheater} \\
\dot{m}_w = \frac{\dot{m}_s Cp_w}{\dot{m}_g Cp_g}, & \text{heat transfer for preheater and evaporator} \\
\psi_{sh} = \psi_{sho}\frac{St}{St_o}, & \text{heat transfer for preheater and evaporator} \\
\frac{\dot{m}_w}{1-\dot{m}_w}ln\frac{T_{g,5''} - T_{sw}}{T_{g,5''} - T_{vap}}ln\frac{T_{g,5'} - T_{vap}}{T_{g,5''} - T_{vap}} = \psi, & \text{heat transfer for preheater and evaporator}
\end{cases}
\tag{2.8}
$$

$$
\begin{cases}
Q_{WHR} = \dot{m}_g Cp_g(T_{g,4} - T_{g,5}), & \text{ST cycle waste heat input} \\
P_{st} = \dot{m}_s \eta_{ms}\Delta H(P_{st}, T_{st}, P_{SC}, \eta_{ps}), & \text{ST power output} \\
\eta_{st} = \frac{P_{st}}{\dot{m}_g(T_{g,4} - T_{amb})}, & \text{ST cycle efficiency}
\end{cases}
\tag{2.9}
$$

2.3.3 P.J. Dechamps approach

In 1994, Dechamps et al. published a method for evaluating part load operation and performance of combined cycle power plants [37]. The method comprises of a system of 11 non-linear equations with 11 unknowns. The system of the equations is shown in equation 2.10, where subscripts *su*, *va*, and *ec* correspond to superheater, evaporator and economiser, respectively. The subscripts for the temperature profile are denoted according to figure 2.8. The unknowns that the system is solved for are: pressure, temperature profiles, steam mass flow, and the energy. Dechamps pointed that the system of equations
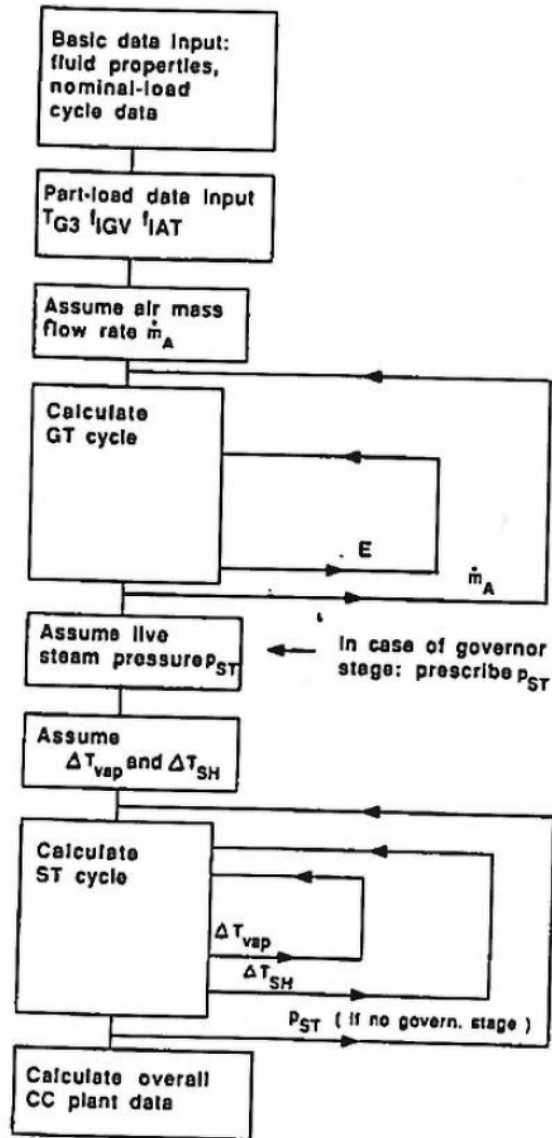
Fig. 2.7 Gyarmathy approach: off-design calculations procedure for predicting CCPP performance parameters [36]
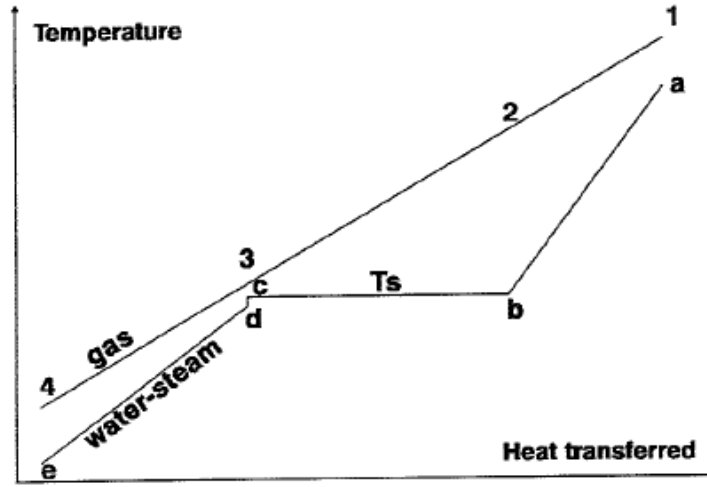
Fig. 2.8 Heat transfer diagram and notations for one pressure system using Dechamps approach

can be solved either simultaneously with global method based on matrix formulation, or sequentially with a small number of guesses and checks. He concluded that latter is better suited for this application, especially when considering that the system of equations gets larger if additional elements are added to the system and if multiple pressure systems are considered. The procedure for solving a 1 pressure system of non-linear equations sequentially is shown in figure 2.9. At the beginning of the process the variables that must be estimated are: P, T_a, T_2, T_3 and Q_{ec}.

$$
\begin{cases}
Q_{su} = S_{su}h_{su}\Delta T_{lm_{su}}, & \text{heat transfer balance of superheater} \\
Q_{su} = \dot{m}_g(h_{g_1} - h_{g_2}), & \text{energy balance of superheater} \\
Q_{su} = \dot{m}_s(h_{s_a} - h_{s_b}), & \text{energy balance of superheater} \\
Q_{va} = S_{va}h_{va}\Delta T_{lm_{va}}, & \text{heat transfer balance of evaporator} \\
Q_{va} = \dot{m}_g(h_{g_2} - h_{g_4}), & \text{energy balance of evaporator} \\
Q_{va} = \dot{m}_s(h_{s_b} - h_{s_d}), & \text{energy balance of evaporator} \\
Q_{ec} = S_{ec}h_{ec}\Delta T_{lm_{ec}}, & \text{heat transfer balance of economiser} \\
Q_{ec} = \dot{m}_g(h_{g_3} - h_{g_4}), & \text{energy balance of economiser} \\
Q_{ec} = \dot{m}_s(h_{s_d} - h_{s_e}), & \text{energy balance of economiser} \\
T_s = f(P), & \text{saturation temperature} \\
\frac{\dot{m}_s\sqrt{T_{st}}}{P} = constant, & \text{Stodola choking relation}
\end{cases}
\qquad (2.10)
$$
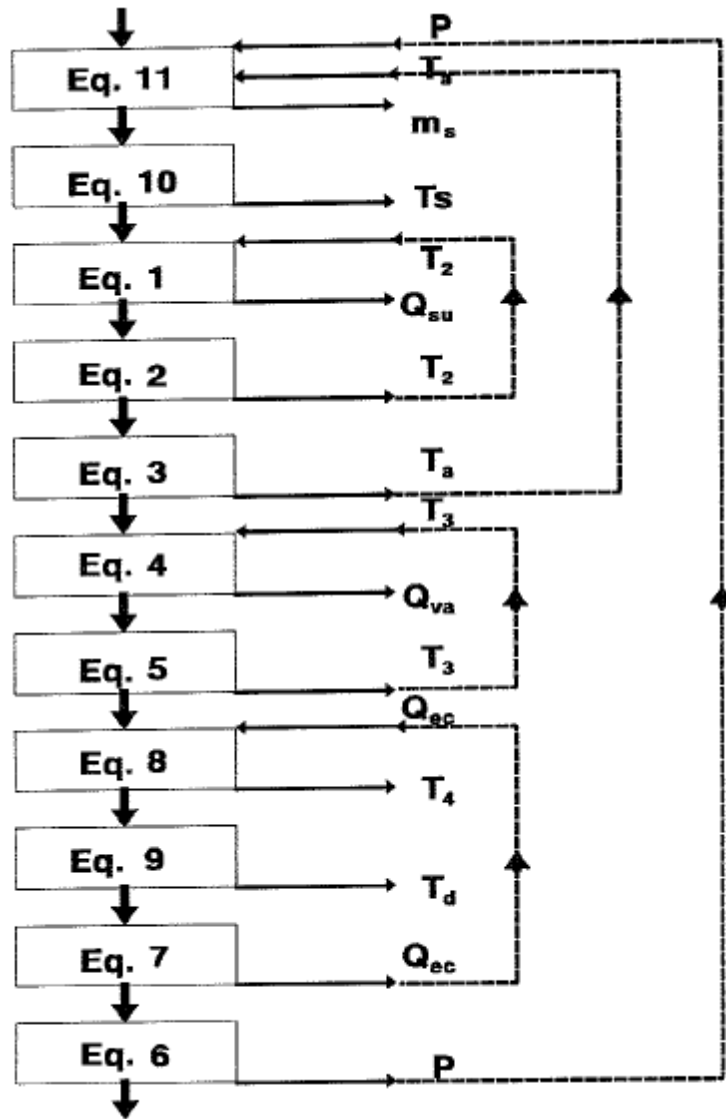
Fig. 2.9 Dechamps approach: off-design calculations procedure for predicting CCPP performance parameters [37]

2.3.4   V. Ganapathy approach

In 1990, Ganapathy published a simplified method for estimating off-design performance of heat recover steam generators [38]. He assumed that the $T_{g,in}^{OD}$, $\dot{m}_g^{OD}$, P_s^{OD} and feed water temperature are known. The energy and heat transfer equation based on the LMTD method are formed for each heat exchanger according to equation 2.11. The relation of design to off-design performance is done by adjusting the product of overall heat transfer coefficient and heat transfer surface area , UA, at the design point to the off-design conditions. The correlations for superheater, evaporator, and economiser are calculated with equations 2.12, 2.13, and 2.14, respectively. The design point variables are denoted by a subscript o, and factors Fg and K are evaluated for each heat exchanger separately. The number of equations is increased with the number of heat exchangers in the cycle, e.g. a 2P steam cycle would contain 12 equations and 12 unknowns.

The iterative procedure is initiated with a guess for steam mass flow rate. Ganapathy suggested that a good estimate is obtained by using a ratio of the design to off-design gas flows and temperature drop. The steam mass flow rate is then adjusted in each iteration until heat and energy balance equations for all heat exchangers are satisfied with an error of less than 0.5%. He concluded that a very high number of iterative calculations are involved in the process, and the complexity increases further if multi-pressure systems are investigated.

$$
\begin{cases}
\dot{Q}_{sh} = UA_{sh}\Delta T_{lm}, & \text{heat transfer balance of superheater} \\
\dot{Q}_{sh} = \dot{m}_s\Delta h_s = \dot{m}_g\Delta h_g^{OD}, & \text{energy balance of superheater} \\
\dot{Q}_{va} = UA_{va}\Delta T_{lm}, & \text{heat transfer balance of evaporator} \\
\dot{Q}_{va} = \dot{m}_s\Delta h_s = \dot{m}_g\Delta h_g^{OD}, & \text{energy balance of evaporator} \\
\dot{Q}_{ec} = UA_{ec}\Delta T_{lm}, & \text{heat transfer balance of economiser} \\
\dot{Q}_{ec} = \dot{m}_s\Delta h_s = \dot{m}_g\Delta h_g^{OD}, & \text{energy balance of economiser}
\end{cases}
\tag{2.11}
$$

$$
UA_{sh} = \dot{m}_g^{0.65}FgK\left(\frac{\dot{m}_s}{\dot{m}_{s,o}}\right)^{0.15}
\tag{2.12}
$$

$$
UA_{va} = \dot{m}_g^{0.65}FgK
\tag{2.13}
$$

$$
UA_{ec} = \dot{m}_g^{0.65}FgK
\tag{2.14}
$$

Where

$$
Fg = \frac{Cp^{0.33}k^{0.67}}{\mu^{0.32}}
$$

$$
K = \frac{\dot{Q}}{\Delta T_{lm}\dot{m}_g^{0.65}Fg}
$$

2.3.5 S. Gullen et al. approach

In recent years new studies are emerging for implementing exergy analysis (i.e. second law approach) to performance evaluations. In 2002, Lior urged the research community that exergy analysis must be added to conventional power plant performance analysis, in every phase of the project [39]. He argued that only exergy analysis can identify the specific irreversibilities, much needed to develop innovative power generation systems of the 21st century. He also added that the exergy analysis serves as an excellent basis for economic study. In et al. applied exergy analysis to optimisation of design point performance of combined cycle power plants [40]. Recently Gulen et al. developed and demonstrated an exergy model applied to off-design performance estimation of combined cycle power plants [41]. He observed that alternatively to an analytical method such as the Kehlhofer approach, which has been discussed in section 2.3.1, exergy approach can be used to estimate off-design performance. Gulen warned that current iterative methods are cumbersome even in their simplified form and require a substantial investment in resources. He concluded that exergy analysis leads to the same conceptual conclusions as iterative procedures and require less then 30 minutes of programming work.

2.3.6 Improvements to existing methods

The method developed by Dechamps et al. has been studied by Valdes et al. who applied the set of non-linear equations to study the optimal design performance of heat recovery steam generators used in combined cycle gas turbine power plants [42]. Instead of solving the set of equations sequentially with Dechamps procedure, he obtained a solution with a new methodology using a Newton-Raphson numerical method for solving the system of 8 non-linear equations with 8 unknowns. As pointed by Valdes, Newton-Raphson numerical iteration is specially suitable for further implementation to optimisation procedures. He warned, however, that the method should be used with caution, because if the first iteration is too far away from the solution, the iterative process may not converge. Further, he concluded that if any of the iterations produce a solution far off the desired one, the method may not continue or may even terminate in a non-physical solution of the system of equations. He suggested that further study into the nature of the system being solved would be helpful, especially in analysing mathematically the convergence conditions.

The difficulties with convergence have been studied by Mohagheghi et al. who analysed Gyarmathy's approach, and developed a hybrid Newton's method for solving the system of non-linear equations [43]. Mohagheghi argued that sequential methods and successive equation solving are very time consuming, non-comprehensive, and require user interaction with a solver. He noticed that the solution obtained by the Newton-Raphson method is very sensitive to the initial guess, and it is desirable to have initial guess as close to the solution as possible. The complexity increases even further if multiple pressure systems are under investigation. Mohagheghi developed a stepped-solution method,

in which the solution of each step is obtained from the solution of the previous step. By doing so, the results were less sensitive to the initial guess in case it is too far away from the actual solution. He then applied his stepped-solution method to study and optimise the heat exchangers layout in the Heat Recovery Steam Generator.

Recently, for the reasons described in chapter 1, increasing number of optimisation studies are conducted. Roviara et al. studied results published by Valdes and developed a thermoeconomic optimisation model considering off-design operation [18]. He pointed that in order to guarantee the convergence of the iterative off-design calculations, the load of the gas turbine engine must be systematically reduced with small steps from full-load to avoid any abrupt changes in variables, which ultimately affects the convergence of the solution. To make it worst, the optimisation requires a large number of simulations of various system layouts at off-design operation. Consequently, using iterative procedures for off-design calculations on a large scale as required by thermoeconomic optimisation, is very time-consuming.

The issues of having to perform large scale simulations were addressed by Zhang et al. who studied performance optimisation of a triple pressure reheat combined cycle by adopting and modifying Ganapathy method [44] [45]. They noticed that current off-design performance evaluation methods suffer from tedious iterations, and proposed a set of concise semi-theoretical and semi-empirical formulas to estimate off-design performance more effectively, and with less complexity. The formulas are shown in equation 2.15, and relate off-design water/steam cycle performance to the gas turbine exhaust temperature and mass flow rate conditions. The subscript D refers to design performance, and η_c is a Carnot cycle efficiency. Zhang's correlations provide performance estimations with less than 1% error for gas turbine load range $50 - 100\%$ and gas turbine exhaust temperature deviation within $110^o C$. However, limitations of the method imply a need to develop a new set of concise formulas if the system layout is changed.

$$\begin{cases} \dot{Q}_{in} = \dot{Q}_{in}^D \left(\dfrac{T_{gt,exhaust}}{T_{gt,exhaust}^D} \right)^2 \left(\dfrac{\dot{m}_g}{\dot{m}_g^D} \right), & \text{HRSG heat transfer} \\[4mm] \eta_s = \eta_s^D \left(\dfrac{T_{gt,exhaust}}{T_{gt,exhaust}^D} \right)^{0.35} \left(\dfrac{\dot{m}_g}{\dot{m}_g^D} \right)^{-0.02}, & \text{HRSG thermal efficiency} \\[4mm] PO_s = PO_s^D \dfrac{\eta_c}{\eta_c^D} \left[-0.32063 + 1.64575 \left(\dfrac{\dot{Q}_{in}}{\dot{Q}_{in}^D} \right) - 0.32872 \left(\dfrac{\dot{Q}_{in}}{\dot{Q}_{in}^D} \right)^2 \right], & \text{Steam turbine power output} \end{cases}$$
$$(2.15)$$

Where

$$\eta_c = 1 - \frac{T_{amb}}{T_{gt,exhaust}}$$

$$\eta_c^D = 1 - \frac{T_{amb}}{T_{gt,exhaust}^D}$$

2.4 Potential techniques for modelling Combined Cycle Power Plants in off-design condition

Given the thesis motivation described in chapter 1, there is a clear need for methods to evaluate off-design operation of combined cycle power plants. It has been pointed out in section 1.2, that the research community needs to focus on developing better methods for studying and improving flexible operation of gas turbines and CCPPs. The following sections provide the rationale and benefits to development of new methods presented in this thesis.

2.4.1 Gas turbine operational map

According to section 2.1.1, the gas turbine flexible operation is dependent on the load reduction strategy. The study becomes more complex when engine degradation is accounted for. The study of various effects of load reduction strategies on engine and CCPP performance is well documented. However, it is the interaction between load reduction strategies that needs to be explored further to expose improvements to operational flexibility. Usually, gas turbine performance with various load reduction strategies is evaluated by calculating or simulating a large number of parameters and corresponding component characteristics. The complexity of the analysis increases even further if one wishes to evaluate a combination of load change strategies, e.g. closing VIGVs and fuel flow reduction at the same time. At each load level in off-design, basic engine performance characteristics are dependent on ambient conditions, physical properties of the working fluid, and the load reduction strategy. It is clear that full variation of engine performance quantities affecting flexible operation involves complex and excessive number of calculations and visual representations, which can make a concise presentation of the results unachievable. The need for more comprehensive methods to evaluate gas turbine part load operation is addressed in the current work. Further, a novel method has been developed to allow concise analysis of performance trade-offs during plant load change. The Gas Turbine Operational Flexibility Map and a Life Consumption Map are presented and discussed in chapter 3.

2.4.2 Genetic Algorithm approach

Rao summarised numerical methods applied in general to finding solution to non-linear equations [46]. He pointed out that Newton-Raphson method is very efficient in solving systems of non-linear equations, however, the algorithm may not converge if the initial guess of variables is not good. Therefore, the procedure involves significant user interaction with the algorithm, which ultimately limits and restricts further technological progress in performance analysis. Moreover, a highly skilled professional is needed in order to understand and interpret the process to make a proper initial approximation. Recently, in the wake of increasing research in the area of optimisation search algorithms,

development of Genetic Algorithm method as alternative to Newton-Raphson method is gaining attention. Mhetre pointed out that compared to traditional techniques, e.g. Newton-Raphson, GAs are more effective as they do not tend to converge in local optima [47]. Mastorakis studied Genetic Algorithm effectiveness to solve a system of non-linear equations [48]. His results prove that the GA is a powerful tool for numerical analysis, and can effectively be applied to non-linear equations. More recently, in a different study, El-Emary et al. concluded that solving non-linear system of equations with GA is effective and represents an efficient approach [49]. Zhou conducted a survey of the state-of-the-art into multi-objective genetic algorithms [50]. He concluded that although GAs are still in early stages, there have been a huge number of publications and interest in developing these systems across wide range of disciplines.

Genetic Algorithms have been applied widely to study design optimisation of Combined Cycle Power Plants. Valdes et al. studied thermoeconomic performance of CCPP using genetic algorithm [51]. He concluded that it is possible to apply GA even to multiobjective optimisation problem. Koch et al. applied genetic algorithm to optimise economic output of the CCPP [52]. He concluded that GA is a powerful tool to optimise the process variables of CCPP; however, he warned that the larger the complexity of the system the more time-consuming the development of the algorithm is. Mohagheghi et al. applied a genetic algorithm to study optimal layout for heat recovery steam generator. More recently, Kaviri et al. modelled exergy based optimisation process of CCPP using a genetic algorithm [53]. Ghazi et al. studied costs of exergy and system design parameters to find optimum values of HRSG design performance using genetic algorithm [54]. It is evident that genetic algorithms are popular in design system optimisation; however, it has not yet been reported in the literature as an alternative method to existing CCPP off-design performance simulation methods.

In summary, compared to existing solving techniques, applying genetic algorithm to the problem eliminates the need to make initial approximation and also eliminates any user interaction with the algorithm during off-design performance modelling. In the current work, a GA method for off-design CCPP performance modelling is developed and is presented in chapter 5.

Theory of Genetic Algorithms

The Genetic Algorithm (GA) is an intelligent evolutionary algorithm which was originally developed to mimic some of the processes observed in natural evolution. Bodenhofer provides a comprehensive overview of the theory and applications of GAs [55]. Since the GA is a nature inspired process, terminology used in genetics is equivalently applied to the framework of mathematical analysis according to table 2.1. Individuals in each population carry numerical values of variables, e.g. temperatures at outlet of gas path and steam

Table 2.1 Terminology of Genetic Algorithm [55]

Natural Evolution	Genetic Algorithm
genotype	coded string
phenotype	un-coded point
chromosome	string
gene	string position
allele	value at a certain position
fitness	objective function value

path in a shell-and-tube heat exchangers. These numerical values are referred to as *phenotypes*. To perform certain operations it is common to represent phenotypes as encoded strings, referred to as *genotypes*. The length of the string in each genotype is known as the *chromosome* where each position is referred to as a *gene*. The chromosomes can be represented or encoded in various ways, e.g. binary , or real-valued string [56]. In binary encoding, the solutions are represented as binary strings, which is a traditional and the most common method. The real-valued encoding the structure of genotypes is identical to the phenotypes. The *fitness* is the objective function, which is evaluated for each individual in the population. Similarly to the natural evolution, only the fittest individuals survive to the next generation. Thus, GA evolves across generations, with the ultimate goal to converge and return the fittest individual. Upon un-coding the genotypes of the fittest individual, a set of phenotypes is reviled which correspond to the set of converged numerical variables.

The genetic algorithm is broken down into three main processes; selection, cross-over and mutation. The selection is a mechanism for selecting individuals (chromosomes) according to their fitness. If the genetic algorithm is applied to a minimisation problem, e.g. the solution should tend to zero, the individuals with the lowest fitness are favoured. Jebari et al. provided a comprehensive study of six well known selection methods often used in genetic algorithms, and proposed a new method to reduce the solution dependence on the choice of the selection method [57]. Once individuals are selected, the genetic information is merged in a cross-over process where genes are exchanged between chromosomes of parent 1 and parent 2 with a probability P_c. If the probability of cross-over is 0%, then no cross-over occurs, whereas 100% suggests that all parents are crossed over to form children. Various methods exist for the cross-over process, such as single-point or multiple-point. A two point cross-over shown in figure 2.10 cuts two binary coded chromosomes at randomly chosen positions, and swaps genes to produce child 1 and child 2. Once all individuals in the selected population have been crossed-over, the newly formed population needs to be diversified, otherwise it risks converging at local optima. A process of mutation with a very low probability, is usually applied to mutate a single gene in a chromosome, i.e. flipping binary number as shown in figure 2.11. If the P_m is too low,

then due to low diversification the genetic algorithm may converge at local minima. If on the other hand P_m is too high, the algorithm may behave chaotically like a random search. Therefore, usually probability of mutation is selected to be in the region of $P_m = 0.1$ to 0.5%.
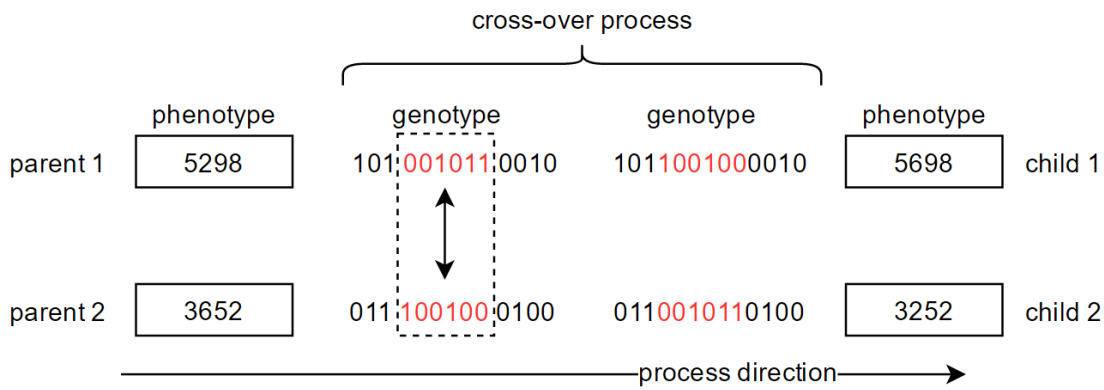

Fig. 2.10 A typical genetic algorithm cross-over process
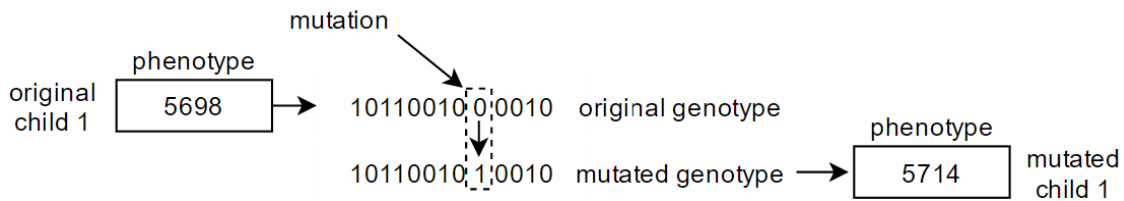
Fig. 2.11 A typical genetic algorithm mutation process

The off-design modelling of CCPPs require constrain handling to control the temperatures and pressures of the system within acceptable region.Therefore, individuals must be checked before they are passed on to the next generation for feasibility. Mezura-Montes et al. provide a comprehensive overview of GA methods applied to constrained optimisation [58].

2.4.3   Direct Solution Method approach

According to section 2.3, the approaches developed by a number of authors in the late twentieth century provide ways to estimate off-design performance; however, as pointed

out by many, these methods are cumbersome even in their simplified form. In recent years increasing number of studies were carried out to improve convergence of either sequential procedures, or numerical methods. However, these are still fundamentally based on the iterative procedures, and have to be approached with caution as results will always contain function residuals. Given the current motivation and the need for performing complex techno-economic optimisation research studies to improve flexible operation of CCPPs, the existing techniques for off-design performance modelling are not sufficiently reliable. In the present work, a different approach has been pursued and a novel method developed, which allows to estimate design and off-design performance of CCPPs with no residual, and no iterations required. The Direct Solution Method allows determination of a simple solution algebraically, which reduces complexity, computational time, and improves accuracy.

Chapter 3

Gas turbine off-design operation

The objective of this chapter is to demonstrate development of a novel gas turbine operational flexibility map. The operational flexibility map provides an easier way to visualise complex and usually conflicting performance parameters for the engine operating at part-load. In the second part of the chapter, a newly developed method is demonstrated which allows for fast estimation of life consumed due to low cycle fatigue and creep mechanisms in critical gas turbine components. The life consumed is highly dependent on the plant load change strategies, which proves the use of proposed maps beneficial to power plant operators.

3.1 Comparative analysis of single and multi-shaft gas turbines using Turbomatch

The comparative analysis of engine architectures has been widely studied in earlier work. The effect of load reduction strategies on engine performance has been demonstrated to be an important aspect contributing to flexible operation. Therefore, in the current study the performance of single and multi-shaft gas turbine engines have been analysed against two load reduction strategies: fuel flow control, and closing VIGVs at constant TET from $0^o - 39^o$ followed by fuel reduction. The objective is to investigate the performance trade-offs in part-load operation, and select important parameters to include in the development of the gas turbine operational flexibility map in section 3.2.

The design engine specifications are shown in table 3.1 for two widely used engines. The engine configurations are similar to the Siemens SGT5800H and the aeroderivative version of RB211 engine for single and multi-shaft arrangements, respectively. The steady state performance and operating characteristics have been simulated with Turbomatch, a software developed by Cranfield University. The performance results are shown in figures 3.1 and 3.2 for the two load reduction strategies.

Table 3.1 Gas turbine engine specifications for single shaft and multi shaft arrangement

Single shaft		Multi shaft	
Inlet air conditions	ISA		ISA
Inlet air mass flow $[\frac{kg}{s}]$	845		97
Compressor pressure ratio	19.2	LP compressor pressure ratio	4.66
Compressor isentropic efficiency [%]	89	LP compressor isentropic efficiency [%]	88
Compressor surge margin [%]	85	LP compressor surge margin [%]	85
Bleed flow [%]	10	LP Bleed flow [%]	5
		HP compressor pressure ratio	4.91
		HP compressor isentropic efficiency [%]	88
		HP compressor surge margin [%]	85
		HP Bleed flow [%]	12
Burner pressure loss [%]	5		5
Burner efficiency [%]	99.9		99.9
Turbine isentropic efficiency [%]	91	HP turbine isentropic efficiency [%]	88
Turbine entry temperature [K]	1680	HP turbine entry temperature [K]	1550
		LP turbine isentropic efficiency [%]	87
Turbine power [MW]	400	Free power turbine power [MW]	32
Exhaust duct total pressure loss [%]	2		2

The combustors in modern gas turbine engines are usually designed to operate in a fuel lean regime, where the fuel-to-air mixture is below stoichiometric conditions to avoid fuel-rich pockets and lower the emissions level. Therefore, reduction in fuel flow will result in lowering flame temperature, which is reflected in figure 3.1 by falling Turbine Entry Temperature (TET) for both single and multi-shaft engines. With less energy supplied to the combustion process the engine begins to produce less power. The control systems then indirectly evaluate the TET, and attempt to maintain the operation of the turbine with choked flow to minimise flow losses and maximise the pressure ratio across the turbine section. Depending on the engine design, the choking will occur most commonly in the throat of the nozzle guide vane, but it may also occur in the turbine rotor, or in the annuls of the outlet from the turbine. The choking at the throat of a flow passage is calculated with non-dimensional air mass flow rate at the design point, and remains unchanged at off-design operation (equation 3.1). Therefore, for a known change in TET, only the engine pressure ratio and air mass flow rate can be controlled. For a single-shaft engine the angular frequency must be maintained as demanded by the electric generator. Therefore, to maintain the choked turbine the engine must operate at lower pressure ratio to compensate for increased gas density (due to lower TET) which at constant speed will progressively increase the surge margin and begin to choke the compressor inlet causing the inlet air mass flow rate to marginally increase. For the compressor to approach chok-

ing it is an unwanted effect, because the increasing inlet flow velocities may cause the blade inlet flow angles to change leading to flow detachment and rapid compressor efficiency deterioration. As the engine power is further reduced, the gradual increase in inlet air mass flow rate is compensated by higher reduction in fuel flow, which in turn results in an almost unchanged exhaust mass flow rate.

In the multi-shaft engine, it is the free power turbine which must maintain constant angular frequency allowing the core of the engine to operate at varying speeds. The benefit of this operation is that the compressor can operate within an optimum range of surge margin resulting in higher compressor efficiency across the load range. There is no risk of compressor inlet choking as compared to single shaft engine; however, flow separation may occur, leading to compressor stall if air inlet mass flow rate is too low at a given engine pressure.

$$\frac{\dot{m}\sqrt{T}}{P} = constant \tag{3.1}$$

Fuel flow reduction on a single shaft engine causes the fuel-air mixture in the fuel nozzle to drastically reduce. This may result in flame-out if the lean limit of combustion is reached (figure 3.11). Therefore, modulation of VIGVs is a common practice to maintain fuel-air mixture relatively constant at part-load to avoid excessively lean conditions. According to the results shown in figure 3.2, closing VIGVs is a good solution for maintaining stable combustion at part load. It is a common practice to vary VIGVs while maintaining TET, which leads to marginally increasing exhaust temperature because the engine operates at a lower pressure when the air mass flow is reduced.

For the bottoming water/steam cycle fundamental parameters are the gas turbine exhaust gas mass flow, the gas temperature, and the gas turbine efficiency. The comparison for the two load reduction strategies on the gas turbine performance are shown in figure 3.3. According to the figure, the gas turbine thermal efficiency across full load range is better with fuel-flow load reduction. However, as demonstrated in appendix section A.2, the change in combined cycle efficiency is negatively related to the change in gas turbine efficiency. Accordingly, improvements in gas turbine efficiency are only feasible if they do not cause to large deterioration in combined cycle efficiency. The VIGV-fuel load reduction at constant TET causes the exhaust gas temperature to rise, which may have adverse effect on the life consumption in downstream components, i.e. HRSG. To counter this effect the exhaust temperature can remain unchanged by regulating the TET (i.e. the fuel flow) while closing the VIGVs, which may lead to higher life-consumption in the hot section because the turbine may now operate in a hotter environment. Therefore, choice of the load change strategy will result in the degree of life consumption in gas turbine and HRSG. In broader terms, taking into account the effect on cycle efficiency and other performance parameters, it is a challenge to deduct from these complex trade-offs the most optimum load reduction strategy, which becomes even more complex when expanding
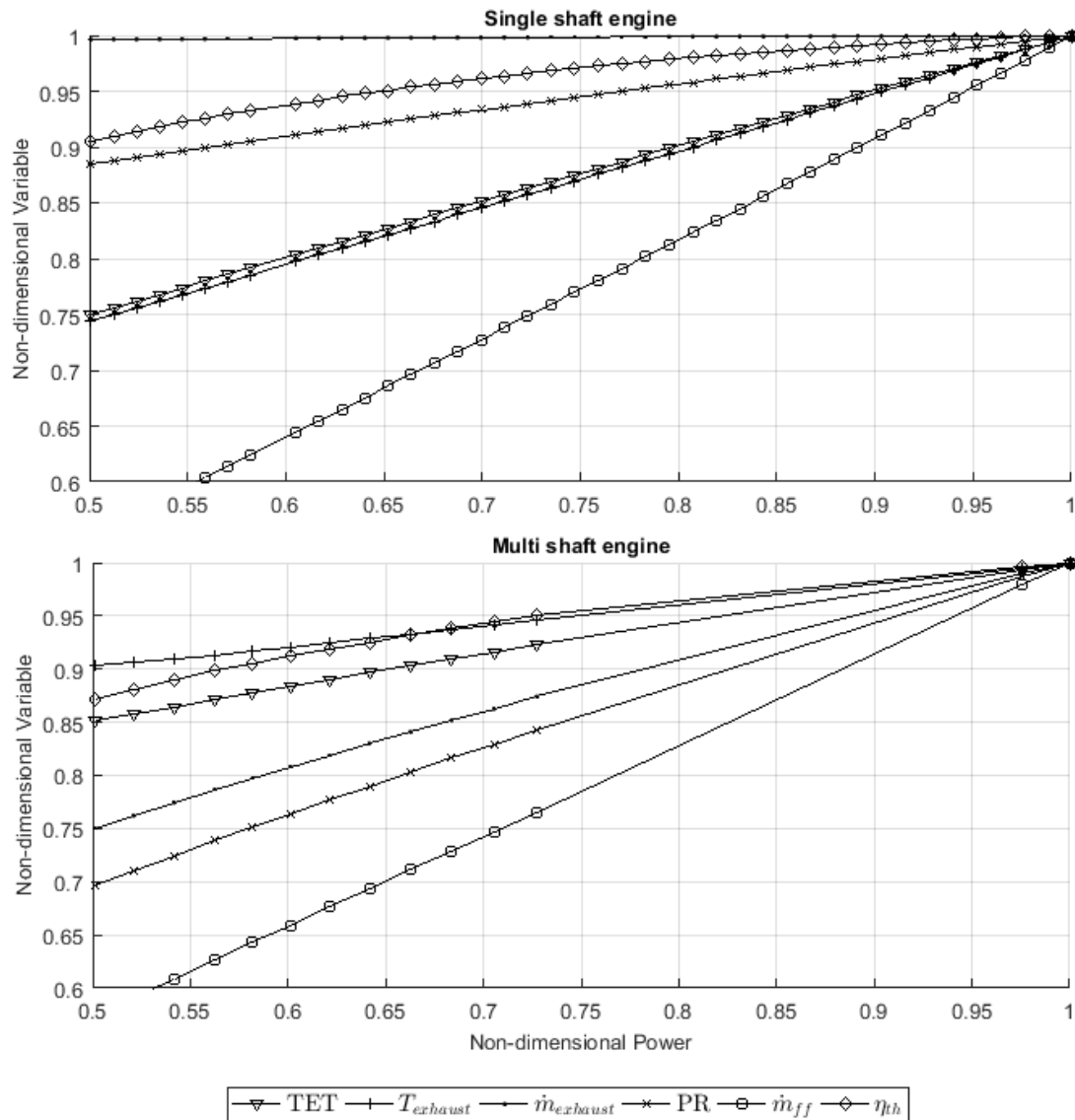
Fig. 3.1 Performance parameters for single and multi-shaft gas turbine with fuel flow load reduction strategy. Plotted using data from Turbomatch simulations

the analysis to account for the effect of alternating between fuel flow and closing VIGV or even controlling both simultaneously. It is the objective of the Operational Flexibility Map to allow for quick interpretation of these complex trade-offs for any combination of load change strategies.
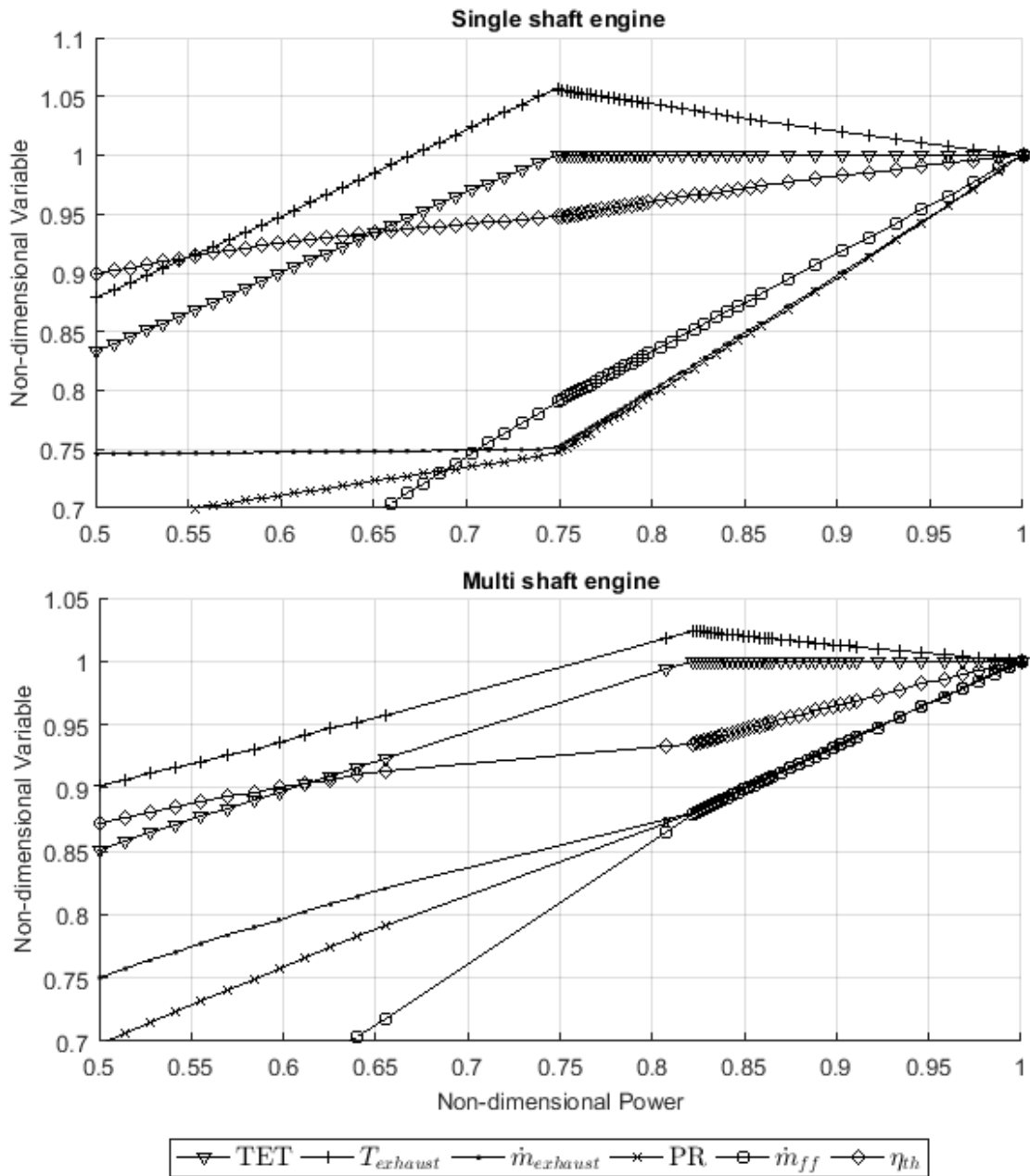
Fig. 3.2 Performance parameters for single and multi-shaft gas turbine with VIGV-fuel load reduction strategy. Plotted using data from Turbomatch simulations
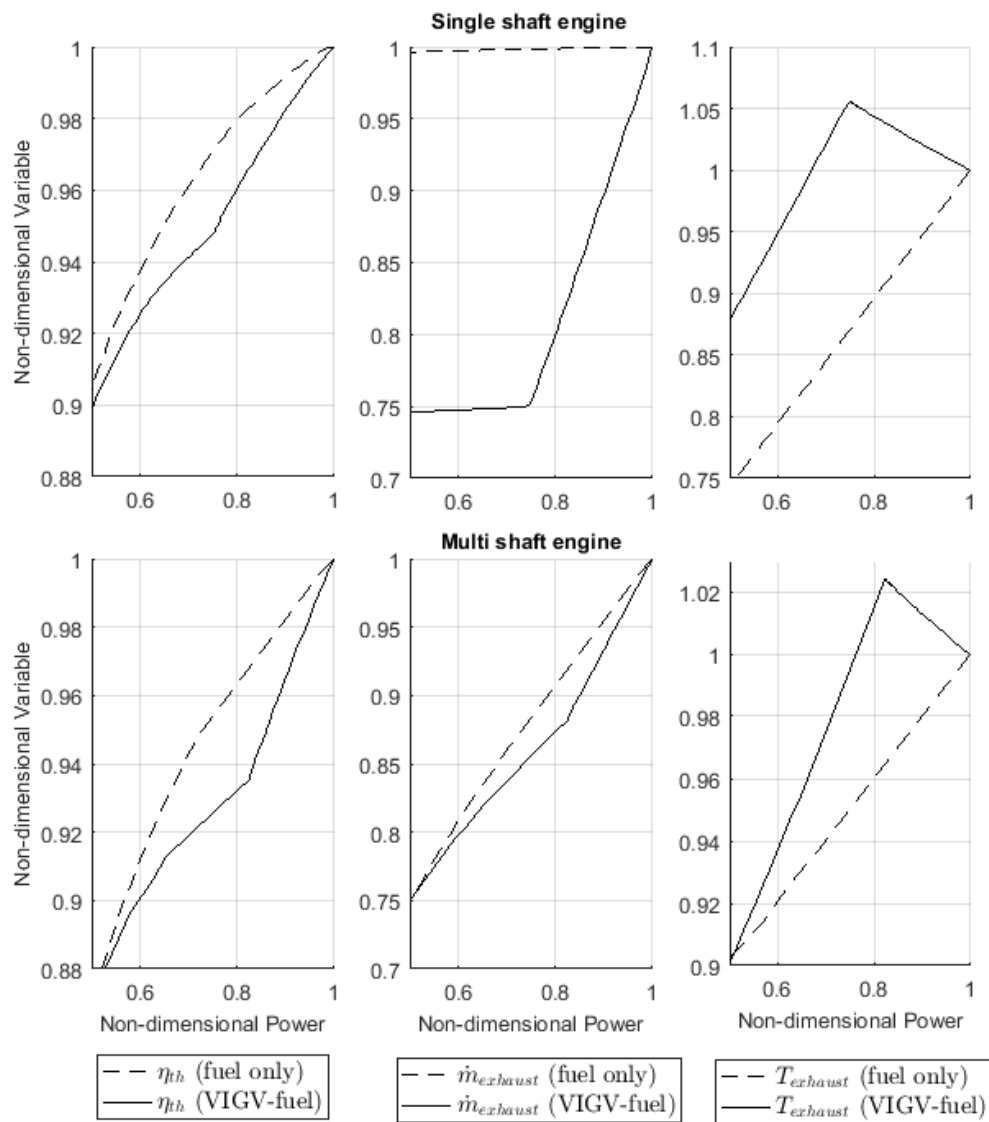
Fig. 3.3 Comparison of performance variables between fuel and VIGV-fuel load reduction strategy. Plotted using data from Turbomatch simulations

3.2   Development of gas turbine operational flexibility map

It has been demonstrated in section 3.1 that with existing techniques many computationally expensive simulations are required to study the effect of load reduction on system performance. The procedure is even more complex if a composite effect of a combination of fuel and VIGV control is investigated. For example, simultaneous reduction in fuel flow and closing VIGVs, or alternating between fuel flow reduction and closing VIGVs, would require simulating and interpreting a large amount of often conflicting performance data. This would make concise representation of the results and drawing conclusions from the studies very difficult. Analogically, in the past these issues were also apparent in the gas turbine performance studies, which led to the development of the compressor and turbine maps. One can analyse the change in part-load performance between any operational points on the map, however, these maps do not directly disclose the effect of how the load is changed. Considering recently evolving global energy markets, the question of how the load is changed and what is corresponding effect on performance becomes increasingly important to understand flexible operation. A novel gas turbine operational flexibility map has been developed as a step towards improving flexible operation and allow for quick interpretation of complex and conflicting operational parameters with various load change strategies.

A Buckingham pi theorem allows analysis of complex systems and combining of variables into smaller dimensionless groups. According to the theorem, *n* variables can be reduced to *n-3* dimensionless groups due to presence of three fundamental units of mass, length and time. The form of the dimensionless groups is highly dependent on the selection of three repeating variables, which appear in all pi terms and should contain all three fundamental units. It has been concluded that these should represent variables which cannot be controlled or changed by the power plant operator, i.e. 1) compressor characteristic diameter representing the engine size, 2) ambient temperature, and 3) ambient pressure. Therefore, the fundamental operation of the gas turbine engine and its corresponding operational flexibility map can be obtained separately for each combination of these repeating variables.

Assuming that the working fluid behaves as an ideal gas, the temperature can be represented as $RT = \frac{P}{\rho}$ with fundamental dimensions of $[l^2 t^{-2}]$. Therefore, the resulting presence of the gas constant, R, allows for analysing the effect of various kinds of working fluids. The rest of the performance parameters considered and their respected fundamental units are listed in table 3.2. The formulation of the set of non-dimensional groups must reflect the practical needs of power plant operators and also considering the application of the operational flexibility map.

Table 3.2 Dimensions of main performance parameters

Variable	Fundamental dimensions	Comments
D	$[l]$	Repeating variable. Compressor characteristic diameter
$(RT)_{amb}$	$[l^2 t^{-2}]$	Repeating variable. Ambient temperature
P_{amb}	$[m l^2 t^{-2}]$	Repeating variable. Ambient pressure
N	$[t^{-1}]$	Engine rotational speed
$\dot{m}_{ff}$	$[m t^{-1}]$	Fuel mass flow
$VIGV$	$[]$	Angle of Variable Inlet Guide Vanes (VIGVs)
PO_{GT}	$[mt]$	Gas turbine power output
$RTET$	$[l^2 t^{-2}]$	Turbine entry temperature
$(RT)_{exhaust}$	$[l^2 t^{-2}]$	Turbine exhaust temperature
$\dot{m}_{GT,in}$	$[m t^{-1}]$	Inlet mass flow
η_{GT}	$[]$	Gas turbine thermal efficiency

3.2.1   Selecting variables for the coordinate system

One of the important decisions a power plant operator needs to make is regarding which load change strategy to follow. For a given gas turbine technology, a chosen strategy determines a degree improvement or deterioration in flexibility which can make a power plant more or less economically attractive. Therefore, abscissa and ordinate for every point on the map should represent a general load change dimensionless group. The load of a gas turbine engine can be changed using various techniques, each of which results in a certain degree of economic consequences. The two main techniques to change the load are to control variable area or fuel flow. The modulation in VIGVs angle at the inlet to the low pressure compressor affects the rate of air mass flow into the compressor. Change in engine inlet mass flow has a large effect on power output. Apart from the preferred method of varying VIGVs angle, the inlet air mass flow and resulting load level can also be changed by preheating inlet air, or extracting bleed from the compressor. Therefore, inlet air mass flow on the x-axis is an important parameter for any load reduction strategy. On the second strategy, modulation in fuel flow results in changes in temperature at the inlet to the turbine, which affects gas energy content and expansion capacity across the turbine. Generally, first stage turbine rotor blades are very sensitive to a variation in flow path temperature. Therefore, the turbine entry temperature on the y-axis is one of the main parameters that must be closely monitored while changing engine load.

As the result, the first two dimensionless groups forming x and y axis on the map are: the non-dimensional inlet air mass flow, π_1, and non-dimensional turbine entry temperature, π_2. The calculations for the first non-dimensional group are shown in section 3.2.2, and same methodology is used to obtain the rest of the groups.

3.2.2 Procedure for obtaining non-dimensional groups

The first three terms in equation 3.2 are repeating variables and the last term represents inlet air mass flow, all with corresponding coefficients a,b,c, and d. Each variable on the left side in the equation is represented with its fundamental dimensions in the right side of the equation.

$$D^a (RT)^b_{amb} P^c_{amb} \dot{m}^d_{GT,in} = [l]^a [l^2 t^{-2}]^b [ml^2 t^{-2}]^c [mt^{-1}]^d \tag{3.2}$$

this gives the following set of linear equations

$$\begin{cases} c + d = 0, & \text{for m} \\ -2b - 2c - d = 0, & \text{for t} \\ a + 2b + 2c = 0, & \text{for l} \end{cases} \tag{3.3}$$

writing all coefficients in terms of d

$$\begin{cases} c = -d, & \text{for m} \\ b = 0.5d, & \text{for t} \\ a = d, & \text{for l} \end{cases} \tag{3.4}$$

inserting coefficients back into original equation, gives the first non-dimensional mass flow group

$$\pi_1 = D^d (RT)^{0.5d}_{amb} P^{-d}_{amb} \dot{m}^d_{GT,in} = \frac{D \dot{m}_{GT,in} \sqrt{(RT)_{amb}}}{P_{amb}} \tag{3.5}$$

the term D and R can be neglected if engine size and fluid type is unchanged. The temperature and pressure is referenced to ISA standard conditions

$$\pi_1 \approx \frac{\dot{m}_{GT,in} \sqrt{\frac{T_{amb}}{T_{ISA}}}}{\frac{P_{amb}}{P_{ISA}}} \tag{3.6}$$

similarly the non-dimensional TET

$$\pi_2 = \frac{RTET}{(RT)_{amb}} = \frac{TET}{T_{amb}} \tag{3.7}$$

non-dimensional gas turbine power

$$\pi_3 = \frac{[(RT)_{amb}]^{3/2} PO_{GT}}{D P_{amb}} \approx \frac{T^{3/2}_{amb} PO_{GT}}{P_{amb}} \tag{3.8}$$

non-dimensional angle of VIGVs

$$\pi_4 = VIGV \tag{3.9}$$

non-dimensional gas turbine efficiency

$$\pi_5 = \eta_{GT} \tag{3.10}$$

and non-dimensional gas turbine exhausts temperature

$$\pi_6 = \frac{T_{exhaust}}{T_{amb}} \tag{3.11}$$

Having determined all of the PI terms, the relation of any selected non-dimensional group can be expressed as function of the others. For example

$$\pi_3 = f(\pi_1, \pi_2, \pi_4, \pi_5) \tag{3.12}$$

or

$$\frac{[(RT)_{amb}]^{3/2}PO_{GT}}{DP_{amb}} \approx \frac{T_{amb}^{3/2}PO_{GT}}{P_{amb}} = f(\frac{\dot{m}_{GT,in}\sqrt{\frac{T_{amb}}{T_{ISA}}}}{\frac{P_{amb}}{P_{ISA}}}, \frac{TET}{T_{amb}}, VIGV, \eta_{GT}) \tag{3.13}$$

rearranging the equation further

$$PO_{GT} = \frac{D}{R_{amb}^{3/2}}\frac{P_{amb}}{T_{amb}^{3/2}}f(\frac{\dot{m}_{GT,in}\sqrt{\frac{T_{amb}}{T_{ISA}}}}{\frac{P_{amb}}{P_{ISA}}}, \frac{TET}{T_{amb}}, VIGV, \eta_{GT}) \tag{3.14}$$

3.2.3 Results and discussion

The performance of a 400MW single shaft gas turbine engine has been simulated with Cranfield in-house software Turbomatch. The obtained results were then studied and post-processed to develop the operational flexibility map. Figure 3.4 shows calculated lines of constant non-dimensional power output as function of non-dimensional inlet mass flow and non-dimensional TET for a single shaft gas turbine engine. Because of the assumption that the turbine remains choked at part-load, the TET must increase to accommodate reduction in inlet mass flow in order for the engine to remain at constant power. Therefore, the constant power output lines have negative slopes. Examining the operational flexibility map in figure 3.4 reveals that engine power can be varied at constant non-dimensional TET, constant non-dimensional inlet mass flow, or perhaps any other combination of these two non-dimensional groups. The most common load change strategies are modulating VIGVs angle at constant $T_{exhaust}$ in CCPP application, modulating VIGVs at constant TET in simple cycle application, or modulating fuel flow [24].

Performance simulation results show that the fuel flow depends linearly on the engine power output. Therefore, non-dimensional power output lines can be replaced with non-dimensional fuel flow, as calculated and shown in figure 3.5. The thermal efficiency
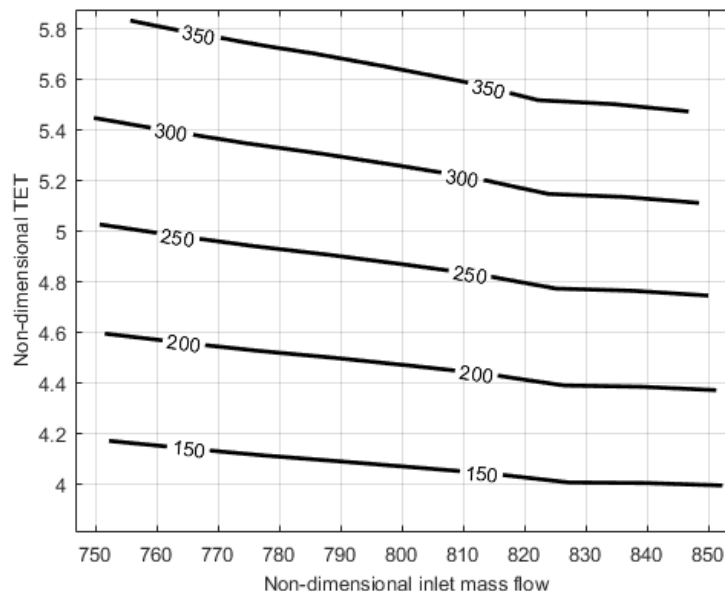
Fig. 3.4 Gas turbine operational flexibility map with constant non-dimensional power output lines for single shaft engine. Plotted using data from Turbomatch simulations

is already a non-dimensional group by definition, of which constant contour lines are calculated and shown in figure 3.6.

Load change by modulating Variable Inlet Guide Vanes angle

The angle of VIGVs is already a non-dimensional group by definition, of which constant lines are calculated and shown in figure 3.7 together with constant non-dimensional power. The angle is referenced from the design position of the variable geometry blades at 0°. At each constant VIGVs line, the non-dimensional inlet mass flow increases slightly with load reduction. This is because for a single shaft gas turbine operating at constant speed, reduction in fuel flow will progressively increase surge margin and begin to choke the compressor causing the inlet mass flow to marginally increase.

Figure 3.8 shows constant non-dimensional exhaust temperature lines together with non-dimensional power and efficiency. The exhaust temperature is an important parameter if a bottoming cycle is used to extract energy from the gas turbine exhaust to improve overall combined cycle efficiency, and power output. It is a common practice to install shell-and-tube type heat exchanger in the exhaust duct to extract energy from the exhaust flow, i.e. HRSG. In this case, the plant operator must monitor the exhaust temperature not to exceed thermal limits of the heat exchanger tube materials; otherwise the component may fail incurring extensive costs during plant shut down for maintenance. As the load of an engine is reduced, the exhaust temperature is kept nearly constant by modulating fuel
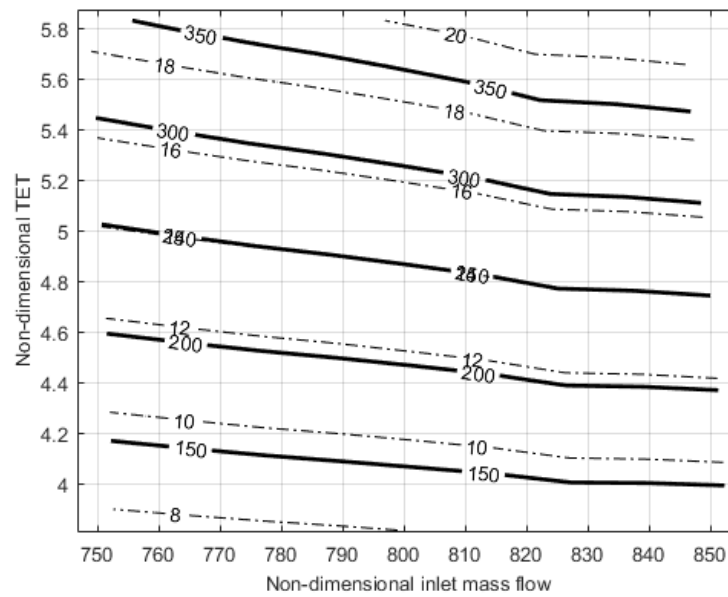
Fig. 3.5 Gas turbine operational flexibility map with additional constant non-dimensional fuel flow dotted lines for single shaft engine. Plotted using data from Turbomatch simulations
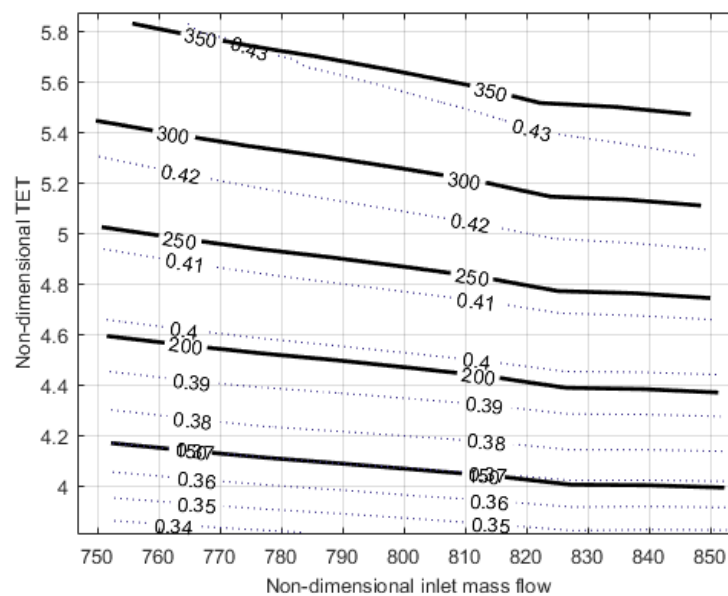
Fig. 3.6 Gas turbine operational flexibility map with additional constant non-dimensional thermal efficiency lines for single shaft engine. Plotted using data from Turbomatch simulations
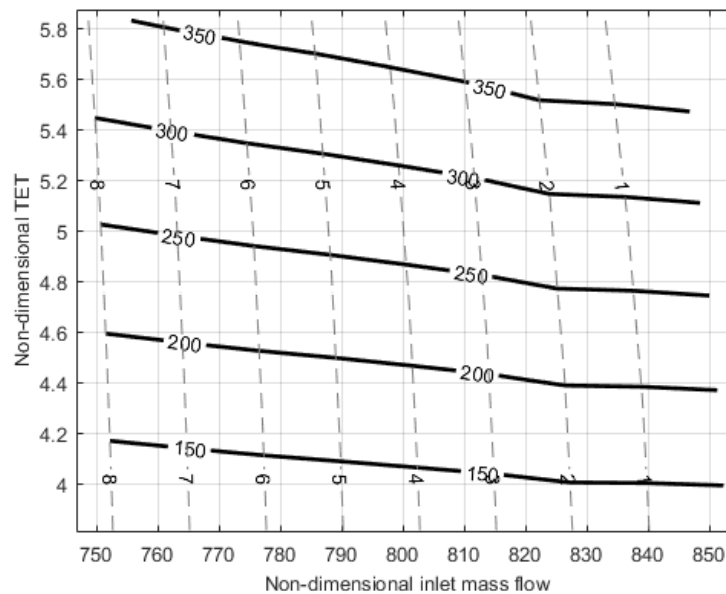
Fig. 3.7 Gas turbine operational flexibility map with additional constant dotted lines of VIGVs angle for single shaft engine. Plotted using data from Turbomatch simulations

flow. A line in figure 3.8 illustrates a load reduction from approximately 310 MW to 270 MW at constant exhaust temperature by closing VIGVs angle from 0° to 8°. The non-dimensional TET is reduced from 5.2 to 5.15, resulting in life reduction of turbine blades due to thermal cycling. The thermal efficiency is reduced from approximately 42.6% to 41.6%. In a real engine, however, the angle of VIGVs can be changed further up to 40°, which implies much greater reduction in TET and consequent greater life consumption.

To avoid thermal cycling of high temperature turbine components, a common strategy for load reduction is to modulate VIGVs angle at constant turbine entry temperature. This load reduction and resulting performance trade-offs are shown in figure 3.9. For a simple cycle this load reduction strategy results in better part-load efficiency as compared to VIGVs modulation at constant exhaust temperature. This is because according to figure 3.6 the constant efficiency lines are degrading much slower at constant TET lines. According to the example in the figure, load reduction from 310 MW to 270 MW by reducing VIGVs angle from 0° to 8° will have constant non-dimensional TET of 5.2 and thermal efficiency reduction from approximately 42.6% to 41.7%. However, this load reduction strategy improves gas turbine component life at the cost of increasing exhaust gas temperature, which could lead to heat recovery steam generator failure.
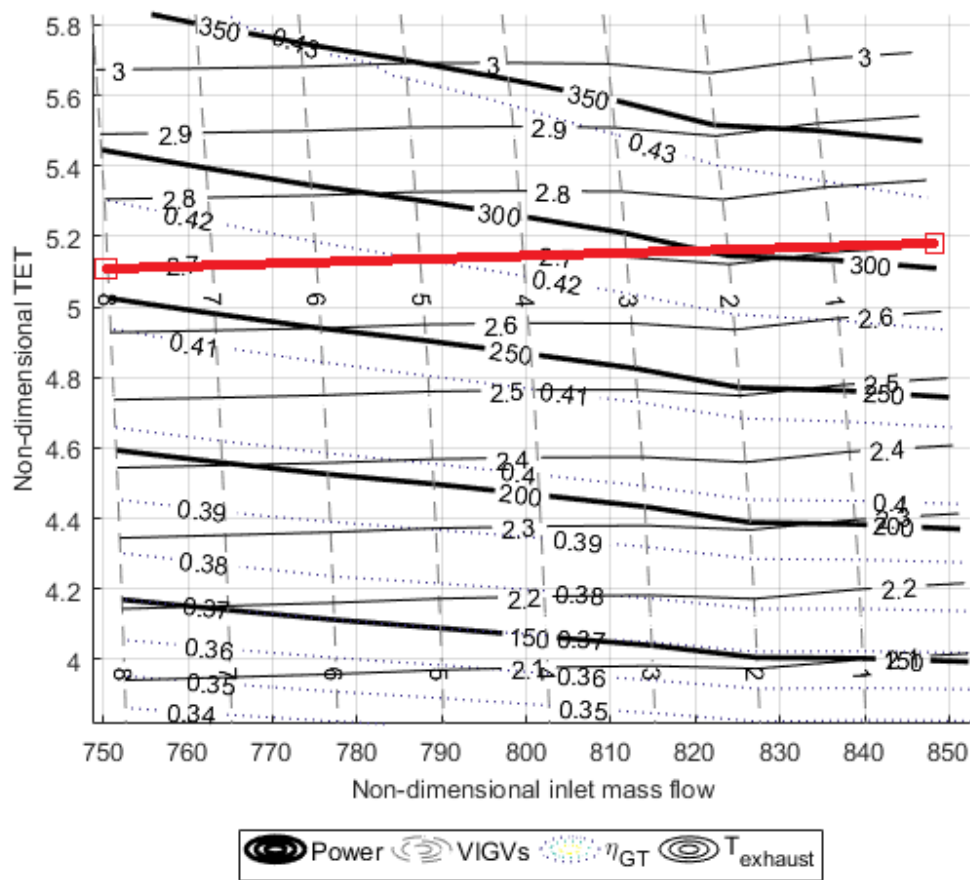
Fig. 3.8 Gas turbine operational flexibility map for single shaft engine. Shown load reduction line by closing VIGVs at constant exhaust temperature (red line). Plotted using data from Turbomatch simulations
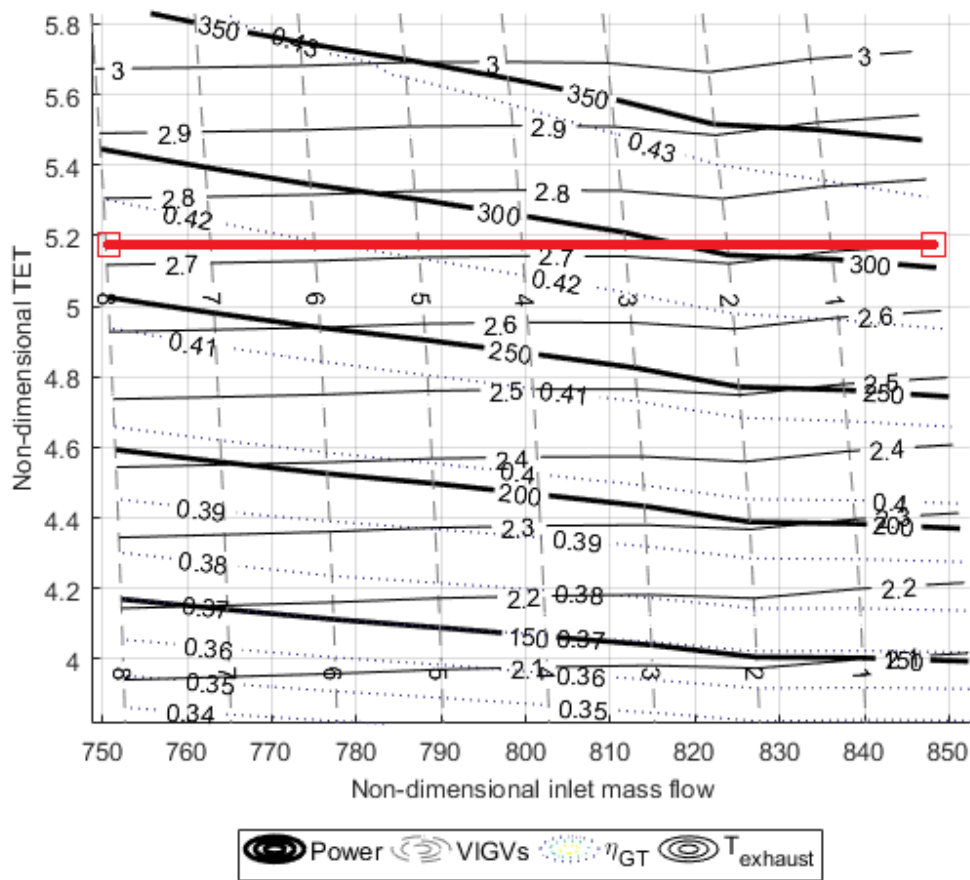
Fig. 3.9 Gas turbine operational flexibility map for single shaft engine. Shown load reduction line by closing VIGVs at constant TET (red line). Plotted using data from Turbomatch simulations

Load change by reducing fuel flow rate

The operation of the engine with power reduced by modulating fuel flow at constant VIGVs angle is calculated and shown on engine operational flexibility map in figure 3.10. The load is reduced from 310 MW to 250 MW at constant 1° VIGVs angle. However, this results in large thermal cycling in the hot-path components and much more rapid reduction in thermal efficiency. Because the engine is operating at lower temperatures, the exhaust temperature will also reduce.
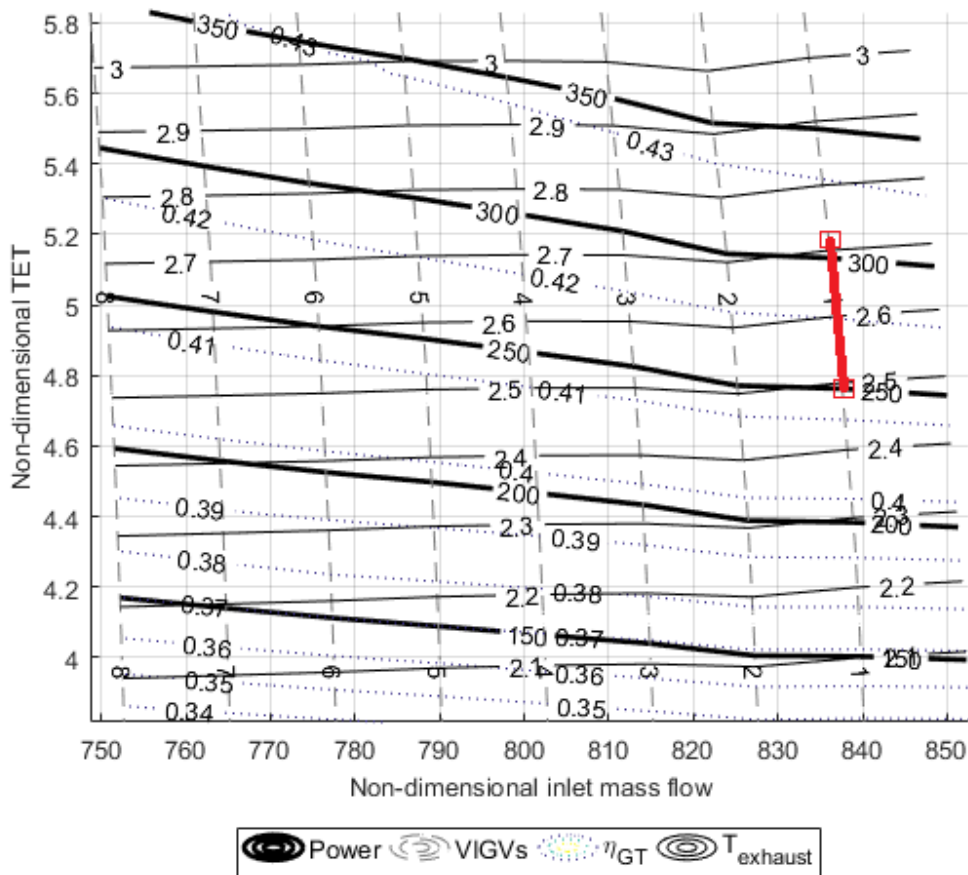
Fig. 3.10 Gas turbine operational flexibility map for single shaft engine. Shown load reduction line by fuel flow modulation at constant VIGVs angle (red line). Plotted using data from Turbomatch simulations

Composite load change strategy for improved flexibility

It appears clearly in figure 3.4 that power reduction at constant non-dimensional inlet mass flow takes place more rapidly than at constant non-dimensional TET. The engine appears to be more responsive to the fuel flow modulation rather than closing VIGVs. It must be noted however, that if air flow is reduced maintaining fuel flow, a risk of overheating the hot section of the turbine is inevitable. Similarly, if fuel flow is reduced maintaining air flow, a flame out in the combustor may occur. This concept is illustrated with a typical combustion chamber stability loop shown in figure 3.11. The boundaries of the stability loop define the region where combustion will occur. The load reduction strategy must therefore account for stable combustion at off-design. Further research is needed to include the stability of the combustion process in the operational flexibility map. Further study is also needed to investigate the engine response time to fuel flow and air mass flow modulations to fully appreciate the benefits of the map.

According to the results obtained herein, it appears that a composite load reduction strategy could be implemented to allow for fast engine response. This seems to be in the normal direction to the constant non-dimensional power lines. For a given engine, keeping all physical parameters unchanged, the most flexible path to change load is therefore from for example 310 MW to 250 MW as shown in figure 3.12. This can be done by a major modulation in non-dimensional TET from 5.2 to 4.8, e.g. by altering fuel flow rate, and simultaneously with a minor change in non-dimensional inlet mass flow, e.g. by pre-heating inlet air to reduce density, inlet air bleed extraction, or variable geometry by closing VIGVs by approximately 0.2^o.
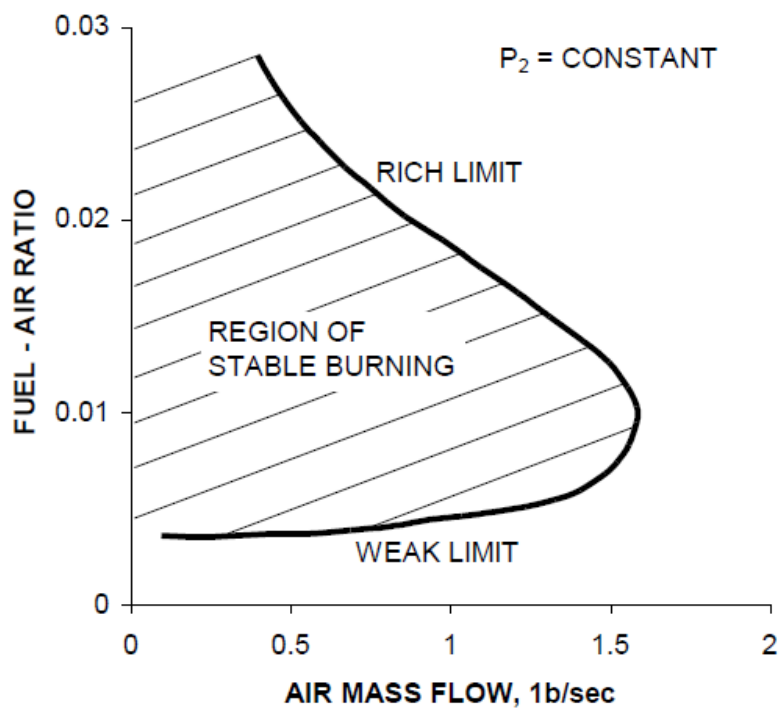
Fig. 3.11 Typical combustor chamber stability loop [59]
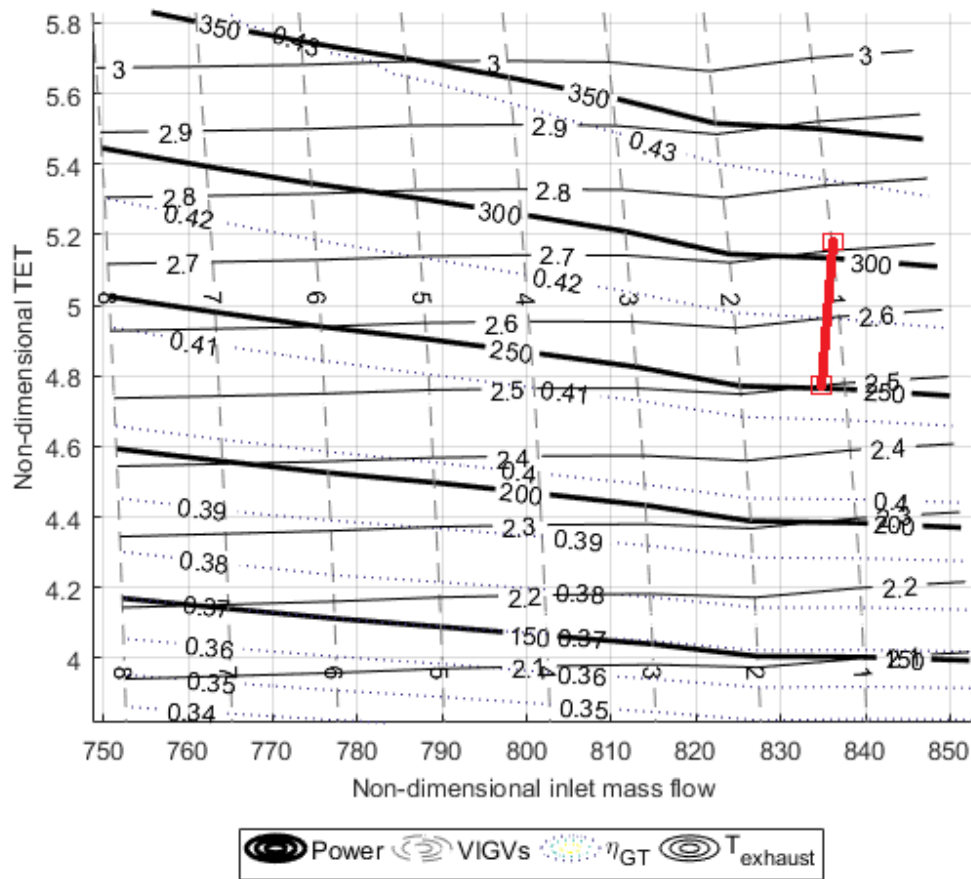
Fig. 3.12 Gas turbine operational flexibility map for single shaft engine. Shown load reduction line by a combination of non-dimensional TET and non-dimensional inlet mass flow modulation to achieve higher operational flexibility. Plotted using data from Turbomatch simulations

3.3   Development of life consumption map

First stage high pressure turbine rotor blades and discs are critical components for failure analysis. The following analysis can be applied to any location within the engine as long as the input parameters are known; however, the focus is on the first stage high pressure turbine rotor blades. These blades operate in harsh environment with temperatures usually exceeding the alloy melting point. Technological progress in blade cooling technologies allows achieving increasingly higher power output, however at the cost of higher component life consumption.

High pressure turbine blades operating in these conditions are prone to failure under various mechanisms. The blade will fail under low cycle fatigue leading to fracture if low frequencies of significantly high stress amplitudes induce plastic strains in the material. This is a typical scenario for plant start-stop cycles, or load changes. On the other hand, the blade will fail under creep deformation leading to fracture under the influence of high temperature and high stress for prolonged periods of time. This is a typical mechanism experienced by high pressure turbine blades when plant is in operation. The following assumptions are made in this study:

1. The blade alloy to be NIMONIC 115, which is a common nickel based alloy used for manufacturing of turbine blades

2. The flow is in steady state conditions

In order to avoid excessive blade temperature, the cooling air is extracted from a location within the engine of similar pressure but lower temperature to maximise heat transfer. If film cooling technology is implemented in the blade, the pressure of the cooling air must be higher then the pressure of the hot path gas. It is a common practice to extract cooling air at temperature, $T_{cooling}$, from the last stage of high pressure compressor at the expense of reduced engine power. The temperature of the blade, T_{blade}, can then be calculated with equation 3.15. Where the blade cooling effectiveness is assumed to be 0.637.

$$T_{blade} = TET - CE(TET - T_{cooling}) \qquad (3.15)$$

Figure 3.13 shows simulated variation of TET, $T_{cooling}$, and T_{blade} in the operating range of single-shaft and multi-shaft gas turbine engine against alloy melting point temperature [60]. Two load reduction strategies have been studied, one with fuel flow control, and second by closing VIGVs from $0 - 40^o$ and following fuel flow control. Since the single shaft engine operates at much higher power, the TET exceeds alloy melting temperature in the high load region and the use of cooling is inevitable.
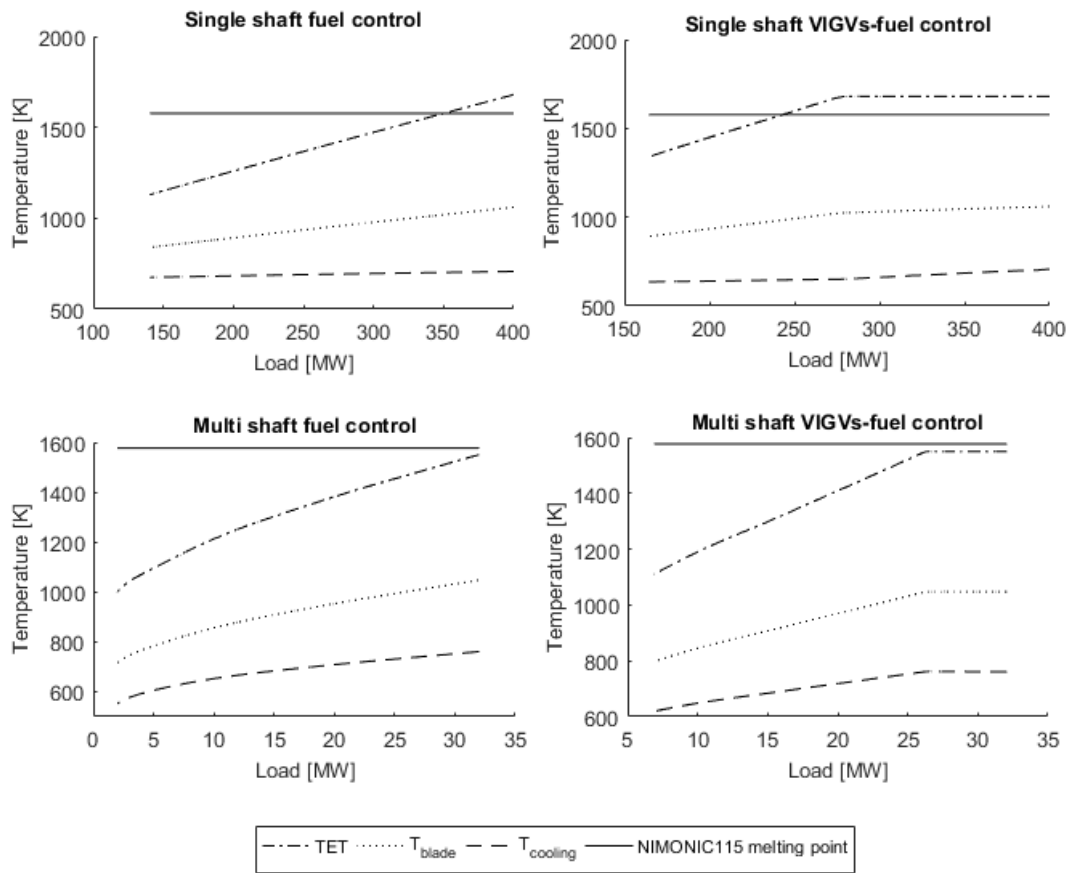
Fig. 3.13 Simulated results of single and multi-shaft gas turbine performance at part-load versus turbine blade melting point temperature

High pressure turbine blades experience various forces, with the highest centrifugal force acting at the root of the blade. Other sources of stress include gas bending moment due to changes in gas momentum and pressure across the blade, gas bending moment due to centrifugal loading if blade centre of mass doesn't align radially above the centroid of the disc, stress due to thermal gradients across the blade, and sometimes vibrations arising from acoustic oscillations in the combustor. In the current study only centrifugal stress is taken into account due to its dominant effect, which is calculated with equation 3.16.

$$\sigma = \frac{\rho \omega^2}{2}(R_t^2 - R_r^2) \tag{3.16}$$

The blade root and tip radii are assumed to be 0.81 and 0.89 meters, respectively. Any geometric modifications to the blade create local regions of stress concentration. These are usually at the blade root to provide adequate mounting, and sealing methods. In the

current study, it was assumed that stress concentration factor at the root of the blade is $K_t = 2.82$. Therefore, the centrifugal stress at the notch is calculated with equation 3.17. Because of the inevitable existence of local region of stress concentration, the region should be carefully examined against failure.

$$\sigma_{notch} = K_t \sigma \qquad (3.17)$$

3.3.1   Low cycle fatigue in high pressure turbine rotor blade

During the power plant start and stop cycles or load changes, a high pressure turbine blade is exposed to variations in stress and gas temperature levels. The stress level is a function of blade rotational speed, therefore single and multi-shaft gas turbine engines will have different blade stress profiles at the same part-load condition. The gas temperature on the other hand is dependent on the load reduction strategy, as discussed in section 3.2. As a result, the blade material will exhibit different mechanical properties as its environment changes at engine off-design conditions.

Figure 3.14 shows simulated results of stress levels at a notched root of high pressure turbine blade against the mechanical properties of the alloy (Nimonic alloy 115), at part-load operation for single and multi-shaft engine. The figure also shows variations in properties depending on whether the load is reduced by modulating fuel flow, or first closing VIGVs from $0 - 40^o$ followed by fuel flow reduction.

According to the figure, the centrifugal stress at the notch of the blade exceeds the yield stress of the material at all load ranges for single and multi shaft engine. Therefore, plastic deformation will occur locally at the stress concentration region leading to un-recoverable deformation; thus life consumption. The single shaft engine operates at constant rotational speed as required by electrical generator to maintain grid frequency of 50Hz in Europe and 60Hz in Americas. This typically leads to 3,000 rpm in Europe; therefore, the stress level remains unchanged with only TET and alloy mechanical properties changing at part-load as function of temperature. The multi-shaft engine contains free power turbine linked to the electrical generator, and a disconnected gas generator with varying rotational speed at part-load operation giving rise to reducing stress level and changing alloy mechanical properties at part-load.

Analytical modelling

If the local stress level at particular engine part-load operation does not exceed yield strength limit of the alloy, only elastic strain deformation, ε^e, will occur. The loading and unloading under this condition is reversible and the local deformation will return to original shape once the load is removed as shown in figure 3.15a, and according to equation
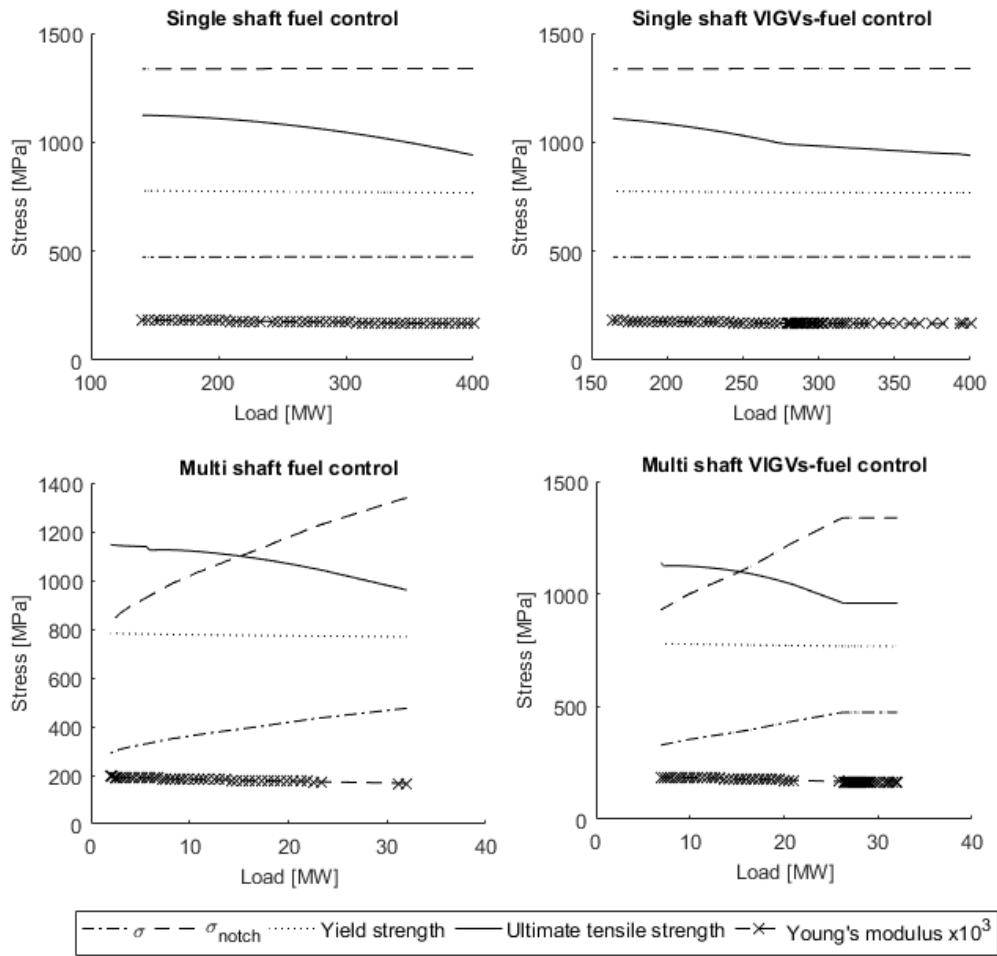
Fig. 3.14 Simulated results of centrifugal stress level in high pressure turbine blade for single and multi-shaft gas turbine against mechanical properties of NIMONIC 115 alloy

3.18. Since the Youngs modulus in figure 3.14 increases with load reduction, the amount of elastic strain deformation will decrease with load reduction.

Figure 3.15b shows that the load level is sufficiently large at point A for the local stress to exceed the yield strength of the material. Therefore, Neuber's rule, given in equation 3.21a, is applied to determine plastic strains and convert an elastically determined stress into actual stress level lying on the materials stress-strain curve. As the result, additionally to elastic deformation, irreversible plastic deformation will occur locally according to equation 3.19. When the load is removed the local region of stress concentration in the blade will be subject to compressive forces, point C, because irreversible plastic de-

formation will exert pressure on the surrounding material, which intends to return to its original shape. If the cycle is then repeated up to the same load level, point A or point B after applying Neuber's rule, the already induced plastic deformation will remain, and only local elastic deformation will take place in the material. According to figure 3.15c, if the stress level is sufficiently high, approximately $> 2\sigma_{ys}$, Massings hypothesis states that the unloading process will follow the Hysteresis stress-strain curve according to equation 3.20.

$$\varepsilon^e = \frac{\sigma}{E} \tag{3.18}$$

$$\varepsilon^p = (\frac{\sigma}{K})^{\frac{1}{n}} \tag{3.19}$$

$$\Delta\varepsilon = \frac{\Delta\sigma}{E} + 2(\frac{\Delta\sigma}{2K})^{\frac{1}{n}} \tag{3.20}$$

Therefore, by solving the set of equations 3.21a and 3.21b, the actual stress and strain levels at local high stress regions are obtained at each plant load level.

$$\begin{cases} \dfrac{(K_t\sigma_A)^2}{E} = \sigma_A\varepsilon_A = \sigma_B\varepsilon_B & (3.21a) \\[2mm] \varepsilon_B = \varepsilon_B^e + \varepsilon_B^p = \dfrac{\sigma_B}{E} + (\dfrac{\sigma_B}{K})^{\frac{1}{n}} & (3.21b) \end{cases}$$

During the unloading however, the local coordinate system is used with the datum at point B according to equation 3.22. Where $\Delta\sigma$ and $\Delta\varepsilon$ represent the actual change in stress and strain level induced by reducing the plant load level, $\Delta Load$.

$$\begin{cases} \sigma_c = \sigma_B - \Delta\sigma \\ \varepsilon_c = \varepsilon_B - \Delta\varepsilon \end{cases} \tag{3.22}$$

The unloading process, path B-D, will follow the Massing curve described by equation 3.20. Neuber's rule is used to convert the stress and strain levels at point C to actual levels at point D. By solving the set of two equations in equation 3.23, actual stress and strain levels are obtained at point D as the result of changing plant load level.

$$\begin{cases} \dfrac{(K_t\Delta\sigma)^2}{E} = (\sigma_B - \Delta\sigma)(\varepsilon_B - \Delta\varepsilon) = \sigma_D\varepsilon_D \\[2mm] (\varepsilon_B - \varepsilon_D) = \dfrac{(\sigma_B-\sigma_D)}{E} + 2(\dfrac{(\sigma_B-\sigma_D)}{2K})^{\frac{1}{n}} \end{cases} \tag{3.23}$$

The prediction of life consumption due to low cycle fatigue has been modelled by Morrow, with consistent validation against observations widely published in the literature [61]. According to Coffin-Manson Strain Life equation 3.24, knowing the $\Delta\varepsilon$ and σ_m terms the number of cycles to failure, N_f, is calculated where coefficients b and c are the fatigue strength and ductility exponents, respectively. The cumulative damage is calculated with
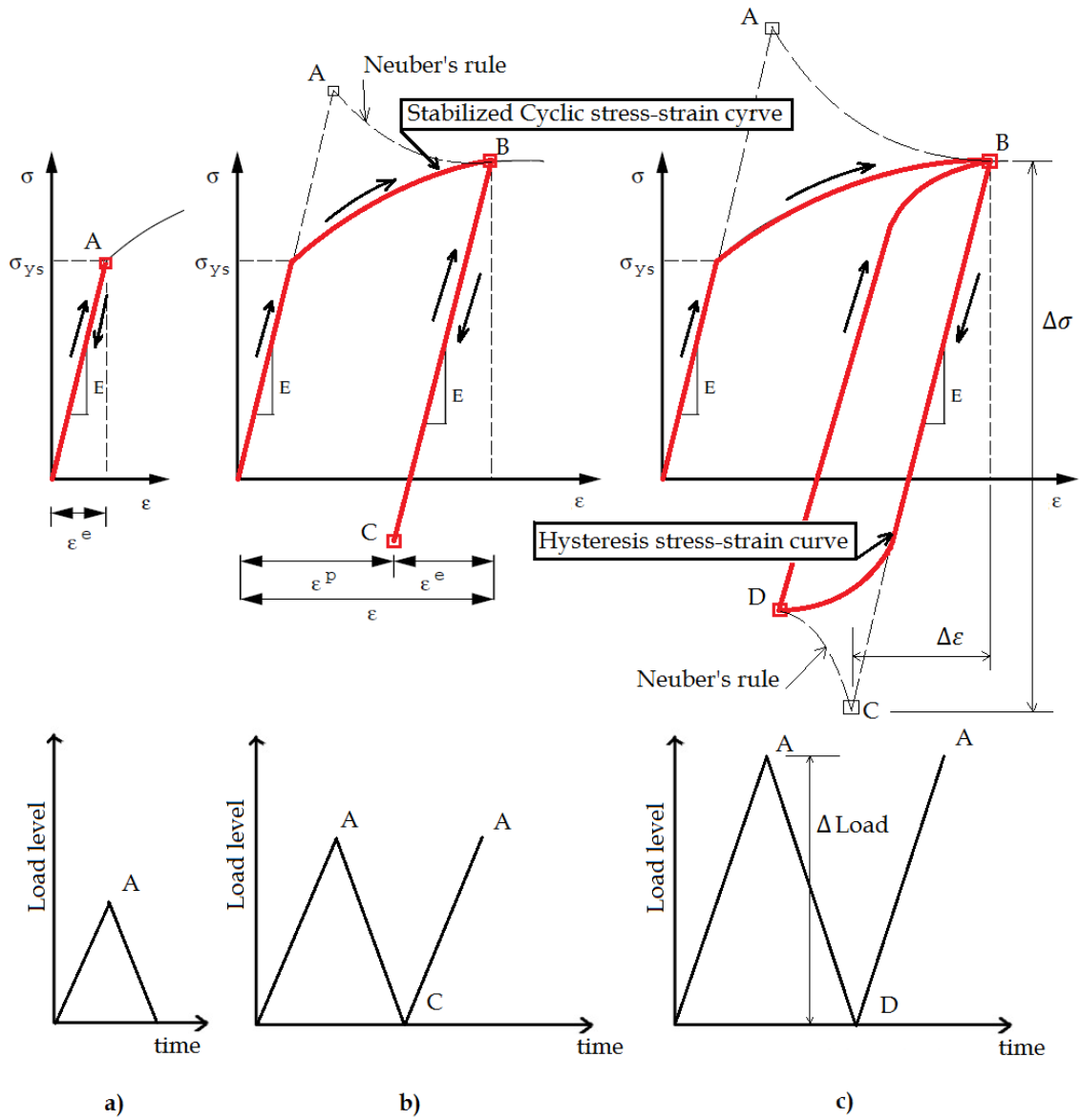
Fig. 3.15 Stress-strain diagram for various load change scenarios. Various states of operation are shown with points A, B, C and D

equation 3.25, such that if the fatigue life consumed is greater than 1, the failure will occur.

$$\frac{\Delta\varepsilon}{2} = \frac{\sigma'_f - \sigma_m}{E}(2N_f)^b + \varepsilon'_f(2N_f)^c \qquad (3.24)$$

$$\text{Fatigue life consumed} = \sum \frac{1}{N_f} \qquad (3.25)$$

3.3.2   Creep in high pressure turbine rotor blade

The strength of a turbine blade alloy reduces with increase in gas temperature as shown in figure 3.14. At high temperatures and with sufficiently long exposure time, the alloy experiences greater mobility of dislocations and an increase in the equilibrium concentration of vacancies. Based on experimental observations, it has been generally accepted that the effect of creep deformation becomes noticeable when temperature is greater than approximately 40% of the material melting point. Since gas turbine engines operate at high temperatures, this limit is often exceeded giving raise to significant creep life consumption. If a high pressure turbine blade is exposed to high stress and temperature for prolonged periods of time, the local stress concentration region will begin to deform, known as primary creep. The strain rate then slows down and becomes nearly constant known as secondary or steady-state creep. At some point in time the strain will start to increase exponentially in tertiary creep leading to fracture. The creep fracture can be predicted using a correlative approach. The Larson-Miller Parameter (LMP) is the most popular parametric method due to its reasonable accuracy in predicting failure. This parametric expression is calculated using equation 3.26.

$$LMP = \frac{T}{1000}(log_{10}t_f + C) \qquad (3.26)$$

The constant, C, is usually taken as 20 for industrial gas turbine engines. The Larson-Miller parameter, LMP, is obtained from alloy experimental curves as function of stress level. Assuming the blade alloy to be NIMONIC 115, which is a common nickel-based alloy used to manufacture high pressure turbine blades, the LMP is calculated with equation 3.27 as function of stress level [62].

$$LMP = \begin{cases} 3.2e^{-5}\sigma^2 - 2.74e^{-2}\sigma + 30.47, & \text{if } \sigma \leq 250 \text{ MPa} \\ 1.0e^{-5}\sigma^2 - 1.65e^{-2}\sigma + 29.13, & \text{if } \sigma > 250 \text{ MPa} \end{cases} \qquad (3.27)$$

The cumulative fraction of creep life consumed is calculated by applying Miners law for linear damage with equation 3.28.

$$\text{Creep life consumed} = \sum \frac{t}{t_f} \qquad (3.28)$$

3.3.3   Results and discussion

Figures 3.16 and 3.17 show simulated results with developed method, illustrating load cycling for single and multi-shaft engines plotted on stress-strain diagram. The contour lines show load levels in MW, the dotted line represents the Hysteresis curve, and each dot corresponds to a stress and strain value at a given engine load.

According to figure 3.16, for a single shaft engine the shaft rotational speed remains unchanged, which is reflected by the unchanged stress value at point A at all levels from 400 MW to 150 MW. The actual stress and strain values at point B have different values of stress due to the fact that mechanical properties of the blade alloy, here modulus of elasticity, vary as function of gas temperature according to figure 3.14. During the unloading, because the shaft speed remains constant, the $\Delta Load$ has no effect on the change in σ_D and ε_D. For example, according to the figure, reducing load from 400 MW to 300 MW and reducing from 400 MW to 150 MW will induce the same compressive stress of approximately -400 MPa and strain of approximately 0.00375.

Figure 3.17, on the other hand, shows modelled loading and unloading stress-strain profiles for a multi shaft engine. Since the gas generator is not physically coupled with the free-power turbine, the load reduction results in changes in engine rotational speed. Therefore, stress varies at point A across the load range from 32 MW to 8 MW, as well as the corresponding actual stress and strain at point B. The contour plot at point D shows the nearly vertical lines, which represent the engine load level in MW, and nearly horizontal lines, which represent the change in load $\Delta Load$ in MW. For example, according to the figure, reducing engine load level from 22 MW to 16 MW will result in the stress level change from 900 MPa in tension at point B to -200 MPa in compression at point D and the strain level reduces from approximately 0.0095 to 0.003, accordingly.

Figure 3.18 shows simulated results of fatigue life consumption for a single shaft engine, whereby load is reduced by modulating fuel flow only. Because the rotational speed remains unchanged at all load levels ($\Delta Load$ has no effect on the change in σ_D and ε_D as discussed in preceding paragraphs), the life consumption contour lines are nearly vertical. According to the figure, a load reduction from 400 MW by $\Delta Load = 300MW$ and reduction from 400 MW by $\Delta Load = 150MW$ will consume the same 0.045% of the low cycle fatigue life. If the engine is cycled again the life consumption will be $0.045\% + 0.045\% = 0.09\%$ according to equation 3.25.

Figure 3.19 shows simulated results of fatigue life consumption for a multi shaft gas turbine engine. The load reduction strategy here is closing VIGVs followed by reduction in fuel flow.

Figure 3.20 shows simulated results of creep life consumption for a single shaft gas
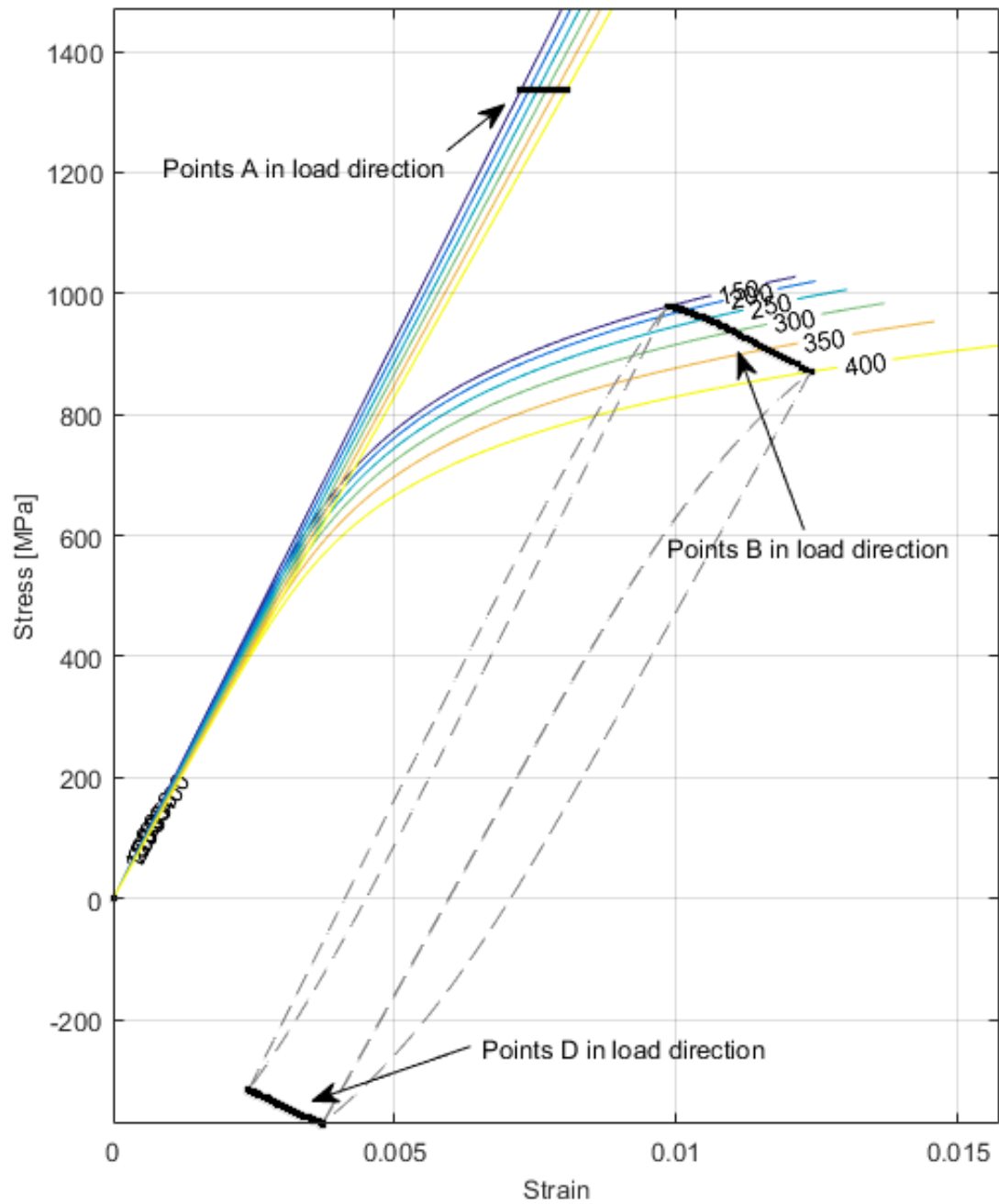
Fig. 3.16 Stress-strain diagram representation of thermal cycling in a high pressure turbine rotor blade at various load levels for single-shaft engine
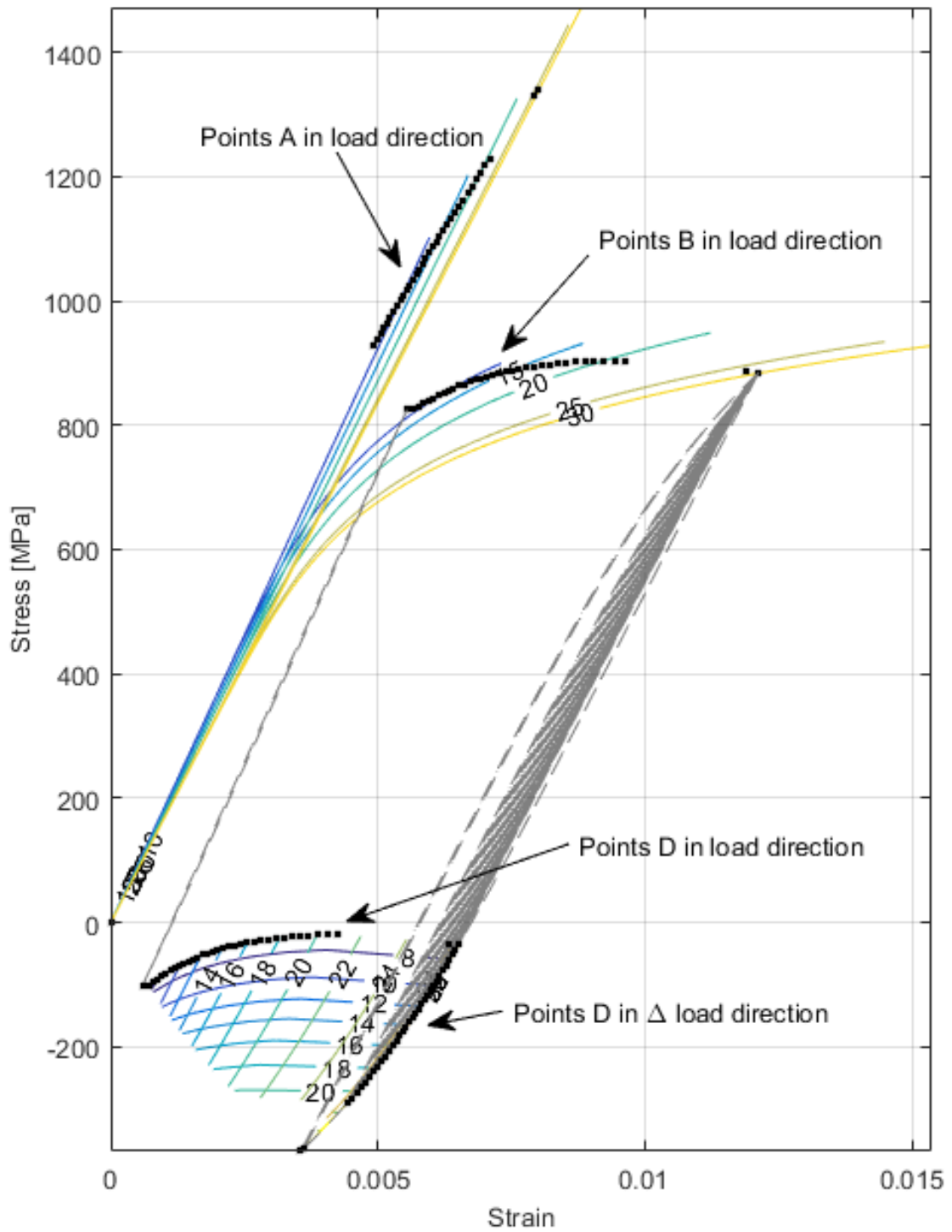
Fig. 3.17 Stress-strain diagram representation of thermal cycling in a high pressure turbine rotor blade at various load levels for multi-shaft engine

Fig. 3.18 Fatigue life consumption map for high pressure turbine rotor blade in single shaft engine. Load reduction by reducing fuel flow

Fig. 3.19 Fatigue life consumption map for high pressure turbine rotor blade in multi-shaft engine. Load reduction by closing VIGVs followed by reduction in fuel flow
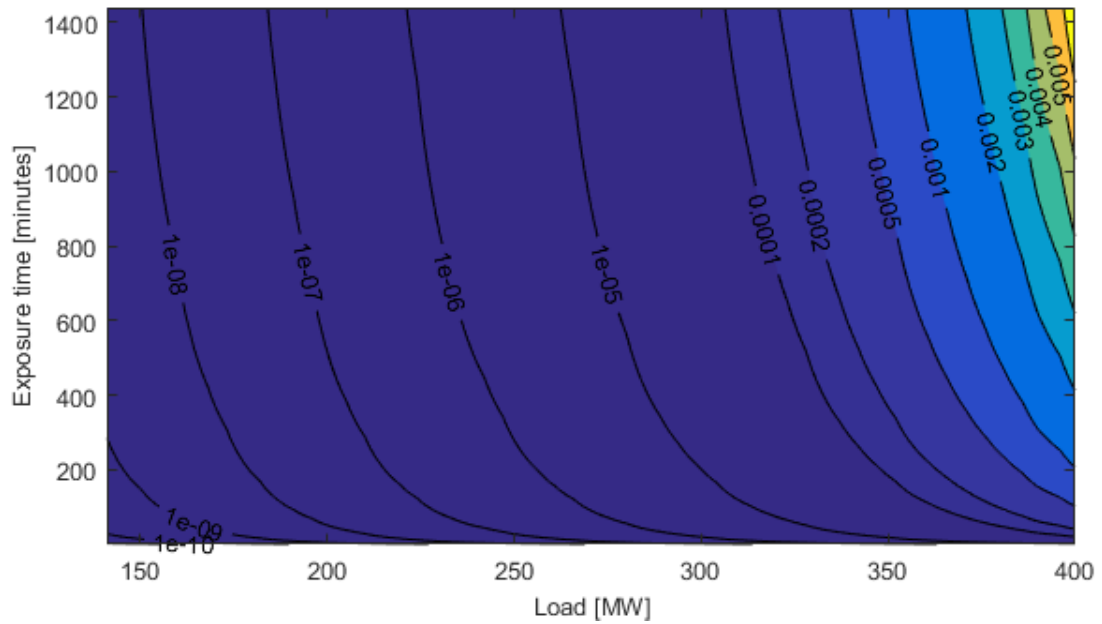
Fig. 3.20 Creep life consumption map for high pressure turbine rotor blade in single shaft engine. Load reduction by reducing fuel flow
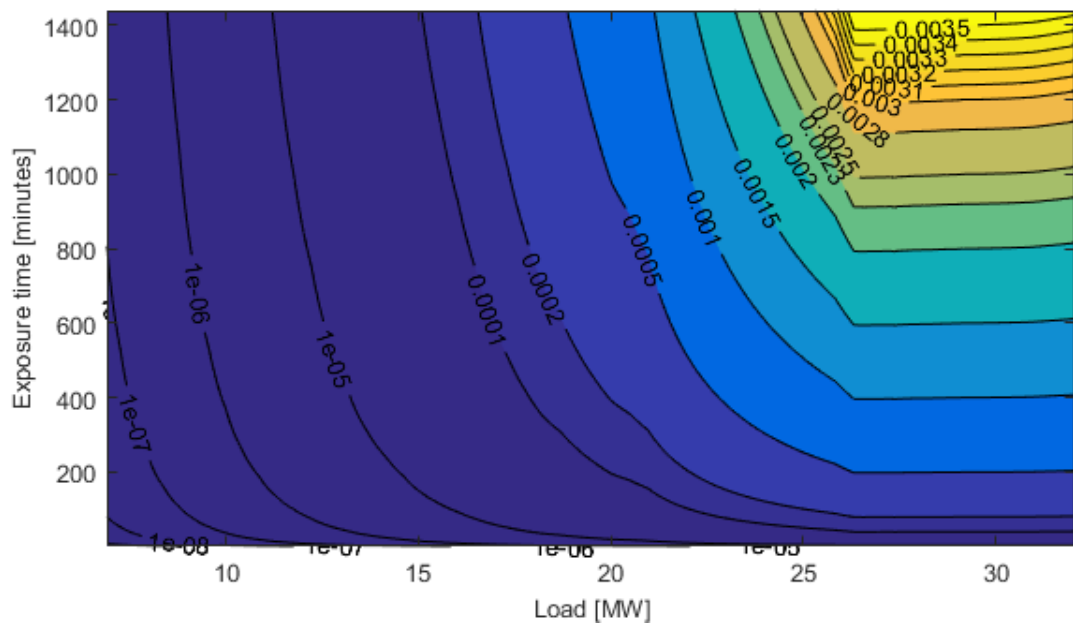
Fig. 3.21 Creep life consumption map for high pressure turbine rotor blade in multi-shaft engine. Load reduction by closing VIGVs followed by reduction in fuel flow

turbine engine. According to the figure, if the engine is operated at 400 MW for 400 minutes, approximately 0.2% of life will be consumed due to creep deformations at the root of the high pressure turbine blade. The life consumption is accumulated linearly, so if engine is next operated at 350 MW for 400 minutes, the cumulative life consumed will be $0.2\% + 0.02\% = 0.22\%$.

Simulated results of creep life consumption for multi-shaft gas turbine engine are shown in figure 3.21. According to the figure, if the engine is operated at 30 MW for 400 minutes, the creep life consumed will be 0.1%. If the load of the engine is then reduced to 20 MW and remains there for 400 minutes, the creep life consumed will be $0.1\% + 0.02\% = 0.12\%$.

3.4   Potential impact assessment of developed maps

The work developed and discussed in this chapter is an attempt to provide a more robust and simpler method to assess gas turbine flexible operation and life consumption of critical power plant components. The operational flexibility map exposes new and potentially economically attractive load reduction strategies to maximise flexibility, and exposes relevant trade-offs in performance. The life consumption study has been done for single and multi-shaft gas turbine engines, with objective to examine the effect of two load reduction strategies: 1) fuel flow control, and 2) VIGVs modulation followed by fuel control. The current study exposes the complexity associated with analysing life consumption, and the high dependence of results on the chosen load reduction strategy. The complexity increases further if composite load reduction strategies were investigated (discussed in section 3.2.3). For example, if one wishes to study a composite load reduction of simultaneously closing VIGVs and reducing fuel flow, this would require a new set of simulations and results. It is clear that full variation of load reduction strategies, and resulting life consumption of critical components involves complex and excessive number of calculations and visual representations, which can make a concise presentation of the results unachievable. Therefore, the gas turbine operational flexibility map provides concise and much less complex way to analyse gas turbine systems at off-design conditions. Some of the prospects for use include:

1. The operational flexibility map allows for a quick assessment of the best route to change the load of an engine.

2. The plant operator may shade areas on the map to visualise regions in which the power plant should not operate. For example in the region of high exhaust temperature in consideration of HRSG failure, in the region of high TET in consideration of turbine failure, or in the region of low mass flow in consideration of compressor stalling.

3. It could be used by traders and financial advisers to make informed decision whether a given power plant can secure enough profit in the balancing market.

4. It could be used to understand hidden costs associated with a decision whether to accept a contract in balancing market. These costs could include increased maintenance costs, or increased fuel costs.

5. It could be used to aid internal plant performance modelling.

6. It could be used by plant operator to quickly perform a preliminary study of any plant upgrades, and assess impact on gas turbine flexible performance.

Chapter 4

Direct Solution Method for steam cycle design-point performance simulation

The chapter is divided into two sections, first a modular algorithm is developed to enable robust and flexible simulation of user-defined CCPP systems. The name of the algorithm is the *db.match.CCPP* with a logo shown in figure 4.1. It provides fundamental structure for modular modelling of CCPP systems at design point and off-design operation.

Fig. 4.1 db.match.CCPP logo

In the second part of the chapter a novel Direct Solution Method (DSM) is developed for evaluating CCPP design point performance, which is later expanded into the off-design operation in chapter 6. The DSM is a method of calculations which is incorporated into the *db.match.CCPP* algorithm.

4.1 Process development

4.1.1 System description and assumptions

A system is defined as a quantity of matter or a region in space chosen for study [63]. Each major component in a bottoming steam cycle is treated as a device that involves mass flow of matter crossing its boundaries to which *open system* or *control volume* is applied. A *Local System* refers to a control volume for individual plant components, whereas a *Global System* refers to a control volume for the whole system of components comprising a bottoming cycle. Any change in which the system goes from one equilibrium state to

another is called a *process*, and a series of states through which a system passes during a given process is called a *path*. The following assumptions are made:

1. The process is permitted to adjust itself internally in such a manner that the rate of change in properties along a path do not change with time. Such a process is called *quasi equilibrium process*.

2. The flow in bottoming steam cycle devices are not pulsating and are considered to be in continuous operation and consequently a fluid flows through the control volume *steadily*.

3. The bottoming steam cycle devices are insulated with no heat loss occurring to the surroundings; therefore, all processes are *adiabatic* with surroundings.

4. The changes in potential and kinetic energy are negligible, and can therefore be omitted.

5. The working fluid has fixed chemical composition throughout, being described as *pure substance*.

6. The fluid thermal capacities are constant over the length of the heat exchanger.

7. The product of Overall Heat Transfer Coefficient and heat transfer surface area, $U^D A$, is constant over the length of the heat exchanger.

State variables listed in table 4.1 are used to describe properties of the fluid at inlet and outlet stations of a control volume. Since the state variables present an ordered set of numbers at inlet and outlet, these are referred to as *Station Vectors*. *Local Station Vector* values refer to state variables of a Local System, whereas *Global Station Vector* values refer to state variables of a Global System. Similarly are defined *Local Performance Parameters* and *Global Performance Parameters*.

Table 4.1 Station Vectors

water-vapour	gas
temperature	temperature
pressure	mass flow
enthalpy	
entropy	
mass flow	

The heat is a form of energy that can be transferred from one system to another as a result of temperature difference [64]. The heat transfer occurring in bottoming steam cycle heat exchangers is considered with the following assumptions:

1. The flow is approximated to be *one-dimensional*. Therefore, the properties of the fluid are assumed to be uniform at any cross section normal to the direction of flow

2. The properties of fluid are assumed to have *bulk average values* over the whole cross section

3. The effect of convection and radiation heat transfer is omitted. Only conduction is considered

System validation

The Direct Solution Method for design and off-design point calculations has been validated against results obtained from commercial software. The PROATES software has been developed by Uniper, with decades of experience in power plant operation. The Ebsilon Professional software is a widely used plant simulation tool.

4.1.2 Process flowchart

The top level flowchart is shown in figure 4.2. The db.match.CCPP written in a Fortran programming language operates in a modular manner where modules communicate with each other via text files. A file path to the main root directory of db.match.CCPP must be written to *db.match.CCPP_installation.txt*, and the installation file must be located in the C: directory.

At the first instance after launching *db.match.CCPP*, the user is prompted to enter in which *mode* of operation the program is to run. Various modes of operation are described in section 4.1.3. Following the mode recognition the program proceeds to design point calculation algorithm. *Operation 1* and *Operation 2* concerns reading input file and initialising Global Station Vector values. An iterative procedure then begins in which if convergence criteria are satisfied, the Global Station Vector Values and Global Performance Parameters are obtained and the program is terminated.

Operation 1 - Process input

In *Operation 1*, a process is programmed which reads the Global System Layout and Brick Data sections from the input file. The algorithm writes each value into a corresponding variable in a sequenced manner for follow-on calculations. Once completed the algorithm proceeds to *Operation 2*.

Operation 2 - Initialise global variables

Each time the program is run, values of Global Station Vectors must be initialised to a value of zero. This is needed to clear the memory from residuals arising from previously done simulations. Each brick has its own result files where Mode, Local Station
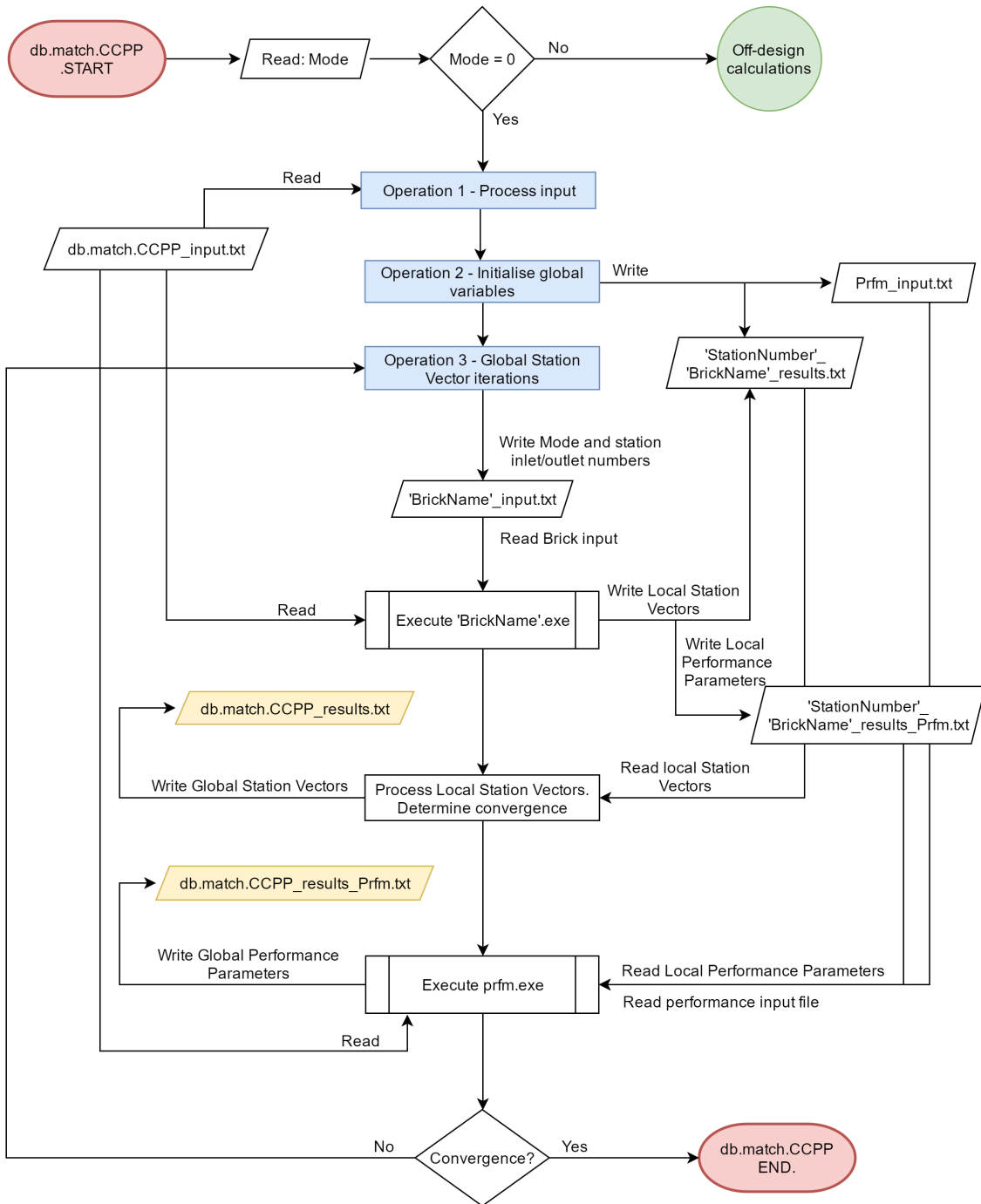
Fig. 4.2 Overall db.match.CCPP program structure
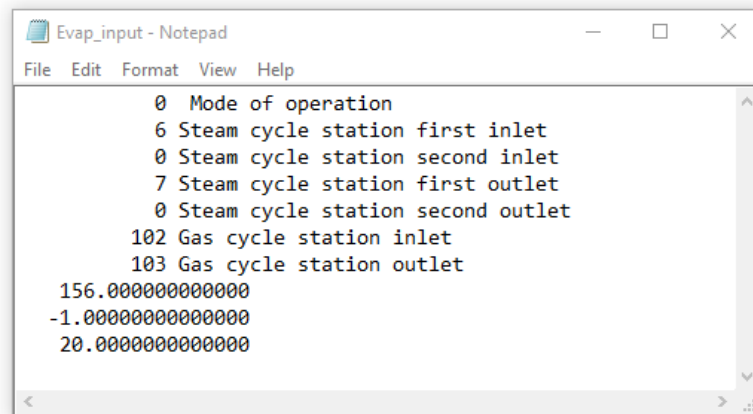
Vectors and Local Performance Parameters are stored. These files take a structure of *'StationNumber'_'BrickName'_results.txt* for Mode and Local Station Vectors, and *'StationNumber'_'BrickName'_results_prfm.txt* for Local Performance Parameters.

The performance brick must also be initialised with a value of Mode, which is done in *Prfm_input.txt*

Operation 3 - Global Station Vector iterations

The objective is to develop a robust performance simulation tool. Therefore, every component in a power plant needs to be considered separately in a modular fashion. This allows for performing rapid maintenance, and locating potential errors within the code. It also allows for easy to implement testing procedures for each brick separately before it is implemented into a global structure of the program.

Every brick, therefore, operates as an individual executable file in its own folder with input and output files. Operation 3 then communicates each brick separately in a sequence obtained from Operation 1. The input file *'BrickName'_input.txt* contains the Mode, Station Vector values, and Brick Data; an example of which for an evaporator is shown in figure 4.3. By reading the input file the brick understands its position with respect to other bricks. It can read Station Vector values at the exit of a previous brick which become inlet conditions, then perform necessary calculations and write Local Station Vector results to *'StationNumber'_'BrickName'_results.txt*. Example of brick results for inlet and outlet steam and the gas path of the evaporator are shown in figure 4.4. For those bricks that also calculate Local Performance Parameters results are written to a *'StationNumber'_'BrickName'_results_prfm.txt* file, of which an example for the evaporator is shown in figure 4.5.

Fig. 4.3 db.match.CCPP brick input file. Contains from the top the mode of operation, station numbers for steam and gas paths, and the brick data

Once a brick has been executed and local results obtained, a process is initiated to transfer Local Station Vectors to Global Station Vectors. This is done by reading local results from executed brick and appending them to the *db.match.CCPP_results.txt* located
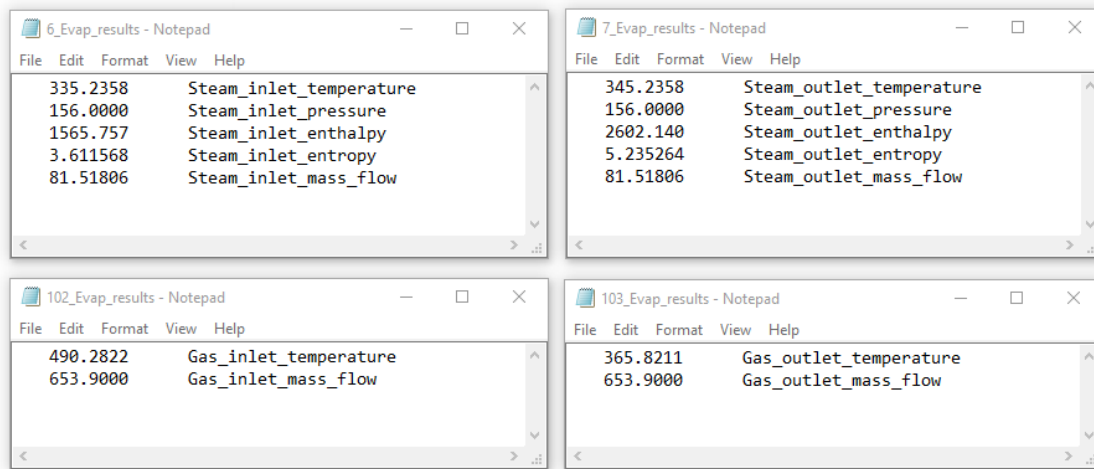
Fig. 4.4 db.match.CCPP brick results files
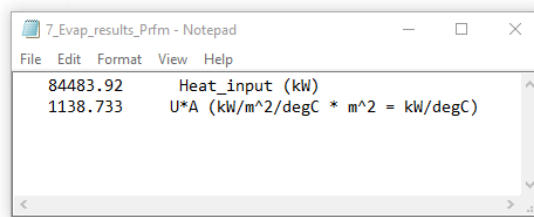
Fig. 4.5 db.match.CCPP brick performance result file

in the root directory, of which example is shown in figure 4.6. The sequence is then repeated by executing the next brick obtained from Operation 1. This process continues until a convergence criterion is met.

Fig. 4.6 db.match.CCPP brick output file

4.1.3 Mode of operation

The objective is to develop a robust and flexible simulation tool. Therefore, the following modes of operation have been programmed:

- Mode = 0, for design point calculations

- Mode = 1, for off-design point calculations using *Genetic Algorithm* approach described in chapter 5

- Mode = 2, for off-design point calculations using *Newton-Raphson* approach. Newton-Raphson has been initially investigated in current work; however, the work was eventually abandoned due to difficulties in integrating it into *db.match.CCPP*. This has led to the development of novel DSM

- Mode = 3, for off-design point calculations using novel *Direct Solution* approach described in chapter 6

4.1.4 Input file structure

The input file for 1 pressure system is shown in figure 4.7. Similarly, for convenience, input files for 2 pressure, 3 pressure, and 5 pressure are shown in appendix figures B.2, B.4 and B.5, respectively. Following these structures, input files for any pressure levels can be assembled with available bricks listed in table 4.2.

The input file is divided into two sections; each between *start.* and *end.* tags. The first section is referred to as the *Global System Layout*. It contains *Codewords* information, which describe in predefined order various bricks to be used together with their Station Vectors and Brick Data. The codeword *S* designates two steam path inlets followed by two outlet station numbers. Up to two inlet and two outlet stations can be modelled per brick allowing for future expansion of program capabilities. A sequence must follow such that inlet S1 is linked with outlet S3 and inlet S2 is linked with outlet S4. For those inlet or outlet ports not in use a value of zero must be assigned.

The codeword *G* designates one gas path inlet followed by one outlet station numbers. It must follow that the station number corresponding to entry into the heat recover steam generator always takes a value of 101. Bricks that do not utilise heat transfer from the hot gas path must have a value of zero assigned.

The codeword *D* refers to a range of numbers linking bricks with their corresponding Brick Data. Consequently, the second section referred to as *Brick Data* corresponds to data items of particular bricks listed in Global System Layout under codeword D. These are initial input data which are not part of Station Vector values and are determined for

each brick as required. The db.match.CCPP model has been programmed with simple procedures to expand or modify list of existing Brick Data values.

```
db.match.CCPP [Single pressure CCPP]
Version: 1

start.

Valv                 S 9 0 1 0       G 0 0                 D 1 2
StTu                 S 1 0 2 0       G 0 0                 D 3 5
Cond                 S 2 0 3 0       G 0 0                 D 6 8
Pump                 S 3 0 4 0       G 0 0                 D 9 10
Econ                 S 4 0 5 0       G 103 104             D 11 13
Drum                 S 5 7 6 8       G 0 0                 D 0 0
Evap                 S 6 0 7 0       G 102 103             D 14 16
SuHe                 S 8 0 9 0       G 101 102             D 17 18

end.

start.
1 -1                 !Valve, steam live pressure (bar), or '-1' for non-use
2 -1                 !Valve, steam live mass flow, or '-1' for non-use

3 541                !Steam turbine, metallurgical temperature limit (degC)
4 84                 !Steam turbine, isentropic efficiency (%)
5 0.05               !Steam turbine, outlet pressure

6 1                  !Condenser, cooling water pressure (bar)
7 13                 !Condenser, cooling water temperature (degC)
8 10                 !Condenser, cooling water temperature rise (degC)

9 7                  !Pump Control, outlet1 number linking to required pressure rise
10 90                !Pump, isentropic efficiency (%)

11 10                !Economizer Control, approach point temperature difference (degC)
12 -1                !Economiser, U*A (kW/m^2/degC * m^2 = kW/degC), or '-1' to non-use
13 7                 !Economiser Control, outlet1 linking to required mass flow rate, or '-1' to non-use

14 112.47            !Evaporator Control, operating pressure (bar), or '-1' for analysis
15 -1                !Evaporator, U*A (kW/m^2/degC * m^2 = kW/degC), or '-1' to non-use
16 20                !Evaporator Control, pinch point temperature difference (degC), or '-1' to non-use

17 -1                !Superheater, U*A (kW/m^2/degC * m^2 = kW/degC), or '-1' to non-use
18 30                !Superheater Control, pinch point temperature difference (degC), or '-1' to non-use

end.
```

Fig. 4.7 db.match.CCPP overall input file

4.1.5   Convergence criteria

The program is set to loop continuously through a sequence of bricks obtained from Operation 1. Each executed brick contributes to selected Local Station Vectors, and if no contribution is made a value of zero is assigned. For example, as Operation 3 will perform first loop through the sequence of all the bricks only when it encounters the evaporator it will calculate steam live pressure and mass flow from the Brick Data, whereas the rest of the Global System will have a value of zero. As the program continues iterating through the sequence of bricks, the Station Vectors will continue changing until no more change is detected. At this instance the system is referred to as converged.

Table 4.2 List of available bricks

Brick name	Brick function
Valv	Valve
StTu	Steam turbine
Cond	Condenser
Pump	Pump
Econ	Economiser
Evap	Evaporator
SuHe	Superheater
ReHe	Reheater
Drum	Drum
Mixi	Flow mixer
Spli	Flow splitter

4.2   Brick structure

For simplicity each brick has the same structure, which is shown schematically in figure 4.8. Each brick has its own executable file *'BrickName'.exe*. When executed, the program begins with declaration of properties and data types of all objects and variables. Objects of array type need their size to be allocated and then initialised, whereas each of these two processes are executed separately. Only selected bricks need to read the gas turbine exhaust results from *TurboMatch_results.txt*, thus this input is marked as optional.

The program then proceeds to read all input files. In all design and off-design cases the program reads the path to the root directory from *db.match.CCPP_installation.txt*, Global System Layout from *db.match.CCPP_input.txt*, and Mode and Station Vectors and Brick Data from *'BrickName'_input.txt*. If the Mode is a non-zero value the brick also reads files supporting off-design calculations, which are discussed in more detail in chapters 5 and 6 for Genetic Algorithm and Direct Solution Method, respectively.

The main body of the brick program structure is divided into sections each corresponding to a value of the Mode. Each section performs specific calculations to evaluate either design or off-design Local Station Vectors at the brick outlet. The Local Performance Parameters are then calculated and the program proceeds to write results to output text files. For all design and off-design cases the program writes Local Station Vectors to *'StationNumber'_'BrickName'_results.txt*, and Local Performance Parameters to *'StationNumber'_'BrickName'_results_prfm.txt*. If the brick is executed in off-design mode, the program also writes results to files supporting off-design calculations. The program execution is then terminated.
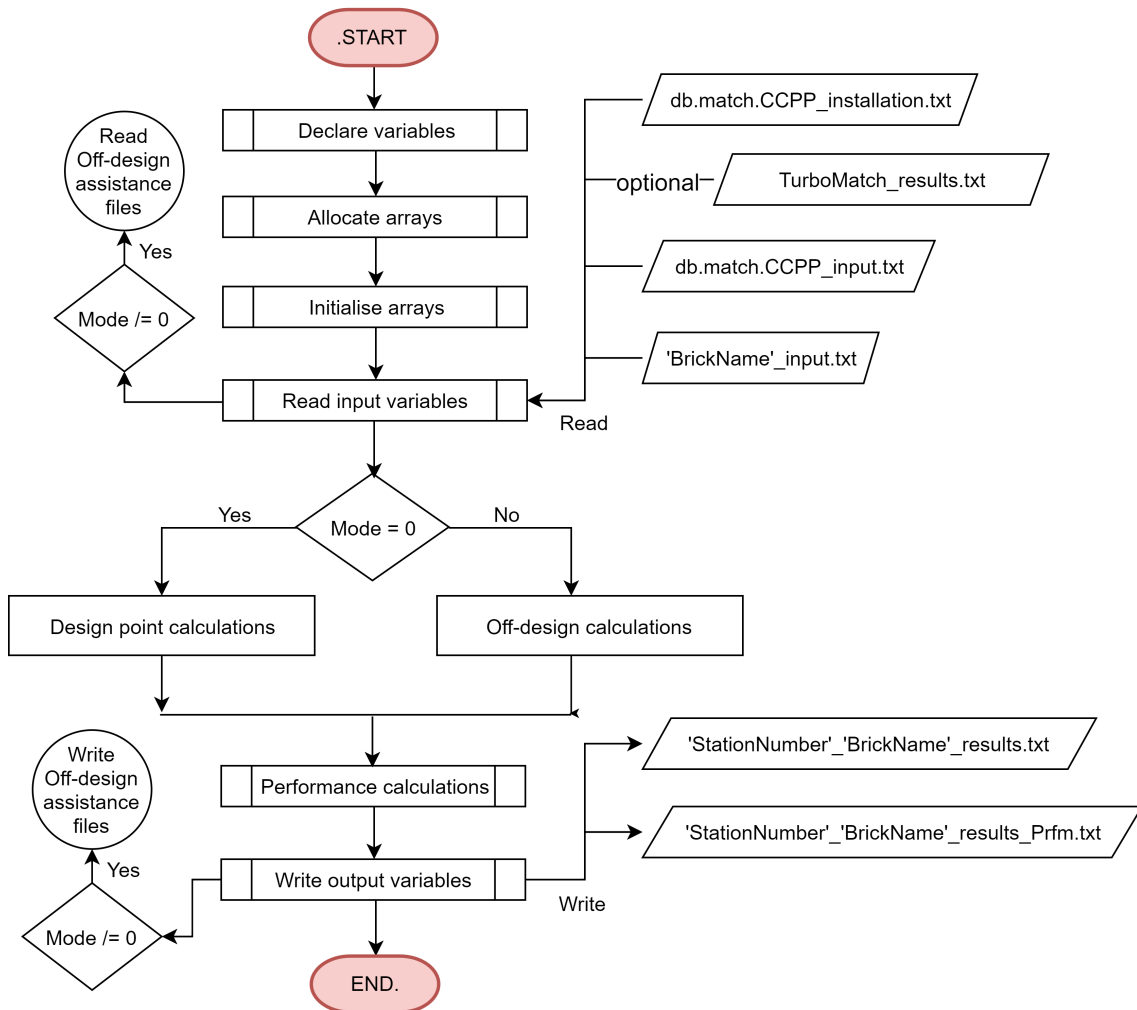
Fig. 4.8 Generic db.match.CCPP brick structure

4.3 Brick matching and control

Each brick contains a local algorithm which performs a *forward* and *backward* search to establish inlet Station Vectors along the water/steam and gas paths. In the global perspective, one loop is referred to as a sequence of calculations for the bricks in the ordered Global System Layout. Notably, in the first loop of brick matching, only the gas turbine exhaust conditions are known. The matching procedure then loops until variables in all bricks are calculated. The control of steam mass flow and pressure is done in the evaporator.

4.4 Model equations

The heat transfer is calculated with equation 4.1, which relates the thermodynamic state of a heat exchanger to its geometry. U is the overall heat transfer coefficient, and in other words a total resistance of heat transfer from one fluid to another. The variable A represents the surface area normal to the direction of heat transfer.

$$\dot{Q}^D = U^D A \Delta T^D_{lm} \tag{4.1}$$

Where the Log Mean Temperature Difference, ΔT^D_{lm}, is the effective average temperature difference between the two heat transfer fluids over the length of the heat exchanger and is calculated with equation 4.2, assuming that the heat exchanger is a pure counter-flow type.

$$\Delta T^D_{lm} = \frac{(T^D_{g,in} - T^D_{s,out}) - (T^D_{g,out} - T^D_{s,in})}{ln(\frac{(T^D_{g,in} - T^D_{s,out})}{(T^D_{g,out} - T^D_{s,in})})} \tag{4.2}$$

The energy balance occurring between gas and steam/water paths is calculated with equation 4.3

$$\begin{cases} \dot{Q}^D = \dot{m}^D_s (h^D_{s,out} - h^D_{s,in}), & \text{for water/steam path} \\ \dot{Q}^D = \dot{m}^D_g (h^D_{g,in} - h^D_{g,out}), & \text{for gas path} \end{cases} \tag{4.3}$$

Equation 4.4 equates the heat transfer balance (equation 4.1) with energy balance (equation 4.3 for gas path). This provides a function of temperature profiles, gas mass flow rate, and heat exchanger geometry.

$$U^D A \Delta T^D_{lm} = \dot{m}^D_g (h^D_{g,in} - h^D_{g,out}) \tag{4.4}$$

The heat transfer can be improved by implementing fined tubes, which increase the heat transfer area. Because in such case the geometry of the tubes are different on the inside (gas side) and outside (water/steam side) the resistance to heat transfer on the inside is greater compared to finned outside geometry. Therefore, higher density of fins can transfer the same amount of heat as another design with plan tubes of higher surface area. Ganapathy, therefore, concluded that a designer should look at a product of $U^D A$ instead of the surface area alone [65]. For this reason, in the following work a product of $U^D A$ is used in parametric analysis.

Equation 4.5 equates energy equations for water/steam and gas paths (equation 4.3). This provides a function of temperature profiles, and gas and water/steam mass flow rates.

$$\dot{m}^D_s (h^D_{s,out} - h^D_{s,in}) = \dot{m}^D_g (h^D_{g,in} - h^D_{g,out}) \tag{4.5}$$

Rearranging equations 4.4 and 4.5 and assuming that enthlapy of gas varies as function of temperature, $\Delta h = Cp\Delta T$, where specific heats, Cp_g^D, is calculated with equation A.9 as function of $T_{g,in}^D$ only.

$$F_1^D = \Delta T_{lm}^D - \frac{\dot{m}_g^D Cp_g^D (T_{g,in}^D - T_{g,out}^D)}{U^D A} = 0 \qquad (4.6)$$

$$F_2^D = \dot{m}_g^D Cp_g^D (T_{g,in}^D - T_{g,out}^D) - \dot{m}_s^D (h_{s,out}^D - h_{s,in}^D) = 0 \qquad (4.7)$$

Equations F_1^D and F_2^D have been arranged such that only F_2^D is a function of $\dot{m}_s^D$. Therefore, Station Vectors can be solved for by first calculating temperature profiles using F_1^D function for given inlet conditions and heat exchanger geometry. Equating $F_1^D = F_2^D$, provides a solution to solve for steam mass flow rate, and the corresponding equation is shown in 4.8.

$$\dot{m}_s^D = \frac{\dot{m}_g^D Cp_g^D \Delta T_g^D}{\Delta h_s^D} \left[1 + \frac{1}{U^D A}\right] - \frac{\Delta T_{lm}^D}{\Delta h_s^D} \qquad (4.8)$$

$$\dot{m}_g^D = \frac{\dot{m}_s^D \Delta h_s^D + \Delta T_{lm}^D}{Cp_g^D \Delta T_g^D (1 + \frac{1}{U^D A})} \qquad (4.9)$$

Equation 4.8 appears to have four distinct terms:

- The heat supplied by the gas, $\dot{m}_g^D Cp_g^D \Delta T_g^D$.

- The specific heat demanded by water/steam, Δh_s^D.

- The heat exchanger geometry, $\left[1 + \frac{1}{U^D A}\right]$.

- The normalised temperature profile $\frac{\Delta T_{lm}^D}{\Delta h_s^D}$.

Preliminary parametric analysis shows that the normalised temperature profile is negligible for all values $\dot{m}_s^D$ reducing dependency on a logarithmic function, which reduces the level of complexity. However, further analysis of the effect of neglecting the normalised temperature profile from the equation are outside of the scope of present work. The $\dot{m}_s^D$ can therefore be treated as a unique mass flow of steam needed to satisfy the required temperature profile of a geometrically predetermined heat exchanger.

Equation 4.9 has been derived for convenience only, and it is not used herein as $\dot{m}_g^D$ is provided by the gas turbine exhaust flow Station Vectors.

4.4.1 Constraints

From the fundamental principles of a counter-flow shell and tube heat exchanger the outlet temperatures of steam and gas paths must fall between $T_{g,in}^D$ and $T_{s,in}^D$. Then assuming that there is no pressure and mass flow loss, $P_{s,out}^D = P_{s,in}^D$, $\dot{m}_{s,out}^D = \dot{m}_{s,in}^D$, and $\dot{m}_{g,out}^D = \dot{m}_{g,in}^D$, respectively.

4.5 Summary of procedures

The method presented herein has been developed to provide a direct solution, which can be obtained with the following steps:

1. Obtain the inlet Local Station Vectors on the steam/water and gas paths

2. Agree which pressure level of water/steam path is the heat exchanger operating at. This is a compromise of a resulting pinch point temperature difference. Then obtain a $T_{s,out}^D$ that satisfies the pressure requirement

3. Calculate the resulting $T_{g,out}^D$ with equation 4.6

4. Agree on a value of $U^D A$ needed to achieve the required $\dot{m}_s^D$ calculated with equation 4.8

   The economiser, evaporator and superheater heat exchangers vary in operation. Therefore, a more detailed procedure has been developed for each of these heat exchangers and the methodology is discussed in the following sections.

4.6 Economiser brick development

The Brick Data and Local Station Vectors for the economiser are outlined in table 4.3.

   In order to avoid steaming occurring at the outlet of the economiser, the outlet temperature is usually below water saturation point. The difference is set by a $T_{approachpoint}$ Brick Data, and the $T_{s,out}^D$ is then calculated with equation 4.10.

$$T_{s,out}^D = T_{s,sat} - T_{approachpoint} \tag{4.10}$$

   The geometry of the economiser is provided with a $U^D A$ Brick Data. The $SN_{\dot{m}_{s,in}^D}$ is a control Brick Data item, which must be defined by a station outlet number with required steam mass flow. This is usually an evaporator outlet at the same pressure level. If the value of $U^D A = -1$ and $SN_{\dot{m}_{s,in}^D} > 0$ then the algorithm calculates a required $U^D A$ to match the operating $\dot{m}_{s,in}^D$. However, if the value of $U^D A > 1$ and $SN_{\dot{m}_{s,in}^D} = -1$ then the algorithm will evaluate the resulting $\dot{m}_{s,in}^D$ for the pre-determined $U^D A$.

Table 4.3 Economiser Brick Data, Local Station Vectors, and Local Performance Parameters

Brick Data items	Inlet Station Vectors	Outlet Station Vectors	Performance Parameters
$T_{approachpoint}$	$T^D_{s,in}$	$T^D_{s,out}$	$\dot{Q}^D$
$U^D A$	$P^D_{s,in}$	$P^D_{s,out}$	
$SN_{\dot{m}^D_{s,in}}$	$h^D_{s,in}$	$h^D_{s,out}$	
	$S^D_{s,in}$	$S^D_{s,out}$	
	——	——	
	$T^D_{g,in}$	$T^D_{g,out}$	
	$\dot{m}^D_{g,in}$	$\dot{m}^D_{g,out}$	

4.6.1   Analysis

The following analysis is performed for a simplified case with $T_{approachpoint} = 0$ to demonstrate a case where the economiser outlet is assumed to be a saturated water. The overall shape of functions F^D_1 and F^D_2 are shown in figure 4.9 for given inlet conditions, where the contour lines represent function values at various $T^D_{s,out}$ and $T^D_{g,out}$. The further away the function results are from the zero line, the further it is from the direct solution. The shape of contour lines are irrelevant as only the intersection point is of importance, which provides a common solution that satisfies F^D_1 and F^D_2 functions simultaneously. It is evident that a single unique solution exists, which provides $T^D_{s,out}$, $T^D_{g,out}$ and $\dot{m}^D_s$ for inlet Local Station Vectors and the Brick Data, $U^D A$.

A set of unique solutions, obtained with equation 4.8 is plotted in the top of figure 4.10 as function of $T^D_{s,out}$ at varying $U^D A$. The vertical contour pressure lines are also shown, with assumption that $T^D_{s,out}$ is at a saturation state, i.e. $T_{approachpoint} = 0$. The analysis, however, can be applied to any value of $T_{approachpoint}$, which would alter the shape but leave unchanged the trend of the curves.

For all $U^D A$ values, $\dot{m}^D_s$ tends to decrease faster at higher $T^D_{s,out}$ values because the heat demanded by water/steam rises faster than heat supplied by the gas. Therefore $\dot{m}^D_s$ must decrease to match the demand with a supply of heat. As the value of $T^D_{s,out}$ approaches $T^D_{s,in}$, the infinitesimally smaller heat demand is satisfied by the dominant heat supply and will result in $\dot{m}^D_s$ asymptotically approaching positive infinity.

The size of the economiser is contained in the constant $U^D A$. Therefore, for unchanged $T^D_{s,out}$ the size of the economiser must increase in the direction of rising $\dot{m}^D_s$. The corresponding $T^D_{g,out}$ as function of $T^D_{s,out}$ is calculated with equation 4.6 and results are shown in the bottom of figure 4.10. A unique solution of $\dot{m}^D_s$, $T^D_{s,out}$ and $T^D_{g,out}$ can be
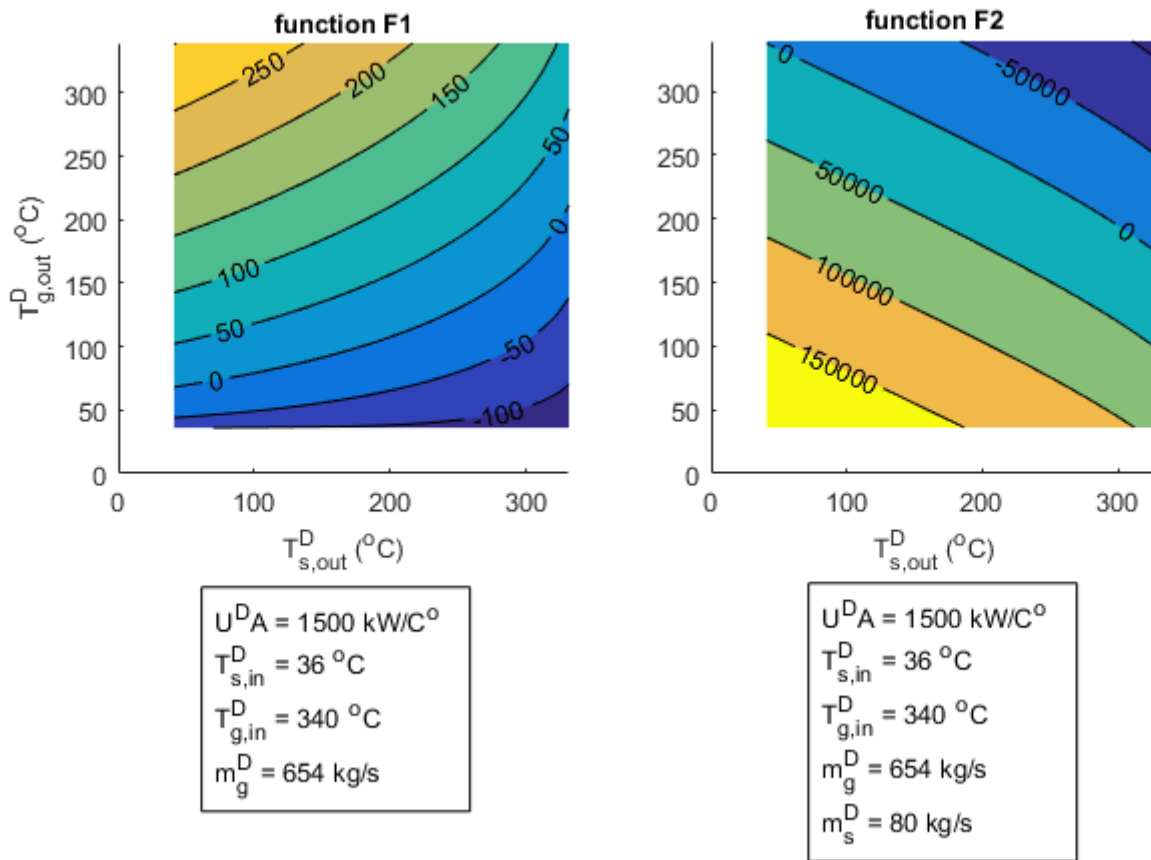
Fig. 4.9 Economiser F1 and F2 functions. Shown residuals as function of gas and steam outlet temperatures

obtained by agreeing on the operating pressure, and geometry of the economiser, $U^D A$. The heat input into the tube bank of the economiser can then be calculated with equation 4.3 for the steam path.
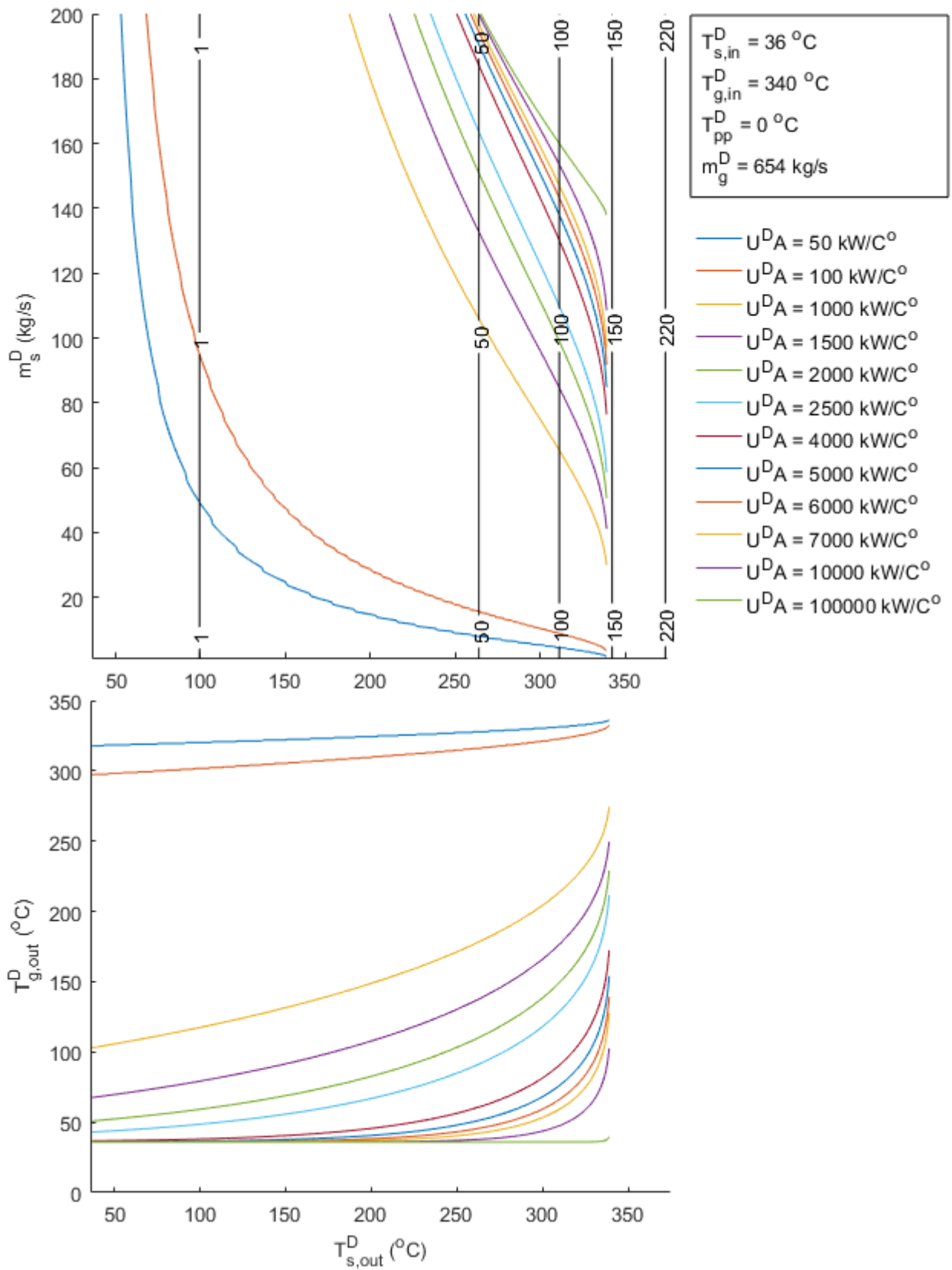
Fig. 4.10 Economiser parametric study of results. Shown variation in steam mass flow and gas outlet temperature

4.6.2 Procedure

A visual procedure has been developed for performance evaluation of a heat exchanger. It allows for quick visualisation which variables must be provided to solve for the variable of interest. The design-point trade-offs triangle for the economiser is shown in figure 4.11. The inputs necessary for performance evaluation are in the cloud which is comprised of 1) Local Station Vectors $T_{g,in}^D$, $\dot{m}_{g,in}^D$, $P_{s,in}^D$, $T_{s,in}^D$, and 2) Brick Data, $T_{approachpoint}$. The outputs are in the triangle, which are comprised of three distinct sections, upper for geometry, lower-left for mass flow rate, and lower-right for temperatures.
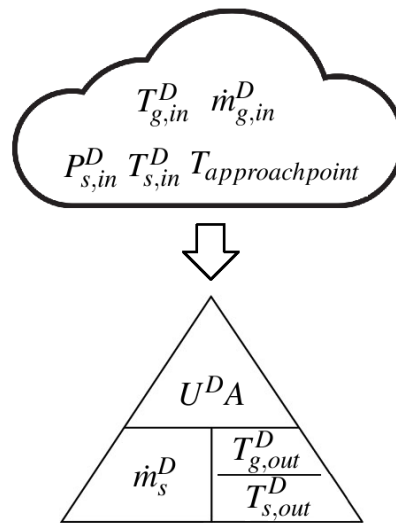
Fig. 4.11 Economiser design point trade-offs triangle

The lower-right section of the triangle contains temperature variables that can be solved for directly if the remaining variable of the same section is known. For example, $T_{g,out}^D$ can be solved directly for if $T_{s,out}^D$ is known, and vice-versa.

To use the triangle, one is prompted to cover the value that needs to be solved for and use the remaining two triangular sections to find it. The following are the possibilities:

- Solve for $U^D A$ only if $\dot{m}_s^D$ and either $T_{g,out}^D$ and/or $T_{s,out}^D$ are known

- Solve for $\dot{m}_s^D$ only if $U^D A$ and either $T_{g,out}^D$ and/or $T_{s,out}^D$ are known

- Solve for $T_{g,out}^D$ and/or $T_{s,out}^D$ only if $U^D A$ and $\dot{m}_s^D$ are known

4.7 Evaporator brick development

The Brick Data and Local Station Vectors for the evaporator are outlined in table 4.4. The operating pressure of the evaporator is set by a Brick Data, P_s^D. If $P_s^D = -1$, then

the algorithm will perform an wide analysis for pressure levels varying from 1 to 220 bars. The geometry of the evaporator is provided with $U^D A$. The T_{pp} is a pinch point temperature difference which is defined with equation 4.11. If the value of $U^D A = -1$ and $T_{pp} > 0$ then the algorithm calculates a required $U^D A$ to satisfy the pre-determined pinch point temperature difference. However, if the value of $U^D A > 1$ and $T_{pp} = -1$ then the algorithm will evaluate the resulting T_{pp} for the pre-determined $U^D A$.

Table 4.4 Evaporator Brick Data, Local Station Vectors, and Local Performance Parameters

Brick Data items	Inlet Station Vectors	Outlet Station Vectors	Performance Parameters
P_s^D	$T_{s,in}^D$	$T_{s,out}^D$	$\dot{Q}^D$
$U^D A$	—	—	
T_{pp}	$h_{s,in}^D$	$h_{s,out}^D$	
	$S_{s,in}^D$	$S_{s,out}^D$	
	$\dot{m}_{s,in}^D$	$\dot{m}_{s,out}^D$	
	$T_{g,in}^D$	$T_{g,out}^D$	
	$\dot{m}_{g,in}^D$	$\dot{m}_{g,out}^D$	

$$T_{pp}^D = T_{g,out}^D - T_{s,in}^D \tag{4.11}$$

4.7.1 Analysis

In a real evaporator, the inlet is slightly below saturation and the outlet is usually a water/steam mixture, where the water part is recirculated from the outlet into the inlet in a continuous manner. In the following analysis, a simplified case is shown in which $T_{s,in}^D = T_{s,out}^D$ with inlet and outlet being saturated, which is represented by T_s^D. The results, however, can easily be obtained and studied for various values of $T_{s,in}^D$ and $T_{s,out}^D$.

The overall shape of functions F_1^D and F_2^D are shown in figure 4.12. Unlike the economiser, the evaporator has two unique solutions, which provide T_s^D, $T_{g,out}^D$ and $\dot{m}_s^D$ for inlet Local Station Vectors and the Brick Data, $U^D A$.

Solutions obtained with equation 4.8 are plotted in the top of figure 4.13 as a function of $T_{s,out}^D$ at varying $U^D A$. For convenience the vertical contours of the pressure lines corresponding to T_s^D are also shown in the figure. Latent heat of evaporation is a function of T_s^D, which decreases with increasing values of T_s^D. Therefore, for all values of $U^D A$ the heat demand is decreasing much slower then the heat supplied by the gas, resulting in decreasing values of $\dot{m}_s^D$ until it reaches a minimum point. If the T_s^D is increased past the minimum point, the further decrease in heat demand begins to dominate the decrease in
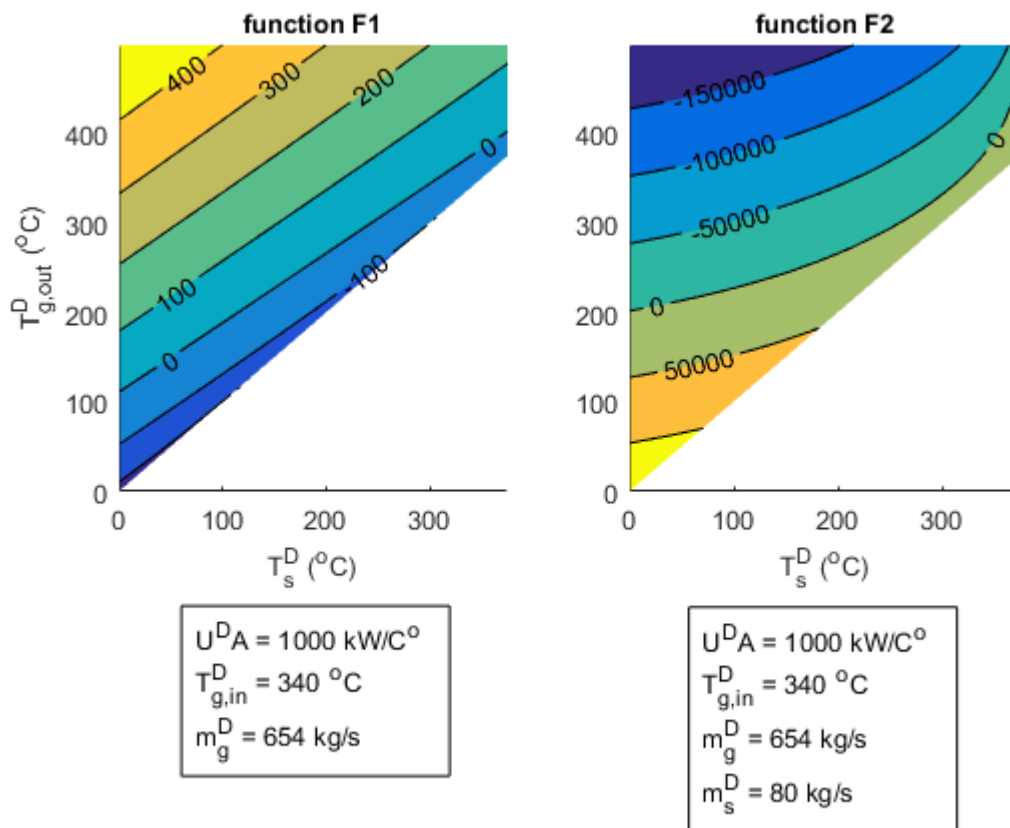
Fig. 4.12 Evaporator F1 and F2 functions. Shown residuals as function of gas and steam outlet temperatures

heat supply resulting significant rise in $\dot{m}_s^D$.

The size of the evaporator is contained in the constant $U^D A$. For unchanged T_s^D, the size of the evaporator must increase in the direction of increasing $\dot{m}_s^D$, because more heat transfer surface area is needed to sustain higher steam mass flow rates.

The corresponding $T_{g,out}^D$ as a function of T_s^D are calculated with equation 4.6 and the results are shown in the middle of figure 4.13. The $T_{g,out}^D$ must rise with higher T_s^D for all values of $U^D A$. The pinch point temperature difference calculated with equation 4.11 is shown in the bottom of figure 4.13. The heat input into the tube bank of the evaporator can then be calculated with equation 4.3 for steam path.
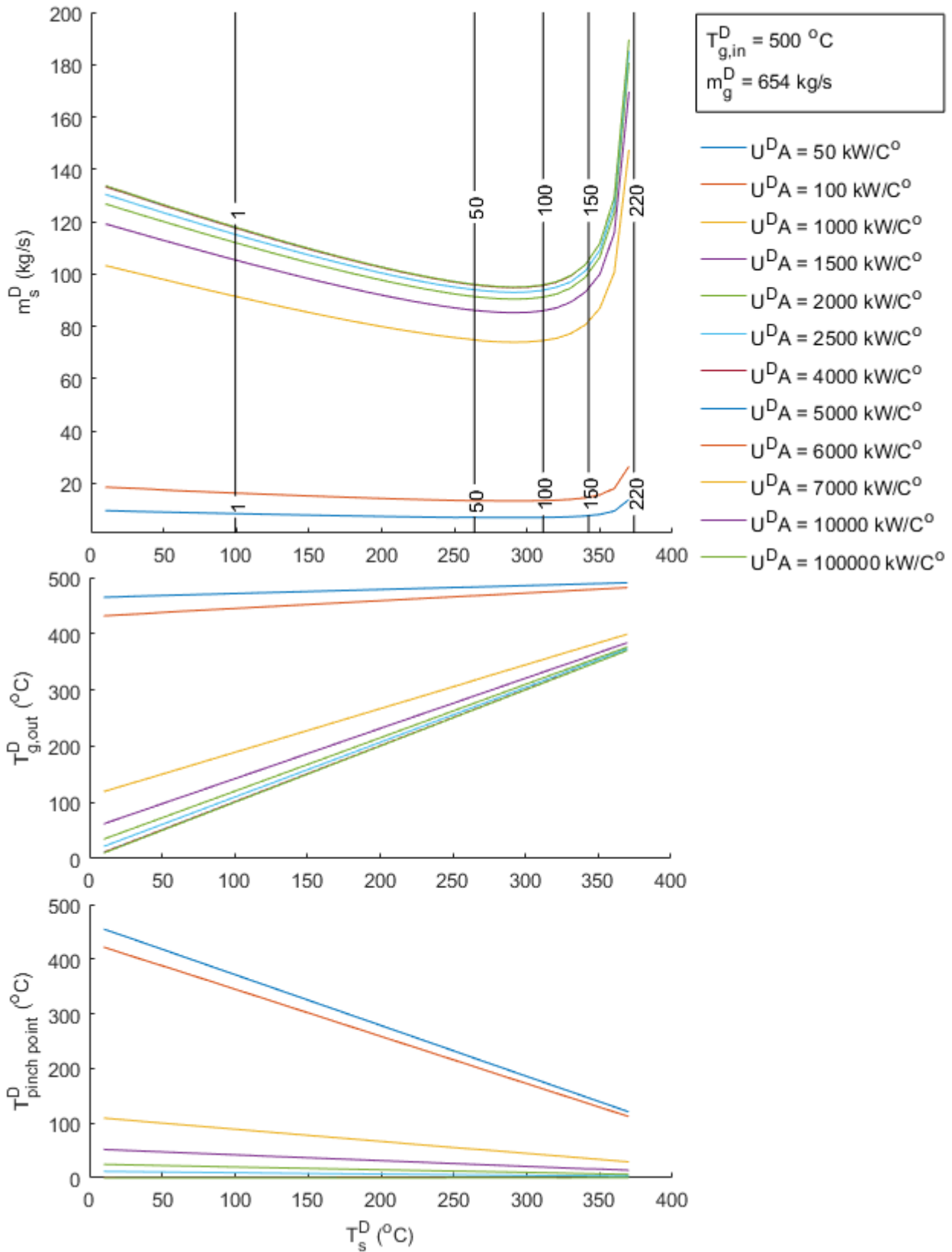
Fig. 4.13 Evaporator parametric study of results. Shown variation in steam mass flow, gas outlet temperature and pinch point temperature difference

4.7.2 Procedure

The design-point trade-offs triangle for the evaporator is shown in figure 4.14. The necessary input variables are Local Station Vectors $T_{g,in}^D$, $\dot{m}_{g,in}^D$, $P_{s,in}^D$, $T_{s,in}^D$. Similarly to the trade-offs triangle for the economiser, the outputs comprise of three distinct sections, upper for geometry, lower-left for mass flow rate, and lower-right for temperatures.
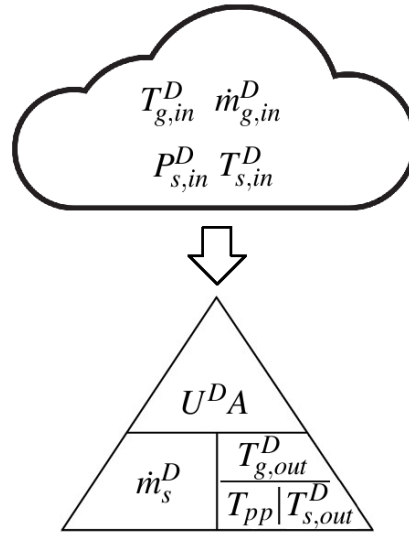
Fig. 4.14 Evaporator design point trade-offs triangle

The lower-right section of the triangle contains temperature variables that can be solved for directly by knowing the remaining variables of the same section. For example, $T_{g,out}^D$ can be solved directly for if $T_{s,out}^D$ and T_{pp}^D are known.

Any sections of the triangle can be solved for, provided that the remaining two are known. The following possibilities exist:

- Solve for $U^D A$ only if $\dot{m}_s^D$ and either $T_{g,out}^D$ and/or $T_{s,out}^D$ and/or T_{pp}^D are known

- Solve for $\dot{m}_s^D$ only if $U^D A$ and either $T_{g,out}^D$ and/or $T_{s,out}^D$ and/or T_{pp}^D are known

- Solve for $T_{g,out}^D$ and/or $T_{s,out}^D$ and/or T_{pp}^D only if $U^D A$ and $\dot{m}_s^D$ are known. This procedure will provide two solutions for the evaporator.

4.8 Superheater brick development

The Brick Data and Local Station Vectors for the superheater are outlined in table 4.5.

The geometry of the superheater is provided with a $U^D A$ Brick Data. The pinch point temperature difference is provided by T_{pp}, which is calculated with equation 4.12. If

Table 4.5 Superheater Brick Data, Local Station Vectors, and Local Performance Parameters

Brick Data items	Inlet Station Vectors	Outlet Station Vectors	Performance Parameters
$U^D A$	$T_{s,in}^D$	$T_{s,out}^D$	$\dot{Q}^D$
T_{pp}	$P_{s,in}^D$	$P_{s,out}^D$	
	$h_{s,in}^D$	$h_{s,out}^D$	
	$S_{s,in}^D$	$S_{s,out}^D$	
	$\dot{m}_{s,in}^D$	$\dot{m}_{s,out}^D$	
	$T_{g,in}^D$	$T_{g,out}^D$	
	$\dot{m}_{g,in}^D$	$\dot{m}_{g,out}^D$	

$U^D A = -1$ and $T_{pp} > 0$, then the algorithm will evaluate required $U^D A$ for a predefined T_{pp}. If however, $U^D A > 1$ and $T_{pp} = -1$, the algorithm will calculate T_{pp} for required superheater geometry, $U^D A$.

$$T_{pp} = T_{g,in}^D - T_{s,out}^D \tag{4.12}$$

4.8.1   Analysis

The overall shape of functions F_1^D and F_2^D are shown in figure 4.15. To demonstrate the concept the inlet into the superheater is assumed to be a saturated steam. Unlike in the analysis of an economiser and evaporator where the operating pressure is the output parameter, in the solution of a superheater it is an input parameter where it is used to determined a value of $T_{s,out}^D$. Thus, the solution is a function of inlet Local Station Vectors, the Brick Data, $U^D A$, and additionally operating pressure level, P_s^D. It is evident that a single unique solution exists at the intersection point of functions F_1^D and F_2^D zero lines. The unique solution provides $T_{s,out}^D$, $T_{g,out}^D$ and $\dot{m}_s^D$.

Solutions obtained with equation 4.8 are plotted in the top of figure 4.16 as function of $T_{s,out}^D$ at varying $U^D A$. For all values of $U^D A$, the $\dot{m}_s^D$ tends to fall with rising $T_{s,out}^D$ as the heat demanded by steam is increasing at a slower rate then the heat supplied by the gas. As $T_{s,out}^D$ approaches $T_{s,in}^D$, the infinitesimally small heat demand will dominate consequent reduction in heat supply causing the $\dot{m}_s^D$ to asymptotically approach positive infinity. Since the $T_{s,out}^D$ is a function of P_s^D, a positive or negative change in operating pressure will shift the curves in either positive or negative direction, respectively.

The size of the superheater, as determined by $U^D A$, must increase to accept higher steam mass flow rate at all values of $T_{s,out}^D$. As a result, the $T_{g,out}^D$, which is calculated with equation 4.6 and shown in the middle of figure 4.16, will fall due larger heat transfer
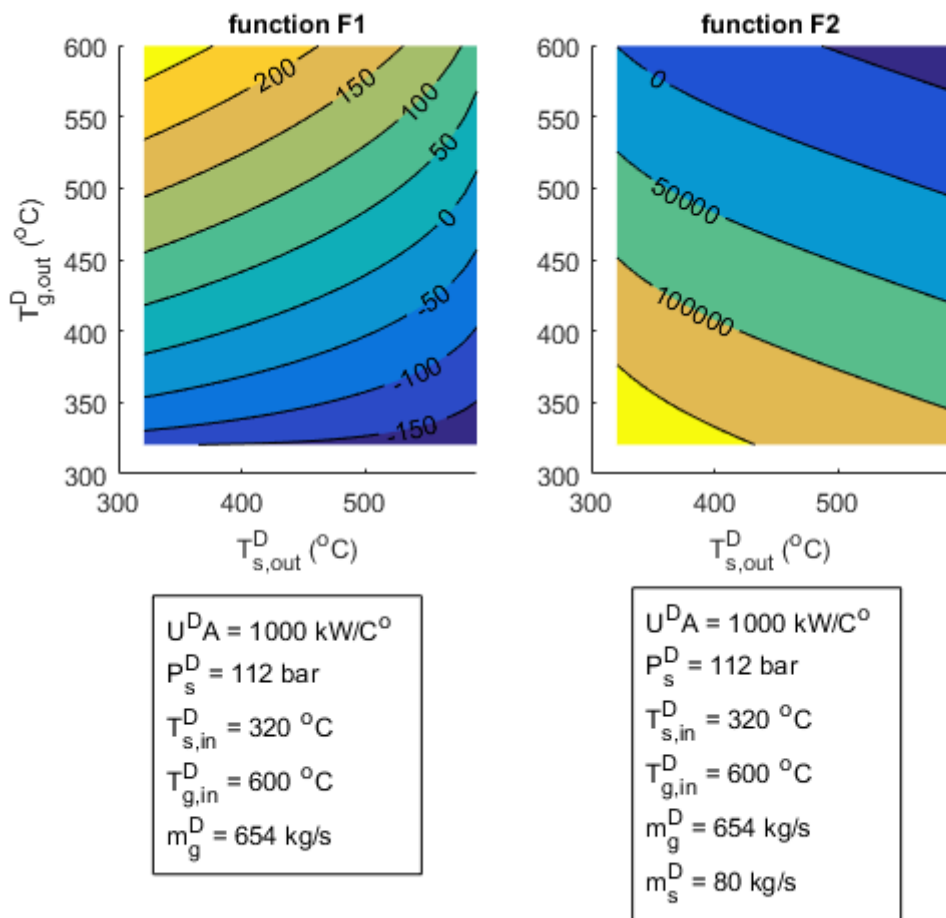
Fig. 4.15 Superheater F1 and F2 functions. Shown residuals as function of gas and steam outlet temperatures

surface area. For an infinitely large superheater, $T_{g,out}^D$ is asymptotically approach $T_{s,in}^D$ for all values of $T_{s,out}^D$.

The pinch point temperature difference for the superheater calculated with equation 4.12 is shown in the bottom of figure 4.16. According to the results, the change in the superheater size does not effect the T_{pp} as $T_{g,in}^D$ remains unchanged and $T_{s,out}^D$ is monotonically increasing. The heat input into the tube bank of the superheater can then be calculated with equation 4.3 for steam path.
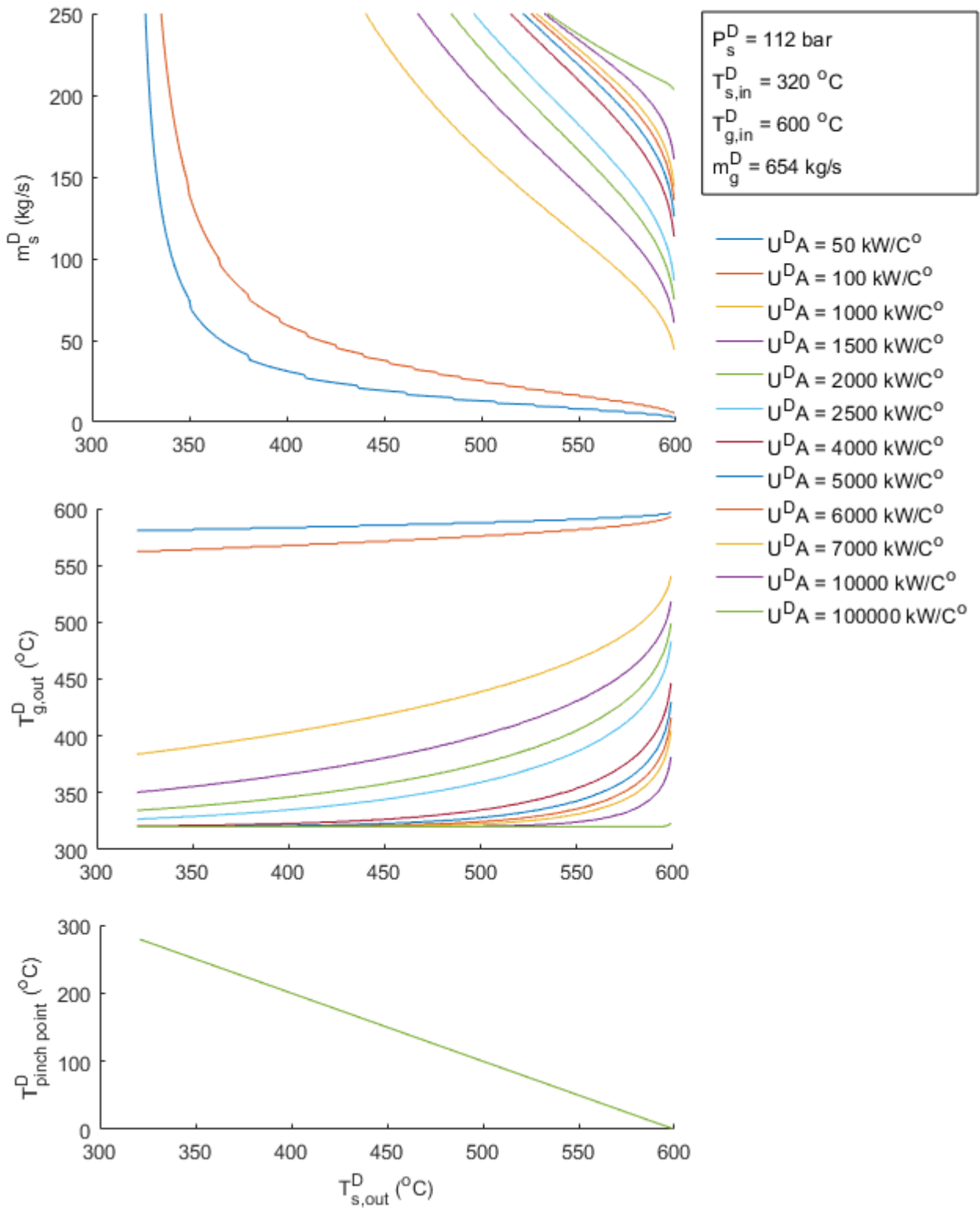
Fig. 4.16 Superheater parametric study of results. Shown variation in steam mass flow, gas outlet temperature and pinch point temperature difference

4.8.2 Procedure

The design point trade-offs triangle for the superheater is shown in figure 4.17. The required input variables in the cloud are the Local Station Vectors $T_{g,in}^D$, $\dot{m}_{g,in}^D$, $P_{s,in}^D$, $T_{s,in}^D$. Similarly to the economiser and evaporator's triangles the results are positioned into three distinct sections.
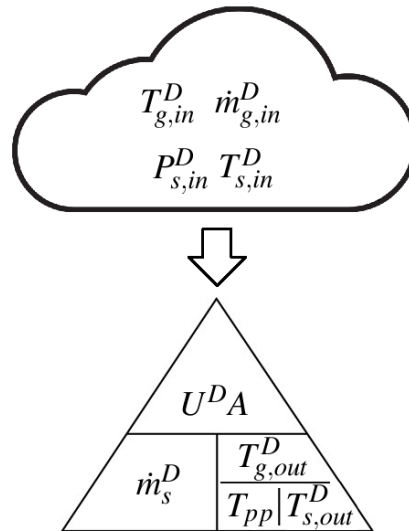
Fig. 4.17 Superheater design point trade-offs triangle

The lower-right section of the triangle contains temperature variables $T_{g,out}^D$, $T_{s,out}^D$ and T_{pp}^D. Any one of the sections can be solved for provided that remaining two are known. To use the triangle, one needs to cover one of the three sections of interest, and use the remaining two sections to find the value of the covered variable. The following possibilities exist:

- Solve for $U^D A$ only if $\dot{m}_s^D$ and either $T_{g,out}^D$ and/or $T_{s,out}^D$ and/or T_{pp}^D are known

- Solve for $\dot{m}_s^D$ only if $U^D A$ and either $T_{g,out}^D$ and/or $T_{s,out}^D$ and/or T_{pp}^D are known

- Solve for $T_{g,out}^D$ and/or $T_{s,out}^D$ and/or T_{pp}^D only if $U^D A$ and $\dot{m}_s^D$ are known

4.9 Other bricks

Additional bricks have been developed to enable simulation of the whole steam bottoming cycle performance. These bricks have not been analysed or studied to the extent of detail provided in the analysis of proceeding sections, however are crucial and are described briefly in this section.

4.9.1   Steam turbine

The steam turbine brick performs basic calculations for the performance with the three Brick Data items outlined in table 4.6. The metallurgical limit of turbine blade material is considered by $T^D_{s,in_{limit}}$. This consideration is in current work disabled, however it presents an opportunity for future development. The Station Vectors at the outlet of the steam turbine are then evaluated with two possible scenarios: 1) the outlet is in superheated region, and 2) the outlet is in water/vapour region. Either solution depends on the outlet pressure level, $P^D_{s,out}$, and the turbine isentropic efficiency, η^D_{isen}. If wetness is too high then erosion issues will appear at the last stage blades. If on the other hand steam has a small degree of superheat at the outlet of the turbine, the heat can quickly be given up before a condensation process begins. If the degree of superheat is sufficiently large, it would take longer to cool the superheated steam to a saturated vapour state, which in fact would lower the efficiency of the steam cycle. The other consideration for avoiding superheated steam at turbine outlet is that temperature gradients may occur over the heat transfer surface area. Therefore, it in ideal design it is a common practice to aim for the outlet to be in a region of approximately 95% wetness fraction.

Table 4.6 Steam turbine Brick Data, Local Station Vectors, and Local Performance Parameters

Brick Data items	Inlet Station Vectors	Outlet Station Vectors	Performance Parameters
$T^D_{s,in_{limit}}$	$T^D_{s,in}$	$T^D_{s,out}$	PO^D
η^D_{isen}	$P^D_{s,in}$	—	
$P^D_{s,out}$	$h^D_{s,in}$	$h^D_{s,out}$	
	$S^D_{s,in}$	$S^D_{s,out}$	
	$\dot{m}^D_{s,in}$	$\dot{m}^D_{s,out}$	

4.9.2   Condenser

The condenser Brick Data, Station Vectors and Performance Parameter are outlined in table 4.7. The cooling medium is accounted for in three Brick Data items. This consideration is however disabled in the current work; however, it provides opportunity for further development. It is assumed that the outlet of the condenser is in a saturated water state.

4.9.3   Pump

The pump Brick Data, and Local Station Vectors are outlined in table 4.8. The pressure rise of the pump is controlled by Brick Data $SN_{P^D_{s,out}}$, which points to a station number of desired pressure. The evaporator outlet station number is usually a choice for the required

Table 4.7 Condenser Brick Data, Local Station Vectors, and Local Performance Parameters

Brick Data items	Inlet Station Vectors	Outlet Station Vectors	Performance Parameters
$P^D_{cooling_{water}}$	$T^D_{s,in}$	$T^D_{s,out}$	$\dot{Q}_in^D$
$T^D_{cooling_{water}}$	$P^D_{s,in}$	$P^D_{s,out}$	
$\Delta T^D_{cooling_{water}}$	$h^D_{s,in}$	$h^D_{s,out}$	
	$S^D_{s,in}$	$S^D_{s,out}$	
	$\dot{m}^D_{s,in}$	$\dot{m}^D_{s,out}$	

pressure level. The pump then calculates water Station Vectors at the outlet by taking into consideration the isentropic efficiency, η^D_{isen}.

Table 4.8 Pump Brick Data, Local Station Vectors, and Local Performance Parameters

Brick Data items	Inlet Station Vectors	Outlet Station Vectors
$SN_{P^D_{s,out}}$	$T^D_{s,in}$	$T^D_{s,out}$
η^D_{isen}	$P^D_{s,in}$	—
	$h^D_{s,in}$	$h^D_{s,out}$
	$S^D_{s,in}$	$S^D_{s,out}$
	$\dot{m}^D_{s,in}$	$\dot{m}^D_{s,out}$

4.9.4 Drum

The Drum brick has been set up to guide future development. It contains no specific calculations, but equates Station Vectors at the outlet to the ones at the inlet for steam and water paths.

4.9.5 Flow splitter

The flow splitter brick is used to diverge the flow in 2 directions. In multiple pressure systems, flow splitter is located after the economiser to split the flow into higher and lower pressure levels. The Brick Data item, $SN_{\dot{m}^D_{s,out1}}$ points to a station number of desired $\dot{m}^D_{s,out1}$. This is usually an outlet of a mixer, as described in more detail in section 4.10. The balance of mass flow is calculated with equation 4.13, and corresponding enthlapy with equation 4.14

$$\dot{m}_{s,in} = \dot{m}_{s,out1} + \dot{m}_{s,out2} \tag{4.13}$$

$$h_{s,in} = h_{s,out1} = h_{s,out2} \qquad (4.14)$$

4.9.6 Flow mixer

The flow is mixed in Mixi brick according to equation 4.15.

$$\dot{m}_{s,in1} + \dot{m}_{s,in2} = \dot{m}_{s,out} \qquad (4.15)$$

Applying energy balance to the controlled volume system

$$E_{in} = E_{out}$$

$$\dot{m}_{s,in1} h_{s,in1} + \dot{m}_{s,in2} h_{s,in2} = \dot{m}_{s,out} h_{s,out}$$

After rearranging terms, the $h_{s,out}$ is calculated with equation 4.16

$$h_{s,out} = \frac{y h_{s,in1} + h_{s,in2}}{y + 1} \qquad (4.16)$$

Where

$$y = \frac{\dot{m}_{s,in1}}{\dot{m}_{s,in2}}$$

4.10   Multiple pressure systems

The performance of multiple pressure systems can also be modelled. The steam mass flow across multiple pressure systems must be balanced according to figure 4.18. Junctions A and B correspond to the inlet of a flow splitter and outlet of a flow mixer, respectively. Therefore, assuming no leaks or bleed occur, the mass flows at A and B must be always be equal at each corresponding pressure level, e.g. mass flow rate at junctions A_1 and B_1 must be $A_1 = B_1 = \dot{m}_1 + \dot{m}_2$. Accordingly, the general formulation is shown in equation 4.17.

$$\dot{m}_n = \begin{cases} \text{equation 4.8,} & \text{for } n = 1 \\ \dot{m}_{A_{n-1}} - \sum_{k=1}^{n-1} \dot{m}_k, & \text{for } tot > n > 1 \\ \sum_{k=1}^{tot-1} \dot{m}_k, & \text{for } n = tot \end{cases} \qquad (4.17)$$

For $tot > n > 1$, rearranging the terms according to equation 4.18 provides a solution to the cumulative steam mass flows flowing into the higher pressure system. The $\dot{m}_n$ can be solved with equation 4.8, and the $\dot{m}_{A_{n-1}}$ is known from the input to the flow splitter. The flow at B_n is mixed according to equation 4.19.

$$\sum_{k=1}^{n-1} \dot{m}_k = \dot{m}_{A_{n-1}} - \dot{m}_n, \text{ for } tot > n > 1 \tag{4.18}$$

$$\dot{m}_{B_{n-1}} = \dot{m}_n + \sum_{k=1}^{n-1} \dot{m}_k, \text{ for } tot > n > 1 \tag{4.19}$$
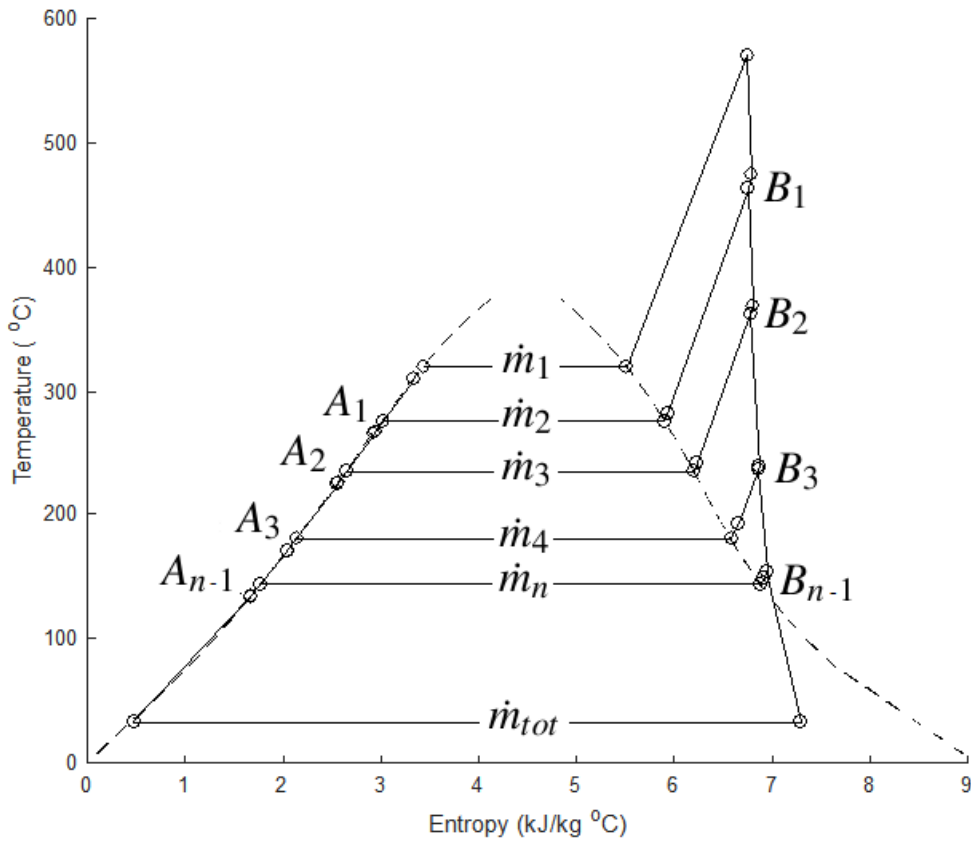
Fig. 4.18 Multiple pressure system functional diagram

4.11 Comparison of results against commercial software

The results obtained with the Direct Solution Method for design point performance of one pressure system have been validated against the PROATES and Ebsilon commercial software. It is crucial for the comparison process to ensure that the system modelled across various platforms is as similar as possible. The exhaust gas from a gas turbine operating on natural gas is composed of various molecular species; i.e. nitrogen, oxygen, carbon

dioxide, and sometimes traces of argon. The molecular weight of these molecules will effect the enthalpy of the gas entering the heat recovery steam generator. It is important, therefore, that the composition of gas across DSM, PROATES, and Ebsilon models is such to represent similar conditions and gas enthalpy. This is confirmed in the results for a variable $SuHe_{h,g,in}$ in table 4.9, where enthalpy is kept similar across validation cases.

The *UA* represents the geometry and heat transfer coefficient for each heat exchanger. It is important that the *UA* is similar across all compared cases, and ultimately it can be assumed that the heat exchangers are the same. This is represented with $Econ_{UA}$, $Evap_{UA}$, and $SuHe_{UA}$, for economiser, evaporator and superheater, respectively. The simulated temperature, pressure and mass flow results in table 4.9 show good correlation and validation of the Direct Solution Method.

Table 4.9 Validation of results for one pressure system

		DSM	PROATES	Ebsilon
$Econ_{T,s,in}$	$[^oC]$	36.0950	36.095	36.095
$Econ_{T,s,out}$	$[^oC]$	309.7949	316.938	316.160
$Econ_{T,g,in}$	$[^oC]$	340.1205	351.007	350.253
$Econ_{T,g,out}$	$[^oC]$	190.0376	191.777	191.269
$Econ_{UA}$	$[\frac{kW}{^oC}]$	1318.023	1318.020	1318.211
$Evap_{T,s,in}$	$[^oC]$	309.7949	316.938	316.160
$Evap_{T,s,out}$	$[^oC]$	319.7949	319.121	319.753
$Evap_{T,g,in}$	$[^oC]$	499.0276	502.394	502.188
$Evap_{T,g,out}$	$[^oC]$	339.5473	351.007	350.253
$Evap_{UA}$	$[\frac{kW}{^oC}]$	1277.969	1277.311	1227.940
$SuHe_{T,s,in}$	$[^oC]$	319.7949	319.121	319.753
$SuHe_{T,s,out}$	$[^oC]$	570.0000	569.814	569.315
$SuHe_{T,g,in}$	$[^oC]$	600.0000	600.000	600.000
$SuHe_{T,g,out}$	$[^oC]$	499.0276	502.394	502.188
$SuHe_{h,g,in}$	$[\frac{kJ}{kg}]$	613.9224	613.124	613.473
$SuHe_{UA}$	$[\frac{kW}{^oC}]$	811.999	811.990	811.363
$StTu_{P,s,out}$	$[bar]$	0.05	0.05	0.05
P_s	$[bar]$	112.470	111.531	112.470
$\dot{m}_s$	$[\frac{kg}{s}]$	82.2755	82.3235	82.525
$\dot{m}_g$	$[\frac{kg}{s}]$	653.900	653.900	653.900
PO	$[MW]$	100.8913	102.383	98.314
η_{st}	$[]$	36.65	36.78	35.27

4.12 Modelling results

To demonstrate robustness of the method developed and presented in this chapter, bottoming steam cycle performance has been simulated for up to five pressure levels. The input files for 1P is shown in figure 4.7, and the 2P, 3P and 5P are shown in the appendix figures B.2, B.4, and B.5, respectively. The design point parameters defined in the Brick Data items for each simulation are summarised in tables 4.10, 4.11, 4.12, and 4.13. The temperature-entropy and heat transfer diagrams are shown in figures 4.19, 4.20, 4.21 and 4.22. The performance parameters have been obtained and summarised in table 4.14 for all simulations.

It has been observed that for multiple pressure systems if the lower pressure level is too close to the higher pressure level, then a resulting small steam mass flow cannot be satisfied in the superheater. It has been investigated and demonstrated in previous sections that for a given pressure level the $\dot{m}_s^D$ is decreasing with $U^D A$; however, it appears that at values of $U^D A \leq 1$, the $\dot{m}_s^D$ tends to increase. This is because having smaller heat exchanger in equation 4.8 outweighs the resulting change in $T_{g,out}^D$ which is asymptotically approaching a value of $T_{s,in}^D$. Therefore, if the $\dot{m}_s^D$ produced by evaporator is lower then the minimum $\dot{m}_s^D$ required by superheater at $U^D A = 1$, the solution is undefined. It is highly unlikely that $U^D A$ will take a value in a region of 1 as this implies a very small heat exchanger with a very small heat transfer surface. This however demonstrates that there exist solutions for the minimal pressure difference between higher and lower pressure levels. The underlying mechanisms are not fully understood and further analysis is outside of the scope of current work.

The result of the error arising from superheater mass flow not being satisfied is demonstrated in figure 4.22, where gas station *114* clearly shows a discontinuity. At this instance the mass flow of steam produced by the evaporator at 20 bar pressure is $\dot{m}_s^D = 3.4516\frac{kg}{s}$ and the minimum mass flow required by the superheater at $U^D A = 1$ is $\dot{m}_s^D = 3.65\frac{kg}{s}$. The problem can be solved by lowering the evaporator operating pressure; this will increase evaporator steam production and therefore a point will eventually be reached where superheater and evaporator mass flow balance is satisfied.

It appears that the lower bound for the number of pressure level in a system is dictated by steam quality at the outlet of a consecutive steam turbine. According to figure 4.22, additional pressure level may result in water/steam mixture at the inlet to the steam turbine, which must be avoided due to corrosion problems. This problem can be overcome by adding a reheat system.

According to table 4.14, the power output increases and plateaus with higher pressure levels. The stack temperature continues reducing as more heat is being transferred from the gas path with increasing number of pressure levels.

Table 4.10 Simulated design parameters for 1P system

		1P
Econ	$U^D A$	1497.31
	$T_{approach}$	10
Evap	$U^D A$	1153.99
	T_{pp}	20
SuHe	$U^D A$	1009.03
	T_{pp}	30
	$\dot{m}_g^D$	653.9
	$\dot{m}_s^D$	81.51
	P_s^D	156

Table 4.11 Simulated design parameters for 2P system

		1P	2P
Econ	$U^D A$	1131.10	1234.10
	$T_{approach}$	10	10
Evap	$U^D A$	1153.99	694.79
	T_{pp}	20	20
SuHe	$U^D A$	1009.03	39.89
	T_{pp}	30	30
	$\dot{m}_g^D$	653.9	653.9
	$\dot{m}_s^D$	81.51	16.73
	P_s^D	156	20

Table 4.12 Simulated design parameters for 3P system

		1P	2P	3P
Econ	$U^D A$	698.07	863.18	1014.21
	$T_{approach}$	10	10	10
Evap	$U^D A$	1268.43	460.43	598.47
	T_{pp}	20	20	20
SuHe	$U^D A$	830.58	19.58	18.19
	T_{pp}	30	30	30
	$\dot{m}_g^D$	653.9	653.9	653.9
	$\dot{m}_s^D$	81.76	9.71	11.74
	P_s^D	112	40	5

Table 4.13 Simulated design parameters for 5P system

		1P	2P	3P	4P	5P
Econ	$U^D A$	405.11	430.86	438.97	453.76	6436.39
	T_a	10	10	10	10	10
Evap	$U^D A$	1153.99	163.01	246.81	270.65	1998047
	T_{pp}	20	20	20	20	20
SuHe	$U^D A$	1009.03	16.66	17.70	17.94	1998047
	T_{pp}	30	10	10	10	10
	$\dot{m}_g^D$	653.9	653.9	653.9	653.9	653.9
	$\dot{m}_s^D$	81.51	3.40	4.79	4.77	3.45
	P_s^D	156	112	70	40	20
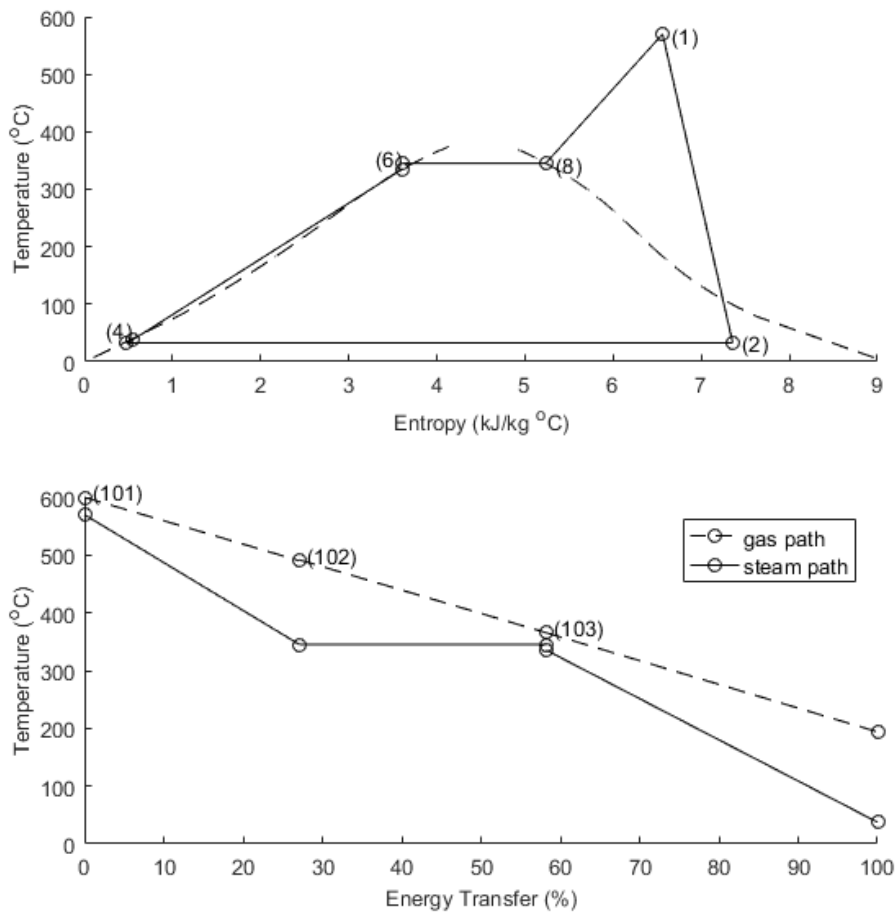
Fig. 4.19 Simulated design performance of a 1P steam cycle
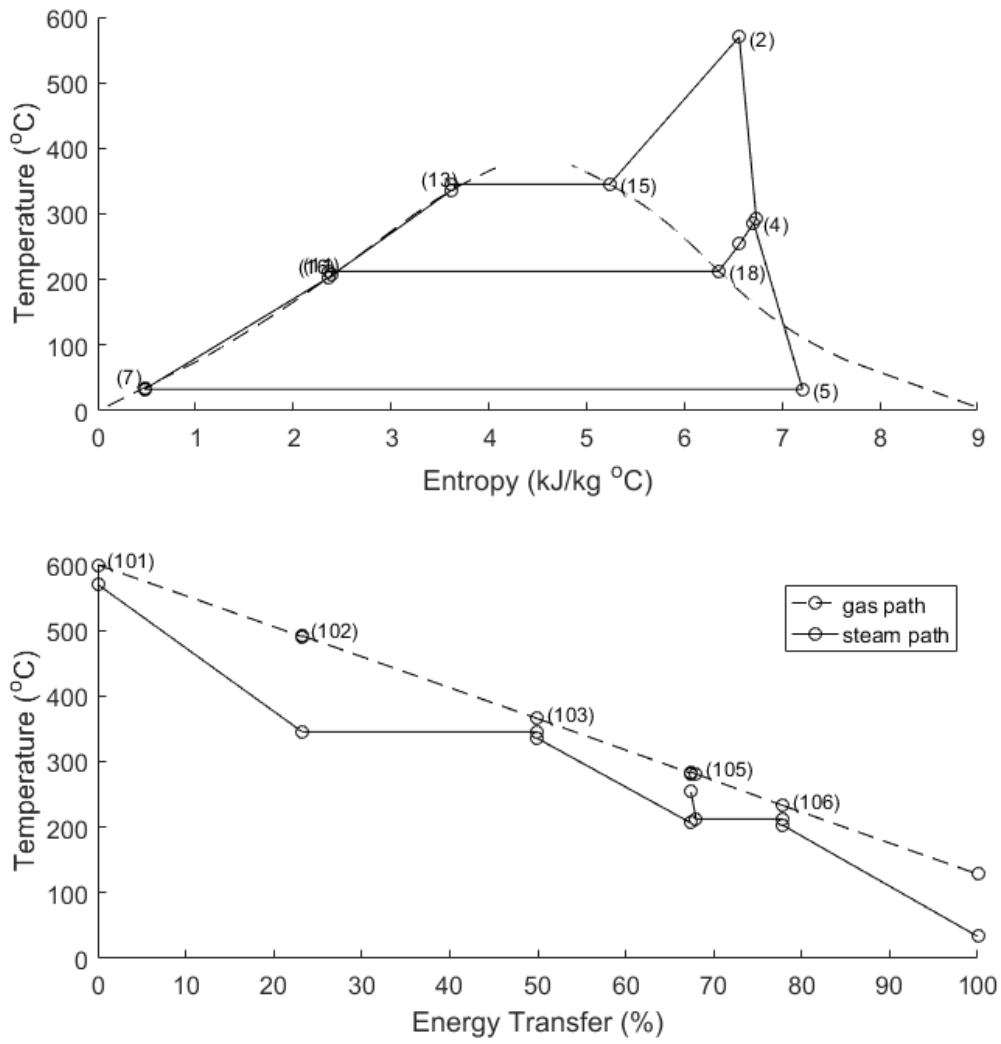
Fig. 4.20 Simulated design performance of a 2P steam cycle
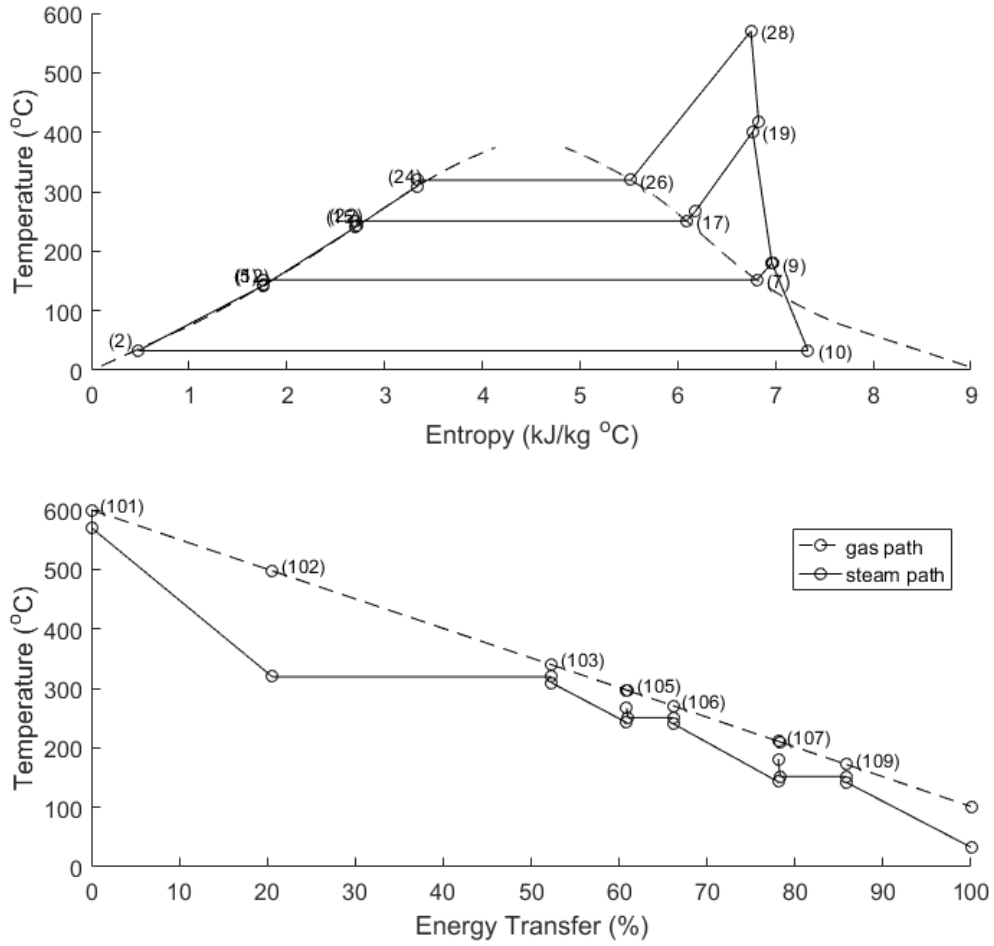
Fig. 4.21 Simulated design performance of a 3P steam cycle
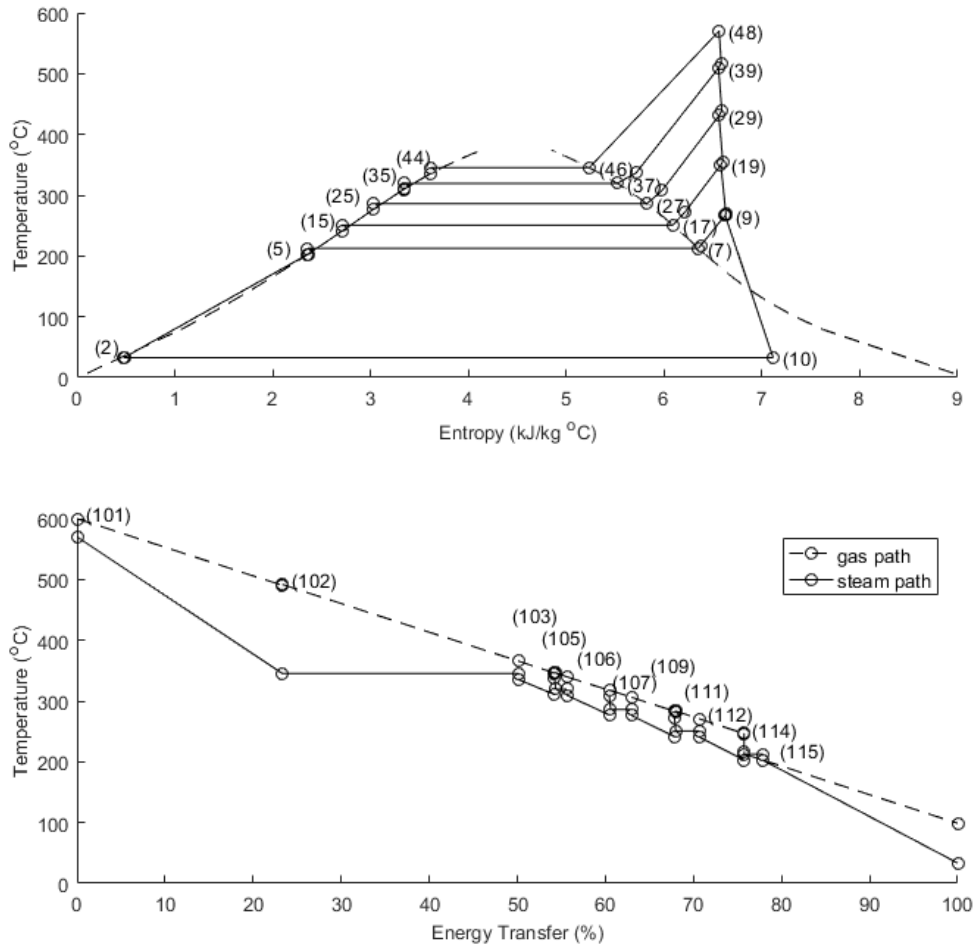
Fig. 4.22 Simulated design performance of a 5P steam cycle

Table 4.14 Comparison of performance results

Performance Parameters				
	1P	2P	3P	5P
$\eta_{ST}[\%]$	37.94	37.39	35.71	37.27
$\dot{Q}_{in}[MW]$	271.18	316.01	335.11	314.96
$\dot{Q}_{out}[MW]$	168.29	197.84	215.44	197.56
$PO[MW]$	102.17	117.48	120.84	120.47
$T_{stack}[^oC]$	193.91	128.53	101.30	98.80

4.13 Discussion

Major components of the steam cycle have been studied with focus on the heat recovery steam generator. A flexible and robust algorithm db.match.CCPP has been developed to allow for modelling of CCPP single and multi-pressure systems in a user-defined modular fashion. The algorithm has enabled to study the whole CCPP performance and has led to the development of the novel Direct Solution Method (DSM) for design point performance calculations. The DSM has been derived from fundamental laws of thermodynamics with assumptions discussed in section 4.1.1. The performance variables have been studied parametrically, where variation in the steam mass flow rate and the heat exchanger temperature profile with the size for economiser, evaporator and superheater are shown in figures 4.10, 4.13 and 4.16, respectively. The DSM allows to visualise complex performance trade-offs and effectively match cycle components by their steam mass flow rates. The method has been compared against results obtained from the commercial software confirming very good correlation.

Comparatively, existing iterative numerical and sequential procedures solve a system of non-linear equations in which convergence is characterised by a solution with a minimal residual. Therefore, existing methods will fundamentally introduce an error in a result. Additionally, the convergence issues may arise from the need to make relatively accurate initial guess for the solution. If the initial approximation is insufficient, the solution will converge at a false value. The DSM, therefore, is a good alternative method to existing modelling techniques, where algorithm complexity is reduced, and reliability and fundamental accuracy improved with no residual error in the solution.

Chapter 5

Genetic Algorithm method for steam cycle off-design performance simulation

The objective of this chapter is to demonstrate a novel application of a Genetic Algorithm as an alternative to existing techniques for modelling off-design performance of a steam cycle. The performance of a system in off-design is related to the design-point operation; therefore, the work discussed in this chapter builds on the results obtained in chapter 4.

5.1   Process development

The underlying purpose for implementing the genetic algorithm is to search for a solution to a system of non-linear equations. The extent of these equations depends on the number of components comprised in the cycle, which increases in complexity with the addition of each component. Commercial software is available that allows for applying genetic algorithm to optimisation. However, an in-house algorithm has been developed to allow for higher degree of control and seamless integration with the *db.match.CCPP* design-point algorithm described in chapter 4.

5.1.1   System description and assumptions

The operation of shell-and-tube heat exchangers can be completely described with heat transfer and energy balance equations. Each heat exchanger brick described in the *db.match.CCPP* input file (e.g. figure 4.7), calculates residuals from functions F_1 and F_2 according to equations 6.14a and 6.14b for heat transfer and energy balance, respectively. These functions have been derived and discussed in chapter 6. Functions F_1 and F_2 represent the fitness function of each heat exchanger brick, with ideal convergence at a fitness function tending to zero.

Each population in the genetic algorithm contains n individuals, which evolve across consecutive generations, g. The probabilities of crossover and mutation are $P_c = 100\%$

and $P_m = 0.5\%$, respectively. Figure 5.1 shows an example of progression across generations for population size $n = 100$. The circle is divided into equal segments corresponding to the size of population, where the radial axis represents the fitness function values of each individual. The algorithm begins with randomly generated individuals in generation $g = 1$, and evolves the solution towards a convergence with minimal fitness.

5.1.2 Process flowchart

The process flowchart is shown in figure 5.2. The design point performance variables are passed from the Direct Solution Method at design-point discussed in chapter 4. The mode of operation to trigger the genetic algorithm calculations is *mode* = 1. The following procedures are initiated with the objective of returning a set of performance parameters describing the system at off-design operation.

Operation 1 - Process input

The input parameters are read from text files. The input file, shown in figure 4.7 for a 1 pressure system is read from *db.match.CCPP_input.txt*. The size of the population and the maximum number of generations are read from the *GA_input.txt*. The gas turbine exhaust conditions including temperature and gas mass flow rate are read from *Turbo-Match_results.txt*.

Operation 2 - Initialise files and folders structure

The algorithm saves results to separate folders for each generation. Initially all of the folders need to be deleted and a new set created according to the total number of generations obtained from operation 1. Three text files are generated in each generations folder, these are *Fitness.txt*, *Genotypes.txt*, and *Phenotypes.txt*, to store values of fitness, genotypes, and phenotypes for each individual in the population, respectively.

Operation 3 - Generate initial population

The initial population is generated randomly within boundary limits. The boundaries are established based on fundamental principles of counter-flow heat exchanger operation where the gas and water/steam temperatures need to be between the maximum and minimum temperature determined by $T_{g,in}$ and $T_{s,in}$, respectively.

Operation 4 - Stochastic selection process

A selection process is designed to determine which individuals from the population will be used to determine the next population. These individuals need to exhibit promising characteristics which are determined by comparing each to the median fitness of the whole population. Since the purpose is to favour individuals with the lowest fitness - the ones
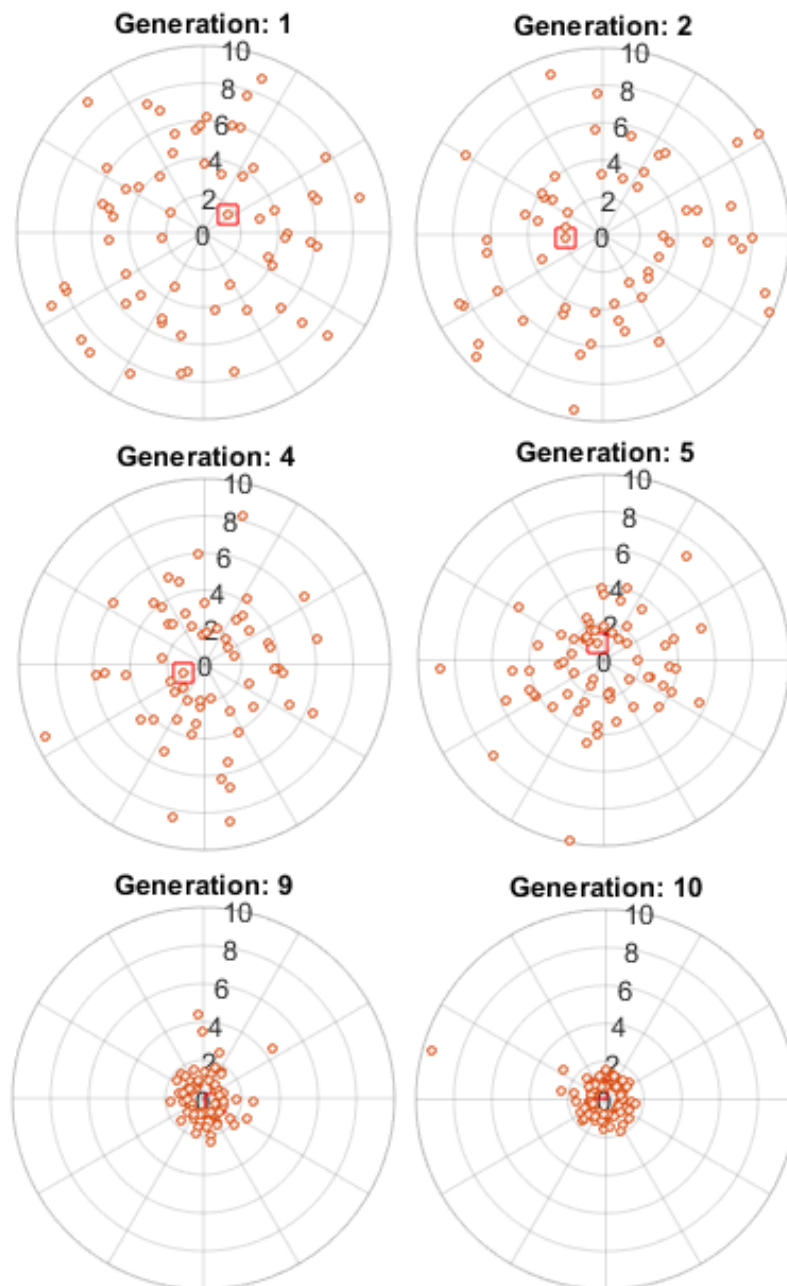
Fig. 5.1 Progressing population of 100 individuals across generations. In each generation, the square points to the location of individual with minimum fitness

with fitness below the median fitness are automatically passed to the next operation. The
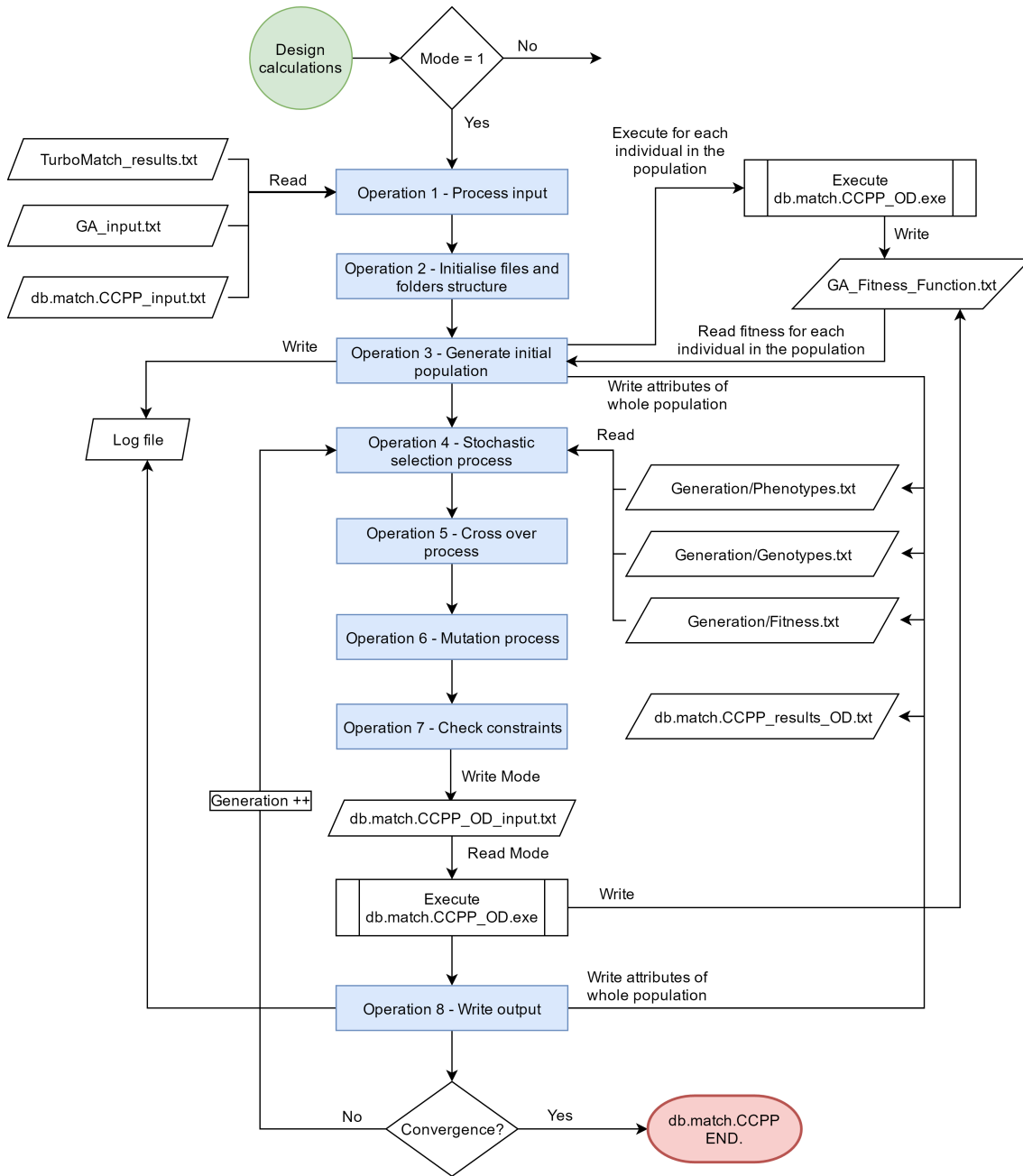
Fig. 5.2 GA program flow diagram

remaining individuals in the population are selected with a Stochastic Universal Sampling method. In this method median fitness is compared to each individual in the population, then ratios are evaluated and arranged in ascending order, where the length of each segment relates to the fitness of the element. The individuals with the longest segments are preferable as they have corresponding fitnesses lower then the median fitness. A roulette

method is then applied, where a random number is generated, and the segment it lands points to the individual that is selected for the next population. The roulette process is repeated until the population is fully filled with individuals.

Operation 5 - Cross over process

The selected individuals obtained from operation 4 are shuffled randomly, and the population is equally divided into two sections: *parent 1* and *parent 2*. The parents are then crossed over using a two-point cross over method, where two random integers are generated between values of 1 and the chromosome length (e.g. figure 2.10). These random numbers locate the points of the split where binary genetic material is swapped between the parents. The off springs resulting from this process are called *child 1* and *child 2*. The procedure is further repeated for every individual pair in the population.

Operation 6 - Mutation process

The child population obtained from operation 5 needs to be diversified. This is done by mutating some of the individuals to introduce randomness into the process (e.g. figure 2.11). Each individual's genotype is scanned, and with a very low probability, $P_m = 0.5\%$, a gene is changed from 0 to 1 or vice versa. If a probability of mutation was zero, effectively no mutation at all, the population may lack diversification and may converge at a local minimum. The mutation is therefore a necessary step to diversify the population, and ensure that some individuals become outliers searching for potentially better solution towards the global minima.

Operation 7 - Check constraints

In the early versions of the algorithm, the phenotypes for each individual were checked against limiting boundaries. If the phenotype fell outside of the boundary the hard limit would bring it to the limiting value. It was found, however, that applying constraints directly in the Genetic Algorithm solver is inefficient and significantly prolongs the computational time. Instead, the constraints are applied internally during execution of each module.

Once the population is established, *db.match.CCPP* executes bricks in a sequence obtained from *db.match.CCPP_input.txt* in operation 1. Each brick overall structure has been discussed in figure 4.8, where the off-design calculations are now performed. The *off-design assistance files* process writes the fitness function values for each brick. Ultimately, it is the overall fitness function value that determines the final convergence of the algorithm.

Operation 8 - Write output

The results for all phenotypes, genotypes, and fitness function values are recorded for further post-processing. The detailed progress of each operation is documented in the *log file*.

5.2 The fitness function

Each individual in a given population contains two classes of information: the fitness function value, FV, and un-coded (phenotype) and coded (genotype) strings of variables. The fitness function values are evaluated with equation 5.1 for all individuals, where for each heat exchanger brick in HRSG the fitness is calculated with equation 5.2. Mastorakis showed that weighting the fitness function value by squaring it, taking absolute value of it, or adding it linearly, has significant impact on the convergence [48]. Therefore, in the current work a coefficient, a, is adopted to take into account various weighting effects according to equation 5.3. If the coefficient is 1 then the function is evaluated linearly. Otherwise, if the function is squared, the fitness values > 1 become amplified and values < 1 become squeezed. Amplifying the fitness is a desired property as the algorithm will assign higher weights to already high FV values; however, it will make already small FV even smaller which may lead to premature convergence. Small fitness values could be amplified by adopting a square root amplifier only for values < 1. In the evaluation of FV, if each term is raised to the power of a, the summed value of FV may fail to favour small fitness values of individual bricks; therefore, alternative approach adopted in current work is to evaluate sum of the fitness values first and then raise the result to the power of a according to the bottom of equation 5.1. The best convergence is achieved when coefficient a is linear, i.e. $a = 1$ when equation 5.2 returns brick's fitness values ≤ 1, and squared, i.e. $a = 2$ for all other fitness values.

The evolution of individuals across generations are shown in figure 5.3. Generation 1 is comprised of a random generation of 80 individuals. The algorithm then proceeds to select the fittest individuals, and parents are crossed-over to produce children, which are then mutated and passed on to the next generation. As individuals evolve, the fitness function values begin to converge at approximately 0.25. The outliers are the result of mutation, which is a necessary procedure to keep the population diversified and avoid premature convergence at local minima. In each generation the best individual is selected to be the one with minimum fitness, and only these are further used to study the convergence.

$$FV = \begin{cases} \left[FV_{Evap}\right]^a + \left[FV_{Evap}\right]^a + \left[FV_{Econ}\right]^a + \left[FV_{SuHe}\right]^a + \ldots \\ \left[FV_{Evap} + FV_{Evap} + FV_{Econ} + FV_{SuHe} + \ldots\right]^a \end{cases} \tag{5.1}$$

Where

$$FV_{\text{heat exchanger brick}} = \left| F_1^{OD} \right| + \left| F_2^{OD} \right| \tag{5.2}$$

$$a = \begin{cases} 1, & \text{for linear relation} \\ 2, & \text{for square relation} \\ \frac{1}{2}, & \text{for squareroot relation} \end{cases} \tag{5.3}$$
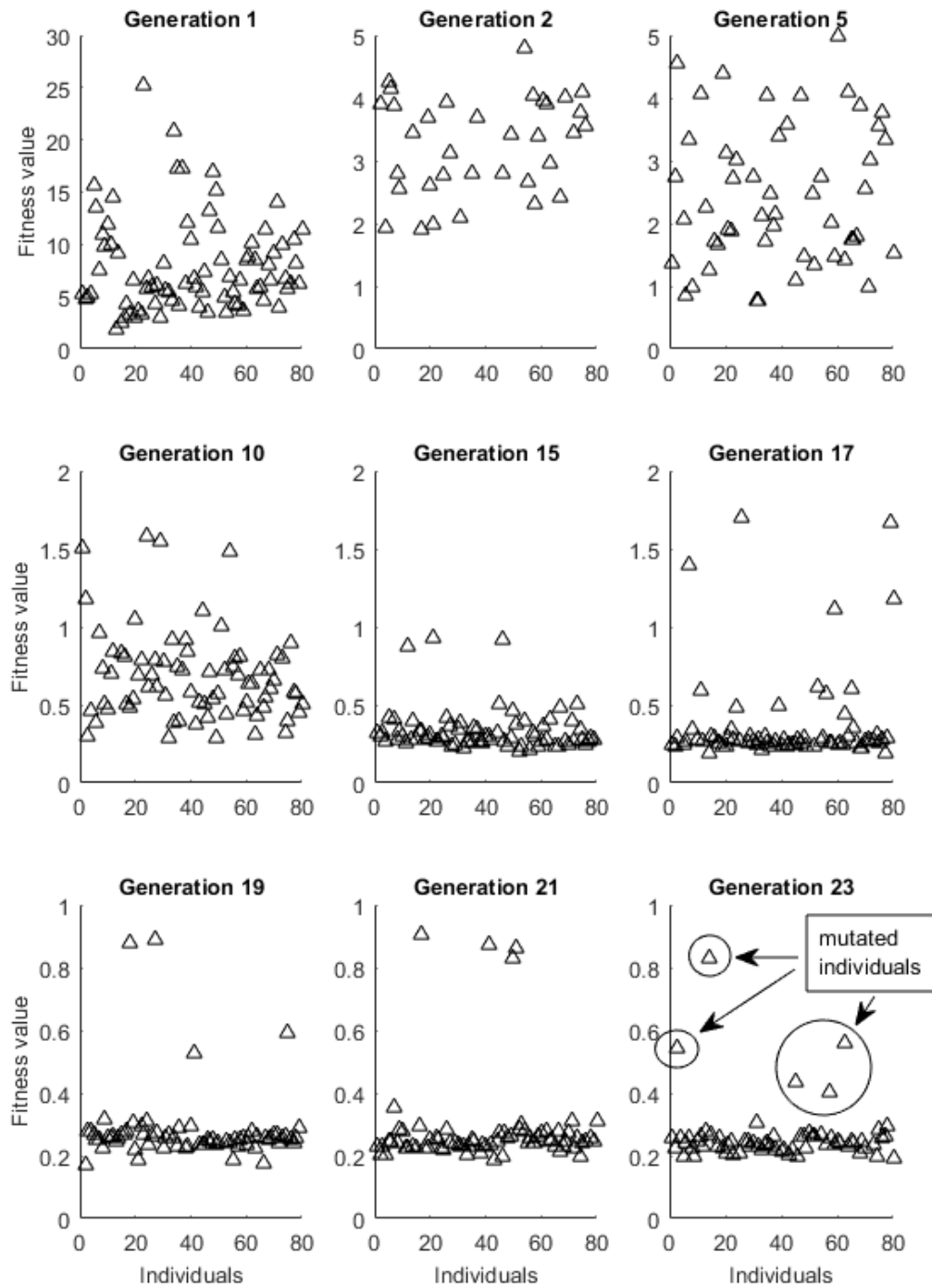
Fig. 5.3 Evolution of 80 individuals across generations

5.3 The convergence criteria

The convergence criteria is set such that the change in fitness function between generations g and $(g-1)$ is very small, i.e. $\varepsilon \leq 0.01$. However, it was noticed that the convergence criteria set on the fitness function does not truly reflect the convergence of the algorithm. At some instances a brick can return a NaN local fitness function value, which correspond to insufficient temperature profile in Log Mean Temperature Difference calculations. It was found that instead of setting a constraint limit on the temperatures within individual bricks, it is more efficient to return and accept a NaN local fitness function and then address the issue on a global scale. A typical fitness function evolution is shown in figure 5.4. Each column in the bar plot corresponds to respective fitness function value returned by a steam turbine, economiser, evaporator and superheater bricks. The overall fitness function is evaluated as a cumulative of all local fitness functions in each generation. This visual representation allows for greater control over the algorithm. The effective population size in the bottom of figure 5.4 takes into account that some individuals in the population may return a NaN fitness function value; therefore, effectively reducing the population capacity. In the initial generation, all phenotypes are generated randomly within specified limits making the effective population size equal to the nominal population size of 200 individuals. As the solution evolves across consecutive generations, the overall fitness function value will converge with $\varepsilon \leq 0.01$. However, the effective population size is approximately 75%, suggesting that the capacity of the algorithm has not yet being fully utilised. Therefore, setting convergence only with ε is insufficient, and the convergence criteria has been expanded with a rule that the effective population size has to be $n_{eff} \geq 90\%$.

5.3.1 Improved convergence

Initially the overall fitness function has been evaluated as a cumulative residual of a set of non-linear equations. This set of equations comprised heat and energy transfer equations 6.14a and 6.14b for heat exchanger bricks, and a Stodola like Law of Cones evaluated with equation 6.49 for a steam turbine brick. The steam mass flow rate is restricted by the steam turbine choking conditions. It, therefore, does not need to be evaluated for with the system of non-linear equations. Instead, it can be calculated directly inside the StTu brick. Consequently the system of non-linear equations can be reduced by taking away the Stodola like Law of Cones, which improves the efficiency of the algorithm, reduces system complexity, and stabilises the progression of the solution across generations.

The convergence of the algorithm for population size of 100 individuals is shown in figure 5.5 where Stodola like Law of Cones equation is included in the set of equations. The algorithm converges after 20th generation. With the Stodola like Law of Cones equations removed from the set, the convergence is shown in figure 5.6. The algorithm converges after the 15th generation.
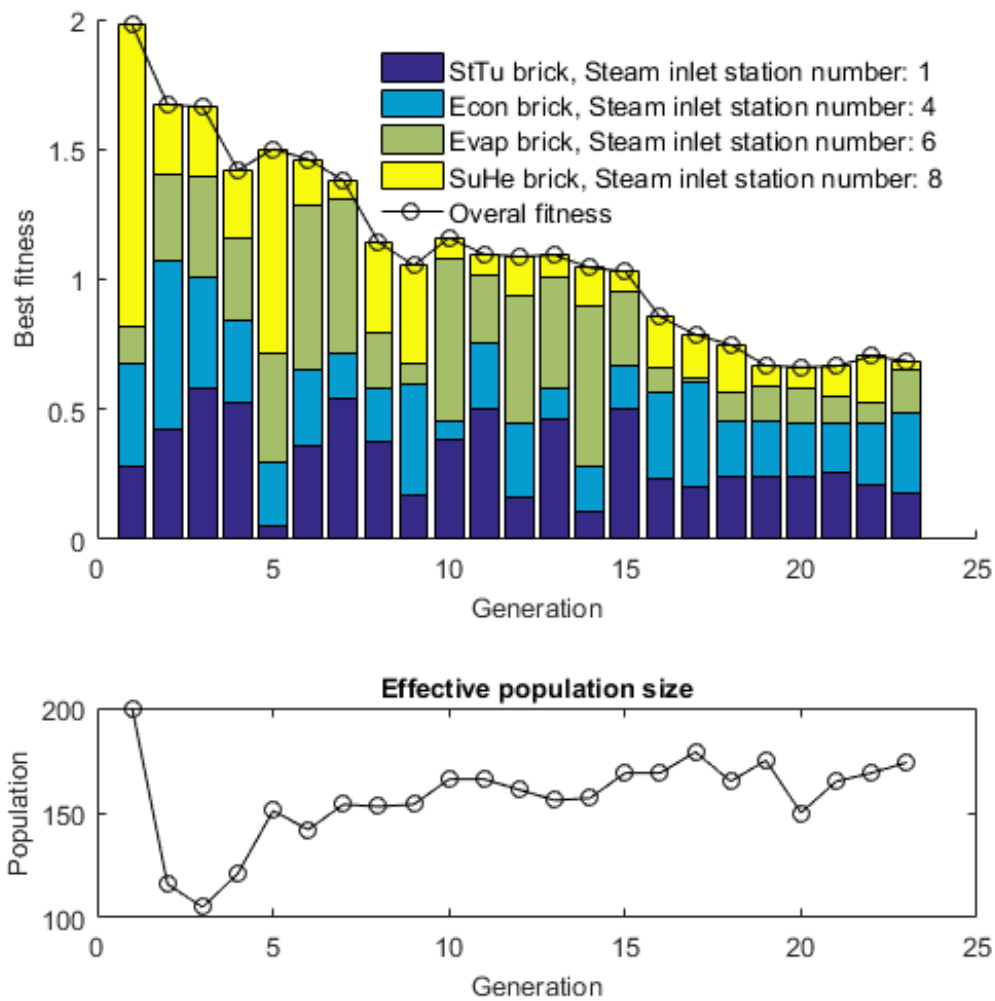
Fig. 5.4 A typical fitness function evolution across generations of 100 individuals
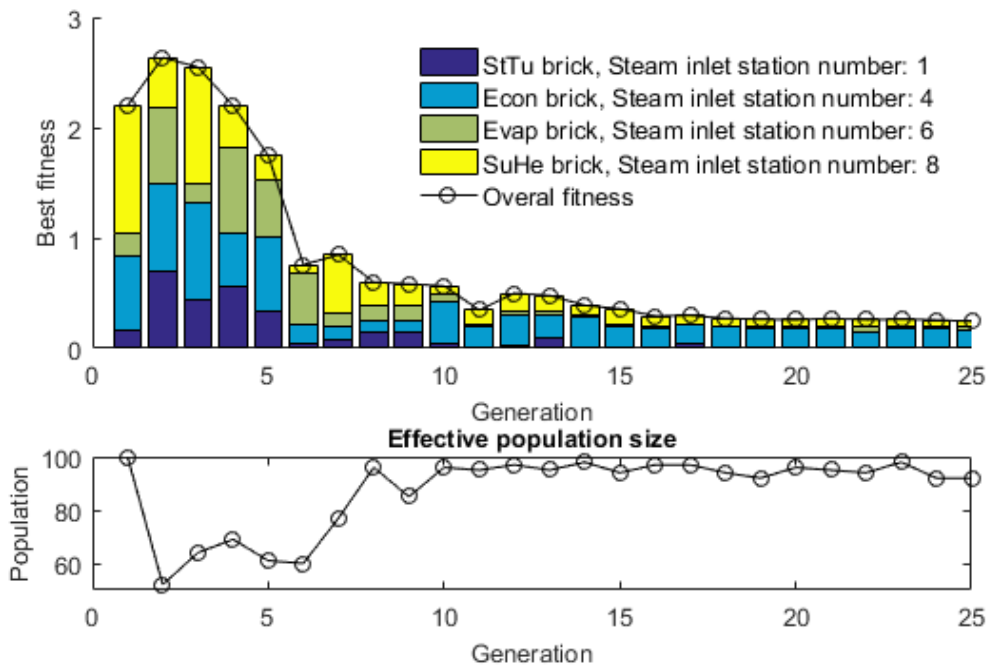
Fig. 5.5 Initial convergence of 100 individuals
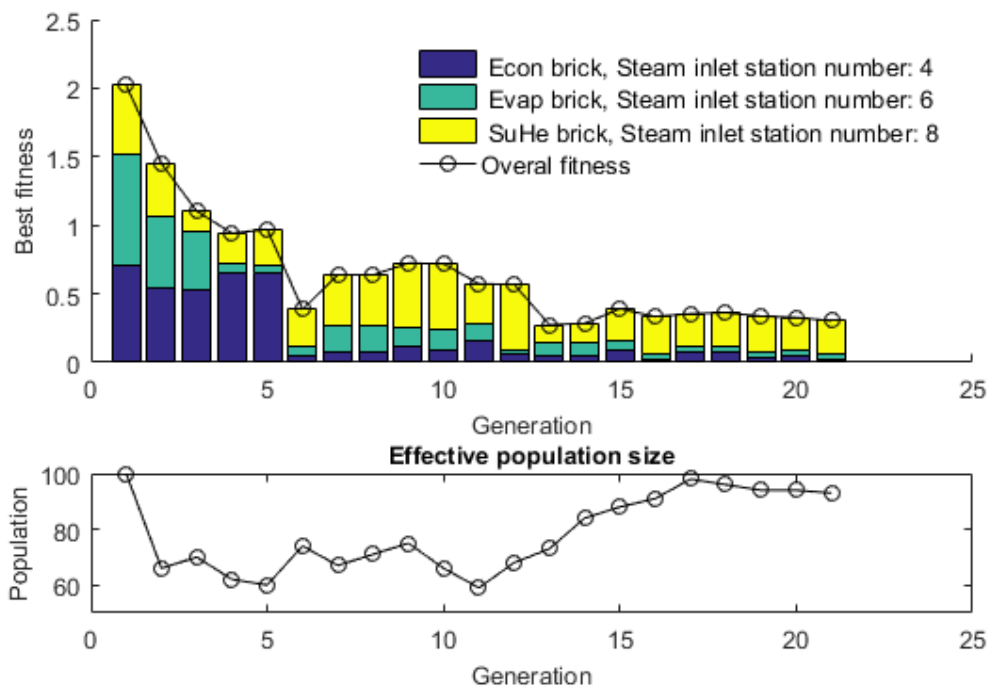
Fig. 5.6 Improved convergence of 100 individuals with smaller set of non-linear equations

5.4   Modelling results and validation

The results obtained from the genetic algorithm have been validated against the Ebsilon software. Each simulation trial is characterised with the gas turbine load reduced to 80%, which corresponds to an exhaust temperature of 637^oC and an exhaust mass flow of $500\frac{kg}{s}$, as shown in figure 6.17. The corresponding performance results are listed in table 5.1 for increasing population size from 50 to 800 individuals. The results clearly show the asymptotic behaviour of the solution approaching Ebsilon trial with increasing population size. With low population sizes the algorithm tends to converge at local minima, which for example is reflected with a large difference in $SuHe_{PP}$ between 50 and 100 individuals. With higher number of individuals in the population the accuracy of the solution improves; however, the computation time required is significantly prolonged. For example the solution obtained with Ebsilon required a fraction of the computational time as compared to the genetic algorithm with population of 800 individuals. The computational time can be improved by redesigning the architecture of the program; however, further action is out of the scope of the current work.

The results obtained with population $n = 800$ show good agreement with the validation trial. This confirms that the genetic algorithm is a good alternative method to existing techniques for off-design performance evaluation of CCPP, and obtaining a solution without a need for initial approximations, e.g. Newton-Raphson method discussed in appendix section A.3.

Table 5.1 Validation of results obtained with Genetic Algorithm at 80% gas turbine load for various population sizes against Ebsilon software

		Ebsilon	n=50	n=100	n=200	n=500	n=800
P_{live}	$[bar]$	100.11	89.78	92.77	96.67	98.01	98.12
$\dot{m}_s$	$[\frac{kJ}{kg}]$	69.64	66.59	67.97	69.08	70.49	70.4352
$Econ_{AP}$	$[^oC]$	0.00	0.00	0.00	0.00	0.00	0.00
$Evap_{PP}$	$[^oC]$	16.84	14.90	14.78	20.66	17.54	16.60
$SuHe_{PP}$	$[^oC]$	26.89	65.69	51.54	21.72	29.51	27.48
T_{live}	$[^oC]$	610.11	571.31	585.46	615.28	607.49	609.52
T_{stack}	$[^oC]$	158.84	167.31	165.87	169.62	165.51	163.99
η_s	$[]$	38.67	35.56	37.01	40.03	39.89	39.88
Q_{in}	$[MW]$	243.86	239.54	240.27	238.36	240.46	241.23
Q_{out}	$[MW]$	149.56	...	...	...	...	...
PO_s	$[MW]$	95.13	85.20	89.14	95.41	95.94	96.21
Fitness		N/A	0.7433	0.4196	0.3082	0.1385	0.0630
Generations		N/A	14	19	14	20	22

Pedro et al. studied the sensitivity of genetic algorithm parameters for the design of water distribution networks [66]. Although the application is different to the current study, the results obtained by Pedro et al. suggest that the success rate of convergence is highly dependent on the probabilities of cross-over and mutation. In the current study cross-over probability is 100%, and it is out of the scope to investigate the effect of a range of these probabilities on the converged solution. However, the sensitivity of mutation has been investigated further, with results shown in table 5.2. According to the results, if the probability of mutation is very low the algorithm seems to converge at local minima. For high probabilities of mutation, the algorithm is behaving as a random search for solution, which does not provide a stable convergence. The effect of mutation on diversity of converged population is shown in figure 5.7. According to the results, there is a case specific optimum at probability $P_m = 1\%$.

Table 5.2 Sensitivity of results to probability of mutation for population $n = 100$

	$P_m = 0\%$	$P_m = 0.5\%$	$P_m = 0.8\%$	$P_m = 1\%$	$P_m = 2\%$	$P_m = 3\%$	$P_m = 5\%$
$P_{live}[bar]$	110.00	92.77	89.74	100.12	99.06	102.21	103.71
$\dot{m}_s[\frac{kJ}{kg}]$	81.43	67.97	65.32	71.91	70.95	73.12	76.05
$T_{live}[^oC]$	573.42	585.46	593.25	609.08	612.34	614.01	584.47
$T_{stack}[^oC]$	167.42	165.87	164.33	163.96	164.27	164.91	159.75
$\eta_s[]$	43.09	37.01	36.11	40.64	40.04	41.72	40.06
$Q_{in}[MW]$	239.48	240.27	241.06	241.25	241.09	240.76	243.39
$PO_s[MW]$	103.20	89.14	87.06	98.05	97.36	100.46	98.87
Fitness	0.6336	0.4196	0.2970	0.1058	0.1357	0.1986	0.6815
Generations	25	19	31	20	21	26	15
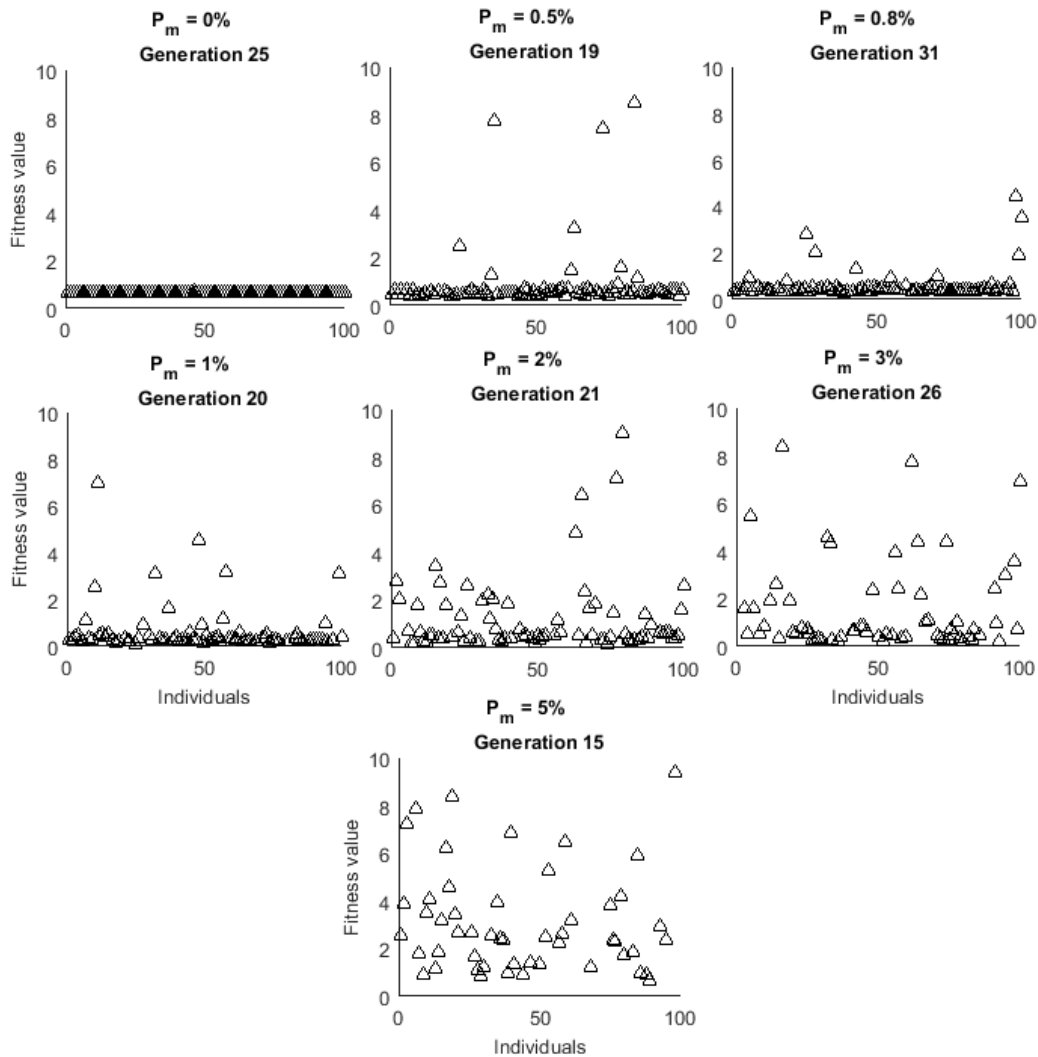
Fig. 5.7 Sensitivity of mutation on converged population diversity

5.5   Discussion

The new application of genetic algorithm to off-design modelling of CCPPs builds on the previous work of researchers discussed in section 2.3. Existing techniques, i.e. sequential or numerical methods, require formulation of initial guess of variables which makes analysing complex systems difficult. According to previous research (section 2.4.2), a genetic algorithm provides a promising alternative to existing techniques, in which a solution can be obtained without the need for initial approximations. The current work investigated the application of a genetic algorithm to the off-design performance mod-

elling of CCPPs.

In the existing techniques, a Law of Cones equation is commonly applied together with heat transfer and energy balance equations. The resulting system of non-linear equations is then solved for unknown variables. In the current work, it is demonstrated that the Law of Cones equation can be removed from the system of equations, which reduces complexity, computational time, and improves stability of progression of the solution (figure 5.6). Instead, the Law of Cones equation is applied in a steam turbine brick, which directly computes required steam mass flow rate, thus also removing the steam mass flow rate variable from the system of equations. A one pressure water/steam bottoming cycle has been analysed, and the results validated against the Ebsilon software. The results show good agreement with validated case. The sensitivity of population size and probability of mutation has been studied, with a conclusion that both have a significant effect on the accuracy of converged solution. With higher population size the results accuracy improves in asymptotic manner; however, at the expense of significantly increasing computational time. Varying the probability of mutation exposes an optimum value at which for given population size best solution can be obtained.

The results show that the genetic algorithm method is a good alternative technique to the Newton-Raphson method for solving a system of non-linear equations with an advantage of no initial approximation required. However, although it presents its own benefits, it has been concluded that the method does not outweigh the benefits of existing techniques. The computational time required to obtain a converged solution is significant, and although it could be improved in future work, it is unlikely that it will compete with the very fast Newton-Raphson computations. The system gets even more complex if multi-pressure CCPPs are modelled with or without reheat or supplemental firing. This conclusion led to the further development of the novel Direct Solution Method expanding its capabilities into off-design operational regime, which provides a simple solution without need for iterations.

Chapter 6

Direct Solution Method for steam cycle off-design performance simulation

The objective of this chapter is to demonstrate work done to further develop a Direct Solution Method (DSM) for off-design simulation of the water/steam bottoming cycle. The performance of a system in off-design is related to the design-point operation; therefore, the work discussed in this chapter builds on the results obtained in chapter 4. The structure of the CCPP off-design modelling follows the algorithm shown in figures 4.2 and 4.8, where the *mode3* is now equal to 3.

6.1   System description and assumptions

The detailed description of the thermodynamic system under analysis is discussed and presented in chapter 4. The overall description of the system also holds true for off-design analysis with four additional assumptions.

1. In order to avoid the computational burden of using detailed heat transfer calculations, Dechamps et.al [37] proposed that U^{OD} at part-load varies according to equation 6.1 with $\alpha = 0.52$ and $\beta = 0.31$.

$$U^{OD} = U^D \left(\frac{\dot{m}^{OD}}{\dot{m}^D}\right)^\alpha \left(\frac{\bar{T}^{OD}}{\bar{T}^D}\right)^\beta \tag{6.1}$$

2. The geometry of a heat exchanger at part-load varies such that $A^{OD} = \beta A^D$, where β is the degradation factor, e.g. effect of fouling or erosion. The current work assumes that $\beta = 1$, thus no degradation effect is taken into account; however, the DSM can be readily expanded to account for these effects.

3. Assuming that the flow has no bleed or leaks, $\dot{m}^{OD}_{s,out} = \dot{m}^{OD}_{s,in}$ and $\dot{m}^{OD}_{g,out} = \dot{m}^{OD}_{g,in}$.

4. The specific heats, Cp_g, are behaving according to equation A.9.

6.2   Heat transfer equation

The heat transfer is calculated with equation 6.2. This equation relates the thermodynamic state of a heat exchanger to its geometry.

$$\dot{Q}^{OD} = U^{OD} A \Delta T_{lm}^{OD} \tag{6.2}$$

Where ΔT_{lm} is calculated with equation 6.3, assuming that the heat exchanger is pure counter-flow type.

$$\Delta T_{lm}^{OD} = \frac{(T_{g,in}^{OD} - T_{s,out}^{OD}) - (T_{g,out}^{OD} - T_{s,in}^{OD})}{ln(\frac{T_{g,in}^{OD} - T_{s,out}^{OD}}{T_{g,out}^{OD} - T_{s,in}^{OD}})} \tag{6.3}$$

The overall heat transfer coefficient, U^{OD}, is used to combine the effects of convection and conduction thermal resistances in the path of heat flow. Assuming that the tube walls are thin and the thermal conductivity of the wall material is high, the U^{OD} can be calculated with equation 6.4. Where h is a convection heat transfer coefficient between water and gas sides. However, to avoid computational burden, the U^{OD} can be approximated with equation 6.1.

$$\frac{1}{U^{OD}} = \frac{1}{h_{water}} + \frac{1}{h_{gas}} \tag{6.4}$$

The steam bottoming cycle follows the operation of a gas turbine engine. When load is reduced, the heat transfer equation needs to be modified to reflect heat transfer state at part-load. Since the geometry of a heat exchanger does not change, such that $A^D = A^{OD}$, it can be used as a link to equate design and off-design performance equations.

$$\frac{\dot{Q}^D}{U^D \Delta T_{lm}^D} = \frac{\dot{Q}^{OD}}{U^{OD} \Delta T_{lm}^{OD}} \tag{6.5}$$

Rearranging as function of $\dot{Q}$ only

$$\frac{\dot{Q}^{OD}}{\dot{Q}^D} = \frac{U^{OD} \Delta T_{lm}^{OD}}{U^D \Delta T_{lm}^D} \tag{6.6}$$

6.3   Energy transfer equation

The energy transfer occurs in the direction from hot path exiting the gas turbine engine into water-steam in the bottoming cycle. The energy equations for gas and water-steam paths are calculated with 6.7.

$$\begin{cases} \dot{Q}^{OD} = \dot{m}_s^{OD}(h_{s,out}^{OD} - h_{s,in}^{OD}), & \text{for water/steam path} \\ \dot{Q}^{OD} = \dot{m}_g^{OD}(h_{g,in}^{OD} - h_{g,out}^{OD}), & \text{for gas path} \end{cases} \tag{6.7}$$

The mass flow rate equation, $\dot{m} = \rho V A$, relates properties of the fluid to a cross-sectional geometry of the flow passage. Therefore, the part load energy balance equation is formed by assuming that the cross-sectional geometry does not change at off-design, such that $A^{OD} = A^D$. Therefore, the energy equation is rearranged

$$\frac{\dot{Q}^D}{\rho^D V^D \Delta h^D} = \frac{\dot{Q}^{OD}}{\rho^{OD} V^{OD} \Delta h^{OD}} \tag{6.8}$$

Rearranging as a function of $\dot{Q}$ only

$$\frac{\dot{Q}^{OD}}{\dot{Q}^D} = \frac{\rho^{OD} V^{OD} \Delta h^{OD}}{\rho^D V^D \Delta h^D} \tag{6.9}$$

Multiplying right and left hand side by a constant $\frac{A^{OD}}{A^D} = 1$

$$\frac{\dot{Q}^{OD}}{\dot{Q}^D} = \frac{\dot{m}^{OD} \Delta h^{OD}}{\dot{m}^D \Delta h^D} \tag{6.10}$$

6.4   Formation of heat exchanger part-load equations

The heat and energy transfer equations 6.6 and 6.10 completely define a heat exchanger at off-design conditions. They relate heat transfer and energy balance to heat exchanger geometry. Therefore, equating equation 6.6 to equation 6.10 for gas path, and rearranging as function of T_{lm}

$$\frac{\dot{m}_g^{OD} \Delta h_g^{OD}}{\dot{m}_g^D \Delta h_g^D} = \frac{U^{OD} \Delta T_{lm}^{OD}}{U^D \Delta T_{lm}^D} \tag{6.11}$$

$$\frac{U^D \dot{m}_g^{OD} \Delta h_g^{OD}}{U^{OD} \dot{m}_g^D \Delta h_g^D} = \frac{\Delta T_{lm}^{OD}}{\Delta T_{lm}^D} \tag{6.12}$$

Equating equation 6.10 for gas and water/steam paths

$$\frac{\dot{m}_g^{OD} \Delta h_g^{OD}}{\dot{m}_g^D \Delta h_g^D} = \frac{\dot{m}_s^{OD} \Delta h_s^{OD}}{\dot{m}_s^D \Delta h_s^D} \tag{6.13}$$

The average mass flow is taken into consideration to allow for accounting any bleed or leak flows. Assuming that enthlapy of gas varies as function of temperature, $\Delta h = Cp\Delta T$, and rearranging equations 6.12 and 6.13

$$
\begin{cases}
F_1^{OD} = \dfrac{\Delta T_{lm}^{OD}}{\Delta T_{lm}^{D}} - \dfrac{U^D}{U^{OD}} \dfrac{\frac{\dot{m}_{g,in}^{OD}+\dot{m}_{g,out}^{OD}}{2} Cp_{g,avg}^{OD}}{\frac{\dot{m}_{g,in}^{D}+\dot{m}_{g,out}^{D}}{2} Cp_{g,avg}^{D}} \dfrac{(T_{g,in}^{OD}-T_{g,out}^{OD})}{(T_{g,in}^{D}-T_{g,out}^{D})} = 0 & \text{(6.14a)} \\[4ex]
F_2^{OD} = \dfrac{\frac{\dot{m}_{g,in}^{OD}+\dot{m}_{g,out}^{OD}}{2}Cp_{g,avg}^{OD}(T_{g,in}^{OD}-T_{g,out}^{OD})}{\frac{\dot{m}_{g,in}^{D}+\dot{m}_{g,out}^{D}}{2}Cp_{g,avg}^{D}(T_{g,in}^{D}-T_{g,out}^{D})} - \dfrac{\frac{\dot{m}_{s,in}^{OD}+\dot{m}_{s,out}^{OD}}{2}(h_{s,out}^{OD}-h_{s,in}^{OD})}{\frac{\dot{m}_{s,in}^{D}+\dot{m}_{s,out}^{D}}{2}(h_{s,out}^{D}-h_{s,in}^{D})} = 0 & \text{(6.14b)}
\end{cases}
$$

A set of two equations 6.14a and 6.14b completely define a heat exchanger at off-design conditions. It must be noted that this arrangement of equations provides great advantage to modelling off-design conditions as F_1^{OD} is a function of temperature profile, heat transfer coefficient, and $\dot{m}_g$. Whereas, F_2^{OD} is a function of temperature profile, $\dot{m}_g$ and $\dot{m}_s$. Given that design point calculations provide Station Vector values at the inlet and outlet of a heat exchanger together with the heat transfer coefficient, and inlet parameters are known at off-design, the outlet parameters at off-design can be calculated. Separating $\dot{m}_s$ in F_2^{OD} allows the decoupling of the temperature profile from the steam mass flow calculations.

The shape of the F_1^{OD} and F_2^{OD} functions is irrelevant, as only an intersection of these two functions provides a solution to the problem. However, before this is done further modifications to the equations are needed. The F_1 function in equation 6.14a is rearranged, and design point variables are grouped together into constants X, Y and Z.

$$
F_1^{OD} = \frac{\Delta T_{lm}^{OD}}{X} - \frac{Y}{U^{OD}}\frac{\frac{\dot{m}_{g,in}^{OD}+\dot{m}_{g,out}^{OD}}{2}Cp_{g,avg}^{OD}(T_{g,in}^{OD}-T_{g,out}^{OD})}{Z} = 0
$$

$$
\boxed{F_1^{OD} = \Delta T_{lm}^{OD} - \frac{XY}{Z}\left[\frac{\frac{\dot{m}_{g,in}^{OD}+\dot{m}_{g,out}^{OD}}{2}Cp_{g,avg}^{OD}(T_{g,in}^{OD}-T_{g,out}^{OD})}{U^{OD}}\right] = 0} \qquad \text{(6.15)}
$$

Where

$$
X = \Delta T_{lm}^{D} \qquad\qquad\qquad \text{(6.16)}
$$

$$
Y = U^D \qquad\qquad\qquad \text{(6.17)}
$$

$$
Z = \frac{\dot{m}_{g,in}^{D}+\dot{m}_{g,out}^{D}}{2}Cp_{g,avg}^{D}(T_{g,in}^{D}-T_{g,out}^{D}) \qquad\qquad \text{(6.18)}
$$

Then function F_2 in equation 6.14b is rearranged, and design point variables are grouped together with additional constant K.

$$
F_2^{OD} = \frac{\frac{\dot{m}_{g,in}^{OD}+\dot{m}_{g,out}^{OD}}{2}Cp_{g,avg}^{OD}(T_{g,in}^{OD}-T_{g,out}^{OD})}{Z} - \frac{\frac{\dot{m}_{s,in}^{OD}+\dot{m}_{s,out}^{OD}}{2}(h_{s,out}^{OD}-h_{s,in}^{OD})}{K} = 0
$$

$$F_2^{OD} = \frac{\dot{m}_{g,in}^{OD} + \dot{m}_{g,out}^{OD}}{2} Cp_{g,avg}^{OD}(T_{g,in}^{OD} - T_{g,out}^{OD}) - \frac{Z}{K}\left[\frac{\dot{m}_{s,in}^{OD} + \dot{m}_{s,out}^{OD}}{2}(h_{s,out}^{OD} - h_{s,in}^{OD})\right] = 0$$

(6.19)

Where

$$K = \frac{\dot{m}_{s,in}^D + \dot{m}_{s,out}^D}{2}(h_{s,out}^D - h_{s,in}^D)$$

(6.20)

The solution that will satisfy both functions is obtained by equating $F_1 = F_2$ in equations 6.15 and 6.19, where design point constants have further been grouped together into constants C_1 and C_2.

$$\dot{m}_s^{OD} = C_1\left[\frac{\dot{m}_g^{OD}Cp_g^{OD}\Delta T_g^{OD}}{\Delta h_s^{OD}} - \frac{\Delta T_{lm}^{OD}}{\Delta h_s^{OD}}\right] + C_2\left[\frac{\dot{m}_g^{OD}Cp_g^{OD}\Delta T_g^{OD}}{U^{OD}\Delta h_s^{OD}}\right]$$

(6.21)

Or

$$\dot{m}_g^{OD} = \frac{U^{OD}(\dot{m}_s^{OD}\Delta h_s^{OD} + C_1\Delta T_{lm}^{OD})}{Cp_g^{OD}\Delta T_g^{OD}(C_1 U^{OD} + C_2)}$$

(6.22)

Where

$$C_1 = \frac{K}{Z}$$

(6.23)

$$C_2 = \frac{KXY}{Z^2}$$

(6.24)

Equation 6.21 is called the *Steam Flow Curve*, and it represents the amount of steam mass flow rate required to sustain the temperature profile of a heat exchanger at off-design conditions. Arranging the equations in this particular way provides an advantage to be able to obtain a solution without the need for iterations. Equation 6.15 is called the *Temperature Profile Curve*, and it represents the gas and water/steam inlet and outlet temperatures. These two equations fully describe performance of shell-and-tube heat exchanger operated at off-design.

Since the economiser, evaporator and superheater vary in operation, they are considered separately in the following sections. However, all heat exchangers regardless of their operational requirements can be investigated with the above derived equations. In each case the solution can be obtained using the Direct Solution Method, in two possible ways: 1) evaluate steam mass flow rate needed to sustain the required temperature profile, or 2) evaluate the temperature profile needed to sustain required steam mass flow rate. The general procedure below can be inverted to calculate required temperature profile if steam mass flow rate is known.

1. The design point operation Station Vectors, and off-design inlet conditions, $T_{g,in}^{OD}$, $\dot{m}_g^{OD}$, and $T_{s,in}^{OD}$ must be known.

2. A range of $T_{s,out}^{OD}$ is evaluated with lower and upper limits of $T_{s,in}^{OD}$ and $T_{g,in}^{OD}$, respectively. Each $T_{s,out}^{OD}$ is used in F_1^{OD} function, equation 6.15, and a corresponding values of $T_{g,out}^{OD}$ are obtained.

3. At this stage, with known temperature profile, $\dot{m}_s^{OD}$ is calculated with equation 6.21

6.4.1   Explicit formulation for gas outlet temperature

Notably, the steam mass flow equation has been derived into its explicit form, however the form of F_1^{OD} is implicit. Since the outlet temperatures are inside the logarithmic function, it is difficult to extract it into an explicit formulation. Alternatively, the outlet temperatures of either water/steam or gas could be evaluated using bisection method. However, it would be convenient if the $T_{g,out}$ in function F_1^{OD} could also be expressed in explicit terms. This has been investigated by applying the Taylor series to transform F_1^{OD} into a polynomial form, and then solve for $T_{g,out}$ explicitly. The equation 6.15 is rearranged, and a variable C_4 is introduced, such that

$$\Delta T_{lm}^{OD} = C_4(T_{g,in}^{OD} - T_{g,out}^{OD}) \tag{6.25}$$

Where

$$C_4 = \frac{XY\dot{m}_{g,out}^{OD}Cp_{g,avg}^{OD}}{ZU^{OD}} \tag{6.26}$$

Expanding the LMTD term

$$\frac{(T_{g,in}^{OD} - T_{s,out}^{OD}) - (T_{g,out}^{OD} - T_{s,in}^{OD})}{A} = C_4T_{g,in}^{OD} - C_4T_{g,out}^{OD} \tag{6.27}$$

Where

$$A = ln(\frac{T_{g,in}^{OD} - T_{s,out}^{OD}}{T_{g,out}^{OD} - T_{s,in}^{OD}}) \tag{6.28}$$

The term A represents the logarithmic function, which must be modified to allow for Taylor series expansion of the form shown in equation 6.29

$$log(x+1) = -\sum_{n=1}^{\infty} \frac{(-1)^n x^n}{n}, \quad \text{for } |x| < 1 \tag{6.29}$$

Modifying the *A* term

In order satisfy the $|x| < 1$ requirement in equation 6.29, each term in A must be divided by $T_{g,in}^{OD}$

$$A = ln\left(\frac{1 - \frac{T_{s,out}^{OD}}{T_{g,in}^{OD}}}{\frac{T_{g,out}^{OD} - T_{s,in}^{OD}}{T_{g,in}^{OD}}}\right) \qquad (6.30)$$

applying logarithmic property

$$log(1 - \frac{T_{s,out}^{OD}}{T_{g,in}^{OD}}) - log(\frac{T_{g,out}^{OD} - T_{s,in}^{OD}}{T_{g,in}^{OD}}) \qquad (6.31)$$

adding and subtracting 1 inside the second logarithm

$$log(1 - \frac{T_{s,out}^{OD}}{T_{g,in}^{OD}}) - log(\underbrace{\frac{T_{g,out}^{OD} - T_{s,in}^{OD}}{T_{g,in}^{OD}} - 1}_{\text{x term in Taylor series}} + 1) \qquad (6.32)$$

rewriting the equation in terms of *x*

$$A = log(1 - \frac{T_{s,out}^{OD}}{T_{g,in}^{OD}}) - log(x + 1) \qquad (6.33)$$

Where

$$x = \frac{T_{g,out}^{OD} - T_{s,in}^{OD}}{T_{g,in}^{OD}} - 1 = \frac{T_{g,out}^{OD} - T_{g,in}^{OD} - T_{s,in}^{OD}}{T_{g,in}^{OD}} \qquad (6.34)$$

Equation 6.33 has been arranged in this particular form to separate the $T_{g,out}^{OD}$ into the *x* term and allow for Taylor series expansion.

Further derivation of the F_1^{OD} function

Once the *A* term is modified, further rearranging equation 6.27

$$AC_4 T_{g,in}^{OD} - AC_4 T_{g,out}^{OD} = T_{g,in}^{OD} - T_{s,out}^{OD} - T_{g,out}^{OD} + T_{s,in}^{OD} \qquad (6.35)$$

rearranging the right hand side and dividing all terms by $T_{g,in}^{OD}$ to express it as function of *x*

$$AC_4 - AC_4 \frac{T_{g,out}^{OD}}{T_{g,in}^{OD}} = -\underbrace{\frac{T_{g,out}^{OD} - T_{g,in}^{OD} - T_{s,in}^{OD}}{T_{g,in}^{OD}}}_{\text{x term}} - \frac{T_{s,in}^{OD}}{T_{g,in}^{OD}} \qquad (6.36)$$

the $T_{g,out}^{OD}$ term in the left side needs to be expressed as x. Therefore, adding $AC_4 \frac{T_{g,in}^{OD}}{T_{g,in}^{OD}}$ and $AC_4 \frac{T_{s,in}^{OD}}{T_{g,in}^{OD}}$ to both sides of the equation

$$AC_4 - AC_4 \frac{T_{g,out}^{OD}}{T_{g,in}^{OD}} + AC_4 \frac{T_{g,in}^{OD}}{T_{g,in}^{OD}} + AC_4 \frac{T_{s,in}^{OD}}{T_{g,in}^{OD}} = -x - \frac{T_{s,in}^{OD}}{T_{g,in}^{OD}} + AC_4 \frac{T_{g,in}^{OD}}{T_{g,in}^{OD}} + AC_4 \frac{T_{s,in}^{OD}}{T_{g,in}^{OD}} \quad (6.37)$$

factoring out the x term in the left side of the equation, and cancelling equal terms

$$\cancel{AC_4} - AC_4 \underbrace{\left(\frac{T_{g,out}^{OD} - T_{g,in}^{OD} - T_{s,in}^{OD}}{T_{g,in}^{OD}} \right)}_{\text{x term}} = -x - \frac{T_{s,in}^{OD}}{T_{g,in}^{OD}} + AC_4 \cancel{\frac{T_{g,in}^{OD}}{T_{g,in}^{OD}}} + AC_4 \frac{T_{s,in}^{OD}}{T_{g,in}^{OD}} \quad (6.38)$$

rearranging the terms and substituting A

$$-C_4 x \left[log(1 - \frac{T_{s,out}^{OD}}{T_{g,in}^{OD}}) - log(x+1) \right] - C_4 \frac{T_{s,in}^{OD}}{T_{g,in}^{OD}} \left[log(1 - \frac{T_{s,out}^{OD}}{T_{g,in}^{OD}}) - log(x+1) \right] = -x - \frac{T_{s,in}^{OD}}{T_{g,in}^{OD}}$$
$$(6.39)$$

expanding

$$-C_4 x log(1 - \frac{T_{s,out}^{OD}}{T_{g,in}^{OD}}) + C_4 x log(x+1) - C_4 \frac{T_{s,in}^{OD}}{T_{g,in}^{OD}} log(1 - \frac{T_{s,out}^{OD}}{T_{g,in}^{OD}})$$
$$+ C_4 \frac{T_{s,in}^{OD}}{T_{g,in}^{OD}} log(x+1) = -x - \frac{T_{s,in}^{OD}}{T_{g,in}^{OD}} \quad (6.40)$$

moving all x terms to the right hand side and factoring

$$x + log(x+1) \left(C_4 x + C_4 \frac{T_{s,in}^{OD}}{T_{g,in}^{OD}} \right) - C_4 log(1 - \frac{T_{s,out}^{OD}}{T_{g,in}^{OD}}) x$$
$$= C_4 \frac{T_{s,in}^{OD}}{T_{g,in}^{OD}} log(1 - \frac{T_{s,out}^{OD}}{T_{g,in}^{OD}}) - \frac{T_{s,in}^{OD}}{T_{g,in}^{OD}} \quad (6.41)$$

factoring out the x terms

$$\left[1 - C_4 log(1 - \frac{T_{s,out}^{OD}}{T_{g,in}^{OD}}) \right] x + log(x+1) \left(C_4 x + C_4 \frac{T_{s,in}^{OD}}{T_{g,in}^{OD}} \right)$$
$$= C_4 \frac{T_{s,in}^{OD}}{T_{g,in}^{OD}} log(1 - \frac{T_{s,out}^{OD}}{T_{g,in}^{OD}}) - \frac{T_{s,in}^{OD}}{T_{g,in}^{OD}} \quad (6.42)$$

applying Taylor series expansion according to equation 6.29

$$\left[1 - C_4 log(1 - \frac{T_{s,out}^{OD}}{T_{g,in}^{OD}})\right]x$$

$$+\left(C_4 x + C_4 \frac{T_{s,in}^{OD}}{T_{g,in}^{OD}}\right)x - \frac{1}{2}\left(C_4 x + C_4 \frac{T_{s,in}^{OD}}{T_{g,in}^{OD}}\right)x^2 + \frac{1}{3}\left(C_4 x + C_4 \frac{T_{s,in}^{OD}}{T_{g,in}^{OD}}\right)x^3 - (\dots) \quad (6.43)$$

$$= C_4 \frac{T_{s,in}^{OD}}{T_{g,in}^{OD}} log(1 - \frac{T_{s,out}^{OD}}{T_{g,in}^{OD}}) - \frac{T_{s,in}^{OD}}{T_{g,in}^{OD}}$$

expanding the x terms

$$\left[1 - C_4 log(1 - \frac{T_{s,out}^{OD}}{T_{g,in}^{OD}})\right]x$$

$$+\left(C_4 x^2 + C_4 \frac{T_{s,in}^{OD}}{T_{g,in}^{OD}}x\right) - \frac{1}{2}\left(C_4 x^3 + C_4 \frac{T_{s,in}^{OD}}{T_{g,in}^{OD}}x^2\right) + \frac{1}{3}\left(C_4 x^4 + C_4 \frac{T_{s,in}^{OD}}{T_{g,in}^{OD}}x^3\right) - (\dots) \quad (6.44)$$

$$= C_4 \frac{T_{s,in}^{OD}}{T_{g,in}^{OD}} log(1 - \frac{T_{s,out}^{OD}}{T_{g,in}^{OD}}) - \frac{T_{s,in}^{OD}}{T_{g,in}^{OD}}$$

grouping together x terms

$$\left[1 - C_4 log(1 - \frac{T_{s,out}^{OD}}{T_{g,in}^{OD}})\right]x + \left(C_4 + \frac{1}{2}C_4 \frac{T_{s,in}^{OD}}{T_{g,in}^{OD}}\right)x^2 - \left(C_4 + \frac{1}{3}C_4 \frac{T_{s,in}^{OD}}{T_{g,in}^{OD}}\right)x^3 + (\dots)$$

$$= C_4 \frac{T_{s,in}^{OD}}{T_{g,in}^{OD}} log(1 - \frac{T_{s,out}^{OD}}{T_{g,in}^{OD}}) - \frac{T_{s,in}^{OD}}{T_{g,in}^{OD}} \quad (6.45)$$

equation 6.45 reveals the series of x terms, which can be generally expressed as

$$\boxed{\begin{aligned} (1 + C_4 \frac{T_{s,in}^{OD}}{T_{g,in}^{OD}} - C_4 log(1 - \frac{T_{s,out}^{OD}}{T_{g,in}^{OD}}))x + C_4 \sum_{n=2}^{\infty}(-1)^n \left[\frac{1}{n-1} - \frac{T_{s,in}^{OD}}{T_{g,in}^{OD}}\frac{1}{n}\right]x^n \\ = C_4 \frac{T_{s,in}^{OD}}{T_{g,in}^{OD}} log(1 - \frac{T_{s,out}^{OD}}{T_{g,in}^{OD}}) - \frac{T_{s,out}^{OD}}{T_{g,in}^{OD}} \end{aligned}} \quad (6.46)$$

Where

$$x = \frac{T_{g,out}^{OD} - T_{s,in}^{OD}}{T_{g,in}^{OD}} \quad (6.47)$$

$$C_4 = \frac{XY}{Z} \frac{\dot{m}_{g,out}^{OD} Cp_{g,avg}^{OD}}{U^{OD}} \tag{6.48}$$

Investigation into the sensitivity of results on the n-terms in equation 6.46 is shown in figure 6.1 for an arbitrary set of variables. According to the figure, for a given heat exchanger operation higher number of n-terms reduces the relative error of the solution. However, other terms being equal, higher $T_{s,in}^{OD}$ requires a larger number of n-terms to achieve unchanged relative error in the solution. Abel's impossibility theorem states that there is no algebraic solution for polynomials with degrees higher or equal to 5. For a quadratic polynomial equation, e.g. $n = 4$, an explicit solution can be obtained for $T_{g,out}$. However, according to figure 6.1 a large relative error is obtained for $n = 4$, which increases even further if steam inlet temperature is increased. Therefore, equation 6.46 is not used in the current work. However, it is included herein to stimulate further research study to modify equation 6.46 into an explicit formulation of $T_{g,out}$.
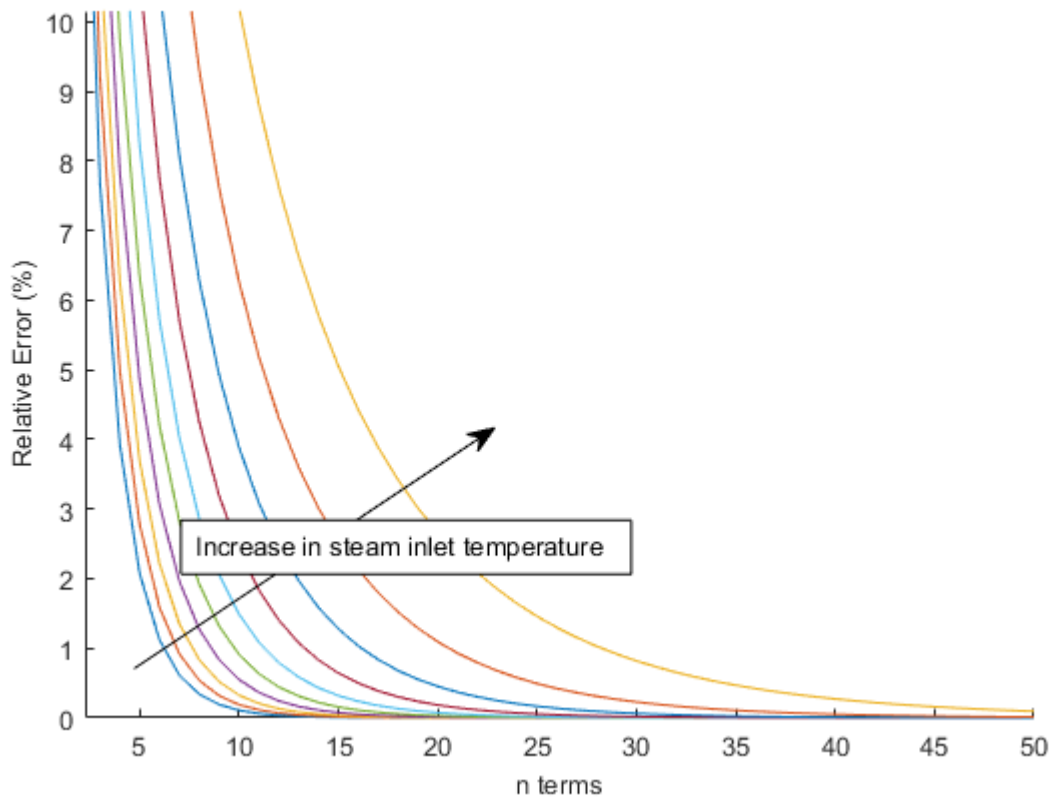
Fig. 6.1 The error of polynomial representation of function F_1^{OD}

6.5 Economiser analysis

The economiser Local Station Vectors are summarised in table 6.1.

Table 6.1 Economiser Station Vector values

Variable	Inlet at Design	Outlet at Design	Inlet at Off-Design
$T_s[°C]$	36	310	Variable
$P_s[bar]$	112	112	Function of $T_{s,in}^{OD}$
$h_s[\frac{kJ}{kg}]$	151	1400	Variable
$\dot{m}_s[\frac{kg}{s}]$	80	80	Variable
$T_g[°C]$	340	190	340 to 290
$\dot{m}_g[\frac{kg}{s}]$	654	654	Variable

The residuals of functions F_1^{OD} and F_2^{OD} are shown in figure 6.2. The $T_{s,out}^{OD}$ is varied from $T_{s,in}^{OD}$ to $T_{g,in}^{OD}$, and corresponding $T_{g,out}^{OD}$ is evaluated according to equations 6.14a and 6.14a for given inlet conditions. The overall heat transfer coefficient, U^D is assumed to be 50. Whereas, the U^{OD} is calculated with equation 6.1. The constant specific heats, Cp_g, is calculated with equation A.9.

The best solution is obtained along the zero-line where the residual is zero, and further away the solution is from the zero-line the larger the error in the result. The shape of these functions changes depending on the inlet conditions, however, it is only the intersection between F_1^{OD} and F_2^{OD} that is of interest. At the intersection point a solution is obtained that satisfies energy and heat transfer balance equations. A unique solution exists, where a set of $T_{g,out}^{OD}$ and $T_{s,out}^{OD}$ are determined for given input Station Vectors.

The effect of varying $\dot{m}_g^{OD}$, and $\dot{m}_s^{OD}$ on the shape of the zero-line is shown in figure 6.3. For an unchanged value of $T_{s,out}^{OD}$ the heat demanded by the water to satisfy the required Δh_s^{OD} remains constant. Therefore any attempt to reduce $\dot{m}_g$ will be balanced by an increase in $T_{g,out}^{OD}$ in function F_1^{OD}. The increase of $\dot{m}_s^{OD}$ in function F_2^{OD}, however, results in a higher heat demand by the water to achieve the same $T_{s,out}^{OD}$. Consequently, this rise in heat demand needs to be satisfied by increased heat supplied by the gas, resulting in lower $T_{g,out}^{OD}$.

For given inlet conditions and $\dot{m}_g^{OD}$, the intersection points for various $\dot{m}_s^{OD}$ values are shown in figure 6.4. According to the figure in the low $\dot{m}_s^{OD}$ region of intersection, a large change in $T_{g,out}^{OD}$ is required to achieve a small change in $T_{s,out}^{OD}$. This is because the heat transfer must occur in the direction from gas to water in this application, which imposes a limitation of water outlet temperature that asymptotically approaches gas inlet temperature with decreasing water mass flow. This phenomenon is understood to be important
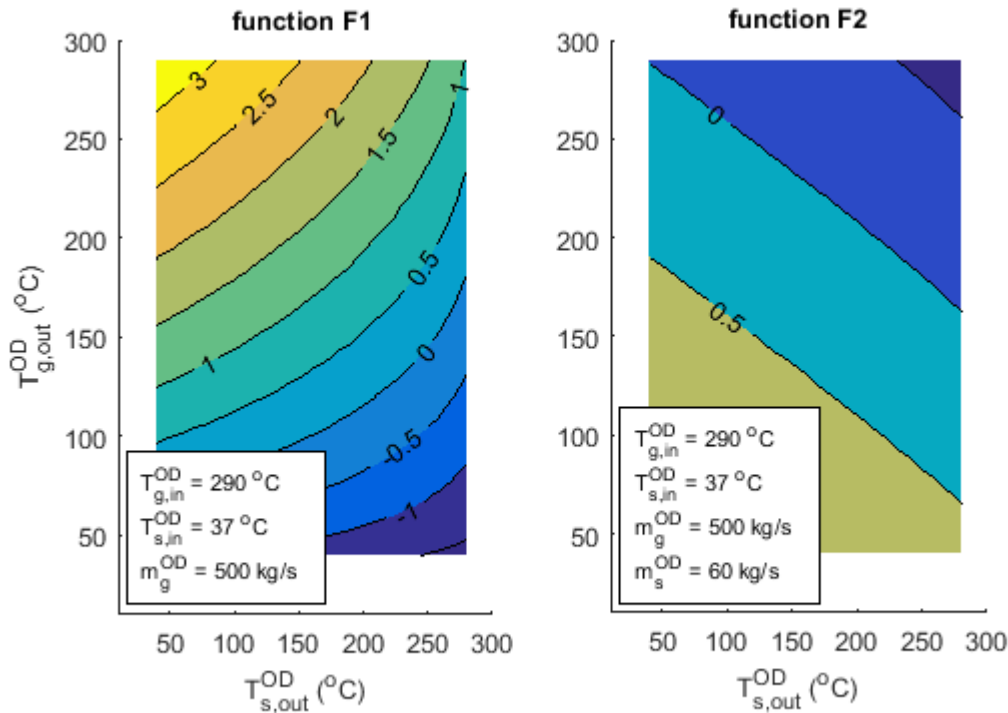
Fig. 6.2 Economiser contour plots of F1 and F2 function residuals

in the part load operation of a heat exchanger as it describes the lower limit region for the steam mass flow. This has led to establishing a term *Heat Demand Saturation State*, which is defined herein as:

> The Heat Demand Saturation State is defined as the state of a heat exchanger in which, all other terms being equal, a sufficiently small water/steam mass flow at off-design operation will require a large change in gas outlet temperature to achieve a marginal change in water/steam outlet temperature. If a heat exchanger operates at this state, it is understood to be saturated with heat demand by water/steam and is consequently not utilising the heat supply very efficiently at the expense of low water/steam mass flow.

It is important to note that the heat exchanger size is already accounted for in the design point calculations, which is unchanged in off-design simulations. Therefore, a low water/steam mass flow could be achieved at off-design operation leading to more efficient heat transfer, however this could lead to an unacceptably low power output from the steam turbine.

In the high $\dot{m}_s^{OD}$ region of figure 6.4, the gas outlet temperature asymptotically approaches $T_{s,in}^{OD}$. Since the specific heat capacity of water is much higher than that of gas, it
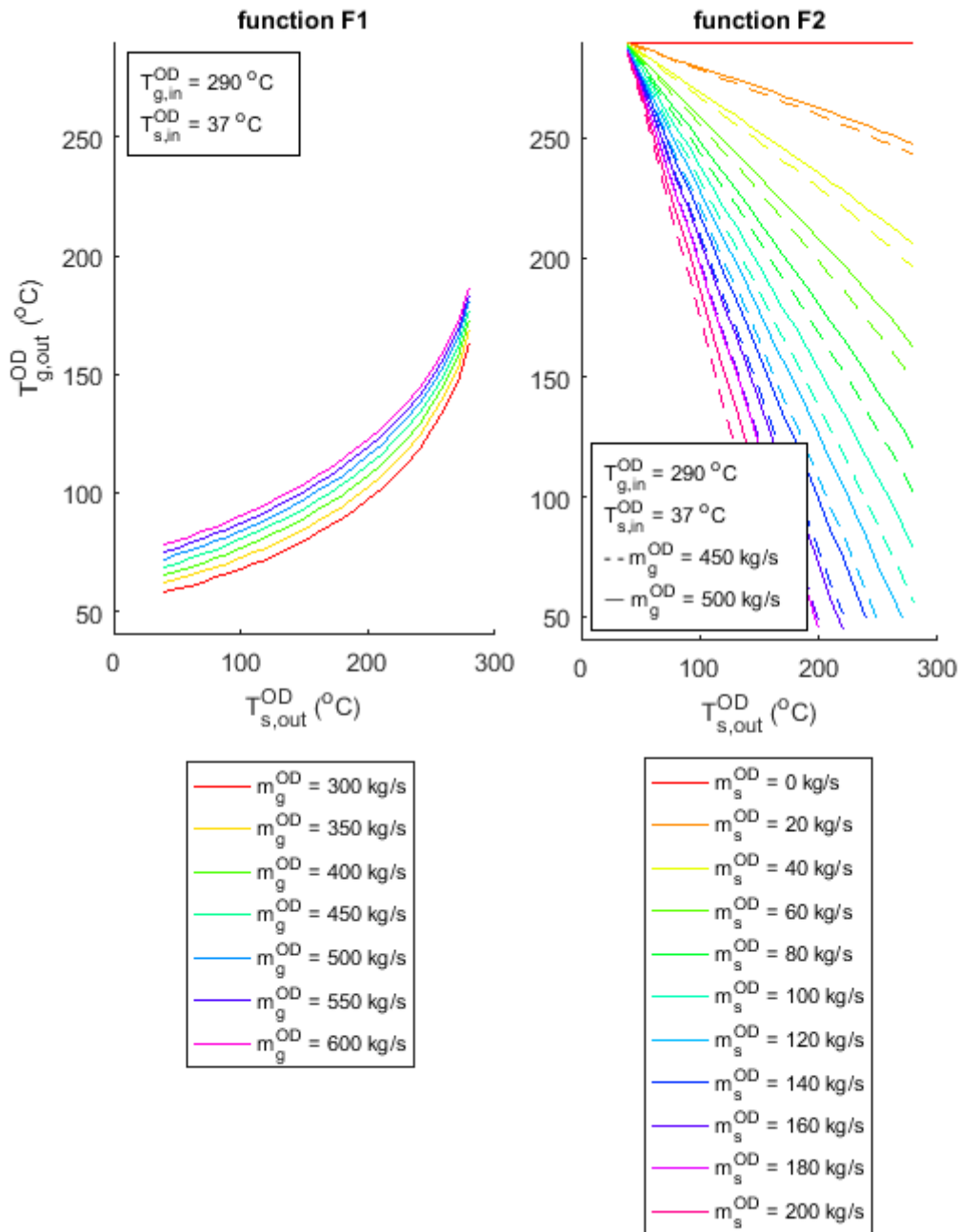
Fig. 6.3 Zero-lines plot of F1 and F2 functions

requires more energy to achieve the same change in temperature. Consequently, as $\dot{m}_s^{OD}$ is increased, the $T_{s,out}^{OD}$ will drop much faster then $T_{g,out}^{OD}$. Therefore, the heat exchanger is

understood to be in the *Heat Supply Saturation State*, which is defined herein as:

> The Heat Supply Saturation State is defined as the state of a heat exchanger in which, all other terms being equal, a sufficiently large water/steam mass flow at off-design operation will require a marginal change in gas outlet temperature to achieve large change in water/steam outlet temperature. If a heat exchanger operates at this state, it is understood to be saturated with heat supply from the gas and is consequently utilising the heat supply very efficiently.

Consequently, the upper limit of water/steam mass flow is determined by the flow capacity of a steam turbine.

The water/steam mass flow curves are shown in figure 6.5, where $\dot{m}_s^{OD}$ is calculated with equation 6.21. The Heat Demand and Heat Supply Saturation States are clearly visible at very high and very low $\dot{m}_s^{OD}$ values, respectively.
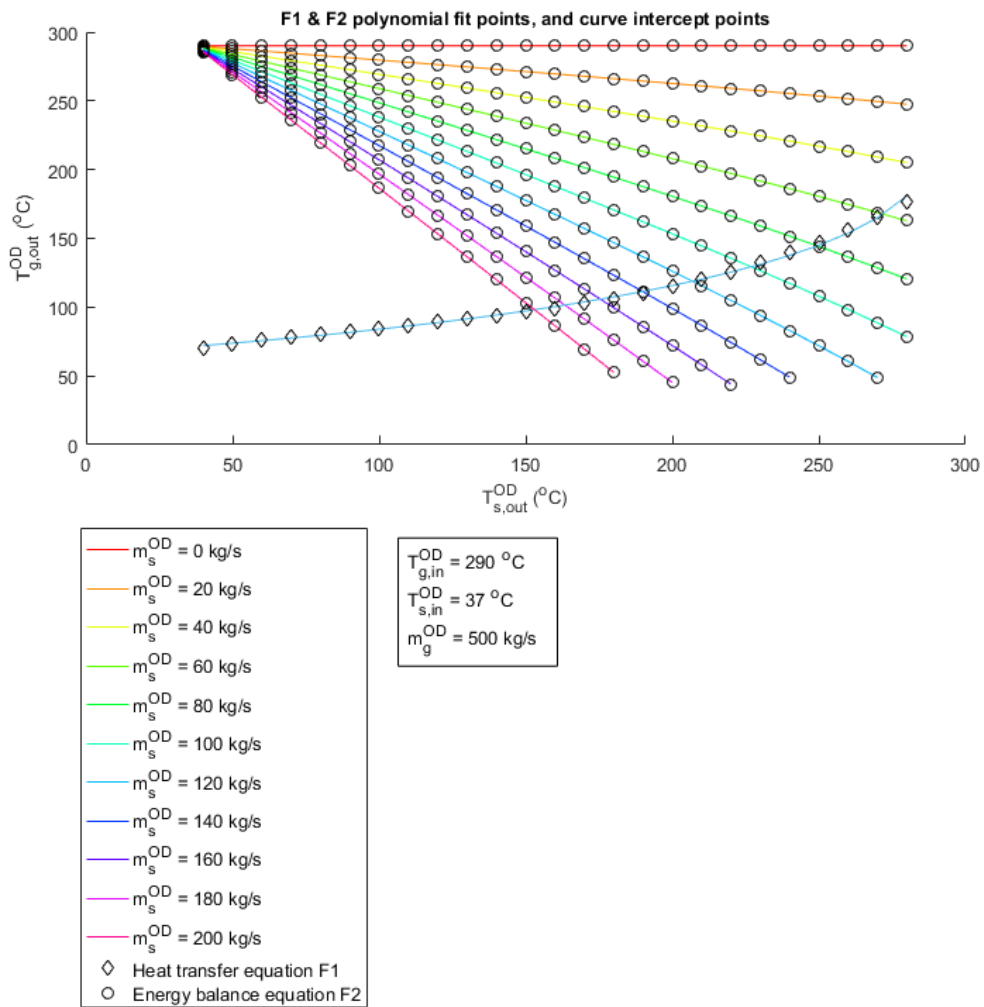
Fig. 6.4 Intersection of F1 and F2 functions
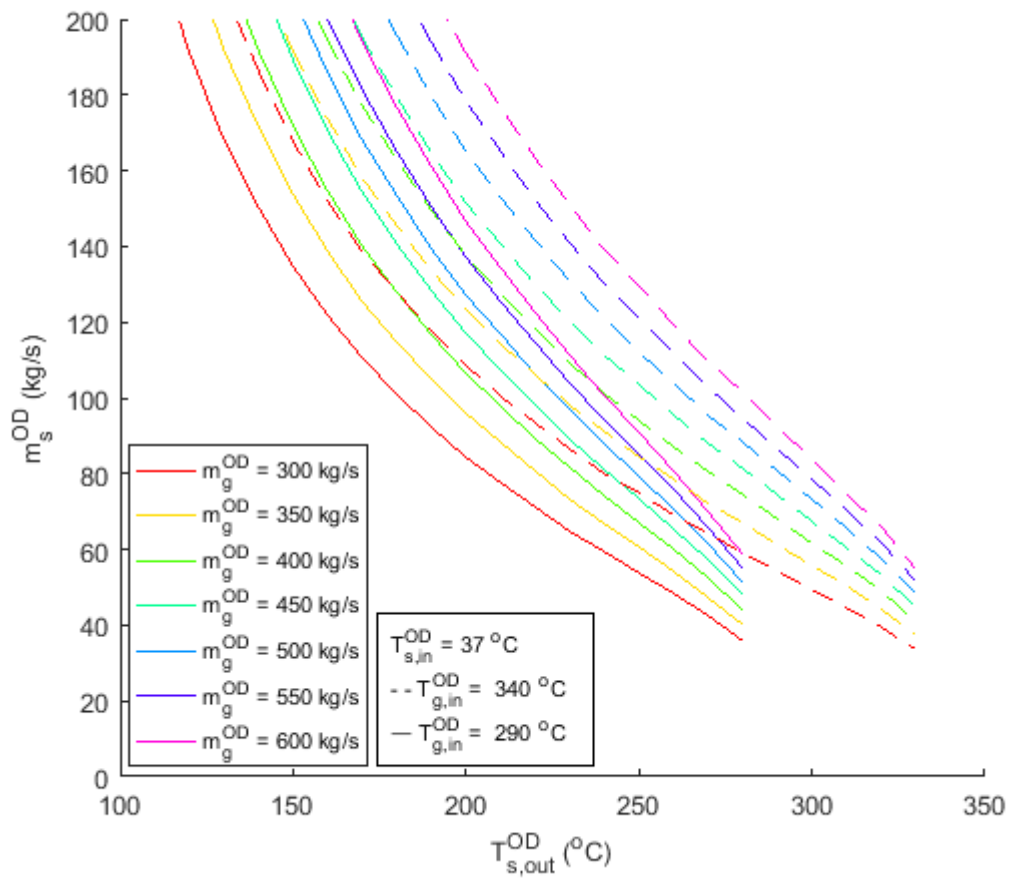
Fig. 6.5 Economiser steam mass flow curve

6.6   Evaporator analysis

The evaporator Local Station Vectors are summarised in table 6.2.

Table 6.2 Evaporator Station Vector values

Variable	Inlet at Design	Outlet at Design	Inlet at Off-Design
$T_s[^\circ C]$	320	320	Variable
$P_s[bar]$	112	112	Function of T_s^{OD}
$h_s[\frac{kJ}{kg}]$	1400	2698	Variable
$\dot{m}_s[\frac{kg}{s}]$	80	80	Variable
$T_g[^\circ C]$	500	340	500 and 450
$\dot{m}_g[\frac{kg}{s}]$	654	654	Variable

In real evaporators, the temperature at the inlet is below saturation temperature, and outlet is in water/steam mixture state where water part is recirculated. Any inlet temperature below saturation can be used and results can be simulated with the DS method. However, for simplicity and concept demonstration the analysis is done at $T_{s,out}^{OD} = T_{s,in}^{OD}$, which is referred to as T_s^{OD}.

Assuming that the inlet water into the evaporator is in a saturation state, the $h_{s,in}^{OD}$ and $S_{s,in}^{OD}$ are calculated with equations A.1 and A.2, respectively. Assuming that the evaporator outlet steam quality is 100% vapour, $h_{s,out}^{OD}$ and $S_{s,out}^{OD}$ are calculated with equations A.3 and A.4, respectively. The pressure of the evaporator is calculated with equation A.5. The $\dot{m}_{s,in}^{OD}$ is varied from $0\frac{kg}{s}$ to $200\frac{kg}{s}$ in increments of $20\frac{kg}{s}$. The $\dot{m}_{g,in}^{OD}$ is varied from $600\frac{kg}{s}$ to $250\frac{kg}{s}$ in increments of $50\frac{kg}{s}$. The overall heat transfer coefficient, U^D, is assumed to be 50. Whereas, the U^{OD} is calculated with equation 6.1.

The residual results of plotting functions F_1^{OD} and F_2^{OD} are shown in figure 6.6. The direction of heat transfer is from gas to water/steam, consequently function F_1^{OD} shows the absence of data points for $T_{g,out}^{OD} \leq T_s^{OD}$. The F_1 and F_2 contour lines represent the variation in evaporator off-design outlet conditions, where the zero-lines represents direct solution with zero residual. The $T_{s,out}^{OD}$ is varied between 10^oC and $374.15^\circ C$, above which there is no change of state where liquid and vapour are indistinguishable.

Similarly to the results obtained for the economiser, the contour lines can be used to illustrate efficiency in convergence of iterative algorithms, e.g. Newton-Raphson or Genetic Algorithm. The closer a solution is to the zero-line the smaller is the residual and more accurate are the results. The shape of the zero-line is characterised by design point performance and off-design inlet conditions of the heat exchanger. It is therefore, of interest to analyse parametrically the influence of inlet conditions on the shape and shift of
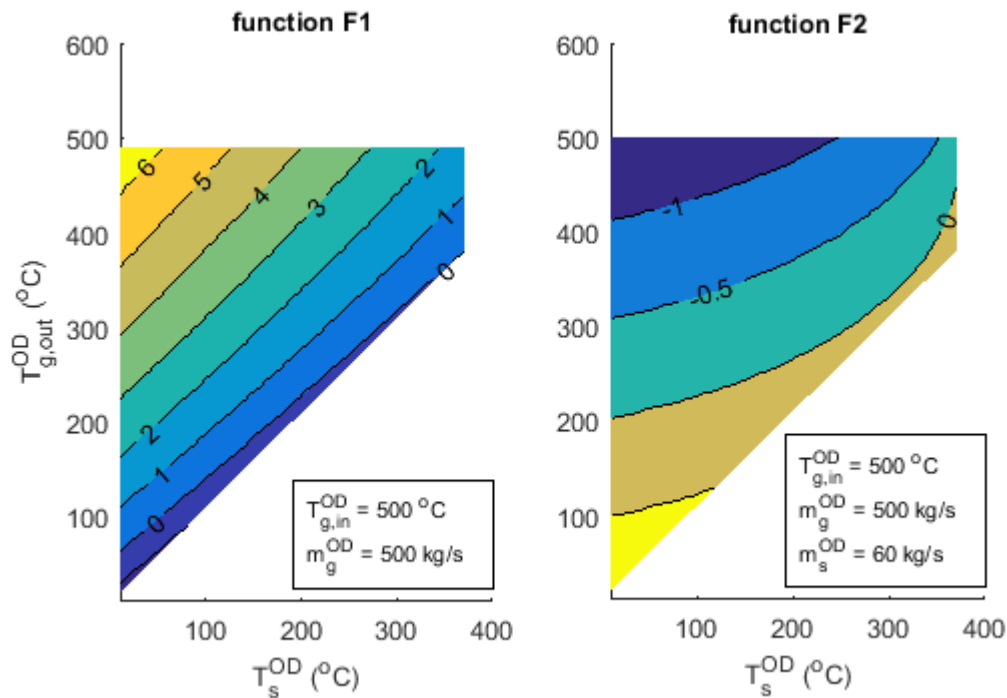
Fig. 6.6 Evaporator contour plots of F1 and F2 function residuals

the zero-lines.

Figure 6.7 shows the variation in zero-lines with gas and steam mass flow rates. The F_1^{OD} zero-line function shows that for given inlet conditions and $\dot{m}_g$, increasing T_s^{OD} effectively reduces Δh_s and the amount of heat transfer required. As a result, ΔT_g will also get smaller causing $T_{g,out}^{OD}$ to increase. As the $\dot{m}_g$ is reduced, a larger drop in $T_{g,out}^{OD}$ is required to maintain the unchanged evaporation temperature, $T_{s,out}^{OD}$.

For given inlet conditions, $\dot{m}_g$ and $\dot{m}_s$, increasing $T_{s,out}^{OD}$ will decrease the amount of energy contained in liquid-vapour mixture. To balance it, the amount of energy in the hot gas path also needs to drop which will cause the $T_{g,out}^{OD}$ to increase. The effect of increasing $\dot{m}_s$ but leaving $T_{s,out}^{OD}$ unchanged will increase the energy content in the liquid-vapour mixture, which is balanced by reduction in $T_{g,out}^{OD}$. Asimilar effect is observed in reducing $\dot{m}_g$, which causes $T_{g,out}^{OD}$ to increase.

The equations F_1 and F_2 need to be satisfied simultaneously. Therefore, the solution will be a point where the two curves intersect. Figure 6.8 shows functions F_1 and F_2 superimposed for $\dot{m}_g = 500\frac{kg}{s}$, where vertical lines represent pressure level in bars in the evaporator and are evaluated with equation A.5. It appears that for a given $\dot{m}_g$ only a
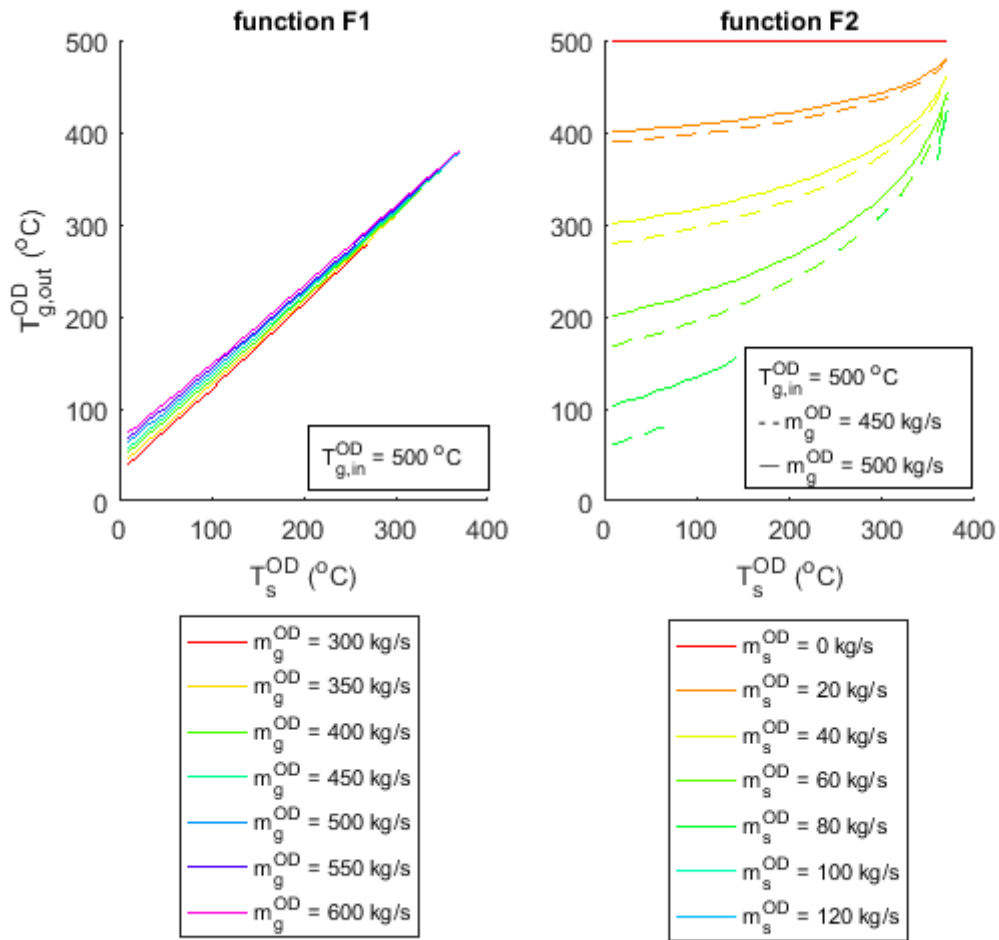
Fig. 6.7 Zero-lines plot of F1 and F2 functions

narrow range of $\dot{m}_s$ provide a solution, where in the figure only $80\frac{kg}{s}$ curve intersects with function F_1. The range can be calculated more accurately by reducing the increment of change in $\dot{m}_s$; however, the current tolerance is acceptable to communicate the concept. The lines in the plot represent simulated results, whereas points are the polynomial curve fitting used to calculate intersection coordinates between F_1 and F_2. Because of the curvature of function F_2^{OD} there are instances in which two solutions exist.

The evaporator mass flow curve is shown in figure 6.9. The effect of varying $\dot{m}_g^{OD}$ on the shape of $\dot{m}_s^{OD}$ curve is shown, with superimposed evaporator pressure contour lines. The effect of varying $T_{g,in}^{OD}$ is also shown on the plot. If the evaporator is operated at hotter gas temperatures and $T_{s,out}^{OD}$ remains unchanged, more steam flow rate is needed to sustain
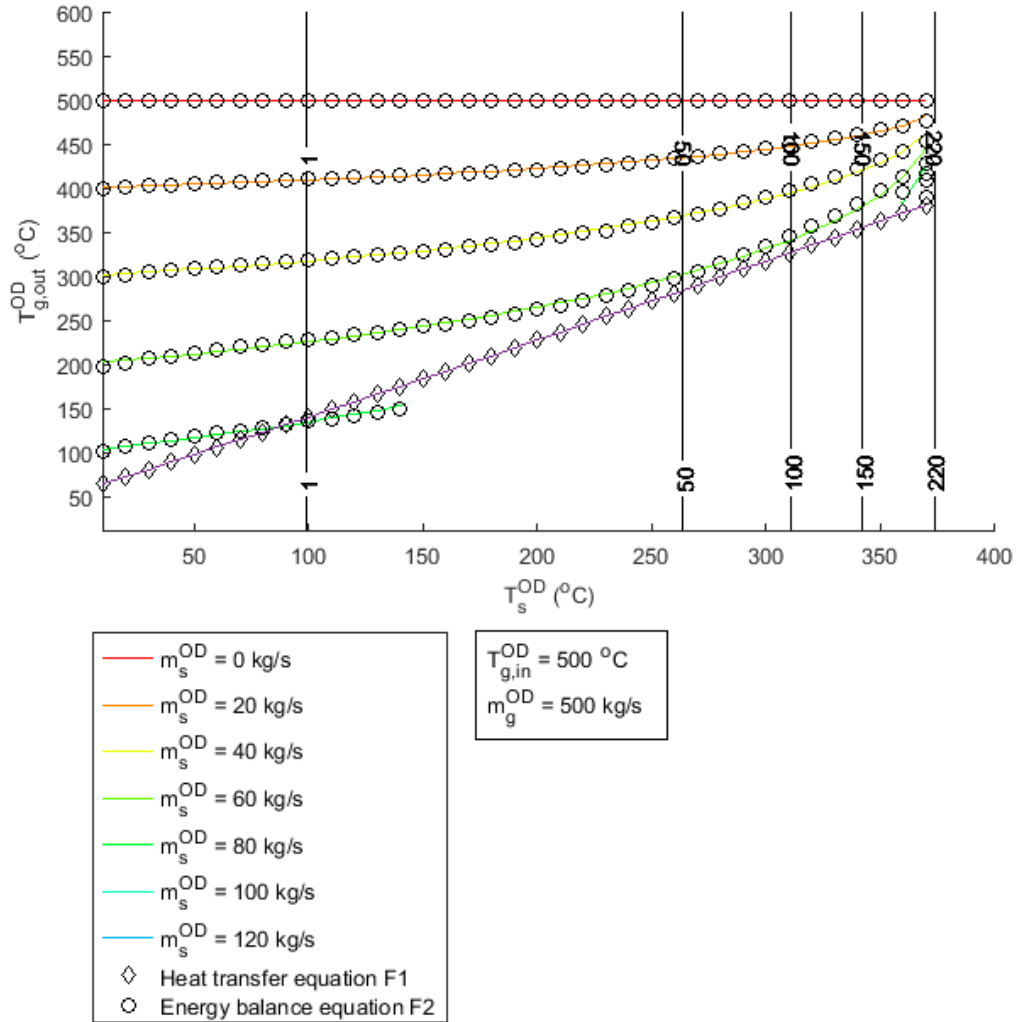
Fig. 6.8 Intersection of F1 and F2 functions

required Δh_s^{OD}. If the flow rate of gas is reduced, $\dot{m}_s^{OD}$ needs to be reduced as well to maintain unchanged temperature profile.

According to figure 6.9, at low $\dot{m}_g^{OD}$ values there is only one solution defining a unique set of T_s^{OD}, $T_{g,out}^{OD}$ and $\dot{m}_s^{OD}$. Because an increase in T_s^{OD} is more dominant than corresponding increase in $T_{g,out}^{OD}$, the curve terminates at a point where $T_{g,out}^{OD} \leq T_{s,out}^{OD}$. However, higher $\dot{m}_g^{OD}$ cause smaller gas temperature drop, which effectively shifts the F_1^{OD} curve upwards causing $\dot{m}_s^{OD}$ curve to terminate at a higher T_s^{OD} values. It became apparent that at high $\dot{m}_g^{OD}$ values, the $T_{g,out}^{OD}$ remains greater than T_s^{OD} for much wider range of T_s^{OD} val-

ues. As a result, the $\dot{m}_s^{OD}$ reaches a minimum, and then continues increasing in asymptotic fashion. Therefore, two solutions exist, one in the higher and one in the lower pressure range for given $\dot{m}_g^{OD}$ and $\dot{m}_s^{OD}$. The minimum $\dot{m}_{s,min}$ is where the F_2^{OD} curve is tangent to the F_1^{OD} curve, which is understood as the minimum steam mass flow rate needed to satisfy heat and energy balance at a given $\dot{m}_g$. At a minimum value of steam mass flow rate, one unique solution exists.

If the steam mass flow rate is increased above the minimum point the solutions diverge, one in the direction of increasing pressure, and one in the direction of decreasing pressure. Therefore, the heat exchanger is able to achieve the required Δh_s^{OD} at both high and low pressure levels having the same steam production. The two distinct regimes are hereafter referred to as *Evaporator Low Pressure Regime* and *Evaporator High Pressure Regime*, whereas the minimum point is referred to as *Evaporator Minimal Steam Production*.

The Evaporator Low Pressure Regime is characterised by progressively increasing heat demand by water/steam in the direction of decreasing pressure. The required $T_{g,out}^{OD}$ also decreases causing an increase in the corresponding heat supply. Therefore, both heat demand and heat supply tend to increase, where the effect of increase in heat supply is more dominant. Since the gas mass flow remains unchanged, the steam mass flow needs to increase to balance the more dominant effect of heat supply. The effect of decreasing T_s^{OD} is more dominant over the corresponding drop in $T_{g,out}^{OD}$, which in turn causes the pinch point temperature difference to increase. A general definition for the Low Pressure Regime is as follows:

> The Evaporator Low Pressure Regime is defined as an operational region of a heat exchanger at part load in which, all other terms being equal, a pressure can be reduced below the Evaporator's Minimal Steam Production point causing a corresponding increase in the production of steam. Operation in this region is dominated by and therefore more sensitive towards the heat supply from the gas. Therefore, a large change in heat supply is needed to achieve a relatively smaller change in heat demand.

The Evaporator High Pressure Regime is characterised by a progressively decreasing heat demand by water/steam in the direction of increasing pressure. Less heat demand will require smaller drop in $T_{g,out}^{OD}$ resulting in lower heat supply by the gas. The effect of decreasing heat demand is more dominant, and given that gas mass flow remains unchanged, the steam mass flow must increase to balance the less dominant decrease in heat supply. The effect of increasing T_s^{OD} is more dominant over the corresponding drop in $T_{g,out}^{OD}$ causing the pinch point temperature difference to decrease. A general definition for the High Pressure Regime is as follows:

> The Evaporator High Pressure Regime is defined as an operational region of a heat exchanger at part load in which, all other terms being equal, pressure can

be increased above the Evaporator Minimal Steam Production point causing a corresponding increase in the production of steam. Operation in this region is dominated by and therefore more sensitive towards the heat demand from the water/steam. Therefore, a large change in heat demand is needed to achieve a relatively smaller change in heat supply.

It is important to note that for the evaporator alone, increasing the rate of steam production has a positive effect on the power output and thermal efficiency. However, the upper limit of steam production is bounded by the choking conditions of a steam turbine. This analysis is however outside of the scope of the current work. The Low Pressure Level, although providing high thermal efficiency and power output, does so at the expense of low superheater pinch point temperature difference as it is demonstrated in the following section.
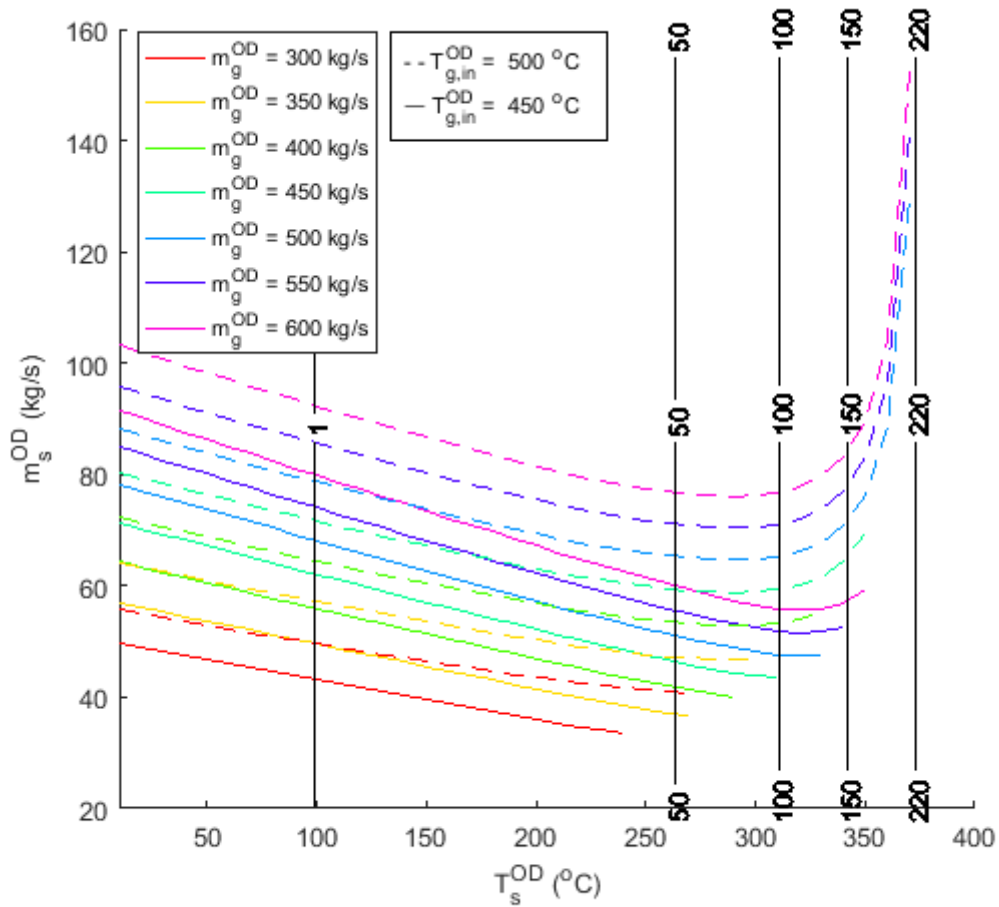
Fig. 6.9 Evaporator steam mass flow curve

6.7 Superheater analysis

The superheater Local Station Vectors are summarised in table 6.3.

Figure 6.10 shows the shape of the contour lines for functions F_1^{OD} and F_2^{OD}. One unique solution exists at a point where zero-lines of both functions intersect, at which $T_{g,out}^{OD}$ and $T_{s,out}^{OD}$ are obtained. The effect of varying $\dot{m}_g^{OD}$ on function F_1^{OD} and $\dot{m}_s^{OD}$ on function F_2^{OD} is shown in figure 6.11. The intersection point for a case with $\dot{m}_g^{OD} = 500\frac{kg}{s}$ is shown in figure 6.12. The steam mass flow curve is shown in figure 6.13.

Table 6.3 Superheater Station Vector values

Variable	Inlet at Design	Outlet at Design	Inlet at Off-Design
$T_s[^{\circ}C]$	320	570	Variable
$P_s[bar]$	112	112	Function of $T_{s,in}^{OD}$
$h_s[\frac{kJ}{kg}]$	2698	3542	Variable
$\dot{m}_s[\frac{kg}{s}]$	80	80	Variable
$T_g[^{\circ}C]$	600	500	600 and 550
$\dot{m}_g[\frac{kg}{s}]$	654	654	Variable
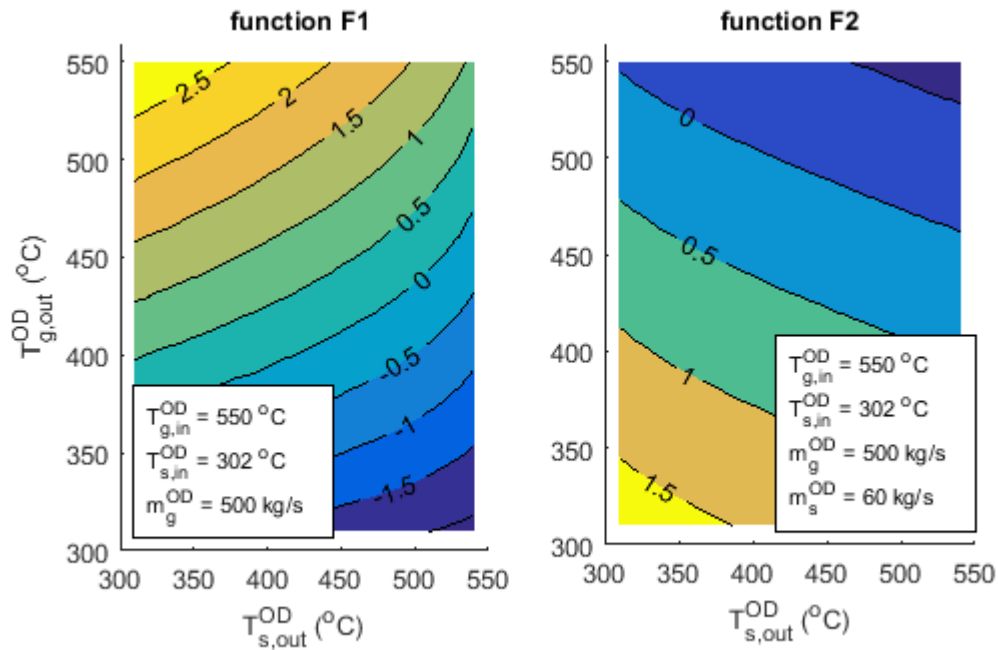
Fig. 6.10 Superheater contour plots of F1 and F2 function residuals
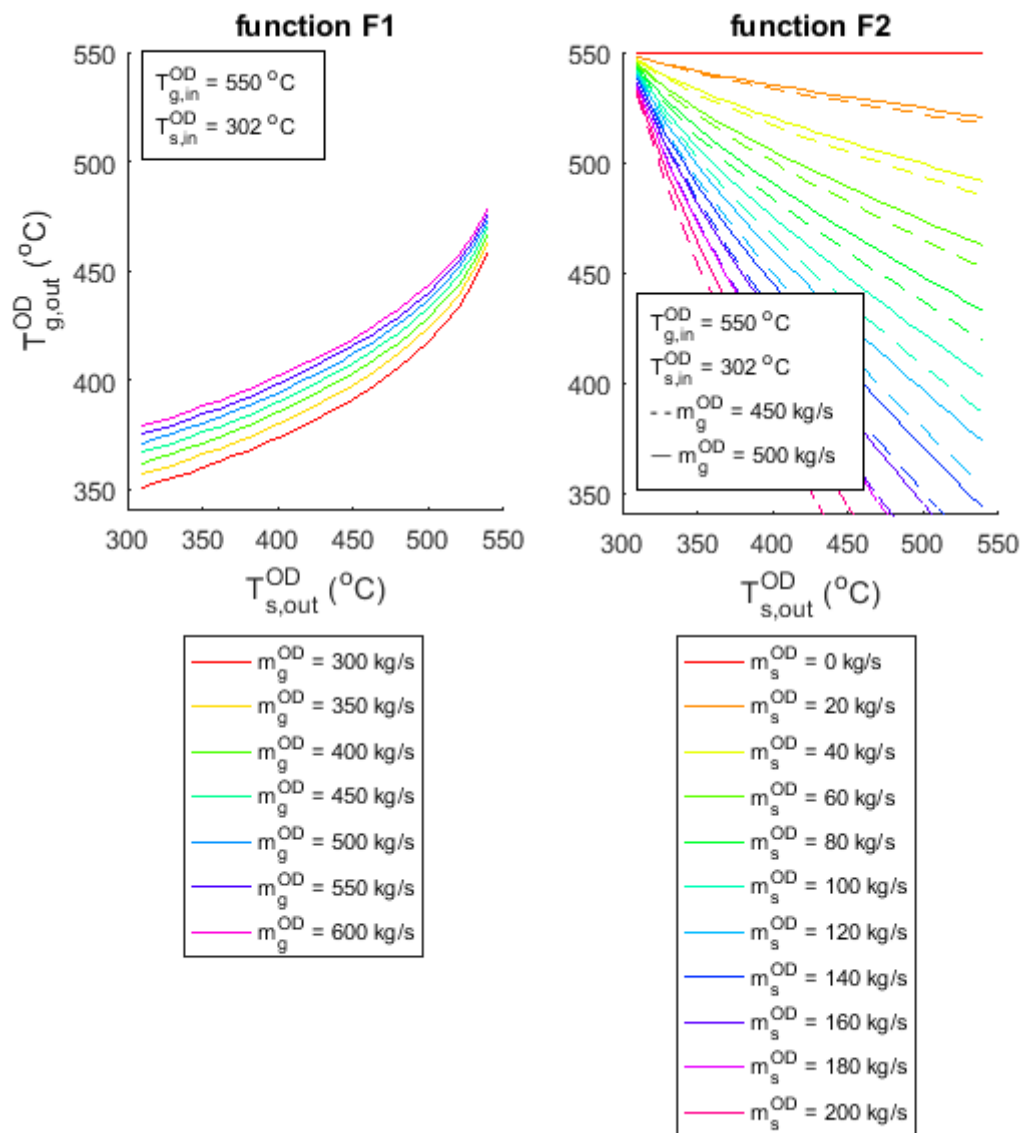
Fig. 6.11 Zero-lines plot of F1 and F2 functions
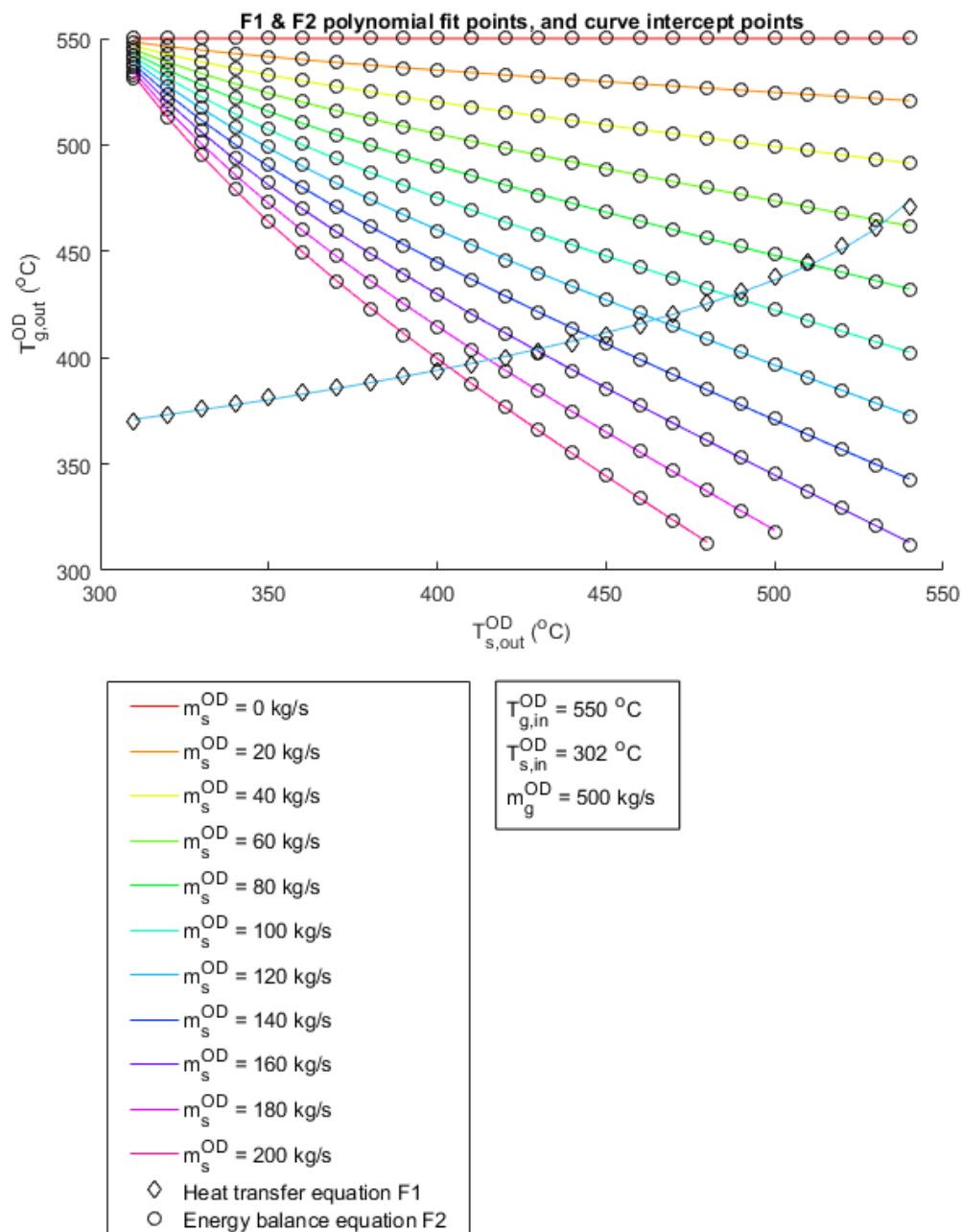
Fig. 6.12 Intersection of F1 and F2 functions
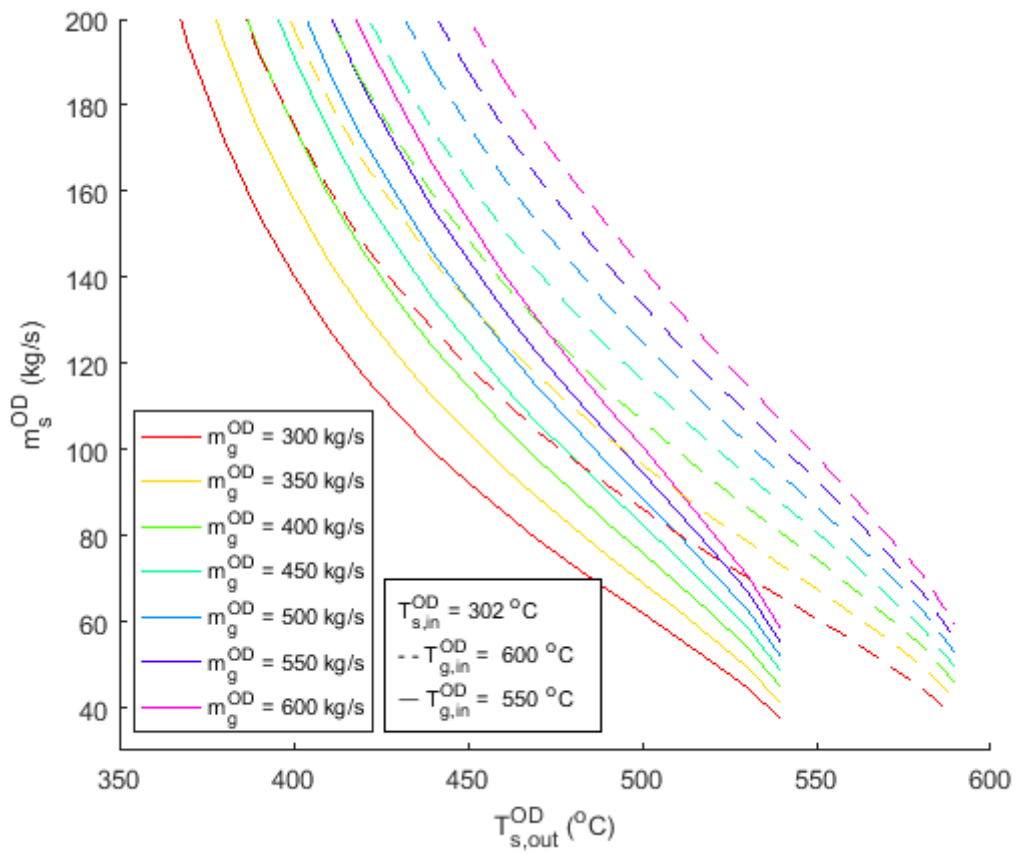
Fig. 6.13 Superheater steam mass flow curve

6.8   Component matching

The matching of plant components is an important procedure to ensure continuity of steam mass flow. The outlet Station Vector Values of one brick become inlet Station Vector Values of the next brick in the sequence. The steam mass flow curves obtained for economiser, evaporator, and superheater are used to match these components. Figure 6.14 shows the steam mass flow curves in solid lines for economiser and dotted lines for the evaporator. The superimposed contour pressure lines are also shown in the figure. For known economiser inlet conditions, the $T_{s,out}^{OD}$ and $\dot{m}_s^{OD}$ are obtained for various $T_{g,in}^{OD}$ values. Assuming isothermal process taking place in the drum, the temperature at the outlet of economiser becomes the inlet temperature to the evaporator; therefore sharing a common x-axis. The locations where the economiser and evaporator lines intersect provide unique set of pressures, $T_{s,out}^{OD}$ for economiser, and T_s^{OD} for the evaporator, that satisfies steam mass flow continuity. These are therefore the only solutions that match economiser and evaporator at various off-design conditions dictated by the gas path.

It is not physically possible in this application for the economiser to have $T_s^{OD} \geq T_{g,in}^{OD}$; otherwise the heat would transfer in the direction from water to gas. Consequently, the economiser lines terminate at a point where $T_{s,out}^{OD}$ exceeds $T_{g,in}^{OD}$. This presents a lower boundary on the available range of $\dot{m}_s^{OD}$ values. The upper boundary is dictated by the $T_{g,in}^{OD}$ of the evaporator.

The superheater steam mass flow curves shown in figure 6.13 have a lower boundary where $T_{s,out}^{OD}$ exceeds $T_{g,in}^{OD}$, and no upper boundary. Therefore, the $\dot{m}_s^{OD}$ obtained from figure 6.14 must be matched with superheater, producing a unique set of $T_{s,out}^{OD}$ and $T_{g,out}^{OD}$ for the superheater. According to the results, a unique set of water/steam and gas temperature profiles across each heat exchanger must exist to satisfy mass flow continuity at all pressure levels.

6.8.1   Procedure

The evaporator determines the amount of steam produced in the cycle. Therefore, the procedure begins with evaporator

1. The design point operation Station Vectors, and off-design inlet conditions, $T_{g,in}^{OD}$, $\dot{m}_g^{OD}$, and $T_{s,in}^{OD}$ must be known

2. Then a range of $T_{s,out}^{OD}$ is evaluated with lower and upper limits of $T_{s,in}^{OD}$ and $T_{g,in}^{OD}$, respectively. Each $T_{s,out}^{OD}$ is used as a variable in the F_1^{OD} function, equation 6.15, and a corresponding values of $T_{g,out}^{OD}$ are obtained.

3. At this stage, with known temperature profile, $\dot{m}_s^{OD}$ is calculated with equation 6.21
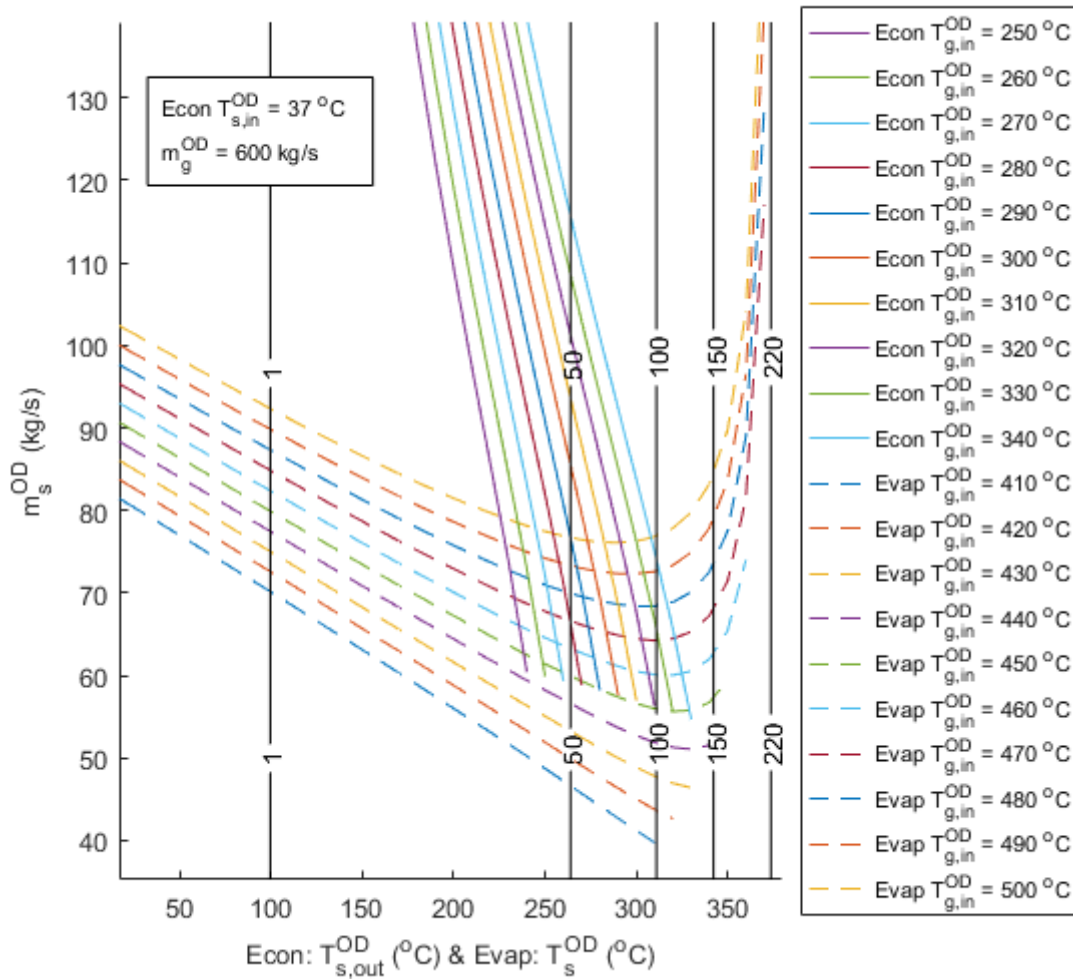
Fig. 6.14 Economiser and evaporator matching

4. The heat exchangers must then be matched for all to maintain the steam mass flow continuity

6.9 Comparison of results against commercial software

Comparison has been performed for an evaporator with the design parameters listed in table 6.4. *D*, *P*, and *E*, denote Direct Solution Method, PROATES, and Ebsilon models, respectively. The size of the evaporator is reflected in the *UA* parameter, thus leaving it unchanged ensures that all three simulated evaporators are the same. The enthalpy of the gas at the inlet must also be the same to reflect the same composition and heat transfer

properties.

The off-design conditions of the evaporator have been compared across a range of steam pressures from 2*bar* to 218*bar*. The evaporator inlet and outlet are assumed to be saturated water and saturated steam, respectively. Therefore, the steam temperature at the inlet and outlet are constant with a value of T_s^{OD}. At each pressure level, the steam mass flow rate has been calculated and shown in figure 6.15. The corresponding gas outlet temperature, $T_{g,out}^{OD}$, is shown in figure 6.16.

Current methods for off-design simulation are highly iterative. Therefore, the PROATES and Ebsilon software iterate until solution converges. If the initial guess is too far from the solution, the iteration diverges and the software returns an error. However, if required, a stepped solution can be applied. In the comparison trials all of the solutions converged, which usually required less than 30 iterations without the need for a stepped solution. The Direct Solution Method shows a very good correlation with commercial software.

Table 6.4 Evaporator design-point values used for validation comparison

Variable	Inlet at Design	Outlet at Design
$P_s^D\,[bar]$	112.470	112.470
$T_s^D\,[^\circ C]$	319.795 (D)	319.795 (D)
	319.753 (P)	319.753 (P)
	319.753 (E)	319.753 (E)
$h_s^D\,[\frac{kJ}{kg}]$	1462.430 (D)	2698.236 (D)
	1460.510 (P)	2701.420 (P)
	1460.528 (E)	2701.419 (E)
$T_g\,[^\circ C]$	509.684	340.007 (D)
		343.568 (P)
		341.553 (E)
$h_g\,[\frac{kJ}{kg}]$	521.511 (D)	
	521.778 (P)	
	521.259 (E)	
$\dot{m}_s^D\,[\frac{kg}{s}]$	90.964 (D)	
	92.306 (P)	
	94.181 (E)	
$\dot{m}_g^D\,[\frac{kg}{s}]$	653.900	
$UA^D\,[\frac{kW}{^\circ C}]$	1504.944 (D)	
	1504.779 (P)	
	1504.720 (E)	
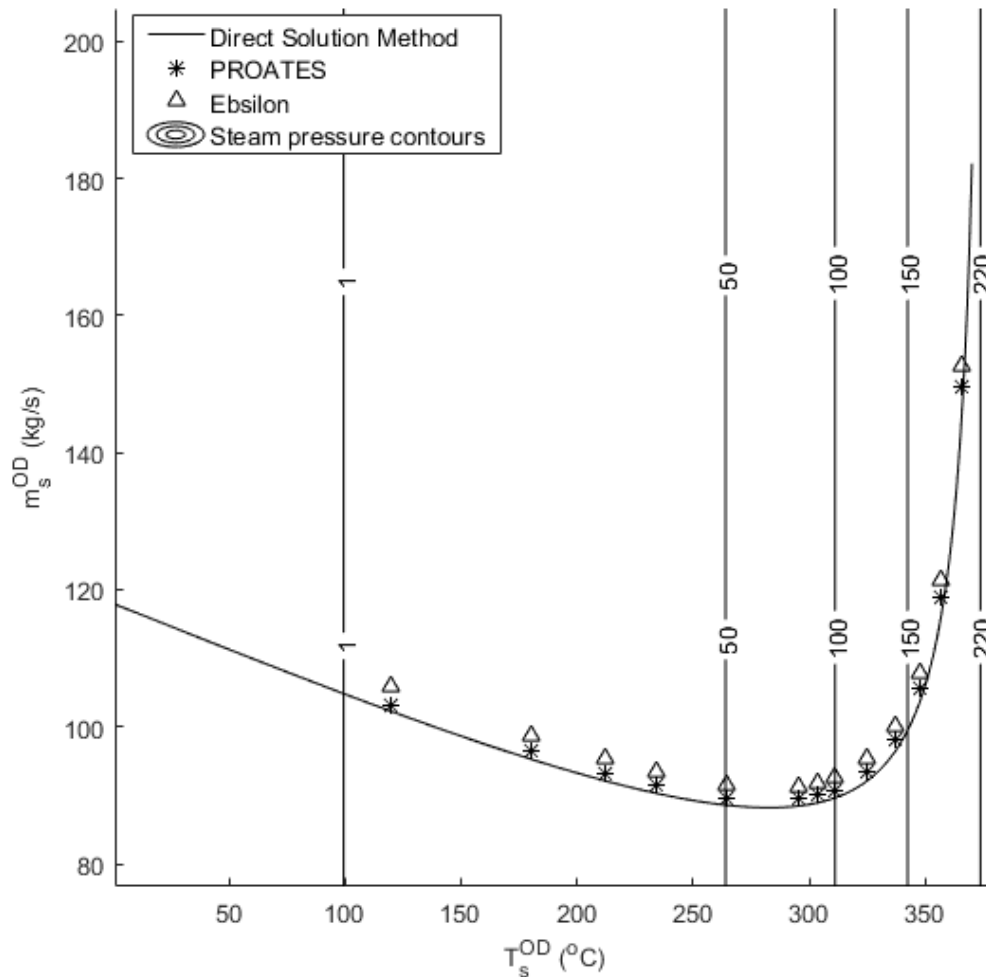
Fig. 6.15 Comparison of the Direct Solution Method for evaporator against commercial software. Steam mass flow profile curve

The small differences in the solution are due to a number of factors:

- The use of different steam table formulations have effect on the results. Most common standards are *UK 1967*, *ASME 1967* and *IAPWS-IF97*. The simulations with PROATES and Ebsilon were done using IAPWS-IF97 steam table formulations. Whereas, the DSM method uses non-standard correlations shown in section A.1. It is therefore necessary to replace the steam table correlations with standard formulations for steam calculations.

- The PROATES and Ebsilon models take into account the gas turbine exhaust gas molecular species, and from there gas enthalpy is evaluated. The DSM method uses
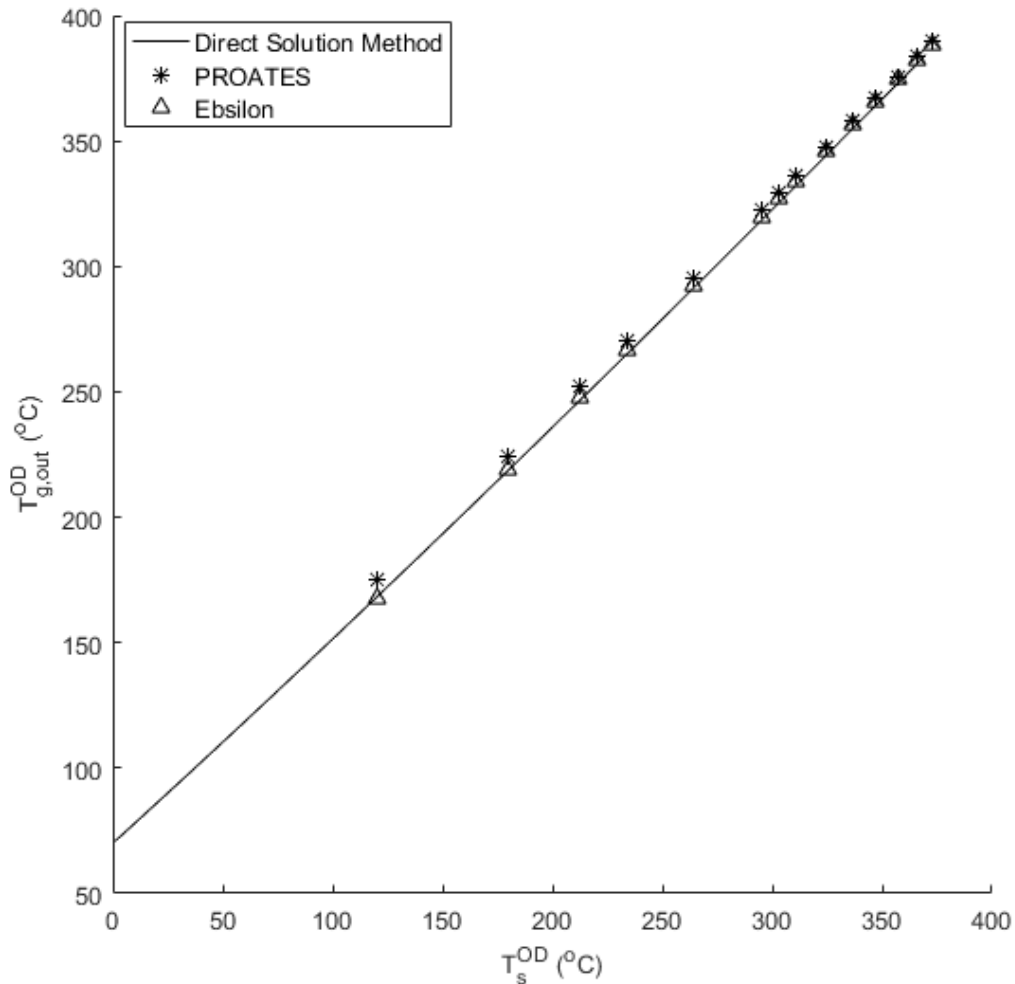
Fig. 6.16 Comparison of the Direct Solution Method for evaporator against commercial software. Temperature profile curve

a correlation to evaluate the constant specific heats, Cp_g, with equation A.9. The design-point validation has been matched so that the gas enthalpy is the same across the simulations, as pointed in section 4.11. In an off-design simulation, however, the exhaust enthalpy varies within 2.5% which is a discrepancy.

- The evaporator modelled with DSM is a simple heat exchanger. The drum module is available to the user as discussed in section 4.1.4. However, developing a mathematical model of the drum is outside of the scope of current work. It is recommended for the further research to incorporate the drum with the heat exchanger. The function of the drum is to separate liquid from vapour, which acts as a heat ex-

changer altering the liquid temperature at the inlet to the evaporator. The PROATES and Ebsilon models simulate an evaporator and a drum together with the natural circulation of the working fluid.

6.10 Modelling results

An arbitrary case has been studied in which the load of the gas turbine engine is reduced from $100 - 80\%$ by closing VIGVs, followed by fuel flow reduction to reduce the load further from $80 - 50\%$. The corresponding variation in gas turbine exhaust temperature and mass flow rate is shown in figure 6.17, where the x-axis represents the non-dimensional power output. The exhaust mass flow rate reduces with closing VIGVs from 653.5 to 500 $\frac{kg}{s}$, after which it remains constant. Since the VIGVs are closing at constant TET, the exhaust temperature will rise from 600 to 637 ^{o}C after which it falls to 527 ^{o}C at 50% load due to further fuel flow reduction.
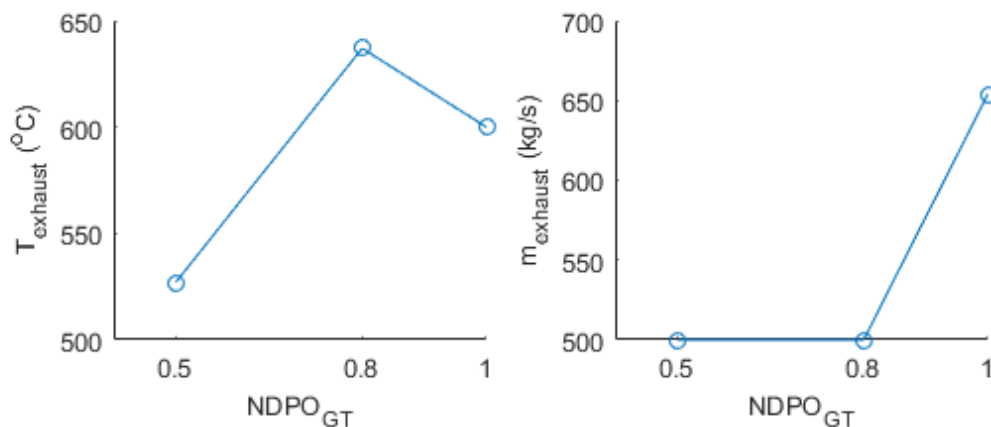
Fig. 6.17 GT exhaust conditions. The x-axis refers to the non-dimensional power output from gas turbine engine

The design-point performance variables have been discussed and shown in section 4.11, with validations against PROATES and Ebsilon commercial software. This one pressure bottoming water/steam cycle has been studied and validated further at off-design conditions.

The off-design performance results are shown in figures 6.18 and 6.19 for a gas turbine operating at 80% load. The dotted line in figure 6.18 represents the steam turbine capacity which is calculated with Stodola Law of Cones according to equation 6.49. The choking conditions of a steam turbine imply the maximum swallowing capacity. Therefore, taking a steam turbine into consideration draws a boundary condition on the allowable range of steam pressures, where $\dot{m}_s$ must be less or equal to the steam turbine capacity; i.e.

$\dot{m}_s \leq \dot{m}_{st,choked}$. The values of pressure at conditions where $\dot{m}_s > \dot{m}_{st,choked}$, are not physically possible. However, the DSM method exposes regimes where the system can be studied across the whole steam pressure range. The system operating at the intersection where $\dot{m}_s = \dot{m}_{st,choked}$ would see the steam turbine being choked. Any further increase in steam pressure where $\dot{m}_s < \dot{m}_{st,choked}$ would un-choke the steam turbine. The operating steam turbine can un-choke if the properties of the working fluid such as temperature, pressure or fluid velocity change at the throat area. For example the rotational speed of the turbine has an effect on the fluid velocities, which if varied may un-choke the turbine. If a blade failure occurs in a preceding turbine section, the flow incidence angle will change affecting the fluid velocities, which again may lead to turbine un-choking. It is important to note, however, that existing power plants which are connected to the grid will operate at a frequency imposed by the grid. Therefore, it is impossible for the steam turbine to reduce rotational speed. In the event of such occurrence, the power plant would immediately disconnect from the grid. Nevertheless, in the event of any unconventional operation of the steam cycle, the effect of key variables for given gas turbine load can readily be investigated.

$$\frac{\dot{m}_s^{OD}\sqrt{T_s^{OD}}}{P_s^{OD}} = constant \tag{6.49}$$

The economiser approach point temperature difference, $Econ_{AP}^{OD}$, takes negative and positive values. The negative values correspond to the operation in which economiser outlet temperature is higher then the saturation temperature at a given pressure level. This is not physically possible because achieving temperature above saturation point would mean that steam is superheated. Therefore, the results in the negative regime are only treated to represent that steaming in the evaporator occurs. It is out of the scope of the current work to incorporate study into the case of economiser steaming, however this should be investigated in further research. This limitation to the current study, however, does not alter the rest of the results, as they are dependent on the operation of the respective heat exchangers. The limitation, however, will alter the amount of heat transfer occurring in the economiser, which in turn will have an effect on the shape of the curves in figure 6.19 at pressure levels where $Econ_{AP}^{OD} < 0$.

The positive values of $Econ_{AP}^{OD}$ correspond to the condition in which economiser outlet steam temperature is below the saturation. It is a common practice to maintain the approach temperature in the region of $5 - 11^oC$ to avoid steaming at the economiser outlet [25]. Therefore, a boundary condition on the allowable range of steam pressures is established only for values greater than or equal to the agreed economiser approach temperature.

The superheater outlet temperature, T_{live}^{OD} needs not to exceed the acceptable limit of the steam turbine materials. Therefore, the live steam temperature is usually limited to 550^oC, which represents a boundary condition on the available choices for operating pres-

sure level.

The lower the stack temperature, T_{stack}^{OD}, the better the utilisation of heat from the gas. However, an excessively low stack temperature may result in condensation of sulphur present in the products of combustion of natural gas, which results in a highly corrosive sulphuric acid. This risk becomes significant if multiple pressure level systems are used. The stack temperature does not vary significantly for a wide range of pressure levels above the steam turbine choking point.

The corresponding performance results at a range of pressure levels which are shown in figure 6.19. Results are obtained for the whole steam cycle performance, and it must be noted that the operation of the condenser was assumed to be unchanged at off-design. This poses a limitation, which has not been addressed in current study. Therefore, the performance results only represent changing conditions of the HRSG at off-design. With this limitation, general trends in performance and trade-offs can be analysed. However, further research is needed to incorporate the Direct Solution Method to the performance evaluation of a condenser.

6.10.1   Full load range results

The full load range of a gas turbine engine with the exhaust conditions shown in figure 6.17 have been analysed. The water/steam cycle performance at each change of gas turbine exhaust conditions is shown in figure 6.20. The off-design cases have also been modelled in PROATES and Ebsilon for the same heat exchangers (i.e. having the same *UA* at the design point), and results are compared against the DSM method.

At each load level, 100%, 80%, and 50%, three plots of the corresponding simulation results were obtained similar to the ones shown in figures 6.18 and 6.19. The performance values were then selected from the plots at a point where steam turbine is operating at choking conditions (i.e. the intersection of solid and dotted mass flow lines in figure 6.18 where $\frac{\dot{m}_s}{\dot{m}_{ST,choked}} = 1$).

There is a very good correlation for P_s, $\dot{m}_s$, T_{live}, and *Power$_s$* against PROATES and Ebsilon. The difference in the rest of the results is due to a number of reasons, which have been discussed in section 6.9.

Excessive live steam temperature

According to figure 6.18, an increase in steam live temperature (i.e. steam turbine entry temperature) above the acceptable limit, could cause damage to steam turbine compo-
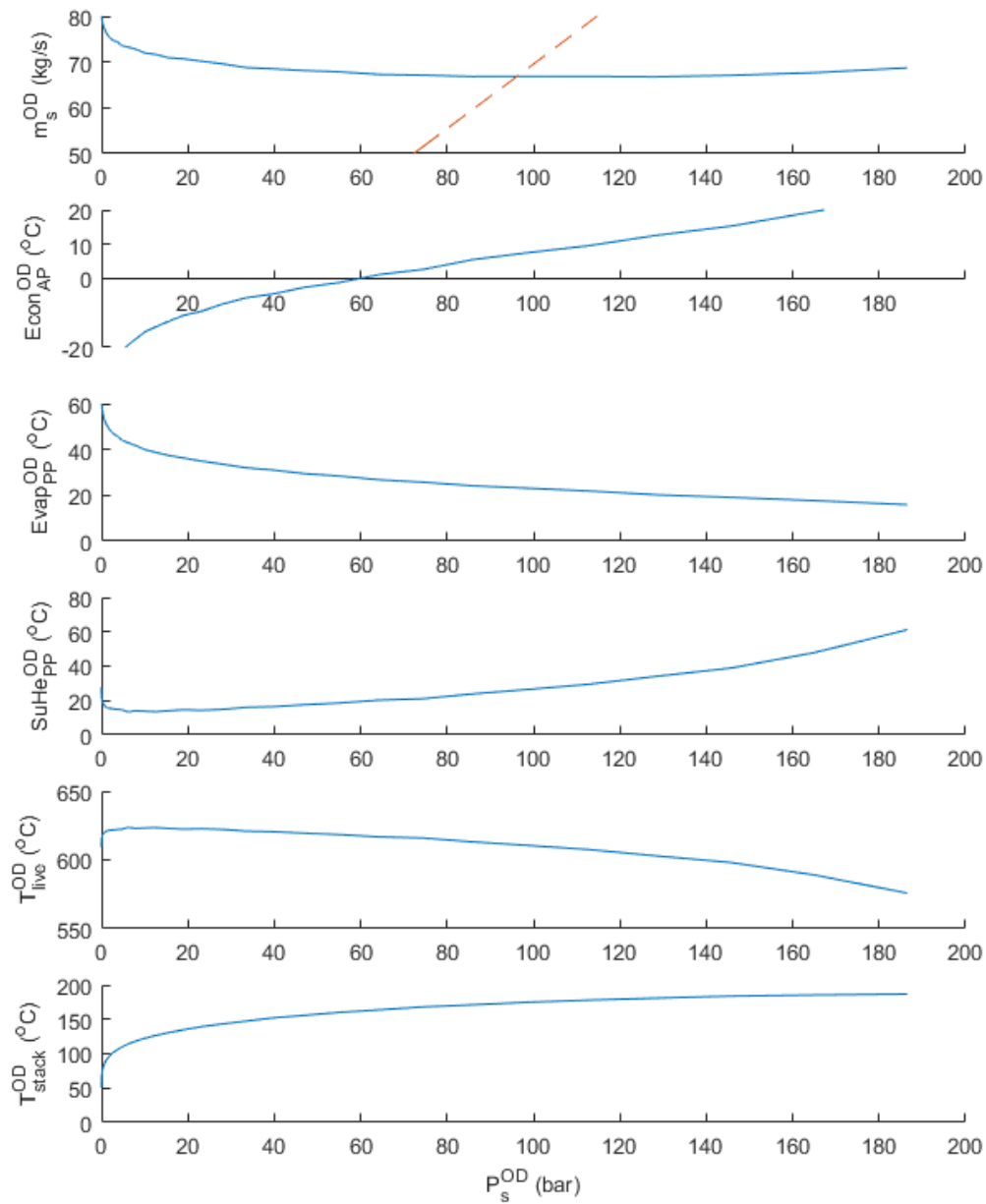
Fig. 6.18 Off-design temperature profiles and steam mass flow for 1P system. The dotted line represents steam turbine Stodola relation. The results shown are for an off-design condition in which the gas turbine is operating at 80% load
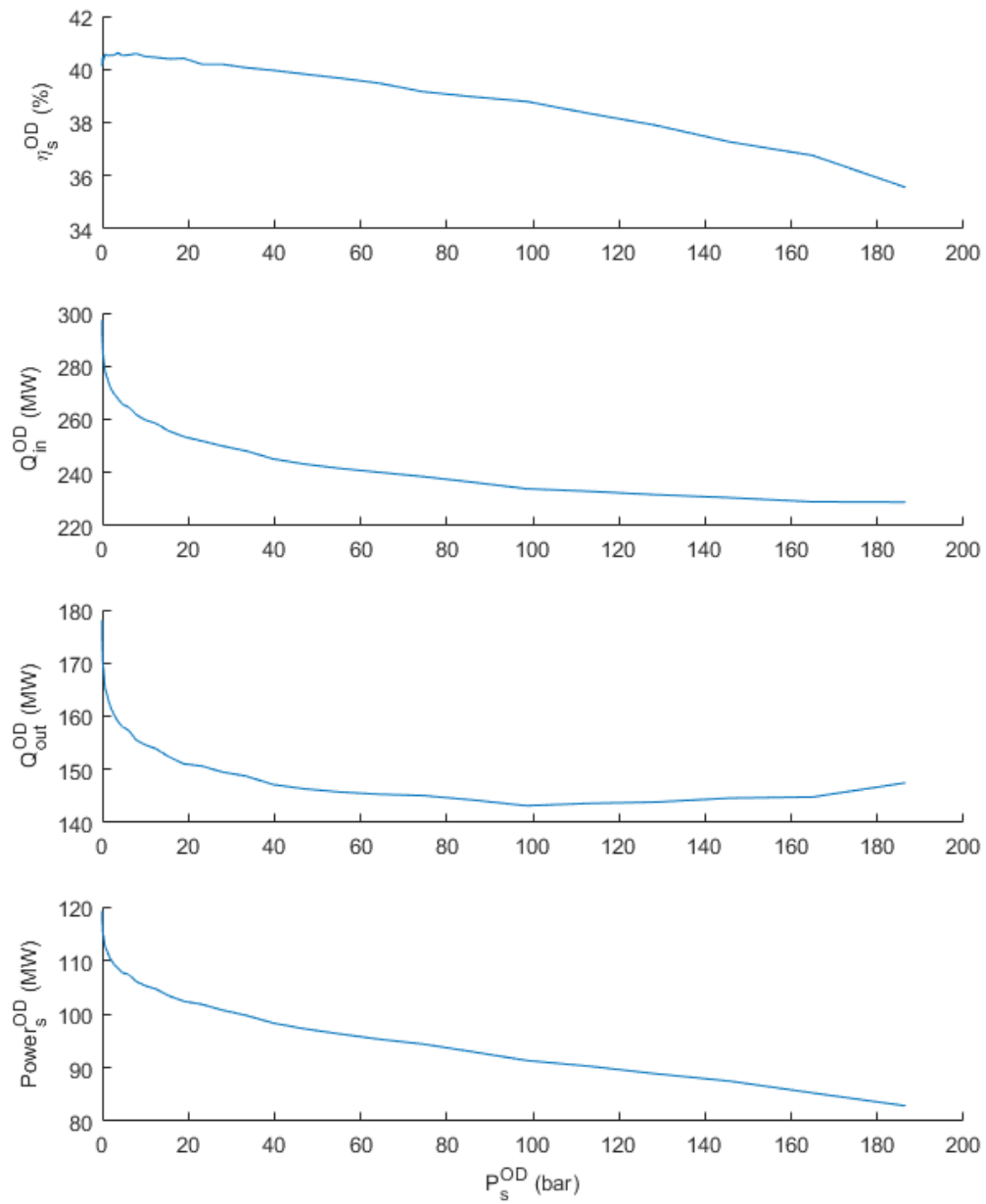
Fig. 6.19 Off-design performance results for 1P system. The results shown are for an off-design condition in which the gas turbine is operating at 80% load

nents. This temperature can be reduced by increasing steam pressure, with a trade-off in decreased power output.

Economiser steaming

At low power, steaming in the economiser may occur. Consequently, excessive noise and vibrations may occur and impact performance due to deposit formation and fouling. The economiser steaming is demonstrated in the results where approach point temperature difference has a negative value. At low power settings, the gas mass flow remains unchanged as only gas turbine fuel flow is used to modulate the power level. Consequently, the reduction in gas turbine exhaust temperature results in lower steam production. The economiser is exposed to two opposing effects: 1) lower steam mass flow rate, and 2) lower gas inlet temperature. According to figure 6.5 lowering $\dot{m}_s$ tends to increase $T_{s,out}$, and lowering $T_{g,in}$ tends to decrease $T_{s,out}$. In net terms, the effect of lower steam mass flow rate is more dominant causing $T_{s,out}$ to increase to a point where it reaches a saturation temperature, which causes vapour to appear at the steam outlet. Steaming can be avoided by reducing gas mass flow rate, $\dot{m}_g$, which can be done with opening a bypass duct at the gas turbine exhaust.

Based on the results shown in figure 6.18 it appears that steaming can also be avoided by increasing the steam pressure, i.e. closing a throttling valve located between the HRSG and the steam turbine. This has been simulated by increasing the economiser approach point temperature difference to 3^oC at 50% load, with corresponding performance results shown as dotted lines in figure 6.20. In this condition the steaming is avoided and the economiser outlet temperature is 3^oC below the saturation point. However, the steaming has been avoided by significantly increasing steam pressure. Also, the steam turbine is now operating in a 40% choked condition, which may not be acceptable. Further study is needed to analyse the effect of modulating steam pressure to avoid economiser steaming.
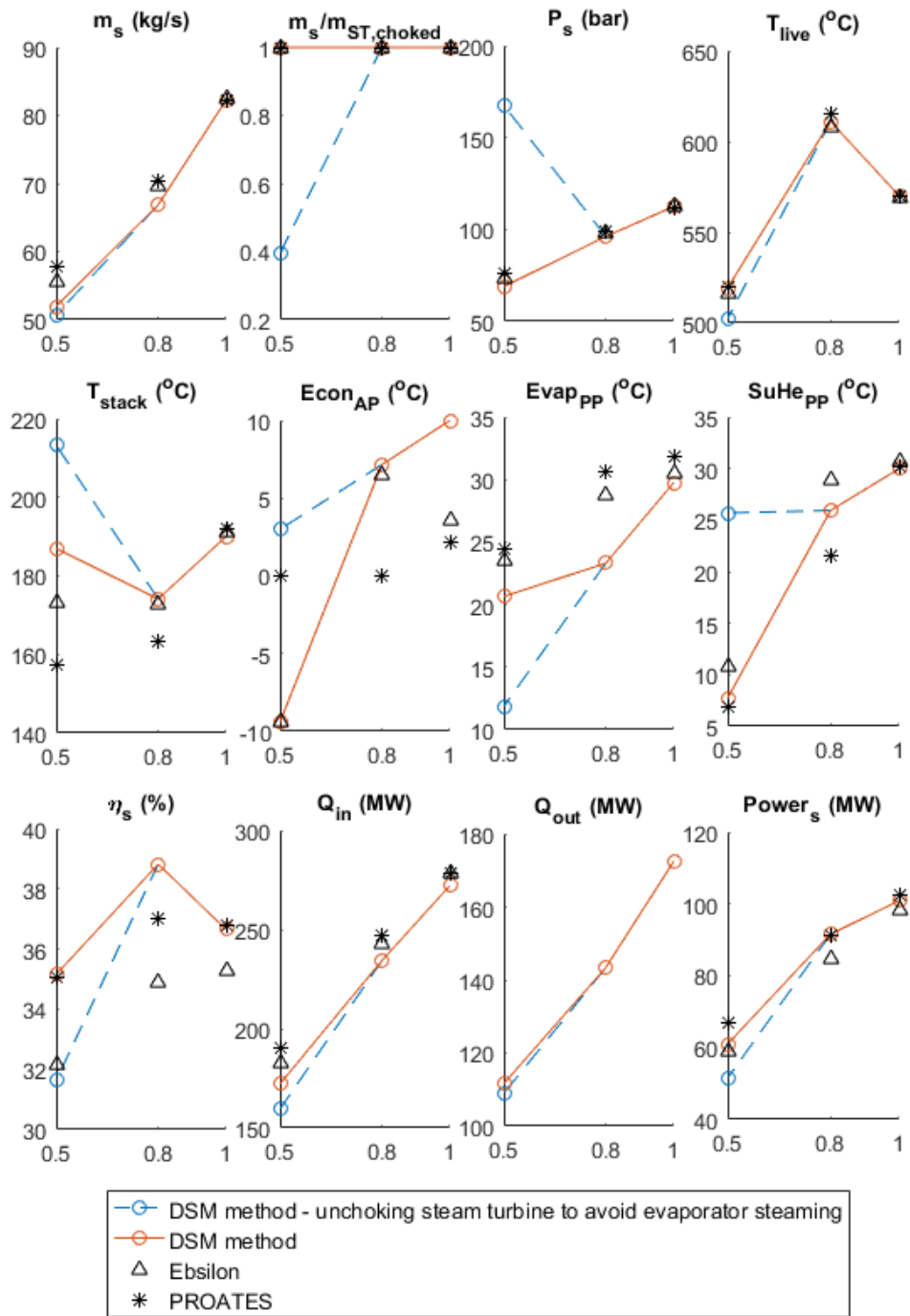
Fig. 6.20 Off-design performance of water/steam cycle maintaining choked steam turbine (solid lines), and avoiding economiser steaming at 50% load (dotted lines). The x-axis refers to the non-dimensional power output from the gas turbine engine at three conditions: 100%, 80%, and 50% load

6.11   Conclusion and discussion

The three main components of the Heat Recovery Steam Generator have been analysed for a one pressure system with objective of developing a new method for off-design performance calculations, called the Direct Solution Method (DSM). These are the economiser, the evaporator and the superheater. The operation of a bottoming water/steam cycle is dictated by the gas turbine exhaust conditions. The attempts to solve off-design performance upon changing either gas turbine exhaust temperature or gas mass flow rate using well documented procedures and methods are highly iterative, complex, and require making initial guesses. If the initial guesses are too far away from the solution, the method may not converge, or converge with misleading results. The Direct Solution Method provides a simple solution without the need for iterations, thereby, reducing complexity and computational time, and improving accuracy.

At each gas turbine load settings, steam cycle off-design performance characteristics are generated similar to the ones shown in figures 6.18 and 6.19. These results give full insight into the off-design operation of steam cycle before any constraints and limitations are applied. The limitations may include temperature, approach points, pinch points, pressure controls, or steam turbine choking. The method then allows for investigation into their effect on the rest of the performance parameters. According to the results, two solutions exist for steam mass flow rate in distinct regions referred to as Low Pressure Regime and High Pressure Regime, and the point of minimum mass flow being the Minimal Steam Production needed to sustain the required change in enthalpy in the evaporator. The performance results for the evaporator have been validated in section 6.9, which show good agreement against commercial software.

Chapter 7

Conclusions and recommendations

7.1 Conclusions

Since the industrial revolution began in 1750, fossil fuels have become widely used to power our economy. It was not until recent decades where the consequences of using polluting fossil fuels become widely acknowledged. The impact of human activities has led to recently alarming concentrations of carbon dioxide in the atmosphere (figure 1.1). This greenhouse gas is particularly harmful to the atmosphere as it contributes to global warming by trapping the heat from the sun. In an attempt to reduce global production of CO2, new renewable technologies are being developed and deployed across the world. Renewable power generation has been deployed on large scales in a very short period of time, which creates significant challenges to balance electricity production when the sources of renewable power are not available. This has created a new market for conventional power generation, in which Combined Cycle Power Plants are operated in a flexible manner to fill the gaps in electricity demand. The energy market participants, e.g. power plant operators, need to quickly adapt to the changing market conditions without knowing with any level of certainty what will the near-term future look like. Not having a clear vision for near-term future and large scale research and deployment of renewable energy has by many been described as the post-industrial energy revolution.

The irregular nature of renewable sources e.g. wind and solar, presents a great challenge to balance when these sources are not available and the demand for electricity needs to be satisfied. In the UK alone, the National Grid's total cost for balancing the grid increased from £642M (2005-06) to £1.08B (2015-16), with projections further to reach £2B by 2020. Most of the existing CCPPs were not designed and built for cyclic operation, and power plant operators are now struggling for solutions to increase flexibility of their units and remain competitive in the market. Therefore, the wider objective of the current research is to develop methods to improve our understanding of flexible CCPP operation as required by increasing mix of renewable capacity, which is ultimately influenced by the changing climate. In this context, it is believed that the gas turbine opera-

163

tional flexibility map and the DSM method for part load performance analysis contribute to the research needs and will enable further technological progress into improving flexible CCPP operation.

In terms of the need for flexible combined cycle operation, the findings in the literature provide evidence that complex techno-economic optimisations of the system are now needed. In recent years a large number of studies are conducted in CCPP layout optimisation, economic optimisation, parametric optimisation, life consumption, and systemic optimisation. All of these areas in research are much needed to adapt CCPP to the new flexible operational requirement. Although the application areas vary, most of these studies in their early stages require modelling of CCPP performance at part-load. Many studies done in this area confirm that the gas turbine load reduction strategy greatly affects CCPP performance [28]. This relates to the first research question, which looked at the ways to improve interpretation of infinite possibilities for gas turbine load reduction, and the developed Gas Turbine Operational Flexibility Map in chapter 3. Life consumption of critical gas turbine components due to low cycle fatigue and creep mechanisms have also been analysed at part load. These maps allow for quick assessment of performance and life consumption trade-offs depending on the particular way the load of the plant is reduced. Analogically to the compressor and turbine maps being used to study overall performance of gas turbines, the operational flexibility map supplements it with the insights into the effects of flexible load change.

Chapters 4, 5, and 6, investigate the second research question. The literature review suggests that current techniques for modelling part-load operation of CCPPs are still based on the ones developed in the late twentieth century. These techniques are broadly based on formulation of a system of non-linear equations, and numerical or sequential methods applied to solve for unknown variables [35], [36], [37], and [38]. A number of authors have acknowledged the difficulties in deploying these techniques to complex optimisation studies, describing them as cumbersome, time-consuming, complex, and highly dependent on the formulation of an initial approximation, which if too far from the solution may lead to divergence. In attempt to reduce dependency of the solution on the initial guess, a novel application of a genetic algorithm to CCPP performance modelling has been developed and described herein. The process, inspired by natural selection, evolves the fitness of non-linear equations towards a solution. The study offers suggestive evidence that genetic algorithm returns feasible solution with acceptable level of accuracy without need for initial approximations, which provides an advantage over the existing methods. However, it concluded that the genetic algorithm based method does not provide a long term benefit because it is still fundamentally based on complex iterations. The computational time required is significant, and the method increases the complexity of the system. Consequently, these results have led to the development of a novel method with the objective of significantly reducing complexity of the system, improving accuracy, and reducing dependency on iterative procedures. The developed method is called the Direct Solution

Method, which has been derived from the fundamental laws of heat transfer and energy balance, and adapted for design-point and off-design point performance modelling. The results show good agreement with validation cases, and expose detailed insights into the performance of CCPPs. Unlike the existing methods, the DSM allows for quick and detailed study of results across the whole spectrum of pressure levels for each part-load condition. The easy to obtain solution can also be applied to study multiple-pressure systems, and complex network of various system layouts.

7.2 Limitations of the study and further recommendations

The results obtained with the current research have a number of limitations. In terms of the development of the operational map, a number of further improvements are proposed:

- Represent gas turbine engine compressor surge and choking lines and draw operational boundary on the map.

- Include performance results for the gas turbine bottoming water/steam cycle simulated with the Direct Solution Method.

- Formulate life-consumption non-dimensional groups representing percentage of life consumed due to low cycle fatigue and creep, and include results in the gas turbine operational map.

- Formulate economic non-dimensional groups representing operational costs and costs of generating electricity, and include results in the gas turbine operational map.

In terms of the Direct Solution Method for design-point modelling, the following limitations must be addressed:

- Formulate a detailed heat transfer calculation for evaluating the overall heat transfer coefficient, U^D, based on the tube bank geometries.

- Develop detailed representations of the steam turbine and condenser bricks.

- Use methodology presented herein, and further develop reheat and supplementary heating bricks.

In terms of the Direct Solution Method for off-design modelling, the following limitations must be addressed:

- Investigate into the case of economiser steaming, including studying effects of steam pressure modulation to avoid steaming.

- Formulate explicit solution for $T_{g,out}^{OD}$ based on results obtained in equation 6.46.

- Develop DSM taking account the effect of component degradation due to fouling or erosion using β factor in the formulations.

- Develop off-design performance module for the condenser.

- Develop off-design performance module for the steam turbine.

- Formulate detailed method for evaluating the overall heat transfer coefficient, U^{OD}.

- Incorporate standard steam formulations, for example the IAPWS-IF97 tables.

- Develop further the drum model required for more accurate estimation of evaporator performance.

7.3   Autobiographical reflection

Undertaking this PhD research study has been an invaluable experience, which gave me the opportunity to learn and understand current European energy market challenges. I realised that commonly people fear chaos and uncertainly, but these appear to be the ultimate stimulants to the progress in research and development of new technology. I investigated not only engineering issues, but also financial, economical, and political factors to gain higher appreciation about the roots of the energy problem. The high need for flexible conventional power plant operation is an understatement. These uncertainties of-course put a lot of strain on businesses, and in all of my encounters, both private and in public conferences/meetings, the conversations were always dominated by a question - "what will the future bring?". I hope that the results of my research will help the research community in producing a clearer picture of the future, in which sustainable, clean and affordable energy will be available to everyone.

References

[1] E.J. Brook. Ice core methods — overview. *Encyclopedia of Quaternary Science (Second Edition)*, page 1145 to 1156, 2007.

[2] A. Laurent, C. Barbante, P.R.F. Barnes, J.M. Barnola, et al. Eight glacial cycles from an antarctic ice core. *Nature*, pages 623–628, 2004.

[3] D. Luthi, M.L. Floch, B. Bereiter, T. Blunier, J.M. Barnola, et al. High-resolution carbon dioxide concentration record 650,000-800,000 years before present. *Nature*, 453:379–382, 2008.

[4] D.M Etheridge et al. Law dome ice core 2000-year co2, ch4, and n2o data. Noaa/ncdc paleoclimatology program, IGBP PAGES/World Data Center for Paleoclimatology Data Contribution, USA, 2010.

[5] NOAA/ESRL. Atmospheric data, 2016.

[6] J. Jouzel, V. Masson-Delmotte, et al. Epica dome c ice core 800kyr deuterium data and temperature estimates. Noaa/ncdc paleoclimatology program, IGBP PAGES/World Data Center for Paleoclimatology Data Contribution Series, USA, 2007.

[7] A. Moberg et al. 2,000-year northern hemisphere temperature reconstruction. Noaa/ngdc paleoclimatology program, IGBP PAGES/World Data Center for Paleoclimatology Data Contribution, USA, 2005.

[8] M.E. Mann. Little ice age. *Encyclopedia of Global Environmental Change*, 2002.

[9] G. Parker. Lessons from the little ice age, 2014.

[10] J.E. Hansen. The greenhouse effect: impacts on current global temperature and regional heat waves. Statement presented to United States Senate Committee on Energy and Natural Resources, 1988.

[11] G. Ceballos, P.R. Ehrlich, A.D. Barnosky, et al. Accelerated modern humaninduced species losses: Entering the sixth mass extinction. *Science Advances*, 1(5), 2015.

[12] President. Adoption of the Paris agreement. Technical report, United Nations, 2015.

[13] L. Jeffery, R. Alexander, B. Hare, M. Rocha, et al. How close are indcs to 2 and 1.5degc pathways? Technical report, Potsdam Institute for Climate Impact Research, 2015.

[14] R. Branson. Climate: the opportunity from paris. http://virgin.com, 2016.

[15] T. Alvarez. Flexible operation: changing power generation structure in europe. May 2016.

[16] R. Howard and Z. Bengherbi. Power 2.0 - building a smarter, greener, cheeper electricity system. Technical report, Policy Exchange, London, UK, 2016.

[17] M. Variny and O. Mierka. Improvement of part load efficiency of a combined cycle power plant provisioning ancillary services. *Applied Energy*, 86:888–894, 2009.

[18] A. Rovira, C. Sanchez, M. Munoz, M. Valdes, and M.D. Duran. Thermoeconomic optimisation of heat recovery steam generators of combined cycle gas turbine power plants considering off-design operation. *Energy conversion and management*, 52:1840–1849, 2011.

[19] J. Zachary. How combined cycle configuration is impacted by current power market requirements. In *ASME Turbo Expo*, pages 607–619, 2012.

[20] G.G. Ol'Khovskii. Prospective gas turbine and combined-cycle units for power engineering (a review). *Thermal Engineering*, 60(2):79–88, 2013.

[21] H. Saravanamuttoo, G. Rogers, and H. Cohen. *Gas turbine theory*. ASME, 6th edition, 2010.

[22] P. Walsh and P. Fletcher. *Gas turbine performance*. Blackwell Science Ltd, 2004.

[23] R. Kehlhofer. *Combined Cycle Gas and Steam Turbine Power Plants*. Fairmont Press, Lilburn GA, 1991.

[24] P.J. Dechamps. Combined cycle power plant short course. Cranfield University, 2016.

[25] M.P. Boyce. *Handbook for cogeneration and combined cycle power plants*. ASME Press, New York, 2010.

[26] J.H. Kim, T.S. Kim, J.L Sohn, and S.T. Ro. Comperative analysis of off-design performance characteristics of single and two-shaft industrial gas turbine. In *ASME Turbo Expo 2002: Power for Land, Sea, and Air. American Society of Mechanical Engineers*, 2002.

[27] F. Haglind. Variable geometry gas turbines for improving the part-load performance of marine combined cycles gas turbine performance. *Energy*, 35(2):562–570, 2010.

[28] T.S. Kim. Comparative analysis on the part load performance of combined cycle plants considering design performance and power control strategy. *Energy*, 29(1):71–85, 2004.

[29] F. Haglind. Variable geometry gas turbines for improving the part-load performance of marine combined cycles combined cycle performance. *Applied Thermal Engineering*, 31(4):467–476, 2011.

[30] J.C. Westcott and L.A. Penna. Degradation in turbo machinery. In *ASME 2008*, pages 487–493, 2008.

[31] A. Zwebek and P. Pilidis. Degradation effects on combined cycle power plant performancepart i: Gas turbine cycle component degradation effects. *Eng. Gas Turbines Power*, 125(3):651, 2003.

[32] R. Kurz, K. Brun, and M. Wollie. Degradation effects on industrial gas turbines. *Eng. Gas Turbines Power*, 131, 2009.

[33] J.H. Horlock. *Combined Power Plants*. Krieger Publishing Company, 2002.

[34] S.C. Gulen and I. Mazumder. An expanded cost of electricity model for highly flexible power plants. *Journal of Engineering for Gas Turbines and Power*, 135(1):011801, Nov 2012.

[35] R. Kehlhofer. Calculation for part-load operation of combined gas/steam turbine plants. *Brown Boveri Review*, pages 672 – 679, 1978.

[36] G. Gyarmathy. On load control methods for combined cycle plants. In *ASME IGTI*, pages 39–50, 1989.

[37] P.J. Dechamps, N. Pirard, and Ph. Mathieu. Part load operation of combined cycle plants with and without supplementary firing. Portland, 1994. ASME Cogen-Turbo.

[38] V. Ganapathy. Simplify heat recover steam generator evaluation. *Hydrocarbon processing*, 1990.

[39] N. Lior. Thoughts about future power generation systems and the role of exergy analysis in their development. *Energy conversion and management*, pages 1187 – 1198, 2002.

[40] J.S. In and S.Y. Lee. Optimization of heat recovery steam generator through exergy analysis for combined cycle gas turbine power plants. *International Journal of Energy Research*, 2008.

[41] S.C. Gulen and J. Joseph. Combined cycle off-design performance estimation: a second-law perspective. *Journal of Engineering for Gas Turbines and Power*, 2012.

[42] M. Valdes and J.L. Rapun. Optimization of heat recovery steam generators for combined cycle gas turbine power plants. *Applied Thermal Engineering*, 2001.

[43] M. Mohagheghi and J. Shayegan. Thermodynamic optimization of design variables and heat exchangers layout in hrsgs for ccgt, using genetic algorithm. *Applied Thermal Engineering*, 2009.

[44] G. Zhang, J. Zheng, A. Xie, Y. Yang, and W. Liu. Thermodynamic analysis of combined cycle under design/off-design conditions for its efficient design and operation. *Energy conversion and management*, 2016.

[45] G. Zhang, J. Zheng, Y. Yang, and W. Liu. Thermodynamic performance simulation and concise formulas for triple-pressure reheat hrsg of gassteam combined cycle under off-design condition. *Energy conversion and management*, 2016.

[46] S.S. Rao. *Applied numerical methods for engineers and scientists*. Prentice Hall, 2002.

[47] P.S. Mhetre. Genetic algorithm for linear and nonlinear equation. *International Journal of Advanced Engineering Technology*, 2012.

[48] N.E. Mastorakis. Solving non-linear equations via genetic algorithm. In *WSEAS International Conference on Evolutionary Computing*, number 6th, 2005.

[49] I.M.M. El-Emary and M.M.A. El-Kareem. Towards using genetic algorithm for solving nonlinear equation systems. *World Applied Sciences Journal*, pages 282–289, 2008.

[50] A. Zhou, B. Y. Qu, H. Li, S. Z. Zhao, et al. Multiobjective evolutionary algorithms: A survey of the state of the art. *Swarm and Evolutionary Computation*, 1:32–49, 2011.

[51] M. Valdes, D. Duran, and A. Rovira. Thermoeconomic optimization of combined cycle gas turbine power plants using genetic algorithm. *Applied Thermal Engineering*, 2003.

[52] C. Koch, F. Cziesla, and G. Tsatsaronis. Optimization of combined cycle power plants using evolutionary algorithm. *Chemical Engineering and Processing*, 2007.

[53] A.G. Kaviri, M. N.M. Jaafar, and T.M. Lazim. Modeling and multi-objective exergy based optimization of a combined cycle power plant using a genetic algorithm. *Energy Conversion and Management*, 2012.

[54] M. Ghazi, P. Ahmadi, A.F. Sotoodeh, and A. Taherkhani. Modeling and thermoeconomic optimization of heat recovery heat exchangers using a multimodal genetic algorithm. *Energy Conversion and Management*, 2012.

[55] U. Bodenhofer. Genetic aalgorithm: theory and applications. Technical report, Fuzzy logic laboratorium Linz-Hagenberg, 2003.

[56] F. Herrera, M. Lozano, and J.L. Verdegay. Tacking real-coded genetic algorithms: operators and tools for behaviour analysis. *Artificial Intelligence Review*, 1998.

[57] K. Jebari and M. Madiafi. Selection methods for genetic algorithms. *International Journal fof Emerging Sciences*, 2013.

[58] E. Mezura-Montes and C.A. Coello. Constraint-handling in nature-inspired numerical optimization: Past, present and future. *Swarm and Evolutionary Computation*, 2011.

[59] R. Singh. Gas turbine combustors volume 1. Cranfield University 2011.

[60] Alloy website. www.specialmetals.com. 1190.

[61] J. Bannantine, J. Comer, and J. Handrock. *Fundamentals of Metal Fatigue Analysis*. Prentice Hall, 1990.

[62] T. Isaiah, S. Dabbashi, D. Bosak, S. Sampath, G. Di-Lorenzo, and P. Pilidis. Life analysis of industrial gas turbines used as a back-up to renewable energy sources. In *Procedia CIRP*, volume 38, pages 239–244, 2015.

[63] Y.A. Cengel and M.A. Boles. *Thermodynamics: an engineering approach*. McGraw-Hill, 2008.

[64] Y.A. Cengel and A.J. Ghajar. *Heat and Mass Transfer: Fundamentals and Applications*. McGraw, 2011.

[65] V. Ganapathy. Heat-recovery steam generators: Understand the basics. *Chemical Engineering Progress*, August 1996.

[66] P.L. Iglesias, D. Mora, F.J. Martinez, and V.S. Fuertes. Study of sensivitiy of the parameters of a genetic algorithm for design of water distribution networks. *Journal of Urban and Environmental Engineering*, 2007.

[67] P. Aref. *Development of a framework for thermoeconomic optimization of simple and combined gas turbine cycles*. PhD thesis, Cranfield University, 2012.

Appendix A

Supporting formulations

A.1   Steam formulations

The following empirical steam formulations have been developed by Dechamps [24].
Saturated liquid equations

$$
\begin{aligned}
h(t) = (((((((((2.788 \times 10^{-19}t - 3.987 \times 10^{-16})t + 2.39894 \times 10^{-13}) \\
t - 7.857 \times 10^{-11})t + 1.521311 \times 10^{-8})t - 1.76274 \times 10^{-6}) \\
t + 1.208711 \times 10^{-4})t - 4.45397 \times 10^{-3})t + 4.25348)t
\end{aligned}
\tag{A.1}
$$

$$
\begin{aligned}
s(t) = ((((8.73065 \times 10^{-13}t - 7.078056 \times 10^{-10})t + 2.341782 \times 10^{-7}) \\
t - 4.794256 \times 10^{-5})t + 1.619232 \times 10^{-2})t - 8.387074 \times 10^{-3}
\end{aligned}
\tag{A.2}
$$

Saturated steam equations

$$
h(t) = \frac{((-7.35167 \times 10^{-3})t + 2.43725)t + 2491.695 + 6349.4}{t - 387.449}
\tag{A.3}
$$

$$
s(t) = ((-1.18467 \times 10^{-7}t + 7.9544 \times 10^{-5})t - 0.024623)t + 9.13
\tag{A.4}
$$

Saturated relations

$$
\begin{aligned}
p(t) = exp(-5.09132 + t(0.0718934 + t(-2.72751 \times 10^{-4} + \\
t(7.65835 \times 10^{-7} + t(-1.29359 \times 10^{-9} + 9.5642 \times 10^{-13}t)))))
\end{aligned}
\tag{A.5}
$$

$$
\begin{aligned}
t(p) = (((0.019523log(p) + 0.2438)log(p) + 2.388)log(p) + \\
27.834)log(p) + 99.6
\end{aligned}
\tag{A.6}
$$

Superheated steam equations

173

$$h(t,p) = (3.04331 \times 10^{-4}t + 1.81687)t + 2503.63 - 21492.63w(\frac{1.93115 \times 10^{-2}}{v^3}$$
$$+ \frac{w^2(1.35956 \times 10^{-2} + 4.06747 \times 10^{-3}w^2)}{v^{14.7866}})$$

(A.7)

Where

$$v = \frac{t + 276.158}{647.719}$$

$$w = \frac{p}{219.345}$$

$$s(t,p) = ((0.907643tr - 3.64635)tr + 6.57334)tr + 2.13856 - 0.461853(log(pr) + \frac{pr}{tr_4} + pr_4^3)$$

(A.8)

Where

$$pr = \frac{p}{219.1963}$$

$$pr_4 = \frac{pr}{tr \times tr_4}$$

$$tr = \frac{t + 271.8659}{645.9763}$$

$$tr_4 = tr^4$$

The constant specific heats correlations for gas turbine flue gas [67].

$$\begin{cases} Cp_g = 1.023204 - 1.76021 \times 10^{-4}T_g + 4.0205 \times 10^{-7}T_g^2 \\ \qquad\qquad - 4.87272 \times 10^{-11}T_g^3, \quad 250 \leq T_g < 600 \\ Cp_g = 0.874334 - 3.22814 \times 10^{-4}T_g + 3.58694 \times 10^{-8}T_g^2 \\ \qquad\qquad - 1.99196 \times 10^{-11}T_g^3, \quad 600 \leq T_g \leq 1500 \end{cases}$$

(A.9)

A.2   Combined cycle efficiency

The following investigation reveals the effect of gas turbine efficiency on the water/steam cycle efficiency [23].

$$\eta_{cc} = \frac{P_{GT} + P_{ST}}{\dot{Q}_{GT} + \dot{Q}_{SF}} \tag{A.10}$$

Where

$$\eta_{GT} = \frac{P_{GT}}{\dot{Q}_{GT}} \tag{A.11}$$

$$\eta_{ST} = \frac{P_{ST}}{\dot{Q}_{GT,exhaust} + \dot{Q}_{SF}} = \frac{P_{ST}}{\dot{Q}_{GT}(1 - \eta_{GT}) + \dot{Q}_{SF}} \tag{A.12}$$

solving equations A.11 and A.12 and substituting results in A.10

$$\eta_{cc} = \frac{\eta_{GT}\dot{Q}_{GT} + \eta_{ST}\left[\dot{Q}_{GT}(1 - \eta_{GT}) + \dot{Q}_{SF}\right]}{\dot{Q}_{GT} + \dot{Q}_{SF}} \tag{A.13}$$

for most combined cycle power plants no supplementary firing is used, $\dot{Q}_{SF} = 0$; therefore equation A.13 becomes

$$\eta_{cc} = \eta_{GT} + \eta_{ST}(1 - \eta_{GT}) = \eta_{GT} + \eta_{ST} - \eta_{ST}\eta_{GT} \tag{A.14}$$

differentiating equation A.14 will reveal the effect of changing η_{GT} on η_{CC}

$$\frac{\delta\eta_{cc}}{\delta\eta_{GT}} = 1 + \frac{\delta\eta_{ST}}{\delta\eta_{GT}} - (\eta_{ST} + \frac{\delta\eta_{ST}}{\delta\eta_{GT}}\eta_{GT}) \tag{A.15}$$

increasing η_{GT} improves η_{CC} only if the slope is positive, thus $\frac{\delta\eta_{cc}}{\delta\eta_{GT}} > 0$. Therefore,

$$1 + \frac{\delta\eta_{ST}}{\delta\eta_{GT}} - (\eta_{ST} + \frac{\delta\eta_{ST}}{\delta\eta_{GT}}\eta_{GT}) > 0$$

$$\frac{\delta\eta_{ST}}{\delta\eta_{GT}}(1 - \eta_{GT}) > \eta_{ST} - 1$$

$$-\frac{\delta\eta_{ST}}{\delta\eta_{GT}} < \frac{1 - \eta_{ST}}{1 - \eta_{GT}} \tag{A.16}$$

$$\frac{\delta\eta_{ST}}{\delta\eta_{GT}} > -\frac{1 - \eta_{ST}}{1 - \eta_{GT}} \tag{A.17}$$

According to equation A.17, the slope is negative which means that improvement in gas turbine efficiency will result in deterioration in steam cycle efficiency [23].

A.3   Newton-Raphson method

Newton-Raphson method is widely used for solving a system of simultaneous non-linear algebraic equations. Given the following set of equations

$$f_1(x_1, x_2, x_3, ..., x_n) = 0$$
$$f_2(x_1, x_2, x_3, ..., x_n) = 0$$
$$\vdots$$
$$f_n(x_1, x_2, x_3, ..., x_n) = 0$$

If the f functions are expended with Taylor's series around an arbitrary guessed solution, the functions can be re-written in the following form

$$\begin{bmatrix} \frac{\partial f_1}{\partial x_1} & \frac{\partial f_1}{\partial x_2} & \frac{\partial f_1}{\partial x_3} & \cdots & \frac{\partial f_1}{\partial x_n} \\ \frac{\partial f_2}{\partial x_1} & \frac{\partial f_2}{\partial x_3} & \frac{\partial f_2}{\partial x_3} & \cdots & \frac{\partial f_2}{\partial x_n} \\ \vdots & \vdots & \vdots & \ddots & \vdots \\ \frac{\partial f_n}{\partial x_1} & \frac{\partial f_n}{\partial x_3} & \frac{\partial f_n}{\partial x_3} & \cdots & \frac{\partial f_n}{\partial x_n} \end{bmatrix} \begin{bmatrix} \Delta x_1 \\ \Delta x_2 \\ \vdots \\ \Delta x_n \end{bmatrix} = \begin{bmatrix} -f_1 \\ -f_2 \\ \vdots \\ -f_n \end{bmatrix} \tag{A.18}$$

The matrix of partial derivatives is known as Jacobian matrix, which is computed at current approximations of x_1, x_2, and x_n. The system of non-linear equations is solved for $\Delta x_1, \Delta x_2$, and Δx_n, and the guess for next iteration is calculated with the following relation, where i and $i+1$ represents current and next iteration number.

$$x_1^{i+1} = x_1^i + \Delta x_1^i \tag{A.19}$$
$$x_2^{i+1} = x_2^i + \Delta x_2^i \tag{A.20}$$
$$\vdots \tag{A.21}$$
$$x_n^{i+1} = x_n^i + \Delta x_n^i \tag{A.22}$$

The iterative process, therefore, starts with initial arbitrary guess at iteration $i = 1$. Partial derivatives in the Jacobian matrix and functions, f, are evaluated, and equation A.18 is solved for the Δx matrix. New solution is then evaluated with equation A.19, and new function values $f_n(x_1, x_2, x_3, ..., x_n)$ are determined. The results are then checked against convergence criteria, which may vary according to the needs. Typical convergence criteria is shown in equation A.23, where ε refers to the maximum acceptable error. However, the algorithm may also be regarded as converged if the difference between f^{i+1} and f^i is sufficiently low.

$$|f(x_1^{i+1}, x_2^{i+1}, ..., x_3^{i+1})| \leq \varepsilon \tag{A.23}$$

Appendix B

Extended results

B.1 db.match.CCPP input files

```
db.match.CCPP [Single pressure + reheat CCPP]
Version: 1

start.

Valv                  S 11 0 1 0        G 0 0              D 1 2
StTu                  S 1 0 2 0         G 0 0              D 3 5
ReHe                  S 2 0 3 0         G 102 103          D 6 6
StTu                  S 3 0 4 0         G 0 0              D 7 9
Cond                  S 4 0 5 0         G 0 0              D 10 12
Pump                  S 5 0 6 0         G 0 0              D 13 14
Econ                  S 6 0 7 0         G 104 105          D 15 15
Drum                  S 7 9 8 10        G 0 0              D 0 0
Evap                  S 8 0 9 0         G 103 104          D 16 16
SuHe                  S 10 0 11 0       G 101 102          D 17 17

end.

start.
1 112.47              !Steam live pressure (bar)
2 -1                  !Steam live mass flow

3 541                 !Steam turbine metallurgical temperature limit (degC)
4 84                  !Steam turbine isentropic efficiency (%)
5 20                  !Steam turbine outlet pressure

6 30                  !Reheat pinch point temperature difference (degC)

7 541                 !Steam turbine metallurgical temperature limit (degC)
8 84                  !Steam turbine isentropic efficiency (%)
9 0.05                !Steam turbine outlet pressure

10 1                  !Condenser cooling water pressure (bar)
11 13                 !Condenser cooling water temperature (degC)
12 10                 !Condenser cooling water temperature rise (degC)

13 112.47             !Pump exit pressure (bar)
14 90                 !Pump isentropic efficiency (%)

15 10                 !Economizer approach point temperature difference (degC)

16 20                 !Evaporator pinch point temperature difference (degC)

17 30                 !Superheater pinch point temperature difference (degC)

end.
```

Fig. B.1 1 pressure with reheat db.match.CCPP input file

```
db.match.CCPP [Dual pressure CCPP]
Version: 1

start.

Valv                S 1  0  2  0    G 0 0              D 1  2
StTu                S 2  0  3  0    G 0 0              D 3  5
Mixi                S 3  19 4  0    G 0 0              D 0  0
StTu                S 4  0  5  0    G 0 0              D 6  8
Cond                S 5  0  6  0    G 0 0              D 9  11
Pump                S 6  0  7  0    G 0 0              D 12 13
Econ                S 7  0  8  0    G 106 107          D 14 16
Drum                S 8  17 9  18   G 0 0              D 0  0
Spli                S 9  0  16 10   G 0 0              D 17 17
Evap                S 16 0  17 0    G 105 106          D 18 20
SuHe                S 18 0  19 0    G 104 105          D 21 22
Pump                S 10 0  11 0    G 0 0              D 23 24
Econ                S 11 0  12 0    G 103 104          D 25 27
Drum                S 12 14 13 15   G 0 0              D 0  0
Evap                S 13 0  14 0    G 102 103          D 28 30
SuHe                S 15 0  1  0    G 101 102          D 31 32

end.

start.
1 -1                !Valve, steam live pressure (bar), or '-1' for non-use
2 -1                !Valve, steam live mass flow, or '-1' for non-use

3 541               !Steam turbine, metallurgical temperature limit (degC)
4 84                !Steam turbine, isentropic efficiency (%)
5 20                !Steam turbine, outlet pressure

6 541               !Steam turbine, metallurgical temperature limit (degC)
7 84                !Steam turbine, isentropic efficiency (%)
8 0.05              !Steam turbine, outlet pressure

9 1                 !Condenser, cooling water pressure (bar)
10 13               !Condenser, cooling water temperature (degC)
11 10               !Condenser, cooling water temperature rise (degC)

12 17               !Pump Control, outlet1 number linking to required pressure at evaporator
13 90               !Pump, isentropic efficiency (%)

14 10               !Economizer Control, approach point temperature difference (degC)
15 -1               !Economiser, U*A (kW/m^2/degC * m^2 = kW/degC), or '-1' to non-use
16 4                !Economiser Control, outlet1 linking to required mass flow rate, or '-1' to non-use

17 17               !Splitter Control, mass flow at outlet1 equal to at outlet station

18 20               !Evaporator Control, operating pressure (bar), or '-1' for analysis
19 -1               !Evaporator, U*A (kW/m^2/degC * m^2 = kW/degC), or '-1' to non-use
20 20               !Evaporator Control, pinch point temperature difference (degC), or '-1' to non-use

21 -1               !Superheater, U*A (kW/m^2/degC * m^2 = kW/degC), or '-1' to non-use
22 30               !Superheater Control, pinch point temperature difference (degC), or '-1' to non-use

23 14               !Pump Control, outlet1 number linking to required pressure at evaporator
24 90               !Pump, isentropic efficiency (%)

25 10               !Economizer Control, approach point temperature difference (degC)
26 -1               !Economiser, U*A (kW/m^2/degC * m^2 = kW/degC)
27 14               !Economiser Control, outlet1 linking to required mass flow rate, or '-1' to non-use

28 156              !Evaporator Control, operating pressure (bar), or '-1' for analysis
29 -1               !Evaporator, U*A (kW/m^2/degC * m^2 = kW/degC), or '-1' to non-use
30 20               !Evaporator Control, pinch point temperature difference (degC), or '-1' to non-use

31 -1               !Superheater, U*A (kW/m^2/degC * m^2 = kW/degC), or '-1' to non-use
32 30               !Superheater Control, pinch point temperature difference (degC), or '-1' to non-use

end.
```

Fig. B.2 2 pressure db.match.CCPP input file

```
db.match.CCPP [Dual pressure + reheat CCPP]
Version: 1

start.

Valv                    S 1  0  2  0    G 0 0              D 1  2
StTu                    S 2  0  3  0    G 0 0              D 3  5
Mixi                    S 3  20 4  0    G 0 0              D 0  0
ReHe                    S 4  0  5  0    G 102 103          D 6  6
StTu                    S 5  0  6  0    G 0 0              D 7  9
Cond                    S 6  0  7  0    G 0 0              D 10  12
Pump                    S 7  0  8  0    G 0 0              D 13 14
Econ                    S 8  0  9  0    G 107 108          D 15 15
Drum                    S 9  18 10  19  G 0 0              D 0  0
Spli                    S 10 0  11 17   G 0 0              D 16 16
Evap                    S 17 0  18 0    G 106 107          D 17 17
SuHe                    S 19 0  20 0    G 105 106          D 18 18
Pump                    S 11 0  12 0    G 0 0              D 19 20
Econ                    S 12 0  13 0    G 104 105          D 21 21
Drum                    S 13 15 14 16   G 0 0              D 0  0
Evap                    S 14 0  15 0    G 103 104          D 22 22
SuHe                    S 16 0  1  0    G 101 102          D 23 23

end.

start.
1 112.47              !Steam live pressure (bar)
2 -1                  !Steam live mass flow

3 541                 !Steam turbine metallurgical temperature limit (degC)
4 84                  !Steam turbine isentropic efficiency (%)
5 40                  !Steam turbine outlet pressure

6 30                  !Reheat pinch point temperature difference (degC)

7 541                 !Steam turbine metallurgical temperature limit (degC)
8 84                  !Steam turbine isentropic efficiency (%)
9 0.05                !Steam turbine outlet pressure

10 1                  !Condenser cooling water pressure (bar)
11 13                 !Condenser cooling water temperature (degC)
12 10                 !Condenser cooling water temperature rise (degC)

13 40                 !Pump exit pressure (bar)
14 90                 !Pump isentropic efficiency (%)

15 10                 !Economizer approach point temperature difference (degC)

16 3                  !Splitter mass flow at outlet1 equal to at station number

17 20                 !Evaporator pinch point temperature difference (degC)

18 20                 !Superheater pinch point temperature difference (degC)

19 112.47             !Pump exit pressure (bar)
20 90                 !Pump isentropic efficiency (%)

21 10                 !Economizer approach point temperature difference (degC)

22 20                 !Evaporator pinch point temperature difference (degC)

23 30                 !Superheater pinch point temperature (degC)

end.
```

Fig. B.3 2 pressure with reheat db.match.CCPP input file

```
db.match.CCPP [Triple pressure CCPP]
Version: 1

start.

Pump          S 1  0   2  0    G 0 0           D 1  2
Econ          S 2  0   3  0    G 109 110       D 3  5
Drum          S 3  6   4  7    G 0 0           D 0  0
Spli          S 4  0   5  11   G 0 0           D 6  6
Evap          S 5  0   6  0    G 108 109       D 7  9
SuHe          S 7  0   8  0    G 107 108       D 10 11
Mixi          S 8  20  9  0    G 0 0           D 0  0
StTu          S 9  0   10 0    G 0 0           D 12 14
Cond          S 10 0   1  0    G 0 0           D 15 17

Pump          S 11 0   12 0    G 0 0           D 18 19
Econ          S 12 0   13 0    G 106 107       D 20 22
Drum          S 13 16  14 17   G 0 0           D 0  0
Spli          S 14 0   15 21   G 0 0           D 23 23
Evap          S 15 0   16 0    G 105 106       D 24 26
SuHe          S 17 0   18 0    G 104 105       D 27 28
Mixi          S 18 29  19 0    G 0 0           D 0  0
StTu          S 19 0   20 0    G 0 0           D 29 31

Pump          S 21 0   22 0    G 0 0           D 32 33
Econ          S 22 0   23 0    G 103 104       D 34 36
Drum          S 23 25  24 26   G 0 0           D 0  0
Evap          S 24 0   25 0    G 102 103       D 37 39
SuHe          S 26 0   27 0    G 101 102       D 40 41
Valv          S 27 0   28 0    G 0 0           D 42 43
StTu          S 28 0   29 0    G 0 0           D 44 46

end.
|
start.

1 6           !Pump Control, outlet1 number linking to required pressure at evaporator
2 93          !Pump, isentropic efficiency (%)

3 10          !Economizer Control, approach point temperature difference (degC)
4 -1          !Economiser, U*A (kW/m^2/degC * m^2 = kW/degC), or '-1' to non-use
5 9           !Economiser Control, outlet1 linking to required mass flow rate, or '-1' to non-use

6 6           !Splitter Control, mass flow at outlet1 equal to at outlet station

7 5           !Evaporator Control, operating pressure (bar), or '-1' for analysis
8 -1          !Evaporator, U*A (kW/m^2/degC * m^2 = kW/degC), or '-1' to non-use
9 20          !Evaporator Control, pinch point temperature difference (degC), or '-1' to non-use

10 -1         !Superheater, U*A (kW/m^2/degC * m^2 = kW/degC), or '-1' to non-use
11 30         !Superheater Control, pinch point temperature difference (degC), or '-1' to non-use

12 541        !Steam turbine, metallurgical temperature limit (degC)
13 84         !Steam turbine, isentropic efficiency (%)
14 0.05       !Steam turbine, outlet pressure

15 1          !Condenser, cooling water pressure (bar)
16 13         !Condenser, cooling water temperature (degC)
17 10         !Condenser, cooling water temperature rise (degC)
18 16         !Pump Control, outlet1 number linking to required pressure at evaporator
19 90         !Pump, isentropic efficiency (%)

20 10         !Economizer Control, approach point temperature difference (degC)
21 -1         !Economiser, U*A (kW/m^2/degC * m^2 = kW/degC), or '-1' to non-use
22 19         !Economiser Control, outlet1 linking to required mass flow rate, or '-1' to non-use

23 16         !Splitter Control, mass flow at outlet1 equal to at outlet station

24 40         !Evaporator Control, operating pressure (bar), or '-1' for analysis
25 -1         !Evaporator, U*A (kW/m^2/degC * m^2 = kW/degC), or '-1' to non-use
26 20         !Evaporator Control, pinch point temperature difference (degC), or '-1' to non-use

27 -1         !Superheater, U*A (kW/m^2/degC * m^2 = kW/degC), or '-1' to non-use
28 30         !Superheater Control, pinch point temperature difference (degC), or '-1' to non-use

29 541        !Steam turbine, metallurgical temperature limit (degC)
30 84         !Steam turbine, isentropic efficiency (%)
31 5          !Steam turbine, outlet pressure

32 25         !Pump Control, outlet1 number linking to required pressure at evaporator
33 90         !Pump, isentropic efficiency (%)

34 10         !Economizer Control, approach point temperature difference (degC)
35 -1         !Economiser, U*A (kW/m^2/degC * m^2 = kW/degC), or '-1' to non-use
36 25         !Economiser Control, outlet1 linking to required mass flow rate, or '-1' to non-use

37 112        !Evaporator Control, operating pressure (bar), or '-1' for analysis
38 -1         !Evaporator, U*A (kW/m^2/degC * m^2 = kW/degC), or '-1' to non-use
39 20         !Evaporator Control, pinch point temperature difference (degC), or '-1' to non-use

40 -1         !Superheater, U*A (kW/m^2/degC * m^2 = kW/degC), or '-1' to non-use
41 30         !Superheater Control, pinch point temperature difference (degC), or '-1' to non-use

42 -1         !Valve, steam live pressure (bar), or '-1' for non-use
43 -1         !Valve, steam live mass flow, or '-1' for non-use

44 541        !Steam turbine, metallurgical temperature limit (degC)
45 84         !Steam turbine, isentropic efficiency (%)
46 40         !Steam turbine, outlet pressure
```

Fig. B.4 3 pressure db.match.CCPP input file

```
db.match.CCPP [Five pressure CCPP]
Version: 1

start.

Pump           S 1  0   2  0      G 0  0           D 1  2
Econ           S 2  0   3  0      G 115 116        D 3  5
Drum           S 3  6   4  7      G 0  0           D 0  0
Spli           S 4  0   5  11     G 0  0           D 6  6
Evap           S 5  0   6  0      G 114 115        D 7  9
SuHe           S 7  0   8  0      G 113 114        D 10 11
Mixi           S 8  20  9  0      G 0  0           D 0  0
StTu           S 9  0   10 0      G 0  0           D 12 14
Cond           S 10 0   1  0      G 0  0           D 15 17

Pump           S 11 0   12 0      G 0  0           D 18 19
Econ           S 12 0   13 0      G 112 113        D 20 22
Drum           S 13 16  14 17     G 0  0           D 0  0
Spli           S 14 0   15 21     G 0  0           D 23 23
Evap           S 15 0   16 0      G 111 112        D 24 26
SuHe           S 17 0   18 0      G 110 111        D 27 28
Mixi           S 18 30  19 0      G 0  0           D 0  0
StTu           S 19 0   20 0      G 0  0           D 29 31

Pump           S 21 0   22 0      G 0  0           D 32 33
Econ           S 22 0   23 0      G 109 110        D 34 36
Drum           S 23 26  24 27     G 0  0           D 0  0
Spli           S 24 0   25 31     G 0  0           D 37 37
Evap           S 25 0   26 0      G 108 109        D 38 40
SuHe           S 27 0   28 0      G 107 108        D 41 42
Mixi           S 28 40  29 0      G 0  0           D 0  0
StTu           S 29 0   30 0      G 0  0           D 43 45

Pump           S 31 0   32 0      G 0  0           D 46 47
Econ           S 32 0   33 0      G 106 107        D 48 50
Drum           S 33 36  34 37     G 0  0           D 0  0
Spli           S 34 0   35 41     G 0  0           D 51 51
Evap           S 35 0   36 0      G 105 106        D 52 54
SuHe           S 37 0   38 0      G 104 105        D 55 56
Mixi           S 38 49  39 0      G 0  0           D 0  0
StTu           S 39 0   40 0      G 0  0           D 57 59

Pump           S 41 0   42 0      G 0  0           D 60 61
Econ           S 42 0   43 0      G 103 104        D 62 64
Drum           S 43 45  44 46     G 0  0           D 0  0
Evap           S 44 0   45 0      G 102 103        D 65 67
SuHe           S 46 0   47 0      G 101 102        D 68 69
Valv           S 47 0   48 0      G 0  0           D 70 71
StTu           S 48 0   49 0      G 0  0           D 72 74

end.
```

```
start.

1 6        !Pump Control, outlet1 number linking to required pressure at evaporator
2 90       !Pump, isentropic efficiency (%)

3 10       !Economizer Control, approach point temperature difference (degC)
4 -1       !Economiser, U*A (kW/m^2/degC * m^2 = kW/degC), or '-1' to non-use
5 9        !Economiser Control, outlet1 linking to required mass flow rate, or '-1' to non-use

6 6        !Splitter Control, mass flow at outlet1 equal to at outlet station

7 20       !Evaporator Control, operating pressure (bar), or '-1' for analysis
8 -1       !Evaporator, U*A (kW/m^2/degC * m^2 = kW/degC), or '-1' to non-use
9 20       !Evaporator Control, pinch point temperature difference (degC), or '-1' to non-use

10 -1      !Superheater, U*A (kW/m^2/degC * m^2 = kW/degC), or '-1' to non-use
11 30      !Superheater Control, pinch point temperature difference (degC), or '-1' to non-use

12 541     !Steam turbine, metallurgical temperature limit (degC)
13 84      !Steam turbine, isentropic efficiency (%)
14 0.05    !Steam turbine, outlet pressure

15 1       !Condenser, cooling water pressure (bar)
16 13      !Condenser, cooling water temperature (degC)
17 10      !Condenser, cooling water temperature rise (degC)

18 16      !Pump Control, outlet1 number linking to required pressure at evaporator
19 90      !Pump, isentropic efficiency (%)

20 10      !Economizer Control, approach point temperature difference (degC)
21 -1      !Economiser, U*A (kW/m^2/degC * m^2 = kW/degC), or '-1' to non-use
22 19      !Economiser Control, outlet1 linking to required mass flow rate, or '-1' to non-use

23 16      !Splitter Control, mass flow at outlet1 equal to at outlet station

24 40      !Evaporator Control, operating pressure (bar), or '-1' for analysis
25 -1      !Evaporator, U*A (kW/m^2/degC * m^2 = kW/degC), or '-1' to non-use
26 20      !Evaporator Control, pinch point temperature difference (degC), or '-1' to non-use

27 -1      !Superheater, U*A (kW/m^2/degC * m^2 = kW/degC), or '-1' to non-use
28 10      !Superheater Control, pinch point temperature difference (degC), or '-1' to non-use

29 541     !Steam turbine, metallurgical temperature limit (degC)
30 84      !Steam turbine, isentropic efficiency (%)
31 20      !Steam turbine, outlet pressure

32 26      !Pump Control, outlet1 number linking to required pressure at evaporator
33 90      !Pump, isentropic efficiency (%)

34 10      !Economizer Control, approach point temperature difference (degC)
35 -1      !Economiser, U*A (kW/m^2/degC * m^2 = kW/degC), or '-1' to non-use
36 29      !Economiser Control, outlet1 linking to required mass flow rate, or '-1' to non-use

37 26      !Splitter Control, mass flow at outlet1 equal to at outlet station

38 70      !Evaporator Control, operating pressure (bar), or '-1' for analysis
39 -1      !Evaporator, U*A (kW/m^2/degC * m^2 = kW/degC), or '-1' to non-use
40 20      !Evaporator Control, pinch point temperature difference (degC), or '-1' to non-use

41 -1      !Superheater, U*A (kW/m^2/degC * m^2 = kW/degC), or '-1' to non-use
42 10      !Superheater Control, pinch point temperature difference (degC), or '-1' to non-use

43 541     !Steam turbine, metallurgical temperature limit (degC)
44 84      !Steam turbine, isentropic efficiency (%)
45 40      !Steam turbine, outlet pressure

46 36      !Pump Control, outlet1 number linking to required pressure at evaporator
47 90      !Pump, isentropic efficiency (%)

48 10      !Economizer Control, approach point temperature difference (degC)
49 -1      !Economiser, U*A (kW/m^2/degC * m^2 = kW/degC), or '-1' to non-use
50 39      !Economiser Control, outlet1 linking to required mass flow rate, or '-1' to non-use

51 36      !Splitter Control, mass flow at outlet1 equal to at outlet station

52 112     !Evaporator Control, operating pressure (bar), or '-1' for analysis
53 -1      !Evaporator, U*A (kW/m^2/degC * m^2 = kW/degC), or '-1' to non-use
54 20      !Evaporator Control, pinch point temperature difference (degC), or '-1' to non-use

55 -1      !Superheater, U*A (kW/m^2/degC * m^2 = kW/degC), or '-1' to non-use
56 10      !Superheater Control, pinch point temperature difference (degC), or '-1' to non-use

57 541     !Steam turbine, metallurgical temperature limit (degC)
58 84      !Steam turbine, isentropic efficiency (%)
59 70      !Steam turbine, outlet pressure

60 45      !Pump Control, outlet1 number linking to required pressure at evaporator
61 90      !Pump, isentropic efficiency (%)

62 10      !Economizer Control, approach point temperature difference (degC)
63 -1      !Economiser, U*A (kW/m^2/degC * m^2 = kW/degC), or '-1' to non-use
64 45      !Economiser Control, outlet1 linking to required mass flow rate, or '-1' to non-use

65 156     !Evaporator Control, operating pressure (bar), or '-1' for analysis
66 -1      !Evaporator, U*A (kW/m^2/degC * m^2 = kW/degC), or '-1' to non-use
67 20      !Evaporator Control, pinch point temperature difference (degC), or '-1' to non-use

68 -1      !Superheater, U*A (kW/m^2/degC * m^2 = kW/degC), or '-1' to non-use
69 30      !Superheater Control, pinch point temperature difference (degC), or '-1' to non-use
```

Fig. B.5 5 pressure db.match.CCPP input file